P-249

NASA Reference Publication 1249

November 1990

Hypervelocity Atmospheric Flight: Real Gas Flow Fields

IN-34
2511

John T. Howe

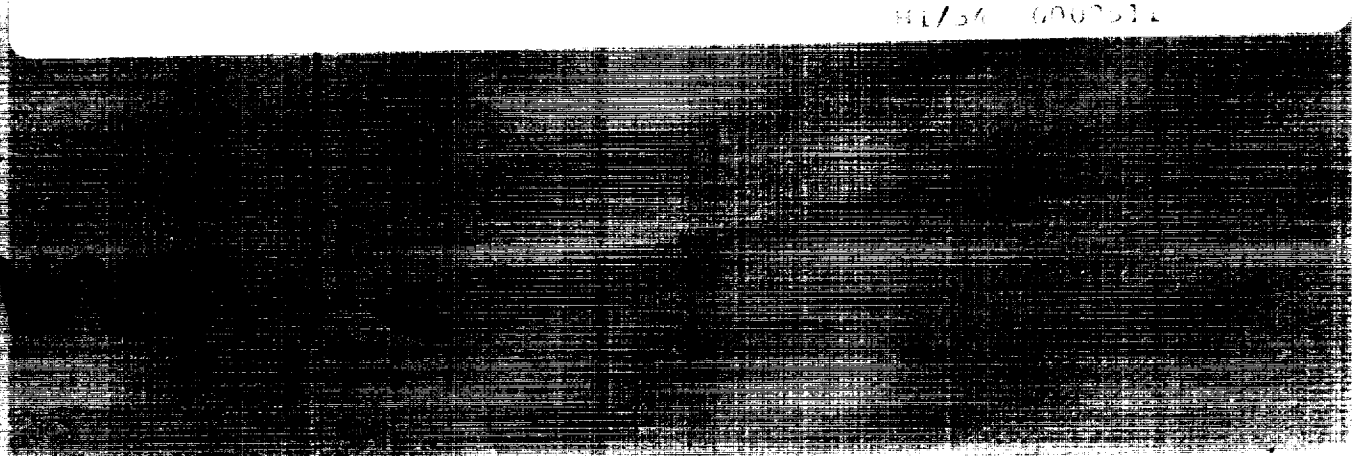

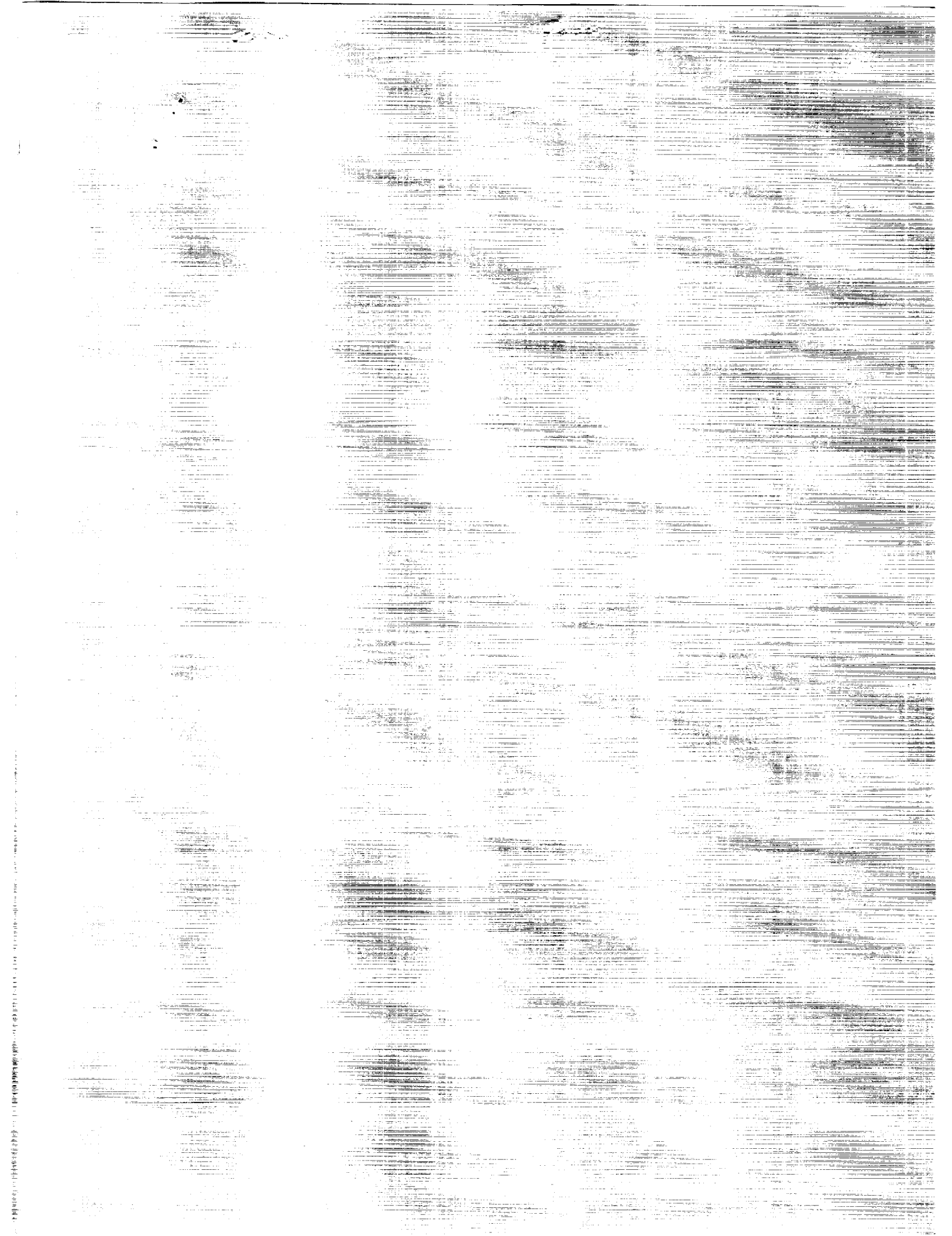

NASA Reference Publication 1249

1990

Hypervelocity Atmospheric Flight: Real Gas Flow Fields

John T. Howe
Ames Research Center
Moffett Field, California

NASA
National Aeronautics and Space Administration
Office of Management
Scientific and Technical Information Division

PREFACE

In days gone by, hypervelocity flight in planetary atmospheres primarily concerned entry into the atmosphere and descent to the ground. But in recent times, the discipline has been broadened in two directions. The first concerns reusable flight configurations that are primarily space vehicles which use the upper layers of an atmosphere to perform hypervelocity aerodynamic maneuvers to change orbital altitude, orbital plane inclination angle, aerocapture on return from another planet, or rendezvous with another space vehicle. The second direction involves vehicle concepts that fly from the ground into orbit by use of air-breathing powered lift. The former is often referred to as an aeroassisted orbital (or space) transfer vehicle (AOTV) (or ASTV) which skips out of the atmosphere and returns to space after the aeromaneuver that was performed during the shallow dip into the upper atmosphere. These vehicles can greatly enhance space payloads because they replace a very costly (in terms of fuel weight) propulsive maneuver with an aerodynamic maneuver. These aeromaneuvering concepts enhance the utilization of space for scientific, commercial, national, and international purposes.

Alas, however, it has come to be that hypervelocity flight is almost a dead language—to a considerable extent, the national institutional memory is failing. In order to guard some of what we have learned, a series of graduate-level courses has been reintroduced. This monograph is an outgrowth of that effort. It contains material that I presented in a series of lectures in 1967 at Stanford University, and began to repeat in 1986. It was apparent to the students in 1986 that the material was reassembled on short notice, consisted largely of work that I was involved with over the years (as a matter of convenience—with no intent to slight the work of many others), and was attended by considerable difficulty for me and surely for the students. It was written in barely legible longhand on the chalkboard. More serious, over the years notebooks and technical papers had been misplaced because of carelessness; the burden of administrative duty that dealt in personpower, budgets, and partially realized plans; and because of many moves by me within NASA, including the worst case—a 2-year assignment to NASA Headquarters in Washington, DC. Thus, for example, my notebook on nonneutral gas effects was found by happenstance in the garage of a friend—a week before the lectures began.

The lectures were televised in 1987 and 1988, which limited my use of the chalkboard and allowed me to be seated most of the time. Moreover, two previous students, Bertrand Delmas-Marsalet and Frederic Laurent Chalot, had prepared a succinct version of the class material by use of a word processor, which I tried to flesh out by use of a portable typewriter. Thus in every way, the lectures in 1987 were improved—or so it seemed to me. In 1989 the Stanford class was unusually responsive and this resulted in some modifications to the text and the addition of some supplemental material.

Thus the current text includes the previous material, but has been expanded to include some brief considerations of one-dimensional compressible flow without transport phenomena early in Chapter 2, more detailed treatment of thermodynamic and transport property correlations in Chapter 5, flight in atmospheres of other planets, very severe flight environments (Chapter 9), explanatory material inserted where appropriate throughout the text, and additional material about hypervelocity flight at high altitude in Chapter 11.

Finally, it is important that the formalism described here can be extended rigorously to include the effects of thermodynamic nonequilibrium in hypervelocity flight. This is significant because the level of approximation can be defined. New developments can be included systematically in such a way that new terms in the equations of change can be sized in a self-consistent way, important terms can be identified and retained (and terms of lesser importance can be neglected—a significant advantage). Thus

one can proceed in a meaningful way and avoid nonessential efforts and the confusion attending ad hoc approximations. This is of significant advantage for future extensions of the analytical treatment.

John T. Howe
1990

. . .keep that which is committed to thy trust, avoiding the profane and vain babblings and oppositions of science falsely so called which some by professing have erred concerning the faith. . .

CONTENTS

CHAPTER 1

INTRODUCTION, CONTENT, AND APPROACH

The purpose of this monograph is simple to state. We intend to develop the equations that describe the flow over an object in hypervelocity flight; assess the relative importance of all of the terms in the equations (and neglect those that are of lesser importance); describe the terms that treat the relevant, highly energetic, real-gas phenomena; solve the set of equations to obtain results, and examine those results to form some mental notions of trends and effects important to hypervelocity flight. We will examine the very severe flight environment of the Jupiter (or other planetary) atmosphere. Finally, some consideration will be given to flight at very high altitude where the flow field is relaxing chemically and even thermodynamically at finite rates. It is important to state this because there is some danger of forgetting what we are about in the process of developing the subject.

Thus we will also find ourselves trying to map flight domains in which particular phenomena are important. To the extent possible, we will be forming notions about those processes that will be most sensitive and those that will be relatively insensitive—before the problem is solved. That is a good thing to do.

Some of our flight experience in the Earth's atmosphere is depicted in figure 1-1, which shows flight regimes in terms of altitude and velocity. On the lower left is a line that represents the flight of the supersonic Concorde. By contrast, as the monograph title suggests, we are primarily concerned with flight toward the right of the figure—hypervelocity flight. We say hypervelocity rather than hypersonic. The former includes both compressible and energetic real-gas effects, while the latter primarily denotes

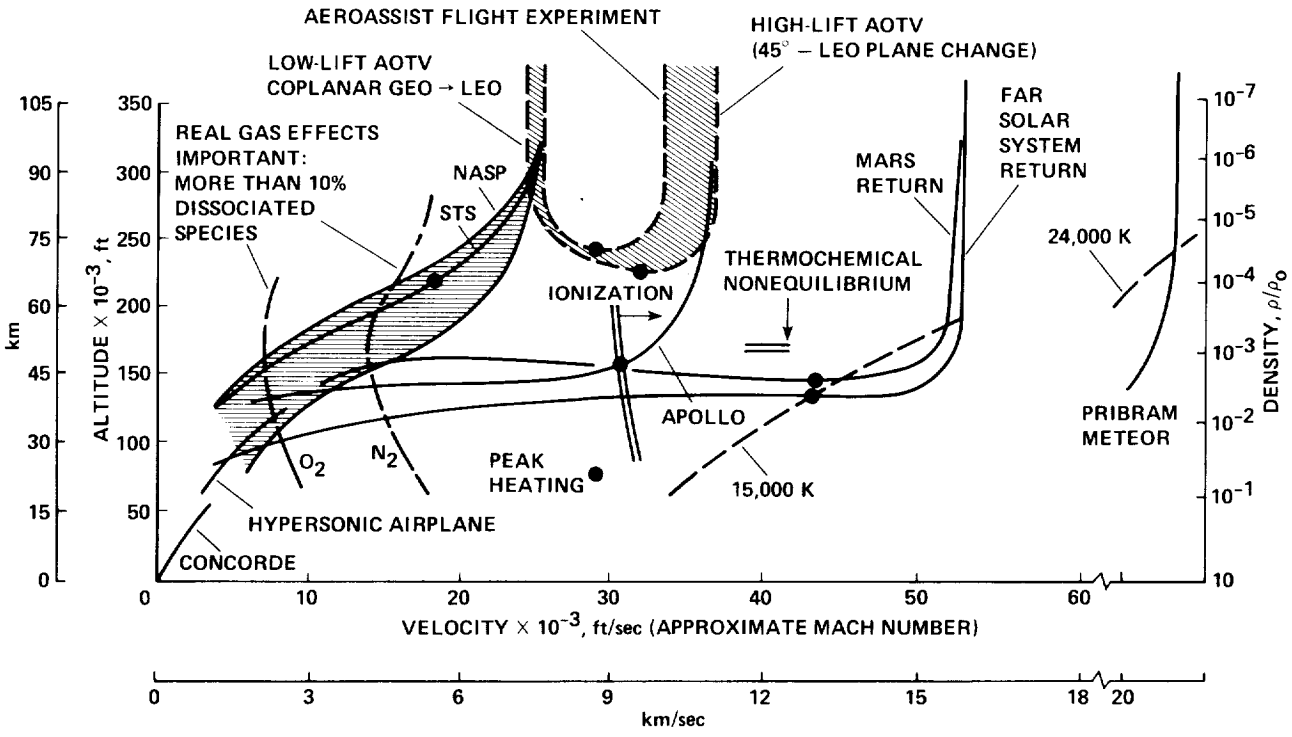

Figure 1-1.– Comparison of vehicle flight regimes in Earth's atmosphere.

compressibility effects—which can occur in a very cold gas that has little energy content per unit mass of gas (low enthalpy, if you will). Thus, atmospheric flight at Mach 10 is only 15% as energetic as entry flight from low Earth orbit. For reference, low Earth orbit circular satellite speed is approximately 7 km/sec. The figure shows domains, trajectories, and some lines that approximately bound some physical and chemical flow-field phenomena associated with hypervelocity. Note four such lines. To the right of the lines labeled O_2 and N_2, 10% or more of the oxygen and nitrogen molecules in the air behind a normal shock wave are dissociated to form atoms. To the right of the double vertical line at about 9 km/sec, electrons are stripped from the atoms and molecules to a significant extent, and ionization effects become important. Finally, at an altitude above about 50 km, the frequency of collisions among air particles is diminished to the extent that the rate at which physical and chemical processes proceed must be considered. That is, the air may be out of equilibrium chemically and thermodynamically, or both. This is the real world of hypervelocity flight. We will have occasion to refer to and modify this figure in more detail subsequently. For reference purposes, pressure and temperature contours for air in chemical equilibrium behind a normal shock wave are shown in figure 1-2 as a function of flight speed and altitude (adapted from ref. 1).

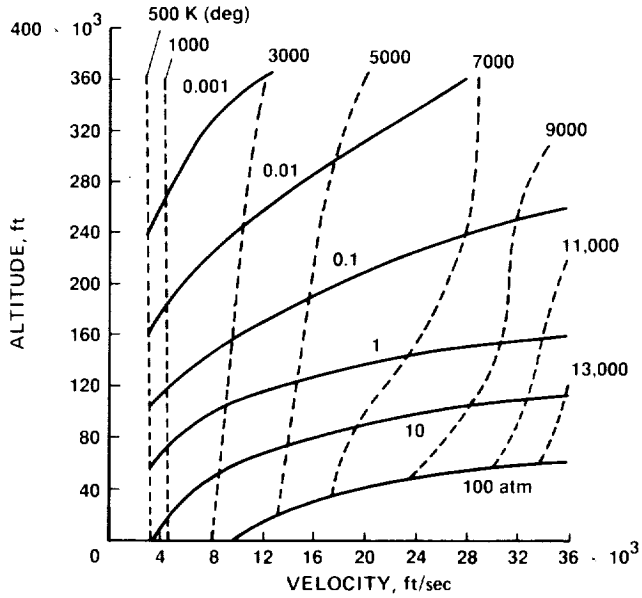

Figure 1-2.– Pressure and temperature contours for air in chemical equilibrium behind a normal shock wave (ref. 1).

Phenomenologically, in describing real-gas flows over objects in hypervelocity flight in an atmosphere, we must deal with the above phenomena and other effects of the dissipation of the kinetic energy of the probe in the atmosphere—energy that is often sufficient to vaporize the probe. Thus the flow field may be complicated by the presence of gases that have vaporized from the probe surface, and in extreme cases by solid particles that have spalled from the surface because of thermal stress in the probe material. Even at that, the surface temperature is generally much lower than the gas temperature behind the shock wave. Thus a flow-field energy equation which treats real-gas thermal phenomena is essential. Often the energy equation is strongly coupled to the momentum equation because velocity terms are common to both, and the energy level is related to velocity squared. On the other hand, the solution of the momentum equation is not always greatly affected by the corresponding solution of the energy equation. Sometimes momentum equations can be solved without an energy equation to yield shock shapes and pressure distributions that bear some resemblance to real flight—depending on the domain and how particular we are.

Since the kinetic energy imparted to the atmosphere by a hypervelocity vehicle is large enough to break molecular bonds or displace electrons, we must consider chemically reacting flows (and also the possibility of electric fields and their effects) even at some distance removed from the displaced electron. Moreover, in some regions of the flow, the gas temperature exceeds the apparent temperature of the Sun, and we suspect that the emission and transfer of thermal radiation should be considered in the gas—which may be complicated by chemical reactions that give rise to local sources and sinks of energy.

Nevertheless, it is very important that we not consider the analysis of a hypervelocity flow field to be intractable; it actually involves a number of scientific disciplines that are tractable—fluid dynamics; chemical kinetics; electrodynamics; transport of mass, momentum, energy, chemical species, and surplus charge; and radiative transfer. Further, we must consider local thermodynamic nonequilibrium—do we need more than one local temperature to characterize the gas mixture? It appears that it is necessary under some circumstances.

The task of developing each discipline or each line of thought in detail in one small monograph is out of the question. Thus we are compelled to introduce each discipline at the subjective point where it suits our purpose, combine these interrelated physical and chemical phenomena in a tractable way, and terminate it at a reasonable point. We will leave further development of this continually emerging subject to those with greater perception—to the students during their careers.

Specifically, we adopt the following approach. Rather than begin with the Boltzmann equation, we begin with the hydrodynamic equations, or "the equations of change" which can be derived from the Boltzmann equation (refs. 2, 3). Nor do we take moments of that equation to obtain transport expressions, but use the Chapman-Enskog result (refs. 2-4)—or something akin to it. This is not to minimize the important of the formalism which will be developed by use of the equations of change. It is a tool that has many advantages which cannot be overemphasized. It is compatible with incompressible, subonic, supersonic, hypersonic, and hypervelocity flows. It is self-consistent and it yields expressions for real gas behavior. It is useful for evaluating phenomenological compatibility (a charged gas will be shown to be compatible with the Navier-Stokes equations—although it was thought not to be by some authors). It enables us to express terms in the governing equations in a way wherein we can rank the size and importance of each. Some terms are interesting but negligible and we do not need to expend the effort to study them. The formalism allows various levels of approximation to be formed and provides the constraints that limit their use. Finally, it is extendable to even more severe thermochemical conditions than are considered here in a manner that is self-consistent and consistent with all that has preceded that extension. It is a remarkable tool. Moreover, our treatment of radiative transfer theory is not derived from quantum notions, but rather from developments from stellar literature (which surprisingly can be shown to have been developed independently by the paint and paper industry). Almost exclusively, we adopt the macroscopic approach obtained from the results of kinetic theory—and say very little about that theory. When at last we begin to invade the inner privacy of atoms and molecules explicitly, we will say a few words and draw a few lines and withdraw with our sensibilities partially intact. That invasion is a subject to be dealt with separately. All that we need to know is where in the flight domain it becomes important, and understand some features of that domain in an approximate way. Thus if the reader or student has a nodding acquaintance with compressible fluid mechanics, and a reasonable tolerance for pain, he or she is qualified to begin.

REFERENCES

1. Hansen, C. Frederick: Approximations for the Thermodynamic and Transport Properties of High Temperature Air. NASA TR-R-50, 1959.

2. Hirschfelder, J. O.; Curtiss, C. F.; and Bird, R. B.: Molecular Theory of Gases and Liquids. Wiley, 1954.

3. Bird, R. B.; Stewart, W. E.; and Lightfoot, E. N.: Transport Phenomena. Wiley, 1960.

4. Chapman, S.; and Cowling, T. G.: Mathematical Theory of Non-Uniform Gases. Second ed., Cambridge Univ. Press, 1951.

CHAPTER 2

SOME USEFUL COMPRESSIBLE FLOW RELATIONS FOR AN IDEAL GAS

It will be helpful subsequently to have some simple relationships concerning compressible flow to refer to. The steady one-dimensional flow of an ideal compressible gas in a constant-area duct wherein there is no transport of mass, momentum, energy, or chemical species should be familiar to the reader (ref. 1). Let us consider a normal shock wave in the duct and allow the molecular nitrogen of the approaching gas flow to be altered chemically as it crosses the shock wave such that downstream the gas is a mixture of molecules, atoms, ions, and electrons which are the product of chemical reactions that occurred as the gas crossed the shock wave.

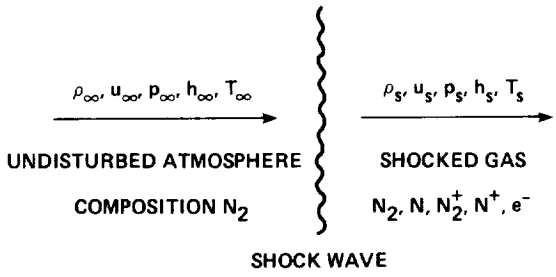

Figure 2-1.– Thermodynamic and chemical change across a normal shock.

That flow is depicted in figure 2-1, and is described by equations of the continuity of mass (where ρ is gas density and u is the gas velocity).

$$\rho u = \text{constant} \tag{1}$$

The momentum balance (where p is the pressure and x is the one-dimensional coordinate) is

$$\rho u \frac{du}{dx} = -\frac{dp}{dx} \tag{2}$$

This is a form of the Euler equation which is related to the zeroth-order perturbation of the Boltzmann equation. It is one-dimensional steady state, without viscous or body forces. Its integrated form is

$$\rho u^2 + p = \text{constant} \tag{3}$$

The simple energy equation (where h is the static enthalpy, and H is the total enthalpy) is

$$h + \frac{u^2}{2} = H = \text{constant} \tag{4}$$

The static enthalpy for a component species of a perfect gas is related to the temperature, T, by

$$h_i(T) = \int_o^T c_{p_i}\, dT + h_{i_o} \tag{5}$$

where c_{p_i} is the specific heat at constant pressure, and h_{i_O} is the heat of formation of that component of the gas at a reference temperature (zero, for example). The enthalpy of the gas mixture of ν components or species is simply

$$h = \sum_{i=1}^{\nu} c_i h_i \tag{6}$$

where $c_i = \rho_i/\rho$ is the local mass fraction of species i in the mixture. An equation of state relates the thermodynamic properties

$$\sum_{i=1}^{\nu} p_i = p = \frac{\rho RT}{M} = \sum_{i=1}^{\nu} \rho_i \frac{RT}{M_i} \tag{7}$$

where R is the universal gas constant and M_i is the molecular weight of species i.

A shock wave normal to the one-dimensional flow in figure 2-1 can be described for present purposes by use of the density ratio across the shock, which we will call ε.

$$\frac{\rho_\infty}{\rho_s} = \varepsilon \tag{8}$$

where the subscript ∞ refers to conditions ahead of the shock, and s refers to conditions behind the shock. Note that ε is affected by a change of chemical composition across the shock, which will be treated subsequently. Also, it is notable that ε is usually much less than unity. Thus the compressible flow relations (1), (3), and (4) can be used to form the relationships

$$u_s = \varepsilon u_\infty \tag{9}$$

$$p_s - p_\infty = \rho_\infty u_\infty^2 (1 - \varepsilon) \tag{10}$$

$$h_s - h_\infty = \frac{u_\infty^2}{2} - \frac{u_s^2}{2} \tag{11}$$

These relations will be used again in Chapter 10 where flows that are not in chemical equilibrium will be examined on a one-dimensional basis.

Flow of a compressible gas over an object in flight is usually not one-dimensional, especially if the object tends to be blunt. Moreover, the shock wave over an object in supersonic flight will generally tend to be a curved shock which is not everywhere normal to the flow nor parallel to the surface of the flight object or body. In Chapters 3 and 4, it will be helpful to have quantitative relationships for all the thermodynamic and flow-field variables across such a shock wave for compressible flow, as well as some "strong shock" approximate expressions for hypervelocity flow. The reason for the latter is that

some of our order-of-magnitude arguments for sizing terms in the flow-field equations can be facilitated by these expressions.

For either a two-dimensional or axisymmetric object flying at hypervelocity, $\bar{U}$, the bow shock wave in the stagnation region of the body is shown schematically in figure 2-2. The stagnation region could be the leading edge of a wing or a fin, or it may be the nose of a fuselage. It could be the inlet to an engine as well. Significantly, it is a region of a nearly normal shock wave, which implies strong compression of the atmospheric gas and potentially serious thermal effects in the flow field. Since the shock wave is generally not parallel to the body, the geometry of each, and the components of velocity normal and tangential to both the shock and the body are shown in figures 2-2 and 2-3. Note that

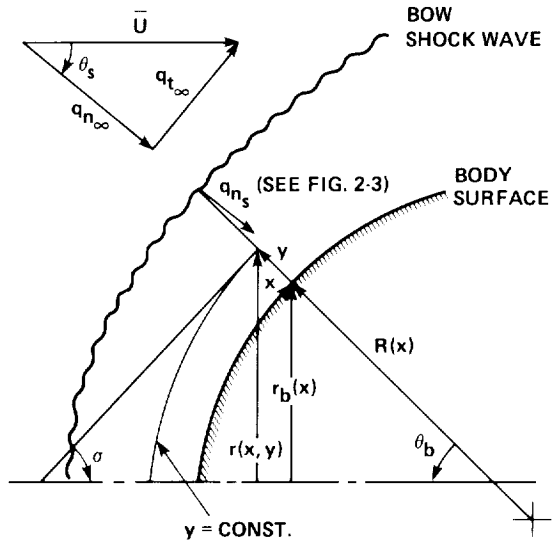

Figure 2-2.– Bow shock wave—not everywhere parallel to the body.

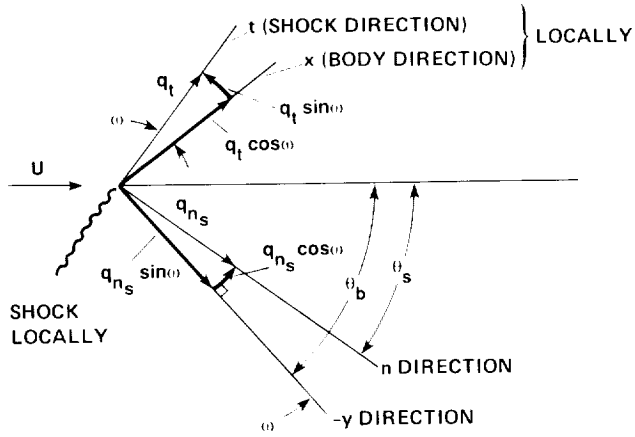

Figure 2-3.– Velocity components behind shock; shock not parallel to body locally.

shock-related velocity components are here denoted by the symbol q for clarity. Moreover, the local radius of curvature of the body is denoted by R here.

Figure 2-3 resolves the velocity components in shock coordinates behind the shock into those in body coordinates. The small angle between the directions normal to the body θ_b and the shock θ_s is

denoted by ω. It can be shown from the ordinary Rankine-Hugoniot compressibility relations for curved shock waves (similar to those shown previously for normal shock waves). From considerations of the conservation of mass

$$\rho_\infty q_{n_\infty} = \rho_s q_{n_s} \tag{12}$$

$$q_{n_s} = \frac{\rho_\infty}{\rho_s} q_{n_\infty} = \varepsilon \bar{U} \cos \theta_s \tag{13}$$

$$q_t = \bar{U} \sin \theta_s \tag{14}$$

(q_t unchanged across the shock)

$$u_s = q_t \cos \omega + q_{n_s} \sin \omega = \bar{U}(\sin \theta_s \cos \omega + \varepsilon \cos \theta_s \sin \omega) \tag{15}$$

$$-v_s = q_{n_s} \cos \omega - q_t \sin \omega = \bar{U}(\varepsilon \cos \theta_s \cos \omega - \sin \theta_s \sin \omega) \tag{16}$$

Also, from a momentum balance,

$$p_\infty + \rho_\infty q_{n_\infty}^2 = p_s + \rho_s q_{n_s}^2 \tag{17}$$

which is similar to the development for equation (10) in the direction normal to the shock. The strong shock approximation

$$p_\infty << p_s \tag{18}$$

used in equations (12) and (13) leads to

$$p_s = \rho_\infty \bar{U}^2 (1 - \varepsilon) \cos^2 \theta_s \tag{19}$$

The energy relations across the shock can be expressed as

$$h_\infty + \frac{1}{2}\left(q_{n_\infty}^2 + q_t^2\right) = h_s + \frac{1}{2}\left(q_{n_s}^2 + q_t^2\right) \tag{20}$$

or

$$h_s - h_\infty = \frac{1}{2}\left(q_{n_\infty}^2 - q_{n_s}^2\right) \tag{21}$$

Use of equation (13) in (21) yields

$$h_s - h_\infty = \frac{1}{2} q_{n_\infty}^2 (1 - \varepsilon^2) \tag{22}$$

Again, for a strong shock, h_∞ can be neglected compared with h_s, and

$$h_s = \frac{1}{2}\overline{U}^2 \cos\theta_s(1-\varepsilon^2) \approx \frac{1}{2}\overline{U}^2 \cos^2\theta_s \tag{23}$$

An equation of state, needed to calculate ε, will be considered subsequently.

Some simple geometric relationships will be useful later. Figure 2-4 shows a portion of the body surface (y = 0), and a line, y = constant.

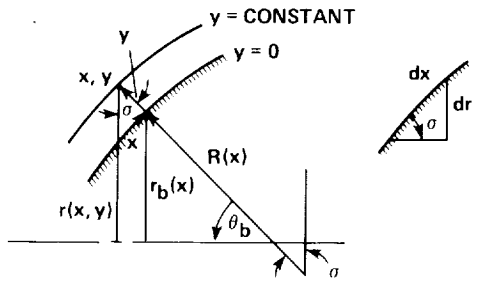

Figure 2-4.– Segment of body surface.

On the body (y = 0), from the right side of the figure,

$$(dr)_{y=0} = \sin\sigma\, dx \tag{24}$$

$$(r)_{y=0} = \int_o^x \sin\sigma\, dx \tag{25}$$

For a surface where y = constant (left side of figure),

$$r(x,y) = r_{y=0} + y\cos\sigma \tag{26}$$

$$r(x,y) = \int_o^x \sin\sigma\, dx + y\cos\sigma \tag{27}$$

$$dx = -R\, d\sigma \tag{28}$$

$$\frac{d\sigma}{dx} = -\frac{1}{R} \tag{29}$$

These relationships will suffice for subsequent reference purposes.

REFERENCE

1. Liepmann, H. W.; and Roshko, A.: Elements of Gas Dynamics. Wiley, 1957.

CHAPTER 3

CONTINUITY AND MASS FLUX CONSIDERATIONS

This chapter begins the formulation of the differential equations that describe real-gas flow fields over objects in hypervelocity flight. Simplifications will be made by use of relationships from Chapter 2. Although the simplification is not great, it is indicative of how it is done for all of the flow-field equations. The development will not be repeated for the other equations.

Continuity relations will be written for any of the individual species present which will include a term that represents the formation or depletion rate of that specie by chemical processes. It will be summed to yield the familiar global continuity equation for compressible fluid flow. It will be specialized to describe only chemical elements, which will add a term that represents the transport of each element relative to the mass averaged motion of the mixture. Further specialization can be made for each chemical specie. Charged species are considered; we will obtain the surplus charge diffusion equation. From that we will obtain the electric current and electric field. The latter gives rise to forces that affect overall motion and individual transport. We will do this in some detail because it is simplest to do so at this point rather than later, when the equations and concepts are more complicated. There is some danger that this development may appear to be tedious. However, perhaps the redeeming feature of this chapter is the wealth of useful relationships that can be derived from continuity considerations applied to real-gas flows.

General Continuity Equation

An element of volume in the coordinate system x,y,z is shown in figure 3-1. The coordinates are orthogonal at their intersections, but are not necessarily Cartesian. The coordinate units themselves do not have to be of physical length, but the product of the coordinate unit and its respective metric (h_1,h_2,h_3) is an arclength in that coordinate direction, and the square of the elemental arclength from the point x,y,z to $x + dx$, $y + dy$, and $z + dz$ is expressed in terms of h_1, h_2, and h_3.

$$h_1 = h_1(x,y,z) \quad \text{etc.} \tag{1}$$

$$\text{arclength } (ds)^2 = (h_1\,dx)^2 + (h_2\,dy)^2 + (h_3\,dz)^2$$

For convenience, consider the chemical specie i.

u_i = absolute velocity of species i

$$u_i = \underset{\text{average}}{u} + \underset{\text{relative}}{U_i} \tag{2}$$

The components of the absolute mass flux of species i in the coordinate directions are

$$\rho_i u_i = \rho_i u + \rho_i U_i \tag{3}$$

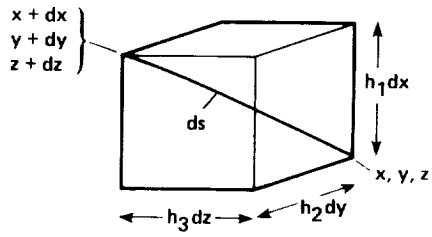

Figure 3-1.– Volume element.

or

$$\rho_i u_i = \rho_i u + J_{ix} \tag{4}$$

similarly

$$\rho_i v_i = \rho_i v + J_{iy} \tag{5}$$

$$\rho_i w_i = \rho_i w + J_{iz} \tag{6}$$

Summing equation (4) over all species i = 1 to ν yields the mass average mass flux in the x direction.

$$\rho u = \sum_{i=1}^{\nu} \rho_i u_i \tag{7}$$

Thus,

$$\sum_{i=1}^{\nu} \rho_i u_i = u\left(\sum_{i=1}^{\nu} \rho_i\right) + \sum_{i=1}^{\nu} J_{ix} = \rho u + \underbrace{\sum_{i=1}^{\nu} J_{ix}}_{0} \tag{8}$$

where the J_i are components of the mass flux vector relative to the mass average in each direction. Note that each component of the species mass flux vector relative to the global mass flux, summed over all species, is zero.

The mass flux of i normal to a surface is

$$\dot{m}_i = c_i \dot{m} + J_{iy} \tag{9}$$

(as before c_i = mass fraction = ρ_i/ρ.)

A mass balance of species i in figure 3-1 is

$$\frac{\partial}{\partial t}(\rho_i h_1\, dx\, h_2\, dy\, h_3\, dz) = -\frac{\partial}{\partial x}(\rho_i u_i h_2\, dy\, h_3\, dz)dx - \frac{\partial}{\partial y}(\rho_i v_i h_1\, dx\, h_3\, dz)dy$$

$$-\frac{\partial}{\partial z}(\rho_i w_i h_1\, dx\, h_2\, dy)dz + K_i h_1\, dx\, h_2\, dy\, h_3\, dz \qquad (10)$$

where the rate of change of the mass of species i per unit volume is shown as the difference of inflow and outflow, plus the rate of mass production per unit volume, that is, K_i = mass rate of production of species i per unit volume.

Thus

$$\frac{\partial \rho_i}{\partial t} + \frac{1}{h_1 h_2 h_3}\left[\frac{\partial}{\partial x}(\rho_i u_i h_2 h_3) + \frac{\partial}{\partial y}(\rho_i v_i h_1 h_3) + \frac{\partial}{\partial z}(\rho_i w_i h_1 h_2)\right] - K_i = 0 \qquad (11)$$

which is the conservation equation for species i. This form of the species conservation is basic, from which other relations will be derived. First let us derive the global conservation of mass flux.

Global Continuity Equation for the Steady State

Assume $\partial/\partial t = 0$ (steady state) and $\partial/\partial z = 0$ (two-dimensional or of revolution); for an axisymmetric body, z represents the cross-flow direction, and the cross flow is taken to be zero. Then substitute equations (4) and (5) into equation (11):

$$\frac{\partial}{\partial x}[h_2 h_3(\rho_i u + J_{ix})] + \frac{\partial}{\partial y}[h_1 h_3(\rho_i v + J_{iy})] = h_1 h_2 h_3 K_i \qquad (12)$$

$$\frac{\partial}{\partial x}(h_2 h_3 \rho_i u) + \frac{\partial}{\partial y}(h_1 h_3 \rho_i v) = -\frac{\partial}{\partial x}(h_2 h_3 J_{ix}) - \frac{\partial}{\partial y}(h_1 h_3 J_{iy}) + h_1 h_2 h_3 K_i \qquad (13)$$

The summation over all the species i gives

$$\frac{\partial}{\partial x}\left(h_2 h_3 u \sum_{i=1}^{v} \rho_i\right) + \frac{\partial}{\partial y}\left(h_1 h_3 v \sum_{i=1}^{v} \rho_i\right) = -\frac{\partial}{\partial x}\left(h_2 h_3 \sum_{i=1}^{v} J_{ix}\right) - \frac{\partial}{\partial y}\left(h_1 h_3 \sum_{i=1}^{v} J_{iy}\right) + h_1 h_2 h_3 \sum_{i=1}^{v} K_i \qquad (14)$$

Equation (8) shows that

$$\sum_{i=1}^{v} J_{ix} = \sum_{i=1}^{v} J_{iy} = 0 \qquad (15)$$

as was mentioned previously. Since

$$\sum_{i=1}^{v} \rho_i = \rho \Rightarrow \frac{\partial}{\partial x}(h_2 h_3 \rho u) + \frac{\partial}{\partial y}(h_1 h_3 \rho v) = h_1 h_2 h_3 \sum_{i=1}^{v} K_i \tag{16}$$

Consider the following chemical reaction:

$$A_2 \rightarrow 2A \tag{17}$$

The rate of mass loss of A_2 equals rate of mass formation of A. We have

$$\sum_{i=1}^{v} K_i = 0 \tag{18}$$

in general. Then equation (16) becomes

$$\frac{\partial}{\partial x}(h_2 h_3 \rho u) + \frac{\partial}{\partial y}(h_1 h_3 \rho v) = 0 \tag{19}$$

The metrics which convert coordinate changes to lengths are for the x, y, and z direction respectively (ref. 1)

$$h_1 = \mathcal{H} = 1 + \frac{y}{R} \tag{20}$$

$$h_2 = 1 \tag{21}$$

$$h_3 = r^j \tag{22}$$

where $j = 0$ (two-dimensional) or $j = 1$ (axisymmetric). (The last assumes no cross flow.) Thus

$$\frac{\partial}{\partial x}(\rho u r^j) + \frac{\partial}{\partial y}(\mathcal{H} \rho v r^j) = 0 \tag{23}$$

which is the steady-state global continuity equation.

Further Simplifications

Equation (23) can be simplified to the "thin shock layer" approximation by an order-of-magnitude argument as follows (where the exponent j is omitted because equation (27) of Chapter 2 is employed without regard to j):

$$\rho u \frac{\partial r}{\partial x} + r \frac{\partial(\rho u)}{\partial x} + \mathcal{H} r \frac{\partial(\rho v)}{\partial y} + \rho v \left(\mathcal{H} \frac{\partial r}{\partial y} + r \frac{\partial \mathcal{H}}{\partial y} \right) = 0 \tag{24}$$

From equations (27) and (29) of Chapter 2 and equation (20), above:

$$\frac{\partial r}{\partial x} = \sin\sigma - y\sin\sigma\frac{d\sigma}{dx} = \sin\sigma\left(1+\frac{y}{R}\right) = \mathcal{H}\sin\sigma \tag{25}$$

For order-of-magnitude estimates, we proceed as follows. Assume that shock and body are essentially parallel. From $\theta_s \approx \theta_b$ ($\omega \approx 0$) and equation (15) of Chapter 2 where we assume ε varies slowly with respect to x,

$$\frac{\partial}{\partial x}(\rho_s u_s) = \frac{\rho_\infty}{\varepsilon}\overline{U}\cos\theta_s\frac{d\theta_s}{dx} \tag{26}$$

$$R\,d\theta_s = R\,d\theta_b \approx dx \tag{27}$$

(from fig. 2-2 of Chapter 2) and

$$\frac{\partial}{\partial x}(\rho_s u_s) \approx \frac{\rho_\infty \overline{U}\cos\theta_s}{\varepsilon R} \tag{28}$$

From equation (16) of Chapter 2:

$$\frac{\partial}{\partial y}(\rho v) \sim O\left(\frac{\rho_s v_s - \rho_w v_w}{\delta}\right) \sim O\left(-\frac{\rho_\infty \overline{U}\cos\theta_s}{\delta}\right) \tag{29}$$

where $\rho_w v_w \sim -\rho_s v_s \sim +\rho_\infty \overline{U}\cos\theta_s$ (that is, surface mass addition as high as the free-stream mass flux is allowed), while $\rho_w v_w = 0$ (no mass addition) is allowed as well, and δ is the shock standoff distance.

From equation (26) of Chapter 2:

$$\frac{\partial r}{\partial y} = \cos\sigma \tag{30}$$

Say, $\delta \sim \varepsilon R$, with $\varepsilon = \rho_\infty/\rho_s$.

Substitute into equation (24) using equation (25) behind the shock and use the right side of equation (15) of Chapter 2 for u_s:

$$0 = \frac{\rho_\infty \overline{U}}{\varepsilon}\sin\theta_s\,\mathcal{H}\sin\sigma + r\frac{\rho_\infty\overline{U}}{\varepsilon R}\cos\theta_s - \mathcal{H}r\frac{\rho_\infty\overline{U}}{\varepsilon R}\cos\theta_s - \rho_\infty\overline{U}\cos\theta_s\left(\mathcal{H}\cos\sigma + \frac{r}{R}\right) \tag{31}$$

Let

$$\mathcal{H} = O(1) \tag{32}$$

$$\frac{r}{R} = O(1) \tag{33}$$

At the most

$$\sin \theta_s \sim O(1) \tag{34}$$

$$\cos \theta_s \sim O(1) \tag{35}$$

$$\sin \sigma \text{ and } \cos \sigma \sim O(1) \tag{36}$$

Multiply equation (31) by $\varepsilon/\rho_\infty \bar{U}$; at the most, the terms are of the order

$$(1) + (1) - (1) - \varepsilon(1 + 1) = 0 \tag{37}$$

Since $\varepsilon << 1$, the last term is negligible and so is the last term in equation (24), which it represents. Thus r can be regarded as $r_b(x)$, and equation (23) can be written as

$$\frac{\partial}{\partial x}(\rho u r_b^j) + \mathcal{H} r_b^j \frac{\partial}{\partial y}(\rho v) = 0 \tag{38}$$

For $\mathcal{H} \approx 1$, the steady-state global continuity equation for two-dimensional or axisymmetric flow, reduced by order-of-magnitude arguments for the thin layer approximation, becomes, from equation (38),

$$\frac{\partial}{\partial x}(\rho u r_b^j) + \frac{\partial}{\partial y}(\rho v r_b^j) = 0 \tag{39}$$

where

$$r_b = r_b(x) \tag{40}$$

Now reduce the species continuity equation for the steady state in a similar way. Rewrite equation (13) using equations (21) and (22), and the definition

$$c_i = \rho_i/\rho \tag{41}$$

$$\frac{\partial}{\partial x}(r^j c_i \rho u) + \frac{\partial}{\partial y}(r^j \mathcal{H} c_i \rho v) = -\frac{\partial}{\partial x}(r^j J_{ix}) - \frac{\partial}{\partial y}(\mathcal{H} r^j J_{iy}) + \mathcal{H} r^j K_i \tag{42}$$

$$c_i \frac{\partial}{\partial x}(\underline{\rho u r^j}) + \rho u r^j \frac{\partial c_i}{\partial x} + \mathcal{H} \rho v r^j \frac{\partial c_i}{\partial y} + c_i \frac{\partial}{\partial y}(\underline{\mathcal{H} \rho v r^j}) = -\frac{\partial}{\partial x}(r^j J_{ix}) - \frac{\partial}{\partial y}(\mathcal{H} r^j J_{iy}) + \mathcal{H} r^j K_i \tag{43}$$

The underlined terms sum to 0 because of equation (39).

We then divide by r^j, consider $r^j \sim r^j(x)$, and ($\mathcal{H} \equiv 1$). We neglect the mass-flux derivatives in x-direction, and obtain the steady-state species continuity equation for species i for two-dimensional or axisymmetric flow

$$\rho u \frac{\partial c_i}{\partial x} + \rho v \frac{\partial c_i}{\partial y} = -\frac{\partial}{\partial y}(J_{iy}) + K_i \tag{44}$$

This is the counterpart of equation (11), for steady-state, two-dimensional, or axisymmetric flow for the "thin layer," where as before

J_{iy} = mass flux vector in y direction

K_i = mass rate of production of species i per unit volume

Elemental Continuity

We next consider the element p.

Define:

M_p = atomic mass of element p

M_i = molecular mass of species i

β_{pi} = number of atoms of element p in molecule i

Also define a set of numbers α_{pi} as

$$\alpha_{pi} = \beta_{pi} \cdot \frac{M_p}{M_i} \tag{45}$$

where α_{pi} is the mass fraction of element p in species i. Multiply the steady-state reduced species continuity equation (44) by α_{pi} and sum all species:

$$\rho u \sum_{i=1}^{v} \alpha_{pi} \frac{\partial c_i}{\partial x} + \rho v \sum_{i=1}^{v} \alpha_{pi} \frac{\partial c_i}{\partial y} = -\sum_{i=1}^{v} \alpha_{pi} \frac{\partial J_{iy}}{\partial y} + \sum_{i=1}^{v} \alpha_{pi} K_i \tag{46}$$

Further define the elemental mass fraction

$$c'_p = \sum_{i=1}^{v} \alpha_{pi} c_i \tag{47}$$

and the elemental relative mass flux

$$J'_p = \sum_{i=1}^{v} \alpha_{pi} J_{iy} \tag{48}$$

Note that no elements are created

$$0 = \sum_{i=1}^{v} \alpha_{p_i} K_i \tag{49}$$

The last expression is true for ionizing flow, as will be demonstrated. Thus we have

$$\rho u \frac{\partial c'_p}{\partial x} + \rho v \frac{\partial c'_p}{\partial y} = -\frac{\partial}{\partial y}(J'_p) \tag{50}$$

which is the simplified elemental diffusion equation for the thin shock layer.

Thus we have defined two sets of constants, α_{p_i} and β_{p_i}, which are the mass of element p in species i, and the number of atoms of element p in species i, respectively. We have also defined the elemental mass fraction and elemental mass flux as c'_p and J'_p, respectively. Moreover, we have asserted the relationship in equation (49) which states that the mass of element p is unchanged by the production of species i, which will be demonstrated subsequently. The steady-state elemental diffusion equation for two-dimensional or axisymmetric flow reduced by order-of-magnitude considerations is the result, as is shown by equation (50).

It is significant that the production term which appeared in the species continuity equation (44) does not appear in the elemental continuity (or diffusion) equation (50). There are two advantages that the elemental diffusion has: (1) the specie production rate need not be specified (which is of practical utility when the flow is in chemical equilibrium) and (2) there are usually fewer elemental diffusion equations than there are species diffusion equations.

As an exercise, to demonstrate equation (49), consider the following reaction:

$$O \rightarrow O^+ + e^- \tag{51}$$

where element p is oxygen, and the species are O, O^+, and e^-. Then

$$\alpha'_{O_O} = 1 \tag{52}$$

$$\alpha'_{O_{O^+}} = \frac{M_O}{M_{O^+}} \tag{53}$$

which is a convenient convention used for the ion, and

$$\alpha'_{O_{e^-}} = 0 \tag{54}$$

$$\sum_{i=1}^{v} \alpha_{p_i} K_i = K_O + \frac{M_O}{M_{O^+}} K_{O^+} = \frac{1}{M_{O^+}} (K_O M_{O^+} + K_{O^+} M_O) \tag{55}$$

From equation (18),

$$\sum_{i=1}^{\nu} K_i = 0 = K_O + K_{O^+} + K_{e^-} = 0 \tag{56}$$

Electrons and ions are produced in the mass rate proportions

$$\frac{K_{e^-}}{K_{O^+}} = \frac{M_{e^-}}{M_{O^+}} \tag{57}$$

By use of equation (57) in the last equality of equation (56),

$$K_O = -\left(K_{O^+} + \frac{M_{e^-}}{M_{O^+}} K_{O^+}\right) = -K_{O^+}\left(1 + \frac{M_{e^-}}{M_{O^+}}\right) \tag{58}$$

Use equation (58) in the last equality of equation (55)

$$\sum_{i=1}^{\nu} \alpha_{p_i} K_i = \frac{1}{M_{O^+}}\left[-M_{O^+}K_{O^+}\left(1 + \frac{M_{e^-}}{M_{O^+}}\right) + M_O K_{O^+}\right] \tag{59}$$

Factor K_{O^+}

$$\frac{K_{O^+}}{M_{O^+}}\left[-(M_{O^+} + M_{e^-}) + M_O\right] = 0 = \sum_{i=1}^{\nu} \alpha_{p_i} K_i \tag{60}$$

which demonstrates equation (49) even for ionizing processes.

Charged-Particle Continuity

Finally, let us consider electrically charged particles.

Again, define a set of numbers:

ω_i = <u>charge number of a particle</u> = 0 neutral

−1 electrons

+1 ions

+2 doubly ionized

Multiply the reduced steady-state diffusion equation (44) by $(-\omega_i) \cdot (M_{e^-}/M_i)$ and sum over all species i:

$$\rho u \frac{\partial}{\partial x}\left[\sum_{i=1}^{\nu} (-\omega_i) \frac{M_{e^-}}{M_i} c_i\right] + \rho v \frac{\partial}{\partial y}\left[\sum_{i=1}^{\nu} (-\omega_i) \frac{M_{e^-}}{M_i} c_i\right] = -\frac{\partial}{\partial y}\left[\sum_{i=1}^{\nu} (-\omega_i) \frac{M_{e^-}}{M_i} J_{iy}\right] + \sum_{i=1}^{\nu} (-\omega_i) \frac{M_{e^-}}{M_i} K_i \tag{61}$$

Define:

$$c'_e = -\sum_{i=1}^{\nu} \left(\omega_i \frac{M_{e^-}}{M_i} c_i \right) \tag{62}$$

$$J'_e = -\sum_{i=1}^{\nu} \left(\omega_i \frac{M_{e^-}}{M_i} J_{iy} \right) \tag{63}$$

Rewrite equation (61)

$$\rho u \frac{\partial c'_e}{\partial x} + \rho v \frac{\partial c'_e}{\partial y} = -\frac{\partial}{\partial y} J'_e \tag{64}$$

which is the surplus charge diffusion equation.

We should take note of five things:

1. We have set

$$\sum_{i=1}^{\nu} (-\omega_i) \frac{M_{e^-}}{M_i} K_i = 0 \tag{65}$$

which can be demonstrated.

2. c'_e is proportional to the surplus charge density, ρ_c, as follows:

$$\rho_c = e \sum_{i=1}^{\nu} \omega_i n_i = en \sum_{i=1}^{\nu} \omega_i \frac{n_i}{n} = en \sum_{i=1}^{\nu} \omega_i x_i \tag{66}$$

where e is the electron charge, ω_i is the charge number for species i, n_i is the number of species i per unit volume of fluid, and $x_i = n_i/n$. From the relations of equations (62) and (66) and Avagadro's rule,

$$m_i = \frac{M_i}{L}, \quad n_i m_i = \rho_i, \quad \frac{nM}{L} = \rho \tag{67}$$

$$c'_e = \sum_{i=1}^{\nu} (-\omega_i) \frac{M_{e^-}}{M_i} c_i = \frac{M_{e^-}}{M} \sum_{i=1}^{\nu} (-\omega_i x_i) = -\left(\frac{M_{e^-}}{e \rho_L} \right) \rho_c \tag{68}$$

where L is Avagadro's number. For a neutral gas, even though it is ionized,

$$c'_e = 0 \tag{69}$$

or there is no surplus charge locally.

3. J'_e is proportional to the y component of electrical current J_y. From equation (5) we have

$$J_{iy} = \rho_i V_i = n_i m_i V_i = \frac{n_i M_i}{L} \cdot V_i \tag{70}$$

From equation (63) we have the mass flux of electrons relative to the mass average

$$J'_e = \sum_{i=1}^{\nu} (-\omega_i) \frac{M_{e^-} n_i V_i}{eL} = -\frac{M_{e^-}}{eL} \sum_{i=1}^{\nu} e\omega_i n_i V_i = -\frac{M_{e^-}}{eL} J_y \tag{71}$$

which also defines the y component of the current, which is the flow of charge relative to the mass average as

$$J_y = \sum_{i=1}^{\nu} e\omega_i n_i V_i \tag{72}$$

4. By summing over all species, it can be shown that

$$c'_e + \sum_{p=1}^{\eta} c'_p = 1 \tag{73}$$

5. By summing the elemental diffusion equation (50), adding the surplus charge diffusion equation (64), making use of equation (73), and integrating leads to the useful relation

$$J'_{e_y} + \sum_{p=1}^{\eta} J'_{p_y} = 0 \tag{74}$$

Thus we have derived several relations which will prove to be useful from continuity considerations for the conservation of mass, species, elements, and electric charge. Subsequently, we will combine these with the equations of momentum and energy.

REFERENCE

1. Hayes, Wallace D.; and Probstein, Ronald F.: Hypersonic Flow Theory. Academic Press, 1959, p. 168.

CHAPTER 4

THE EQUATIONS OF CHANGE; THE HYDRODYNAMIC EQUATIONS

In the previous chapter we derived some equations which properly belong in combination with those of this chapter. That is, in Chapter 3 we have derived the chemical species continuity equation, equation (11), in generalized orthogonal curvilinear coordinates; specialized that to two orthogonal coordinates for the steady state, equation (13); summed that over all species to yield the corresponding global continuity equation, equation (19); specialized it to two-dimensional or axisymmetric flow, equation (23); and finally simplified that by an order-of-magnitude analysis which allows mass addition at a rate comparable to the free-stream mass flux. From this reduced form of the global continuity equation, equation (39), we rewrote the corresponding reduced species continuity equation, equation (44); summed to yield the elemental continuity equation, equation (50), and derived the surplus charge diffusion equation, equation (64). Moreover, we established some useful statements expressed by equations (18), (49), (65), (73), and (74); related charge density to surplus charge, equation (68); and obtained expressions for the electric current, equations (71) and (72). All of this was obtained from continuity considerations, allowing for mass addition at a boundary, transport phenomena, and species production at a finite rate.

In this chapter, we will combine statements concerned with momentum and energy considerations with the above. But we will not derive these in detail as we did in Chapter 3. Rather, let us simply state the procedure for obtaining these expressions, and write the result (refs. 1-3).

Governing Differential Equations

When the equations of change (ref. 4, p. 698) are written in orthogonal curvilinear coordinates and applied to the hot gas between a body in hypervelocity flight and its bow shock wave (fig. 4-1), the

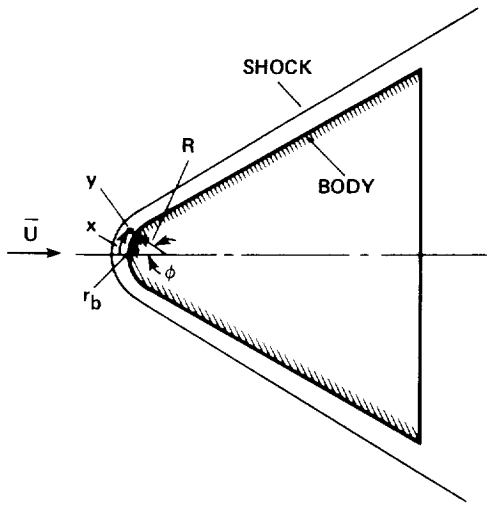

Figure 4-1.– Typical bluff configuration.

formalism leads to two momentum equations and an energy equation, each of which contains about 100 terms. To simplify, we have eliminated all of the higher order terms by an order of magnitude analysis (ref. 1).[1] The body configuration used for this analysis typifies a bluff flight object, or the nose or leading edge of a vehicle in which aerodynamic heating may be severe. The individual terms in the equations were sized in six regions of the flow: in the stagnation region, near the curved shoulder; and on the conical flank (both behind the shock wave and near the surface). Basic assumptions are that the shock layer is thin and that mass addition at the body surface can be as large as the free-stream mass flux. Terms of the order ε, $(\varepsilon Re)^{-1}$, and $(\varepsilon Re')^{-1}$ are neglected compared with unity (Re is Reynolds Number and Re' is based on bulk viscosity). Details of the simplification are too voluminous to display. However, the resulting hydrodynamic equations (which can be compared to simple hydrodynamic equations (ref. 6, p. 319)) are

x-momentum

$$\rho u \frac{\partial u}{\partial x} + \rho v \frac{\partial u}{\partial y} = \frac{\partial}{\partial y}\left(\mu \frac{\partial u}{\partial y}\right) - \frac{\partial p}{\partial x} \tag{1}$$

where μ is viscosity.

y-momentum

$$\frac{\partial p}{\partial y} = \frac{\rho u^2}{R} + \sum_{i=1}^{v} n_i Y_i \tag{2}$$

where Y_i is the y component of a body force (such as an electrical force which arises from an induced electric field caused by charge separation).

energy

$$\rho u \frac{\partial H}{\partial x} + \mathcal{H} \rho v \frac{\partial H}{\partial y} = \underbrace{-\mathcal{H} \frac{\partial}{\partial y}(q_y)}_{\text{conduction}} + \frac{\partial}{\partial y}\left(\mu u \frac{\partial u}{\partial y}\right) \underbrace{-\mathcal{H} \operatorname{div} \vec{q}_r}_{\text{radiative transfer}} + \sum_{i=1}^{v} Y_i \frac{J_{iy}}{m_i} \tag{3}$$

where the underlined terms concern transport of energy by conduction, and energy transfer by gaseous and surface radiation. An alternate form of the energy equation will be presented subsequently. To these we add the global and species continuity equations, equations (39) and (44) from chapter 3:

continuity, the global version

$$\frac{\partial}{\partial x}(\rho u r_b) + \frac{\partial}{\partial y}(\rho v r_b) = 0 \tag{4}$$

[1]Ho and Probstein (ref. 5) performed an order-of-magnitude analysis to size the terms in the stagnation region of a sphere in hypersonic rarefied flight for a perfect gas, with constant Prandtl Number, and without mass addition.

or the species version

$$\rho u \frac{\partial c_i}{\partial x} + \rho v \frac{\partial c_i}{\partial y} = -\frac{\partial}{\partial y}(J_{iy}) + K_i \tag{5}$$

These are essentially the boundary-layer equations for a reacting gas, but importantly, they apply throughout the flow about the body and are valid for strong ablation. Because ionized species are present at high-speed flight, we have retained force terms arising from electric fields in the y-momentum and energy equations. We write the elemental continuity equation for element p and for electrons

$$\rho u \frac{\partial c'_p}{\partial x} + \mathcal{H}\rho v \frac{\partial c'_p}{\partial y} = -\frac{\partial}{\partial y}(\mathcal{H} J'_p) \tag{6}$$

which is the elemental form, and

$$\rho u \frac{\partial c'_e}{\partial x} + \rho v \frac{\partial c'_e}{\partial y} = -\frac{\partial}{\partial y} J'_e \tag{7}$$

which is in the surplus charge continuity form. Equation (6) is useful for the case of chemical equilibrium, for which it would replace equation (5); the advantage being that there are fewer elements than there are species. Thus species concentrations would be calculated by other means. Equation (7) would be used if there is significant electrical charge separation.

To equations (1)–(5), we add the equation of state (for the sixth unknown):

$$p_i = \frac{\rho_i RT}{M_i} = \frac{c_i}{M_i}\rho RT = \frac{n_i m_i RT}{M_i} = n_i \frac{RT}{L} = n_i kT \tag{8}$$

where R is the universal gas constant, L is Avagadros number, n_i is the number of species i per unit volume, and k is the Boltzmann constant. Dalton's law relates partial and static pressure

$$p = \sum_{i=1}^{v} p_i = \rho RT \sum_{i=1}^{v} \frac{c_i}{M_i} = \frac{\rho RT}{M} \tag{9}$$

where it may be noted that the mixture molecular weight is

$$\left(\sum_{i=1}^{v} \frac{c_i}{M_i} \right)^{-1}$$

Other useful relations are

$$H = h + \frac{u^2}{2} + \frac{v^2}{2} \approx h + \frac{u^2}{2} \tag{10}$$

$$h = \sum_{i=1}^{v} c_i h_i \tag{11}$$

$$h_i = \int_0^T c_{p_i}\, dT + h_i^\circ \tag{12}$$

and for thermochemical equilibrium

$$c_i = c_i(\rho, T, c_p') \tag{13}$$

In these expressions, H and h are total and static enthalpy, R is the universal gas constant, and M is the mixture molecular weight (defined by eq. (9)). Equation (13) is for chemical equilibrium, and can be expressed by the law of mass action or by free energy minimization relations. For chemical nonequilibrium, reactions proceed at rates that can be expressed in the Arhennius form: first the reaction rate

$$k = AT^\alpha e^{-\Phi_1/T} \tag{14}$$

secondly

$$K_e = BT^\beta e^{-\Phi_2/T} \tag{15}$$

The latter is the equilibrium coefficient or law of mass action.

Energy Equation Expressed in Temperature Form

It is often convenient to write the energy equation, equation (3), in terms of temperature as follows. From equation (11):

$$\frac{\partial h}{\partial y} = \sum_{i=1}^{v}\left(c_i \frac{\partial h_i}{\partial y} + h_i \frac{\partial c_i}{\partial y}\right) = \sum_{i=1}^{v}\left(c_i \frac{\partial h_i}{\partial T}\frac{\partial T}{\partial y} + h_i \frac{\partial c_i}{\partial y}\right)$$

$$= \frac{\partial T}{\partial y}\sum_{i=1}^{v} c_i \frac{\partial h_i}{\partial T} + \sum_{i=1}^{v} h_i \frac{\partial c_i}{\partial y} = \frac{\partial T}{\partial y}\sum_{i=1}^{v} c_i c_{p_i} + \sum_{i=1}^{v} h_i \frac{\partial c_i}{\partial y} \tag{16}$$

or

$$\frac{\partial h}{\partial y} = \bar{c}_p \frac{\partial T}{\partial y} + \sum_{i=1}^{v} h_i \frac{\partial c_i}{\partial y} \tag{17}$$

where $\bar{c}_p$ is called the frozen specific heat, and is

$$\bar{c}_p = \sum_{i=1}^{v} c_i c_{p_i} \tag{18}$$

Differentiating equation (10), where the partial derivatives of v are negligible compared to derivatives of u and H leads to

$$\frac{\partial H}{\partial x} = \frac{\partial h}{\partial x} + u\frac{\partial u}{\partial x} \tag{19}$$

$$\frac{\partial H}{\partial y} = \frac{\partial h}{\partial y} + u\frac{\partial u}{\partial y} \tag{20}$$

Substituting equations (17)–(20) in equation (3) with $\mathcal{H} \approx 1$ yields

$$\rho u\left[\left(\bar{c}_p\frac{\partial T}{\partial x}\right) + \sum_{i=1}^{v} h_i\frac{\partial c_i}{\partial x} + u\frac{\partial u}{\partial x}\right] + \rho v\left(\bar{c}_p\frac{\partial T}{\partial y} + \sum_{i=1}^{v} h_i\frac{\partial c_i}{\partial h} + u\frac{\partial u}{\partial y}\right)$$

$$= -\frac{\partial}{\partial y}q_y + \frac{\partial}{\partial y}\left(\mu u\frac{\partial u}{\partial y}\right) - \operatorname{div}\vec{q}_r + \sum_{i=1}^{v} Y_i\frac{J_{iy}}{m_i} \tag{21}$$

We rewrite equation (21):

$$\rho u\left[\left(\bar{c}_p\frac{\partial T}{\partial x}\right) + \sum_{i=1}^{v} h_i\frac{\partial c_i}{\partial x}\right] + \rho v\left(\bar{c}_p\frac{\partial T}{\partial y} + \sum_{i=1}^{v} h_i\frac{\partial c_i}{\partial y}\right) + \left(\rho u^2\frac{\partial u}{\partial x} + \rho uv\frac{\partial u}{\partial y}\right)$$

$$= -\frac{\partial}{\partial y}q_y + \frac{\partial}{\partial y}\left(\mu u\frac{\partial u}{\partial y}\right) - \operatorname{div}\vec{q}_r + \sum_{i=1}^{v} Y_i\frac{J_{iy}}{m_i} \tag{22}$$

Multiplying equation (1) by u, we obtain

$$\rho u^2\frac{\partial u}{\partial x} + \rho uv\frac{\partial u}{\partial y} = u\frac{\partial}{\partial y}\left(\mu\frac{\partial u}{\partial y}\right) - u\left(\frac{\partial p}{\partial x}\right) \tag{23}$$

Subtracting equation (23) from equation (22) gives

$$\rho u\left[\left(\bar{c}_p \frac{\partial T}{\partial x}\right) + \sum_{i=1}^{v} h_i \frac{\partial c_i}{\partial x}\right] + \rho v\left(\bar{c}_p \frac{\partial T}{\partial y} + \sum_{i=1}^{v} h_i \frac{\partial c_i}{\partial y}\right)$$

$$= -\frac{\partial}{\partial y} q_y + \mu\left(\frac{\partial u}{\partial y}\right)^2 - \operatorname{div} \vec{q}_r + \sum_{i=1}^{v} Y_i \frac{J_{iy}}{m_i} + u\left(\frac{\partial p}{\partial x}\right) \tag{24}$$

which is the temperature form of the energy equation.

This completes the formulation of the differential equations reduced by order-of-magnitude arguments. They apply throughout the flow about the forebody shown in figure 4-1, and are representative of the flow wherein severe heating may occur, such as forebodies in axisymmetric or two-dimensional flow. This would include forward stagnation regions, leading edges of lifting surfaces (and perhaps engine inlets), and bluff inclined surfaces. Among other things, the equations allow for chemical reactions (equilibrium or nonequilibrium), electrical charge separation (and the electrical fields that are induced), and ablation at rates up to the free-stream mass flux rate. Subsequently, various terms in the equations pertaining to heat conduction, radiative transfer, electric fields, and the transport of mass by four kinds of diffusion (concentration gradients of species, thermal, pressure, and (electrically) forced diffusion) will be described and assessed as to the relative importance of each. This will be done in the next chapter.

Thus we have the governing differential equations concerning mass conservation (eq. (4)), statements of the x and y components of momentum (eqs. (1) and (2)), the energy equation expressed in terms of total enthalpy (eq. (3)), the species continuity equation (eq. (5)), and the equation of state (eq. (8) or (9)); effectively six equations in six unknowns, p, ρ, u, v, H, and c_i (at least for an electrically neutral gas). Alternatively, equation (6) can replace equation (5); the energy equation, equation (3), can be expressed in terms of temperature and can be replaced by equation (24); and for a nonneutral gas, the surplus charge equation, equation (7), would be used along with an electrodynamic or electrostatic equation which will be presented later.

Illustrative Boundary Conditions

For the balance of this chapter, we consider some illustrative boundary conditions for these differential equations. These are shown in equations (25)-(35) for $y = \delta$ (behind the shock wave), and $y = 0$ (at the wall). Recall that ε is required to calculate all the unknowns listed previously behind the shock wave. That requires an equation of state (eq. (8) or (9)), which in turn requires some knowledge or assumptions about the chemical state of the gas. For example, if we assume the gas to be frozen across the shock, the species are unchanged, equation (30); while for equilibrium we would have equation (31). Similarly, temperature and electron concentration are treated according to whatever assumption we make (eqs. (32), (33), and (35)). It can be seen that these boundary conditions can be written in various forms, depending on the assumptions made and the choice of alternate dependent variables, as long as we are consistent.

Boundary conditions at the wall are also shown for no mass addition (eqs. (36)-(42)). Equations (43)-(45) illustrate steady-state mass addition at the wall in response to flow-field heating; that is, the excess heating is compensated by the appropriate mass injection or ablation at the wall. Figure 4-2 is a schematic diagram corresponding to equation (45).

Boundary conditions– At $y = \delta$

$$u = u_s \tag{25}$$

$$v = v_s \tag{26}$$

$$p = p_s \tag{27}$$

$$H \approx \frac{\overline{U^2}}{2} \tag{28}$$

$$c_i = c_{is} \tag{29}$$

for chemical nonequilibrium

$$c_{i_\infty} = c_{is} \tag{30}$$

while for chemical equilibrium

$$c_{is} = f\left(p, T, c'_p\right) \tag{31}$$

For chemical equilibrium with species diffusion

$$T = T_s\left(h_s, p_s, c_{is}\right) \tag{32}$$

or with elemental diffusion

$$T = T_s\left(h, p, c'_p, c'_e\right) \tag{33}$$

$$c'_p = c'_{ps} = c'_{p_\infty} \tag{34}$$

$$c'_e = c'_{es} = c'_{e_\infty} \tag{35}$$

At $y = 0$, with no velocity slip at the wall

$$u = 0 \quad \text{(no-slip condition)} \tag{36}$$

For no mass transfer by transpiration or ablation at the wall

$$\dot{m}_w = (\rho v)_w = 0 \tag{37}$$

Total enthalpy at the wall equals the static enthalpy

$$H_w = h_w = \sum_{i=1}^{v} (c_i h_i)_w \tag{38}$$

The last equality corresponds to equation (6) of Chapter 2. Moreover,

$$h_{iw} = \int_0^{T_w} c_{p_i}\, dT + h_i^\circ \tag{39}$$

From equation (5) of Chapter 3 written for atmospheric species which we say do not penetrate the wall

$$\dot{m}_{iw} = c_i \dot{m}_w + J_{iyw} = 0 \tag{40}$$

The equivalent statement for atmospheric elements would be

$$\dot{m}'_p = c'_p \dot{m}_w + J'_{pw} = 0 \tag{41}$$

Equation (41) would not equal zero if element p originated in the wall. For no flux of electric charge to the wall

$$\dot{m}'_e = c'_e m_w + J'_{ew} = 0 \tag{42}$$

It may be noted that the boundary condition (eq. (40)) states that chemical species which originate in the atmosphere do not penetrate the wall. Equation (41) is not zero for elements which originate in the wall, and is zero for elements that do not originate in the wall. Of course for transpiration or suction in which the boundary layer is being sucked into the wall, the zero does not pertain. Note also that equation (41) does not require the wall to be neutral electrically. The boundary condition (eq. (42)) states that there is no absolute flux of charge into the wall. These statements are illustrative only and can be rewritten to describe any particular requirement. For steady-state ablation, heating at the wall gasifies the wall material as shown in figure 4-2, where the subscript m refers to species which originate in the wall material.

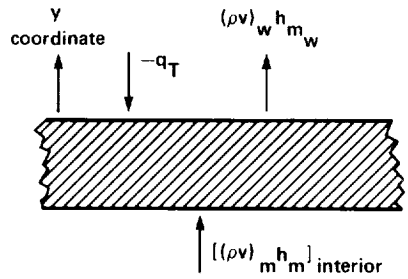

Figure 4-2.– Ablating material in coordinates relative to the surface (wall).

For steady-state ablation, the energy out = energy in

$$(\rho v)_w h_{m_w} = -q_T + \left[(\rho v)_m h_m\right]_{interior} \tag{43}$$

where the total heat flux, q_T, is positive in the y direction. Thus $-q_T$ is a positive quantity.

The mass balance is expressed by

$$(\rho v)_w = (\rho v)_{interior} = (\rho_m v_m)_w \tag{44}$$

It will be shown in equations (7) and (8) of Chapter 8 that the left side of equation (44) contains the mass average velocity v, and the term v_m is the absolute velocity of the wall gases that originated in the material. Thus we have from equations (43) and (44) for steady-state ablation

$$\dot{m}_w = (\rho v)_w = -q_T / \left(h_{m_w} - h_{m_{interior}}\right) \tag{45}$$

In summary, the governing differential equations are typically equations (1)–(5) (with alternatives eqs. (6) and (7) replacing eq. (5), and eq. (24) replacing eq. (3)) and the equation of state; either equation (8) or (9). Illustrative boundary conditions behind the shock wave are equations (25)–(29), with alternate choices equations (32)–(35). At the wall they are equations (36)–(40), with alternate choices equations (41) and (42). Steady-state ablation at the wall is typically described by equation (45), and will be developed in more detail in Chapter 8.

REFERENCES

1. Howe, J. T.; and Sheaffer, Y. S.: Role of Charge Separation and Pressure Diffusion in the Gascap of Entry Objects. AIAA J., vol. 7, no. 10, Oct. 1969, pp. 1971-1977.

2. Ho, H. T.; and Probstein, R. F.: The Compressible Viscous Layer in Rarefied Hypersonic Flow. ARL TN 60-132, Aug. 1960, Div. of Engineering, Brown Univ.

3. Hoshizaki, H.; and Wilson, K. H.: Viscous Radiating Shock Layer about a Blunt Body. AIAA J., vol. 3, no. 9, Sept. 1965, pp. 1614-1622.

4. Hirschfelder, J. O.; Curtiss, C. F.; and Bird, R. B.: Molecular Theory of Gases and Liquids. Wiley, 1954.

5. Ho, Hung Ta; and Probstein, Ronald F.: The Compressible Viscous Layer in Rarefied Hypersonic Flow. ARL TN 60-132, Div. of Eng., Brown Univ., Aug. 1960.

6. Liepmann, H. W.; and Roshko, A.: Elements of Gas Dynamics. Wiley, 1957.

CHAPTER 5

TRANSPORT PROCESSES AND EXPRESSIONS

At this point, the differential equations concerning conservation of matter, momentum balances in two coordinate directions, and the exchange of energy in the flow field have been developed in their most simple forms. The equations contain terms that represent viscous effects (μ, in eqs. (1) and (3) of Chapter 4), the transport of mass by diffusive processes (eqs. (5), (6), and (7) of Chapter 4), forces that are induced electrically (eqs. (2), (3), (5), (6), and (7) of Chapter 4), and the transport of energy (eq. (3) of Chapter 4). In this chapter, we will describe those terms and assess their relative importance. Other terms also appear that describe the transfer of energy by the emission and absorption of radiation, and the formation and disappearance of species by chemical reactions. These will be treated in separate chapters (6 and 10).

With respect to transport, we will not derive the transport expressions in this monograph. They are a subject unto themselves. An outline of the derivation appears in references 1, 2, 3, and 4. The expressions for the transport terms were derived independently by Chapman and Enskog. They were able to derive the Navier-Stokes equations from the Boltzmann equation, and in so doing arrived at formulas for the transport expressions as well as for the coefficients that appear in the expressions. Generally, the coefficients are very difficult to calculate. We will not do that either, but will simply write the transport expressions and make some evaluations concerning their application.

General Transport Expressions

Our first object is to examine the diffusive transport terms which appear in the hydrodynamic equations to assess the importance of diffusive processes in the flow fields of flight objects in severe thermal environments. The general Chapman-Enskog expressions used include three vectors: the macroscopic gradient vector, the mass flux vector, and the energy flux vector (ref. 2, pp. 483, 485, 489, 516, and 522).

The macroscopic gradient vector of species i is defined as

$$\underline{d}_i = \frac{\partial \chi_i}{\partial \underline{r}} + (\chi_i - c_i)\frac{\partial(\ln p)}{\partial \underline{r}} - \frac{c_i}{p}\left(\frac{\rho}{m_i}\underline{X}_i - \sum_{k=1}^{\nu} n_k \underline{X}_k\right) \tag{1}$$

The mass flux vector in a ν component gas mixture is the mass flux of species i relative to coordinates moving with the mass averaged velocity. Its expression (general case) is

$$\underline{J}_i = \frac{n^2}{\rho}\sum_{j=1}^{\nu} m_i m_j D_{ij}\underline{d}_j - D_i^T \frac{\partial \ln T}{\partial \underline{r}} = n_i m_i \underline{V}_i = \rho_i \underline{V}_i \tag{2}$$

(note that $D_{ii} = 0$).

The energy flux vector is (the subscript c for "conductive" will be omitted for $\underline{q}$ in this chapter)

$$\underline{q} = -\lambda \frac{\partial T}{\partial \underline{r}} + \sum_{i=1}^{v} h_i \underline{J}_i - nkT \sum_{i=1}^{n} \frac{1}{n_i m_i} D_i^T \underline{d}_i \tag{3}$$

The $\underline{d}_i$ expression contains three kinds of terms: concentration gradient, pressure gradient, and external force. It appears in the mass-flux vector multiplied by a multicomponent diffusion coefficient D_{ij} along with a thermal-diffusion term containing the thermal-diffusion coefficient D_i^T. Thus, four kinds of diffusive transport (concentration, pressure, forced, and thermal) are represented in the mass-flux vector, the diffusive velocity V_i, and the energy flux vector $\underline{q}$

The nomenclature is

χ_i = mole fraction of species i

c_i = mass fraction of species i

$\underline{X}_i$ = electrostatic force on particle i

D_{ij} = multicomponent diffusion coefficient of species i in species j

D_i^T = thermal diffusion coefficient

$\underline{V}_i$ = diffusive velocity of species i relative to mass average velocity

λ = "modified" translational thermal conductivity

Importantly, (1) D_{ij} is a function of p, T, and local composition. Thus it is very difficult to evaluate for more than a ternary mixture. (2) Moreover, for argon, at 1 atm at 17,000 K, λ differs by only 5% from the ordinary λ', the "ordinary" translational thermal conductivity.

Let us now use the basic relations, equations (1)–(3), to derive some transport expressions that are in common use, and note their limitations.

Effective Thermal Conductivity

The assumptions are pressure and forced diffusion are neglected; $\partial p/\partial r \cong 0$, the gas mixture is neutral in chemical equilibrium, and the elemental composition is fixed. Equation (1) becomes

$$\underline{d}_i = \frac{\partial \chi_i}{\partial \underline{r}} \tag{4}$$

Equation (2) becomes

$$\underline{J}_i = \frac{n^2}{\rho} \sum_{j=1}^{v} m_i m_j D_{ij} \frac{\partial \chi_j}{\partial \underline{r}} - \frac{D_i^T}{T} \frac{\partial T}{\partial \underline{r}} \tag{5}$$

Under the assumption of fixed elemental composition and chemical equilibrium (ref. 5)

$$\chi_i = \chi_i(p,T) \tag{6}$$

Differentiation of the mole fraction by the chain rule yields

$$\frac{\partial \chi_i}{\partial \underline{r}} = \left(\frac{\partial \chi_i}{\partial T}\right)_p \frac{\partial T}{\partial \underline{r}} + \left(\frac{\partial \chi_i}{\partial p}\right)_T \frac{\partial p}{\partial \underline{r}} \tag{7}$$

Substituting equation (7) into equation (5) gives

$$\underline{J}_i = \frac{n^2}{\rho} \sum_{j=1}^{v} m_i m_j D_{ij} \left(\frac{\partial \chi_j}{\partial T} \frac{\partial T}{\partial \underline{r}} + \frac{\partial \chi_j}{\partial p} \frac{\partial p}{\partial \underline{r}} \right) - \frac{D_i^T}{T} \frac{\partial T}{\partial \underline{r}} \tag{8}$$

Since $\partial p/\partial \underline{r} = 0$

$$\underline{J}_i = \frac{n^2}{\rho} \sum_{j=1}^{n} m_i m_j D_{ij} \left(\frac{\partial \chi_j}{\partial T} \frac{\partial T}{\partial \underline{r}} \right) - \frac{D_i^T}{T} \frac{\partial T}{\partial \underline{r}} \tag{9}$$

Substituting equation (9) into equation (3) leads to

$$\underline{q} = -\left[\lambda - \sum_{i=1}^{v} h_i \left(\frac{n^2}{\rho} \sum_{j=1}^{v} m_i m_j D_{ij} \frac{\partial x_j}{\partial T} - \frac{D_i^T}{T} \right) + nkT \sum_{i=1}^{v} \frac{D_i^T}{n_i m_i} \frac{\partial \chi_i}{\partial T} \right] \frac{\partial T}{\partial \underline{r}} \tag{10}$$

The brackets can be called an effective thermal conductivity. Thus

$$\underline{q} = -\lambda_{eff} \frac{\partial T}{\partial \underline{r}} \tag{10a}$$

which is a Fourier conduction format with

$$\lambda_{eff} = \lambda_{eff}(p,T) \tag{11}$$

Although the application has limitations noted above, this approach has been very useful, as will be apparent when the equations are solved subsequently. It is noted that

$$c_i = c_i(p,T) \tag{12}$$

$$h(p,T) = \sum_{i=1}^{\nu} c_i h_i \tag{13}$$

$$c_p = \left(\frac{\partial h}{\partial T}\right)_p = \sum_{i=1}^{\nu} c_i \left(\frac{\partial h_i}{\partial T}\right)_p + \sum_{i=1}^{\nu} h_i \left(\frac{\partial c_i}{\partial T}\right)_p \tag{14}$$

or if $\bar{c}_p$ represents the "frozen" specific heat

$$c_p = \left(\frac{\partial h}{\partial T}\right)_p = \bar{c}_p + \sum_{i=1}^{\nu} h_i \left(\frac{\partial c_i}{\partial T}\right)_p \tag{15}$$

Partially differentiate equation (13):

$$\frac{\partial h}{\partial \underline{r}} = \left(\frac{\partial h}{\partial T}\right)_p \frac{\partial T}{\partial \underline{r}} + \left(\frac{\partial h}{\partial p}\right)_T \frac{\partial p}{\partial \underline{r}} = \left(\frac{\partial h}{\partial T}\right)_p \frac{\partial T}{\partial \underline{r}} \tag{16}$$

Since $\partial p/\partial \underline{r}$ is zero, we obtain

$$\frac{\partial h}{\partial \underline{r}} = c_p \frac{\partial T}{\partial \underline{r}} \tag{17}$$

Then equation (11) becomes

$$\underline{q} = -\frac{\lambda_{eff}}{c_p} \frac{\partial h}{\partial \underline{r}} = -\frac{\mu}{Pr_{eff}} \frac{\partial h}{\partial \underline{r}} \tag{18}$$

We define an effective Prandtl number as

$$Pr_{eff} = \frac{c_p \mu}{\lambda_{eff}} \tag{19}$$

which will appear subsequently as well.

Binary Mixture Approach; Fick's Law

The assumptions are forced, thermal, and pressure diffusion are neglected ($\partial p/\partial r \cong 0$, and the gas mixture is neutral). This leads to the following expressions for equations (1) and (2):

$$\underline{d}_i = \frac{\partial \chi_i}{\partial \underline{r}} \tag{19a}$$

$$D_i^T = 0$$

$$\underline{J}_i = \frac{n^2}{\rho} m_1 m_2 \mathcal{D}_{12} \frac{\partial \chi_2}{\partial \underline{r}} \tag{20}$$

where $\mathcal{D}_{12}$ is the binary diffusion coefficient. Moreover

$$\chi_i = c_i \frac{M}{M_i}, \quad i = 1,2 \tag{21}$$

where the mixture molecular weight is expressed as in equation (9) of Chapter 4. (Note that $\sum_{i=1}^{2} \chi_i = 1$, so that $\frac{\partial \chi_1}{\partial \underline{r}} = -\frac{\partial \chi_2}{\partial \underline{r}}$ and $\underline{d}_1 = -\underline{d}_2$ because of Eq. (19a).)

$$M = \sum_{i=1}^{2} \chi_i M_i = \chi_1 M_1 + \chi_2 M_2 \tag{22}$$

Differentiate equation (21) with respect to the space coordinate

$$\frac{\partial \chi_1}{\partial \underline{r}} = \frac{M}{M_1} \frac{\partial c_1}{\partial \underline{r}} + \frac{c_1}{M_1} \frac{\partial M}{\partial \underline{r}} \tag{23}$$

Using equation (22)

$$\frac{\partial \chi_1}{\partial \underline{r}} = \frac{M}{M_1} \frac{\partial c_1}{\partial \underline{r}} + \frac{c_1}{M_1} \left(M_1 \frac{\partial \chi_1}{\partial \underline{r}} + M_2 \frac{\partial \chi_2}{\partial \underline{r}} \right) \tag{24}$$

From the note above equation (22):

$$\frac{\partial c_1}{\partial \underline{r}} = \frac{M_1}{M} \left[\frac{\partial \chi_1}{\partial \underline{r}} + \left(\frac{M_2}{M_1} - 1 \right) c_1 \frac{\partial \chi_1}{\partial \underline{r}} \right] \tag{25}$$

$$\frac{\partial c_1}{\partial \underline{r}} = \frac{1}{M} \frac{\partial \chi_1}{\partial \underline{r}} (M_2 c_1 + M_1 - c_1 M_1) \tag{26}$$

$$\frac{\partial c_1}{\partial \underline{r}} = \frac{M_1 M_2}{M^2} \frac{\partial \chi_1}{\partial \underline{r}} \tag{27}$$

or

$$\frac{\partial c_1}{\partial \underline{r}} = \frac{n^2 m_1 m_2}{n^2 m^2} \frac{\partial \chi_1}{\partial \underline{r}} = -\frac{n^2}{\rho^2} m_1 m_2 \frac{\partial \chi_2}{\partial \underline{r}} \tag{28}$$

Substituting equation (28) into equation (20) yields

$$\underline{J}_i = -\rho \, \mathcal{D}_{12} \frac{\partial c_i}{\partial \underline{r}} \tag{29}$$

This is the binary diffusion approximation, or Ficks Law. It is useful for either equilibrium or nonequilibrium flow. Then equation (3) can be written (for no thermal diffusion)

$$\underline{q} = -\lambda \frac{\partial T}{\partial \underline{r}} - \sum_{i=1}^{2} h_i \rho \mathcal{D}_{12} \frac{\partial c_i}{\partial \underline{r}} \tag{30}$$

From equations (15) and (17) in Chapter 4:

$$\frac{\partial h}{\partial \underline{r}} = \bar{c}_p \frac{\partial T}{\partial \underline{r}} + \sum_{i=1}^{2} h_i \frac{\partial c_i}{\partial \underline{r}} \tag{31}$$

$$\frac{\partial T}{\partial \underline{r}} = \frac{1}{\bar{c}_p} \left(\frac{\partial h}{\partial \underline{r}} - \sum_{i=1}^{2} h_i \frac{\partial c_i}{\partial \underline{r}} \right) \tag{32}$$

Equation (30) becomes

$$\underline{q} = -\frac{\lambda}{\bar{c}_p} \left(\frac{\partial h}{\partial \underline{r}} - \sum_{i=1}^{2} h_i \frac{\partial c_i}{\partial \underline{r}} \right) - \sum_{i=1}^{2} h_i \rho \mathcal{D}_{12} \frac{\partial c_i}{\partial \underline{r}} \tag{33}$$

$$\underline{q} = -\frac{\lambda}{\bar{c}_p} \frac{\partial h}{\partial \underline{r}} - \sum_{i=1}^{2} h_i \frac{\partial c_i}{\partial \underline{r}} \left(\rho \mathcal{D}_{12} - \frac{\lambda}{\bar{c}_p} \right) \tag{34}$$

Define the frozen Prandtl number

$$\overline{Pr} = \frac{\bar{c}_p \mu}{\lambda} \tag{35}$$

and the frozen Lewis number

$$Le = \frac{\rho \mathcal{D}_{12} \bar{c}_p}{\lambda} \tag{36}$$

Thus for a variable elemental composition (even for nonequilibrium), we have

$$\frac{\rho \mathcal{D}_{12}}{Le} = \frac{\lambda}{\bar{c}_p} = \frac{\mu}{Pr} \tag{37}$$

$$\underline{q} = -\frac{\mu}{Pr}\frac{\partial h}{\partial \underline{r}} - \sum_{i=1}^{2} \rho \mathcal{D}_{12} h_i \left(\frac{\partial c_i}{\partial \underline{r}}\right)\left(1 - \frac{1}{Le}\right) \tag{38}$$

This is the energy flux vector for a binary gas mixture without pressure gradients, electrical fields, or thermal diffusion. But it allows chemical nonequilibrium with variable elemental composition. Of course, the y component of $\underline{q}$ is of most interest, and thus are the partial derivatives of h and c_i with respect to y. This form of the energy-flux vector has been used extensively from the earliest days of spaceflight (refs. 6 and 7). The relationship is often approximated by allowing Le = 1, such that

$$\underline{q} = -\frac{\mu}{Pr}\frac{\partial h}{\partial \underline{r}} \tag{38a}$$

for a reacting gas in or out of chemical equilibrium. Although it applies to a binary mixture, it has also been applied extensively to multicomponent mixtures (ref. 7) that are "sortable" into two classes wherein each class has a "common" molecular weight and collision cross section among the species. For example, species "1" may include O_2, N_2, C_2, CO, CN, and NO; while species "2" may include O, N, and C—but must exclude such species as H_2, H, e^-, etc.

The Stefan-Maxwell Approach, and the Bifurcation Approximation

Generally, the hot gas cap about a hypervelocity flight object is truly "multicomponent" chemically. Pressure gradients, temperature gradients, electric fields, and variable elemental composition may all be important. If we apply equations (1)–(3) to determine transport phenomena, we find that D_{ij} is very difficult to obtain. For any two species i and j, D_{ij} is not a function of T and p alone, even for chemical equilibrium. It is also a function of the concentration of all other species (ref. 3). It should be calculated at every point—even for a ternery mixture, it is an enormous task. It would be desirable to calculate the transport fluxes and avoid the complication. The Stefan-Maxwell approximation does that (ref. 2, p. 718, and ref. 3, p. 570). Moreover, the more recent "bifurcation" approximation extends that concept conveniently.

Recall equation (2), and consider a binary mixture for the moment. Replace ρ_i with $n_i m_i$, and the right-hand equality of equation (2) such that

$$\underline{V}_i = \frac{\underline{J}_i}{n_i m_i} \tag{39}$$

$$\underline{V}_i = \frac{n^2}{n_i \rho} \sum_{j=1}^{2} m_j D_{ij} \underline{d}_j - \frac{D_i^T}{n_i m_i}\frac{\partial \ln T}{\partial \underline{r}} \tag{40}$$

which in the case of a binary mixture is

$$\underline{V}_1 = \frac{n^2}{n_1\rho} m_2 \mathcal{D}_{12} \underline{d}_2 - \frac{D_1^T}{n_1 m_1} \frac{\partial \ln T}{\partial \underline{r}} \tag{41}$$

$$\underline{V}_1 = \frac{n^2}{n_1\rho} m_2 \mathcal{D}_{12} \left(\underline{d}_2 - \frac{D_1^T \rho}{n^2 m_1 m_2 \mathcal{D}_{12}} \frac{\partial \ln T}{\partial \underline{r}} \right) \tag{42}$$

$$\underline{V}_2 = \frac{n^2}{n_2\rho} m_1 \mathcal{D}_{21} \left(\underline{d}_1 - \frac{D_2^T \rho}{n^2 m_1 m_2 \mathcal{D}_{21}} \frac{\partial \ln T}{\partial \underline{r}} \right) \tag{43}$$

Since $\sum_{i=1}^{2} J_i = 0$ (eq. (15) of Chapter 3), $\mathcal{D}_{12} = \mathcal{D}_{21}$, thus

$$m_1 n_1 \underline{V}_1 + m_2 n_2 \underline{V}_2 = 0 \tag{44}$$

Therefore

$$0 = \left(\frac{m_1 n^2 m_2 \mathcal{D}_{12}}{\rho} \right) \left(\underline{d}_2 - \frac{D_1^T \rho}{n^2 m_1 m_2 \mathcal{D}_{12}} \frac{\partial \ln T}{\partial \underline{r}} \right)$$

$$+ \left(\frac{m_2 n^2 m_1 \mathcal{D}_{12}}{\rho} \right) \left(\underline{d}_1 - \frac{D_2^T r}{n^2 m_1 m_2 \mathcal{D}_{12}} \frac{\partial \ln T}{\partial \underline{r}} \right) \tag{45}$$

which gives

$$\underline{d}_1 + \underline{d}_2 = \left(D_1^T + D_2^T \right) \frac{\rho}{n^2 m_1 m_2 \mathcal{D}_{12}} \frac{\partial \ln T}{\partial \underline{r}} \tag{46}$$

from the definition of $\underline{d}_i$ (ref. 2, p. 470)

$$\sum_{i=1}^{2} \underline{d}_i = \underline{d}_1 + \underline{d}_2 = 0 \Rightarrow D_1^T = -D_2^T \tag{47}$$

Subtracting equation (42) from equation (43) gives

$$\underline{V}_2 - \underline{V}_1 = \frac{n^2 m_1 n_1}{\rho n_2 n_1} \mathcal{D}_{12} \left(\underline{d}_1 - \frac{D_2^T \rho}{n^2 m_1 m_2 \mathcal{D}_{12}} \frac{\partial \ln T}{\partial \underline{r}} \right)$$

$$+ \frac{n^2 m_2 n_2}{\rho n_1 n_2} \mathcal{D}_{12} \left(-\underline{d}_2 + \frac{D_1^T \rho}{n^2 m_1 m_2 \mathcal{D}_{12}} \frac{\partial \ln T}{\partial \underline{r}} \right) \tag{48}$$

$$\underline{V}_2 - \underline{V}_1 = \frac{n^2 \mathcal{D}_{12}}{\rho n_1 n_2} (\rho_1 + \rho_2) \left(\underline{d}_1 - \frac{D_2^T \rho}{n^2 m_1 m_2 \mathcal{D}_{12}} \frac{\partial \ln T}{\partial \underline{r}} \right) \tag{49}$$

$$\frac{n_2 n_1}{n^2 \mathcal{D}_{12}} (\underline{V}_2 - \underline{V}_1) = \underline{d}_1 - \frac{\partial \ln T}{\partial \underline{r}} \left[\frac{n_2 n_1 \rho}{n^2 m_1 n_1 \mathcal{D}_{12}} \left(\frac{D_2^T}{n_2 m_2} \right) \right] \tag{50}$$

$$\frac{n_2 n_1}{n^2 \mathcal{D}_{12}} (\underline{V}_2 - \underline{V}_1) = \underline{d}_1 - \frac{\partial \ln T}{\partial \underline{r}} \left[\frac{n_2 n_1}{c_1 n^2 \mathcal{D}_{12}} \left(\frac{D_2^T}{n_2 m_2} \right) \right] \tag{51}$$

which is the Stefan-Maxwell relation for a binary gas and where $\underline{d}_i$ includes chemical concentration, and thermal, pressure, and forced diffusion. Curtiss and Hirschfelder (ref. 2) have generalized this Stefan-Maxwell relation to multicomponent gas mixtures. The following discusses that development. The generalization leads to

$$\sum_{\substack{j=1 \\ j \neq i}}^{\nu} \frac{n_i n_j}{n^2 \mathcal{D}_{ij}(1)} (\underline{V}_j - \underline{V}_i) = \underline{d}_i - \frac{\partial \ln T}{\partial \underline{r}} \sum_{\substack{j=1 \\ j \neq i}}^{\nu} \frac{n_i n_j}{n^2 \mathcal{D}_{ij}(1)} \left(\frac{D_j^T}{n_j m_j} - \frac{D_i^T}{n_i m_i} \right) \tag{52}$$

where $\mathcal{D}_{ij}(1) \neq D_{ij}(1)$; that is, equation (52) is approximately valid for a multicomponent mixture, but employs pseudobinary diffusion coefficients $\mathcal{D}_{ij}(1)$ as described below, and replaces equation (2). Note that

$$\underline{V}_i = \frac{\underline{J}_i}{n_i m_i} = \frac{\underline{J}_i}{\rho_i} = \frac{\underline{J}_i}{c_i \rho} \tag{53}$$

and

$$\frac{n_i}{n} = \chi_i \tag{54}$$

$$\underline{d}_i = -\sum_{j=1}^{\nu} \frac{\chi_i \chi_j}{\rho \mathcal{D}_{ij}} \left(\frac{\underline{J}_i + D_i^T \frac{\partial \ln T}{\partial \underline{r}}}{c_i} - \frac{\underline{J}_j + D_j^T \frac{\partial \ln T}{\partial \underline{r}}}{c_j} \right) \tag{55}$$

from equation (52), where $\mathcal{D}_{ij}(1)$ (which is explained in what follows) is written $\mathcal{D}_{ij}$ (the binary diffusion coefficient).

Now concerning the Stefan-Maxwell equation (52) applied to multicomponent gas mixtures, the derivation is lengthy and goes deeply into transport coefficient theory—beyond the scope of this monograph. The derivation is outlined in Chapter 7 of reference 2. Briefly, (1) the function that is used to perturb the Maxwell-Boltzmann distribution expression is expressed as a sum of integrals wherein the integrands contain infinite series of Sonine polynomials. (2) Only one term in the series is used which yields the "first approximation" to the multicomponent diffusion coefficient, $\mathcal{D}_{ij}(1)$. (3) Then by relations

shown, and steps outlined in reference 2, equation (52) is derived. We should note that equation (52) is valid for a multicomponent mixture, but uses only binary diffusion coefficients which are comparatively easy to obtain, and are insensitive to the mixture composition. Equation (52) is generally called the Stefan-Maxwell relation. It is an equation for V_i or J_i in terms of binary diffusion coefficients and replaces equation (2).

An interesting development by Kendall, Rindal, and Bartlett (ref. 8), called the "bifurcation approximation," extends this development and has been in use in recent years. It makes use of equations (53)-(55). They have found that over a broad range of particles $\mathcal{D}_{ij}$ can be represented semiempirically to remarkable accuracy by the expressions in equations (57) and (58). The development is particularly noteworthy because it can be used for mixtures which contain the chemical components of reacting air as well as species that were produced by an ablating heat shield in the extreme thermal environment of the gas cap over a hypervelocity flight vehicle. The development continues as follows.

From equation (55) with thermal diffusion retained, define $\bar{J}_i$ and $\bar{J}_j$ so that

$$\underline{d}_i = \sum_{j=1}^{v} \frac{\chi_i \chi_j}{\rho \mathcal{D}_{ij}} \left(\frac{\bar{J}_j}{c_j} - \frac{\bar{J}_i}{c_i} \right) \tag{56}$$

$$\bar{D} = \bar{D}(p,T) \tag{57}$$

$$F_i = \text{constant} \quad \text{such that} \quad \mathcal{D}_{ij} = \frac{\bar{D}}{F_i F_j} = \mathcal{D}_{ji} \tag{58}$$

Substituting in equation (56)

$$\underline{d}_i = \sum_{j=1}^{v} \frac{\chi_i F_i \chi_j F_j}{\rho \bar{D}} \left(\frac{\bar{J}_j}{c_j} - \frac{\bar{J}_i}{c_i} \right) \tag{59}$$

but

$$\frac{\chi_i}{c_i} = \frac{M}{M_i} \tag{60}$$

Therefore

$$\underline{d}_i = \frac{1}{\rho \bar{D}} \sum_{j=1}^{v} \left(c_i \frac{M}{M_i} F_i \frac{M}{M_j} F_j \bar{J}_j - c_j \frac{M}{M_i} F_i \frac{M}{M_j} F_j \bar{J}_i \right) \tag{61}$$

Equation (1) becomes

$$\underline{d}_i = \frac{\partial \chi_i}{\partial \underline{r}} + (\chi_i - c_i)\frac{\partial \ln p}{\partial \underline{r}} - \frac{c_i}{p}\left(\frac{\rho}{m}\underline{X}_i - \sum_{k=1}^{v} n_k \underline{X}_k\right)$$

$$= \frac{M^2}{\rho \overline{D}}\left(\frac{c_i F_i}{M_i}\sum_{j=1}^{v}\frac{F_j \bar{\underline{J}}_j}{M_j} - \frac{F_i \bar{\underline{J}}_i}{M_i}\sum_{j=1}^{v}\frac{c_j F_j}{M_j}\right) \tag{62}$$

Multiplying by M_i/F_i and summing over all i

$$\sum_{i=1}^{v}\left[\frac{M_i}{F_i}\frac{\partial \chi_i}{\partial \underline{r}} + \frac{M_i}{F_i}(\chi_i - c_i)\frac{\partial \ln p}{\partial \underline{r}} - \frac{M_i c_i}{F_i p}\left(\frac{\rho \underline{X}_i}{m_i} - \sum_{k=1}^{v} n_k \underline{X}_k\right)\right]$$

$$= \frac{M^2}{\rho \overline{D}}\sum_{i=1}^{v}\left(c_i \sum_{j=1}^{v}\frac{F_j \bar{\underline{J}}_J}{M_j} - \bar{\underline{J}}_i \sum_{j=1}^{v}\frac{c_j F_j}{M_j}\right) \tag{63}$$

and noting that

$$\sum_{i=1}^{v} D_i^T = 0 \Rightarrow \sum_{i=1}^{v} \bar{\underline{J}}_i = 0 \quad \text{and} \quad \sum_{i=1}^{v} c_i = \sum_{i=1}^{v} \chi_i = 1 \tag{64}$$

Equation (63) becomes

$$\sum_{j=1}^{v}\frac{F_j \bar{\underline{J}}_j}{M_j} = \frac{\rho \overline{D}}{M^2}\sum_{i=1}^{v}\left[\frac{M_i}{F_i}\frac{\partial \chi_i}{\partial \underline{r}} + \frac{c_i}{F_i}(M - M_i)\frac{\partial \ln p}{\partial \underline{r}} - \frac{M_i c_i}{F_i}\frac{\rho}{p}\frac{\underline{X}_i}{m_i} + \frac{M_i c_i}{F_i p}\sum_{k=1}^{v} n_k \underline{X}_k\right] \tag{65}$$

We now solve equation (62) for $\partial \chi_i/\partial r$ and substitute equation (65) for $\sum_{j=1}^{v} F_j \bar{\underline{J}}_j/M_j$.

$$\frac{\partial \chi_i}{\partial \underline{r}} = \frac{c_i F_i}{M_i}\sum_{i=1}^{v}\frac{M_i}{F_i}\frac{\partial \chi_i}{\partial \underline{r}} - \frac{M^2}{\rho \overline{D}}\frac{F_i \bar{\underline{J}}_i}{M_i}\sum_{j=1}^{v}\frac{c_j F_j}{M_j} + \frac{c_i F_i}{M_i}\sum_{j=1}^{v}\frac{c_j}{F_j}\left[\frac{M_i}{p}\sum_{k=1}^{v} n_k \underline{X}_k + (M - M_j)\frac{\partial \ln p}{\partial \underline{r}} - M_j \frac{\rho}{p}\frac{\underline{X}_j}{m_j}\right]$$

$$-\frac{c_i}{M_i}\left[(M - M_i)\frac{\partial \ln p}{\partial \underline{r}} - \frac{M_i \rho \underline{X}_i}{p m_i} + \frac{M_i}{p}\sum_{k=1}^{v} n_k \underline{X}_k\right] \tag{66}$$

Further, define

$$\mu_2 = \sum_{j=1}^{v} \frac{M_j \chi_j}{F_j} \tag{67}$$

and

$$Z_i = \frac{M_i \chi_i}{F_i \mu_2} \ , \quad \sum_{i=1}^{v} Z_i = 1 \tag{68}$$

Then, the chain rule of differentiation gives (from eq. (68))

$$\mu_2 \frac{\partial Z_i}{\partial \underline{r}} + Z_i \frac{\partial \mu_2}{\partial \underline{r}} = \frac{M_i}{F_i} \frac{\partial \chi_i}{\partial \underline{r}} \tag{69}$$

Solving for $\partial \chi_i / \partial r$:

$$\frac{\partial \chi_i}{\partial \underline{r}} = \frac{F_i}{M_i} \left(\mu_2 \frac{\partial Z_i}{\partial \underline{r}} + Z_i \frac{\partial \mu_2}{\partial \underline{r}} \right) \tag{70}$$

Combining equations (70) and (66), multiplying by M_i/F_i, using $\Sigma Z_i = 1$ and $\Sigma \partial Z_i / \partial r = 0$ from equation (68) produces

$$\mu_2 \frac{\partial Z_i}{\partial \underline{r}} + Z_i \frac{\partial \mu_2}{\partial \underline{r}} = c_i \frac{\partial \mu_2}{\partial \underline{r}} - \frac{M^2 \underline{\bar{J}}_i}{\rho \bar{D}} \sum_{j=1}^{v} \frac{c_i F_i}{M_j} + c_i \sum_{j=1}^{v} \left[(M - M_j) \frac{\partial \ln p}{\partial \underline{r}} - L \frac{\rho}{p} \underline{X}_j + \frac{M_j}{p} \sum_{k=1}^{v} n_k \underline{X}_k \right] \tag{71}$$

where L is the Avogadro's constant.

Define

$$\mu_1 = M \sum_{j=1}^{v} \frac{c_j F_j}{M_j} \tag{72}$$

We solve equation (71) for $\underline{\bar{J}}_i = \underline{J}_i + D_i^T \partial \ln T / \partial \underline{r}$, using $M_i \chi_i = c_i M$:

$$\underline{J}_i + D_i^T \frac{\partial \ln T}{\partial \underline{r}} = - \frac{\rho \bar{D}}{M \mu_1} \left\{ \left(\mu_2 \frac{\partial Z_i}{\partial \underline{r}} + Z_i \frac{\partial \mu_2}{\partial \underline{r}} \right) - c_i \frac{\partial \mu_2}{\partial \underline{r}} - c_i \sum_{j=1}^{v} \frac{c_j}{F_j} \left[(M - M_j) \frac{\partial \ln p}{\partial \underline{r}} - L \frac{\rho}{p} \underline{X}_i + \frac{M_i}{p} \sum_{k=1}^{v} n_k \underline{X}_k \right] \right.$$

$$\left. + \frac{c_i}{M_i} \left[(M - M_i) \frac{\partial \ln p}{\partial \underline{r}} - \frac{L \rho \underline{X}_i}{p} + \frac{M_i}{p} \sum_{k=1}^{v} n_k \underline{X}_k \right] \right\} \tag{73}$$

Further, define

$$\mu_3 = \sum_{j=1}^{v} \frac{c_j}{F_j}(M - M_j) \tag{74}$$

$$\underline{\mu}_4 = \sum_j \frac{c_j}{F_j}\left(-L\rho\underline{X}_j + M_j \sum_{k=1}^{v} n_k \underline{X}_k\right) \tag{75}$$

Equation (73) becomes the bifurcation approximation, generalized here to include all four types of diffusion.

$$\underline{J}_i = \overbrace{-D_i^T \frac{\partial \ln p}{\partial \underline{r}} - \frac{\rho \overline{D}}{M\mu_1}\left\{\mu_2 \frac{\partial Z_i}{\partial \underline{r}} + (Z_i - c_i)\frac{\partial \mu_2}{\partial \underline{r}}\right.}^{\text{KRB code}}$$

$$\left. + \frac{c_i}{p}\left[\left(\frac{M - M_i}{F_i} - \mu_3\right)\frac{\partial p}{\partial \underline{r}} + \frac{1}{F_i}\left(-L\rho\underline{X}_i + M_i \sum_{k=1}^{v} n_k \underline{X}_k - \underline{\mu}_4\right)\right]\right\} \tag{76}$$

Equation (76) is an expression for the mass-flux vector of species i. The portion concerning transport by chemical concentration gradients is labeled KRB and is from reference 8. To this we have added the transport terms associated with thermal, pressure, and forced (electrical) diffusion. It is not a pleasant appearing expression, but it is profoundly simpler than the approach which calculates multicomponent diffusion coefficients, or even that which uses only one term of the Sonine polynomial series in the integrand. The mass-flux vector expressed in equation (76) can be used to replace equation (2), and can be used with equation (1) in equation (3) to obtain the energy-flux vector.

Summary of Transport Expressions

This is as far as we will pursue the various transport expressions and their approximations. These are summarized in table 5-1, with some comment on applicability. It should be said that the comments partly reflect convenience. That is, the λ_{eff} approach, though strictly limited to a fixed elemental composition, is employed for an elemental composition that is assumed to vary negligibly. Thus, for convenience, the properties have been calculated, tabulated, and published for the fixed elemental composition of air without reference to a flow-field solution by Hansen (ref. 5), Yos (ref. 9), Moeckel and Weston (ref. 10), and others. Some of these results have been expressed as analytical correlations by Viegas and Howe (ref. 11), and subsequently have been used as input to flow-field solutions by a number of analysts including Howe and Viegas (ref. 12), implying that the elemental composition was fixed or that its variation was of small consequence. The analytical expression for equilibrium air showing the normalized ratio of density-viscosity product to the Prandtl number (the latter expressed in terms of an approximate λ_{eff}) is presented as a function of normalized static enthalpy for three pressure levels in figure 5-1 (adapted from ref. 11), wherein the correlation expression is a ghastly-looking formula. The circles noted as references 1 and 2 on the figure are references 5 and 10 of this monograph. The appendix presents the correlation and its results, and is the partial text of reference 11. The correlation

TABLE 5-1.– TRANSPORT EXPRESSIONS

	Macroscopic gradient vector	Mass flux vector	Energy flux vector	Comment
General	$\underline{d}_i = \frac{\partial x_i}{\partial \underline{r}} + (x_i - c_i)\frac{\partial \ln p}{\partial \underline{r}}$ $-\frac{c_i}{p}\left(\frac{\rho}{m_i}\underline{X}_i - \sum_{k=1}^{v} n_k \underline{X}_k\right)$	$\underline{J}_i = \frac{n^2}{\rho}\sum_{\substack{j=1 \\ j\neq i}}^{v} m_i m_j D_{ij} \underline{d}_j - D_i^T \frac{\partial \ln T}{\partial \underline{r}}$	$\underline{q} = -\lambda \frac{\partial T}{\partial \underline{r}} + \sum_{i=1}^{v} h_i \underline{J}_i - nkT \sum_{i=1}^{v} \frac{1}{n_i m_i} D_i^T \underline{d}_i$	Chapman-Enskog D_{ij} is a function of p, T, and local comp. Very difficult to evaluate for more than a ternary mixture.
λ_{eff} approach	$\underline{d}_i = \frac{\partial x_i}{\partial \underline{r}}$	$\underline{J}_i = \left(\frac{n^2}{\rho}\sum_{\substack{j=1 \\ j\neq i}}^{n} m_i m_j D_{ij} \frac{\partial x_j}{\partial T} - \frac{D_i^T}{T}\right)\frac{\partial T}{\partial \underline{r}}$	$\underline{q} = -\lambda_{eff}\frac{\partial T}{\partial \underline{r}} = -\frac{\mu}{Pr}\frac{\partial h}{\partial \underline{r}}$ where $\lambda_{eff} = \left[\lambda - \sum_{i=1}^{v} h_i\left(\frac{n^2}{\rho}\sum_{j=1}^{v} m_i m_j D_{ij}\frac{\partial x_j}{\partial T} - \frac{D_i^T}{T}\right) + nkT\sum_{i=1}^{v}\frac{D_i^T}{n_i m_i}\frac{\partial x_i}{\partial T}\right]$ $Pr = \frac{c_p \mu}{\lambda_{eff}}$	$\partial p/\partial \underline{r} = 0$, neutral, fixed elemental comp., chem. equilibrium. D_{ij} difficulty (above). But: multicomponent OK. Thermal diffusion OK.

TABLE 5-1.– CONCLUDED

	Macroscopic gradient vector	Mass flux vector	Energy flux vector	Comment
Binary mix	$\underline{d}_i = \frac{\partial x_i}{\partial \underline{r}}$	$\underline{J}_i = -\rho \mathcal{D}_{12} \frac{\partial c_i}{\partial \underline{r}}$ (Ficks law)	$\underline{q} = -\frac{\mu}{\overline{Pr}} \frac{\partial h}{\partial \underline{r}} - \sum_{i=1}^{2} \rho \mathcal{D}_{12} h_i \frac{\partial c_i}{\partial \underline{r}} \left(1 - \frac{1}{Le}\right)$ where $\overline{Pr} = \frac{\bar{c}_p \mu}{\lambda}$ $Le = \frac{\rho \mathcal{D}_{12} \bar{c}_p}{\lambda}$ $\bar{c}_p$ is frozen spec. heat λ is "translational" conductivity*	$\partial p/\partial \underline{r} = 0$, neutral. No thermal diffusion. Binary (but "grouping" is allowed). Variable elemental comp. OK. Chem. nonequilibrium OK.
Stefan-Maxwell (with $\overline{D}$ approx.)	$\underline{d}_i = \frac{\partial x_i}{\partial \underline{r}} + (x_i - c_i) \frac{\partial \ln p}{\partial \underline{r}}$ $- \frac{c_i}{p} \left(\frac{\rho \underline{X}_i}{m_i} - \sum_{k=1}^{v} n_k \underline{X}_k \right)$	$\underline{J}_i = -D_i^T \frac{\partial \ln T}{\partial \underline{r}} - \frac{\partial \overline{D}}{M \mu_1} \left\{ \mu_2 \frac{\partial z_i}{\partial \underline{r}} \right.$ $+ (z_i - c_i) \frac{\partial \mu_2}{\partial \underline{r}}$ $+ \frac{c_i}{p} \left[\left(\frac{M - M_i}{F_i} - \mu_3 \right) \frac{\partial p}{\partial \underline{r}} \right.$ $\left. \left. + \frac{1}{F_i} \left(-L \rho \underline{X}_i + M_i \sum_{k=1}^{v} n_k \underline{X}_k - \mu_4 \right) \right] \right\}$	$\underline{q} = -\lambda \frac{\partial T}{\partial \underline{r}} + \sum_{i=1}^{v} h_i \underline{J}_i - nkT \sum_{i=1}^{v} \frac{1}{n_i m_i} D_i^T \underline{d}_i$	Anything goes: $\partial p/\partial \underline{r} \neq 0$, nonneutral, variable elemental comp., chem. non-equilibrium, multicomponent, $\overline{D}(p,T)$ easy to evaluate, F_i = constant

*Our λ is "modified translational" conductivity (called λ' in ref. 2, p. 491), but it is very nearly equal the translational conductivity (for Argon at T up to 17,000 K).

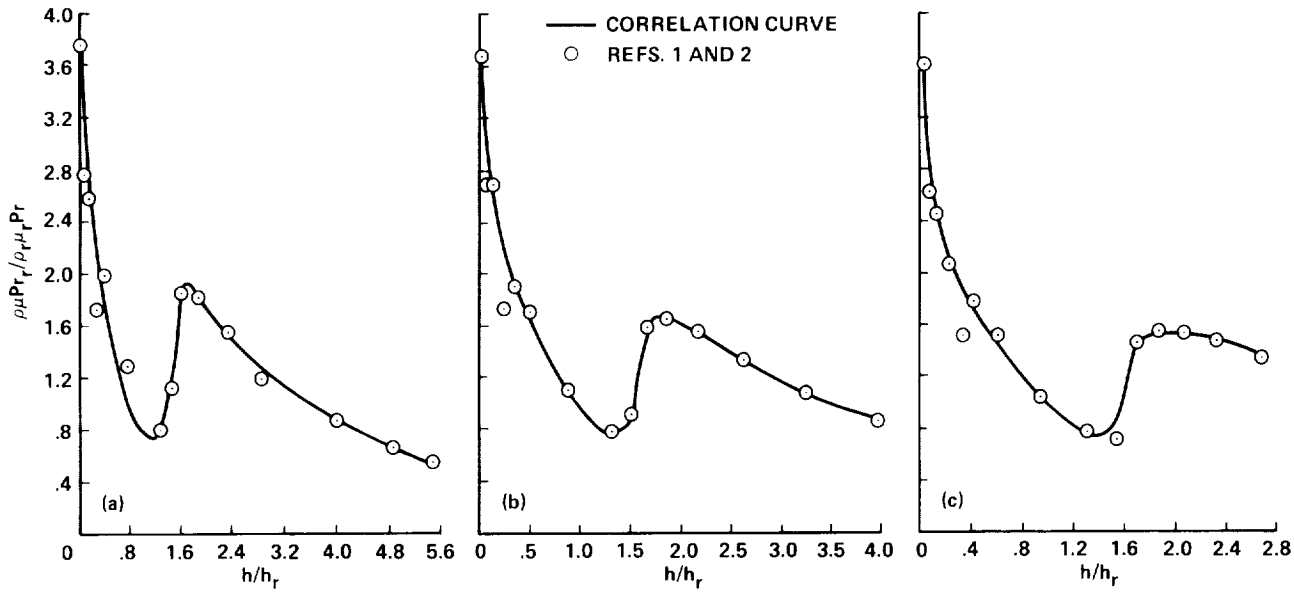

Figure 5-1.– Normalized ratio of density-viscosity product to effective Prandtl number—equilibrium air. (a) p = 10^{-1} atm; (b) p = 1 atm; (c) p = 10 atm.

function will be seen subsequently included in the solution of the flow-field equations. As assessment of the sensitivity of errors in transport properties as they affect surface heating is presented in reference 13.

Diffusion Assessment, and Compatibility of a Charged Gas With Linear Flux Theory

Four kinds of diffusive transport have been considered: those driven by chemical concentration gradients, pressure gradients, temperature gradients, and forces arising from induced electric fields (corresponding to electric charge separation). Each of these phenomena adds to the complexity of the treatment, so it is appropriate to ask, what is their relative importance—can some of them be neglected? If so, under what circumstances? Ahtye (ref. 1) showed that thermal diffusion is important in ionizing gases, and chemically driven diffusion is generally considered to be important (and is so treated). But what of pressure and forced diffusion? Are they negligible? They have not been treated to any large degree in the literature. Moreover, Meador and Staton (ref. 14) have argued that the Navier-Stokes equations are not compatible with a charged gas, which would preclude charge separation and thus forced diffusion as well. We should assess these things. Much of what follows is drawn from Howe and Sheaffer (ref. 15). We begin by assessing diffusion caused by pressure gradients relative to diffusion caused by chemical concentration gradients for various stages of chemical dissociation and ionization in some regions of the flow field. Then electrically forced diffusion is assessed in an approximate manner.

Pressure Diffusion

Since the pressure and concentration gradient terms appear together in the expression of the macroscopic gradient vector, we compare them to evaluate the role of the pressure diffusion. For that purpose, the electrical-force terms are neglected in this paragraph. Using equation (54), equation (1) can be written as

$$\underline{d}_i = \frac{\partial}{\partial \underline{r}}\left(\frac{n_i}{n}\right) + \left(\frac{n_i}{n} - \frac{n_i m_i}{\sum_{i=1}^{v} n_i m_i}\right)\frac{\partial \ln p}{\partial \underline{r}} \tag{77}$$

$$\underline{d}_i = \frac{\partial}{\partial \underline{r}}\left(\frac{n_i}{n}\right) + \frac{n_i}{n}\left(1 - \frac{n m_i}{\sum_{i=1}^{v} n_i m_i}\right)\frac{\partial \ln p}{\partial \underline{r}} \tag{78}$$

We look at the y-component of the pressure gradient with the approximation that the density ratio across the shock wave is small, $\varepsilon \ll 1$. From equations (14) and (18) in chapter 2, and from equation (2) in chapter 4:

$$\frac{\partial p}{\partial y} \sim \frac{\rho u^2}{R} \tag{79}$$

$$u_s \approx \bar{U} \sin \theta_s \tag{80}$$

$$p_s \approx \rho_\infty \bar{U}^2 \cos^2 \theta_s \tag{81}$$

Behind the shock, the order-of-magnitude analysis of the Navier-Stokes equations applied to the shock layer of a blunted cone indicates that the transverse pressure gradient is such that

$$\frac{\partial \ln p}{\partial y} = \frac{1}{p}\frac{\partial p}{\partial y} \approx O\left(\frac{\rho_s \bar{U}^2 \sin^2 \theta_s}{\rho_\infty \bar{U}^2 \cos^2 \theta_s R}\right) = O\left(\frac{\tan^2 \theta_b}{\varepsilon R}\right) \tag{82}$$

With the assumption

$$\frac{\delta}{R} \sim \varepsilon \tag{83}$$

Equation (82) becomes

$$\frac{\partial \ln p}{\partial y} \approx O\left(\frac{\tan^2 \theta_b}{\delta}\right) \tag{84}$$

In the stagnation region $\theta_b = 0$, so that from equations (84) and (78) pressure diffusion is negligible (electrical forces are neglected). But in the shoulder region, $\tan^2 \theta_b = 0(1)$, and equation (84) yields

$$\frac{\partial \ln p}{\partial y} = \frac{1}{p}\frac{\partial p}{\partial y} \approx O\left(\frac{1}{\delta}\right) \tag{85}$$

Consider a dissociating gas and the reaction

$$A_2 \rightarrow 2\,A \tag{86}$$

that we will write

$$M \rightarrow 2\,A \tag{87}$$

Then

$$n = n_A + n_M \tag{88}$$

$$m_M = 2\,m_A \tag{89}$$

From equation (40), with $D_i^T = 0$

$$V_{iy} = \frac{n^2}{\rho n_i} \sum_{j=1}^{\nu} m_j \mathcal{D}_{ij}\, d_{jy} \tag{90}$$

From equation (78) for atoms:

$$V_{Ay} = \frac{n^2}{n_A}\frac{m_M}{\rho}\mathcal{D}_{AM}\left[\frac{\partial}{\partial y}\left(\frac{n_M}{n}\right) + \frac{n_M}{n}\left(1 - \frac{m_M n}{n_A m_A + n_M m_M}\right)\frac{1}{\delta}\right] \tag{91}$$

From equation (88)

$$\frac{\partial}{\partial y}\left(\frac{n_M}{n}\right) = -\frac{\partial}{\partial y}\left(\frac{n_A}{n}\right) = O\left[\frac{\left(\frac{n_A}{n}\right)_s - \left(\frac{n_A}{n}\right)_w}{\delta}\right] \approx O\left[-\frac{1}{\delta}\left(\frac{n_A}{n}\right)_s\right] \tag{92}$$

Substituting equation (92) into equation (91),

$$V_{Ay} = \frac{2n^2 m_A}{n_A \rho}\mathcal{D}_{AM}\left[-\frac{1}{\delta}\left(\frac{n_A}{n}\right)_s + \left(1 - \frac{n_A}{n}\right)\left(\frac{-\frac{n_A}{n}}{2 - \frac{n_A}{n}}\right)\frac{1}{\delta}\right] \tag{93}$$

Similarly,

$$V_{My} = \frac{n^2 m_A}{(n - n_A)\rho}\mathcal{D}_{AM}\left[\frac{1}{\delta}\left(\frac{n_A}{n}\right)_s + \frac{n_A}{n}\left(1 - \frac{n}{2n - n_A}\right)\frac{1}{\delta}\right] \tag{94}$$

$$V_{My} = \frac{nm_A}{\left(1 - \frac{n_A}{n}\right)\rho} \mathcal{D}_{AM} \left[\frac{1}{\delta} \left(\frac{n_A}{n} \right)_s + \frac{n_A}{n} \left(\frac{1 - \frac{n_A}{n}}{2 - \frac{n_A}{n}} \right) \frac{1}{\delta} \right] \tag{95}$$

1. With very little dissociation near the shock

$$\frac{n_A}{n} = \left(\frac{n_A}{n} \right)_s \approx O(\varepsilon) \ll 1 \tag{96}$$

From equations (93) and (95)

$$V_{Ay} = \frac{2nm_A}{\varepsilon\rho} \mathcal{D}_{AM} \left[-\frac{1}{\delta}(\varepsilon) + \left(-\frac{\varepsilon}{2} \right) \frac{1}{\delta} \right] = -\frac{3nm_A}{\rho\delta} \mathcal{D}_{AM} \tag{97}$$

which can be large

$$V_{My} = \frac{nm_A}{\rho} \mathcal{D}_{AM} \left[+\frac{1}{\delta}(\varepsilon) + \left(\frac{\varepsilon}{2} \right) \frac{1}{\delta} \right] = \frac{3nm_A}{2\rho\delta} \varepsilon \mathcal{D}_{AM} \tag{98}$$

which is <u>small</u>.

2. Half-dissociation gives

$$n_A = n_M, \quad \frac{n_A}{n} = \frac{1}{2}$$

Equations (93) and (95) become

$$V_{Ay} = \frac{4nm_A}{\rho} \mathcal{D}_{AM} \left[-\frac{1}{\delta} \left(\frac{1}{2} \right) + \frac{1}{\delta} \left(\frac{1}{6} \right) \right] \tag{99}$$

$$V_{My} = \frac{2nm_A}{\rho} \mathcal{D}_{AM} \left[\frac{1}{\delta} \left(\frac{1}{2} \right) + \frac{1}{\delta} \left(\frac{1}{6} \right) \right] \tag{100}$$

Thus the diffusive velocities of atoms and molecules are comparable, and pressure diffusion is important to both.

3. For nearly complete dissociation, pressure diffusion can be shown to be negligible for both atoms and molecules by similar arguments.

4. For an ionizing gas wherein we consider $A \rightarrow A^+ + e^-$ for simplicity, or replacing the symbol A^+ by I for the ion, assess the importance of pressure diffusion as follows:

From equation (40), with $D_i^T = 0$ (recall that $D_{ii} = 0$):

$$\underline{V}_A = \frac{n^2}{n_A \rho}\left(m_I D_{AI}\,\underline{d}_I + m_e D_{Ae}\,\underline{d}_e\right) \tag{101}$$

$$\underline{V}_I = \frac{n^2}{n_I \rho}\left(m_e D_{Ie}\,\underline{d}_e + m_A D_{IA}\,\underline{d}_A\right) \tag{102}$$

$$\underline{V}_e = \frac{n^2}{n_e \rho}\left(m_A D_{eA}\,\underline{d}_A + m_I D_{eI}\,\underline{d}_I\right) \tag{103}$$

From equation (78) we have, for example,

$$\underline{d}_e = \frac{\partial}{\partial \underline{r}}\left(\frac{n_e}{n}\right) + \left(\frac{n_e}{n}\right)\left(1 - \frac{m_e n}{n_e m_e + n_I m_I + n_A m_A}\right)\frac{1}{p}\frac{\partial p}{\partial \underline{r}} \tag{104}$$

Noting that $m_A \approx m_I \gg m_e$ and for $n_A \gg n_I \approx n_e$ (slightly ionized gas) we see that pressure gradient is not important for d_A and d_I, but is important for d_e (exercise).

It can be shown, from what we have seen so far, that pressure diffusion is

1. Not important in the stagnation region (unless charge separation induces $\partial p/\partial y$)

2. Important in the shoulder region for the diffusive velocity of
   a. Atoms in a slightly dissociated gas
   b. Atoms and molecules in a half-dissociated gas
   c. Atoms and ions in a slightly ionized gas
   d. Atoms, ions, and electrons in a highly ionized gas

Forced Diffusion

The electric force on a particle is

$$\underline{X}_i = \omega_i e \underline{E} \tag{105}$$

where

$\underline{X}$ = dynes

e = 1.602×10^{-12} erg/V (the electron charge)

$\underline{E}$ = V/cm (the induced electric field)

(recall that ω_i = number of electron charge on species i)

We allow charge separation, so that, from electrodynamics

$$\text{div}\,\underline{E} = \frac{\rho_c}{\psi} \neq 0 \tag{106}$$

where

ρ_c = erg/(V·cm^3)

ψ = 8.855×10^{-7} erg/(V^2 cm), which is the dielectric constant.

For convenience, useful conversions of physical units are

Joule = Coulomb·Volt = 10^7 erg
Farad = Coulomb/Volt
Amp = Coulomb/sec

We consider the electric field to be primarily a function of the coordinate normal to the surface, and obtain

$$\frac{\partial E_y}{\partial y} = \frac{\rho_c}{\psi} \tag{107}$$

The boundary condition at $y = 0$ is

$$(E_y)_w = \frac{\Gamma_w}{\psi} \tag{108}$$

where Γ_w = surface charge density. The integration of equation (107) gives

$$E_y = \frac{1}{\psi}\int_0^y \rho_c\, dy' + \frac{\Gamma_w}{\psi} \tag{109}$$

Assuming a grossly neutral, locally nonneutral gas we write for a strip in the y direction of cross-section dA,

$$(dA)\,\psi E_y = 0 = dA\Gamma_w + dA\int_0^\delta \rho_c\, dy = 0 \tag{110}$$

which leads to

$$\Gamma_w = -\int_0^\delta \rho_c\, dy \tag{111}$$

From equations (109) and (111) we obtain

$$E_y(y) = -\frac{1}{\psi}\int_y^{\delta} \rho_c \, dy' \tag{112}$$

For convenience, we assume that a thin stratum (of thickness Δ) of charged gas (with average charge density ρ_c) exists behind the shock as shown in figure 5-2.

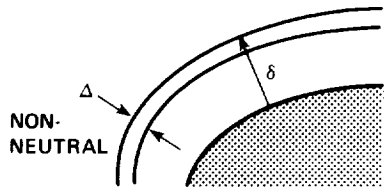

Figure 5-2.– Locally nonneutral flow field.

The field behind this layer is, from equation (112)

$$E_y(\delta - \Delta) = -\frac{1}{\psi}\int_{\delta-\Delta}^{\delta} \rho_c \, dy = -\frac{\rho_c}{\psi}[\delta - (\delta - \Delta)] = -\frac{\rho_c \Delta}{\psi} \tag{113}$$

Since

$$\rho_c = e\sum_{i=1}^{\nu} \omega_i n_i$$

$$E_y(\delta - \Delta) = -\frac{\delta}{\psi}\frac{\Delta}{\delta}\left(e\sum_{i=1}^{\nu} \omega_i n_i\right) \tag{114}$$

We consider only A, A^+, e^-, and the ionization reaction

$$A \rightarrow A^+ + e^-$$

We define the degree of charge separation S for a ternary mixture of atoms, ions, and electrons as

$$S = 1 - \frac{n_{e^-}}{n_{A^+}} = \frac{1}{n_{A^+}}(n_{A^+} - n_{e^-}) = \frac{1}{n_{A^+}}\sum_{i=1}^{3} \omega_i n_i \tag{115}$$

Equation (114) becomes

$$E_y = -\left(\frac{\delta}{\psi}\right)\left(\frac{\Delta}{\delta}\right) e n_{A^+} S \tag{116}$$

From equation (105), the y component of $\underline{X}_i$ is

$$Y_i = -\omega_i e^2 \left(\frac{\delta}{\psi}\right)\left(\frac{\Delta}{\delta}\right) n_A{}^+ S \tag{117}$$

(In order to compare the forced and concentration diffusion terms, we will neglect pressure diffusion.) The y component of equation (1) can be expressed as

$$d_{iy} = \frac{\partial \chi_i}{\partial y} - \frac{c_i}{p}\left(\frac{\rho}{m_i} Y_i - \sum_{k=1}^{3} n_k Y_k\right) \tag{118}$$

Approximate

$$\frac{\partial \chi_i}{\partial y} \sim O\left(\frac{\chi_{is} - \chi_{iw}}{\delta}\right) \tag{119}$$

Then, substituting equations (117) and (119) into equation (118) yields

$$d_{iy} \sim \frac{\chi_{is} - \chi_{iw}}{\delta} - \left\{\frac{c_i}{p}\left[-\frac{\rho\omega_i}{m_i} - \sum_{k=1}^{3} n_k(-\omega_k)\right] e^2 \frac{\delta}{\psi}\frac{\Delta}{\delta} n_A{}^+ S\right\} \tag{120}$$

The equation of state is

$$p_i = \frac{\rho_i RT}{M_i} = n_i m_i \frac{RT}{Lm_i} = n_i \frac{RT}{L} = n_i kT \tag{121}$$

where R is the universal gas constant, and L is Avagadro's number.

Dalton's law for partial pressures is

$$p = \sum_{i=1}^{\nu} p_i = nkT \tag{122}$$

Thus,

$$\frac{n_i}{p} = \frac{n_i}{nkT} = \frac{\chi_i}{kT} \tag{123}$$

and

$$\frac{c_i}{p}\frac{\rho}{m_i}\omega_i = \frac{n_i\omega_i}{pm_i} = \frac{\chi_i\omega_i}{kT} \tag{124}$$

Using the notation

$$A \rightarrow A^+ + e^-$$
$$\|$$
$$I$$

$$\frac{c_i n_I S}{p} = \frac{c_i n_I S}{nkT} = \frac{c_i \chi_I S}{kT} = \left(\chi_i \frac{M_i}{M}\right) \frac{\chi_I S}{kT} \tag{125}$$

And substituting equations (125) and (124) into equation (120) gives

$$d_{iy} \sim \frac{\chi_{is} - \chi_{iw}}{\delta} - \left[\frac{\chi_i}{kT}\left(-\omega_i + \frac{M_i}{M}\chi_I S\right) e^2 \frac{\delta}{\psi}\frac{\Delta}{\delta} n_I S\right] \tag{126}$$

Forced diffusion can be neglected if the second term on the right is much smaller than the first. Multiply the right side of equation (126) by δ/χ_{is}. Thus the criterion for species i becomes

$$\left| e^2 \frac{\delta^2}{\psi} \frac{n_I}{kT} \left(\frac{\Delta}{\delta}\right) S \left(\frac{M_i}{M}\chi_I S - \omega_i\right)\right|_s \ll 1 - \frac{\chi_{iw}}{\chi_{is}} \tag{127}$$

If $\chi_{iw}/\chi_{is} \ll 1$, and $n_i = \chi_i n$, the criterion becomes

$$\left| \frac{e^2 \delta^2 n}{\psi kT} \left(\frac{M_i}{M}\chi_I S - \omega_i\right) \frac{\Delta}{\delta} \chi_I S \right| \ll 1 \tag{128}$$

where for purposes of estimating the effect, all quantities are evaluated behind the shock wave (at high altitude, large gradients exist behind the shock wave as well as at the body surface). For increasing χ_i, the criterion is first violated by the electrons ($M_i/M \ll \omega_i$) in the first parentheses followed closely by the ions. Generally, the most sensitive condition is for the electrons. Note that

$$\frac{n}{kT} = \frac{p}{(kT)^2} \tag{129}$$

Accordingly, the criterion becomes

$$\frac{e^2 \delta^2}{\psi} \frac{p}{(kT)^2} \frac{\Delta}{\delta} \chi_I S \ll 1 \tag{130}$$

The Debye length is defined by

$$\Lambda^2 = \frac{\psi kT}{e^2 n_I} \tag{131}$$

In these terms, the criterion is

$$\frac{e^2 n_I}{\psi kT}\frac{\delta^2\Delta}{\delta} S = \frac{\delta^2}{\Lambda^2}\frac{\Delta}{\delta} S \ll 1 \tag{132}$$

The pressure and temperature for air in chemical equilibrium behind a normal shock is given as a function of flight speed and altitude in reference 12. For a given p and T, χ_I for air can be estimated by

$$\chi_I \approx \chi_{n^+} + \chi_{O^+} + \chi_{N_2^+} + \cdots \tag{133}$$

For assigned values of S, the locus of the criterion equation (132) is shown in figure 5-3, which was abstracted from reference 15. Thus for $\delta = 0.1$ cm and $\Delta = 0.5\,\delta$, forced diffusion can be neglected above the lines for constant S, but is not negligible below the lines. For the trajectories shown, a trace of charge separation can affect d_{e^-}, d_I, and thus the mass flux vectors for atoms, ions, and electrons for most of the entry regime. The above argument could be made more rigorous, but it is sufficient to provide the information that we wish to know.

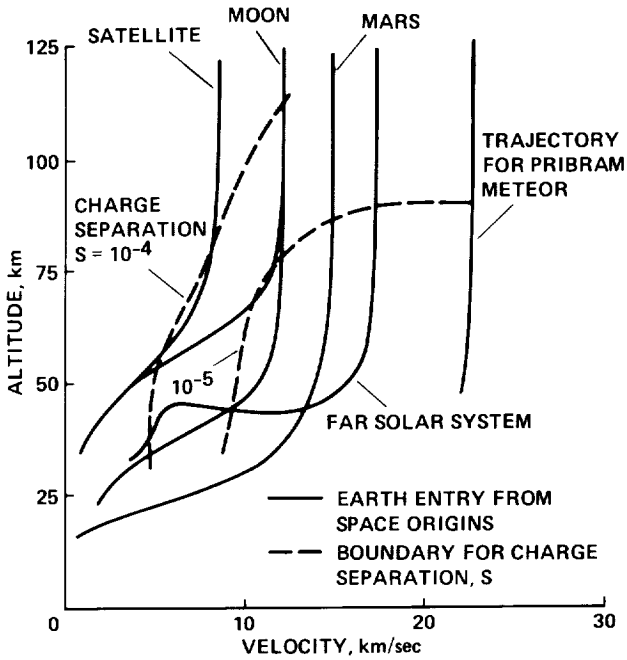

Figure 5-3.– Locus of electronically forced diffusion criterion (eq. (132)).

Compatibility of a Charged Gas With Linear Flux Theory

Finally, inasmuch as we are considering nonneutral or charged gases, we should say a few words about the compatibility of the Navier-Stokes equations with a charged gas. Several writers have raised doubt that they are compatible, and Meador and Staton have offered a proof that the concept is not compatible (ref. 14). The proof argument is presented briefly here, along with my rebuttal (which also appears in ref. 15).

The argument centers around the macroscopic gradient vector (eq. 1), which can be combined with equation (105) to yield

$$\underline{d}_i = \frac{\partial \chi_i}{\partial \underline{r}} + (\chi_i - c_i)\frac{\partial \ln p}{\partial \underline{r}} - \frac{ec_i}{p}\left(\frac{\rho\omega_i}{m_i} - n\sum_{i=1}^{v}\omega_i\chi_i\right)\underline{E} \tag{134}$$

The electrodynamic relation

$$\frac{\partial}{\partial \underline{r}} \cdot E = \frac{\rho_c}{\psi} \equiv en\sum_{i=1}^{v}\frac{\omega_i\chi_i}{\psi} \tag{135}$$

was employed with an assumed relation for the electric current ($\underline{J}$ here)

$$\underline{J} = \sigma_1\underline{E} + \sigma_2\left(\frac{\partial T}{\partial \underline{r}}\right) \tag{136}$$

The current was set to zero, which resulted in the expression for the field

$$\underline{E} = -\frac{\sigma_2}{\sigma_1}\left(\frac{\partial T}{\partial \underline{r}}\right) \tag{137}$$

This expression was used in equations (134) and (135). The charge density, effectively

$$en\sum_{i=1}^{v}\omega_i\chi_i$$

from equation (135) was used in equation (134), which resulted in an expression of the form

$$\underline{d}_i = \frac{\partial \chi_i}{\partial \underline{r}} + (\chi_i - c_i)\frac{\partial \ln p}{\partial \underline{r}} + \left(\frac{c_i\sigma_2}{p\sigma_1}\right)\left[\frac{e\rho\omega_i}{m_i} + \psi\left(\frac{\sigma_2}{\sigma_1}\right)\nabla^2 T\right]\frac{\partial T}{\partial \underline{r}} \tag{138}$$

The last product $\nabla^2 T(\partial T/\partial \underline{r})$ is "third order" in temperature, which is not consistent with linear flux theory. Thus, it was argued, $(\partial/\partial \underline{r})\cdot\underline{E}$ and therefore charge density ρ_c must be zero in equation (135) to avoid the third-order expression.

However, that conclusion seems to be a consequence of the use of two relations where one would suffice. There are hydrodynamic equations to calculate every quantity in equation (134) except $\underline{E}$. One additional relation for $\underline{E}$ (eq. (135)) needs to be solved simultaneously with the hydrodynamic differential equations. Equation (135) is not (in the hydrodynamic sense) an equation for calculating

$$\sum_{i=1}^{v}\omega_i\chi_i$$

because the mole fractions χ_i are calculated from the solutions of the diffusion equations, and ω_i is a set of constants. However, reference 14 used equation (135) to calculate

$$\sum_{i=1}^{\nu} \omega_i \chi_i$$

and used a second relation (eq. (136)) with $\underline{J} = 0$ to calculate $\underline{E}$. Of course, both equation (135) and equation (136) are valid and physical, but if both are used in the hydrodynamic framework, equation (135) should be regarded as a relation for $\underline{E}$, and equation (136) a relation for one more unknown, the current, $\underline{J}$. Clearly, within the hydrodynamic framework, equation (134) is first-order without requiring that ρ_c be zero. The electric field is simply calculable from the electrodynamic differential equation (135), just as the vectors $\partial \ln p/\partial \underline{r}$ and $\partial \chi_i/\partial \underline{r}$ are calculable from the hydrodynamic differential equations for insertion into equation (134). Thus there are no third-order terms and, on these grounds at least, a charged gas is compatible with the hydrodynamic equations.

Alternatively, if it is assumed that there is no current, and the Chapman-Enskog expression for the current (eq. (71) of Chapter 3)

$$\underline{J} = e \sum_{i=1}^{\nu} \frac{\omega_i}{m_i} \underline{J}_i \tag{139}$$

(where $\underline{J}_i$ is the mass flux vector of species i) is set to zero, there obtains for the electric field

$$\underline{E} = A \frac{\partial p}{\partial \underline{r}} + B \sum_{ij} \omega_i m_j D_{ij} \frac{\partial \chi_j}{\partial \underline{r}} + C \frac{\partial T}{\partial \underline{r}} \tag{140}$$

where

$$A = \frac{\sum_{ij} \omega_i m_j D_{ij} (\chi_j - c_j)}{e \sum_{ij} \omega_i m_j D_{ij} c_j \left(\frac{\rho \omega_j}{m_j} - \sum_{k=1}^{\nu} n_k \omega_k \right)} \tag{141}$$

$$B = \frac{p}{\left[e \sum_{ij} \omega_i m_j D_{ij} c_j \left(\frac{\rho \omega_j}{m_j} - \sum_{k=1}^{\nu} n_k \omega_k \right) \right]} \tag{142}$$

and

$$C = \frac{-\left(\frac{\rho k}{n}\right)\sum_{i=1}^{\nu} \omega_i \frac{D_i^T}{m_i}}{e\sum_{ij} \omega_i m_j D_{ij} c_j \left(\frac{\rho\omega_j}{m_j} - \sum_{k=1}^{\nu} n_k \omega_k\right)} \tag{143}$$

Substitution of equations (140) and (105) into equation (1) yields

$$\underline{d}_i = \frac{\partial \chi_i}{\partial \underline{r}} + \left(\chi_i - c_i\left\{1 + eA\left[\left(\frac{\rho}{m_i}\right)\omega_i - n\sum_{k=1}^{\nu}\chi_k\omega_k\right]\right\}\right)\left(\frac{1}{p}\right)\frac{\partial p}{\partial \underline{r}}$$

$$-\left(\frac{c_i e}{p}\right)\left[\left(\frac{\rho}{m_i}\right)\omega_i - \sum_{k=1}^{\nu} n_k w_k\right]\left(B\sum_{kj}\omega_k m_j D_{kj}\frac{\partial \chi_j}{\partial \underline{r}} + C\frac{\partial T}{\partial \underline{r}}\right) \tag{144}$$

Again, there are no third-order terms, and the expression is compatible with linear flux theory (Navier-Stokes equations). It is self-consistent with the Chapman-Enskog solution of the Boltzmann equation. Coefficients A, B, and C can be computed with that theory. As before, the mole fractions of all species are obtained from the solutions of the diffusion equation (eq. (5) of Chapter 4), rather than from equation (134). For the zero current approximation, equation (135) is superfluous, and can be omitted.

APPENDIX
(Adapted from ref. 11)

THERMODYNAMIC AND TRANSPORT PROPERTY CORRELATION FORMULAS FOR EQUILIBRIUM AIR FROM 1,000 K TO 15,000 K

The thermodynamic properties, density, and temperature, as well as transport property parameters involving viscosity, Prandtl number (including diffusion effects), and gaseous radiation absorption coefficients—which will be developed in Chapter 6—have been correlated as a function of enthalpy at four pressure levels (10^{-1}, 10^{0}, 10^{1}, and 10^{2} atm). The correlation formulas are written in a generalized form for which coefficients for a particular property and pressure level are tabulated. The correlation formulas are useful in digital computer programs for nonadiabatic viscous flow problems.

Introduction

Thermodynamic and transport properties of high-temperature air as well as their derivatives with respect to enthalpy at constant pressure are often needed for the computation of flow fields on bodies in high-speed flight. These properties are available in tabular form (refs. 5 and 10). However, this form is often not very convenient for use in digital computers. To facilitate machine computations, it is sometimes faster and easier if the properties are represented by analytical expressions which can also be readily differentiated. Cohen (Ref. 16) correlates density and some transport properties independently of pressure for flight speeds up to 29,000 ft/sec. Correlations are now required for high speeds up to 50,000 ft/sec to facilitate studies of high-speed entry into the Earth's atmosphere.

At these higher speeds, in excess of approximately 30,000 ft/sec, the transport properties of air are significantly affected by ionization. Furthermore, as developed in Chapter 6, at these speeds, gaseous radiation effects can also be important, depending on body size and altitude (ref. 17). Thus, for entry into the Earth's atmosphere on return from the moon, the planets, or far out in the solar system, for which entry speeds will be between 35,000 and 50,000 ft/sec, both ionization and radiation effects may be important and should be considered. For these reasons, thermodynamic and transport properties of equilibrium air at temperatures up to 15,000 K (stagnation temperature for flight at 50,000 ft/sec at approximately 190,00 ft altitude) as presented in references 5 and 10, are correlated as functions of enthalpy at the four pressure levels, 10^{-1}, 10^{0}, 10^{1}, 10^{2} atm. in the present work. The Planck mean mass absorption coefficient for gaseous radiation, as presented by both references 18 and 19, is also correlated as functions of enthalpy at the same pressure levels.

Symbols

a,b,c,d,e	constant and coefficients in equation (A-1)
h	static enthalpy, ft^2/sec^2
K_p	Planck mean mass absorption coefficient, $ft^2/slug$

p	pressure, atm
Pr	Prandtl number
T	temperature, K
x	independent variable in equation (A-1), h/h_r
y	dependent variable in equation (A-1) (appropriate property)
λ	thermal conductivity
ρ	mass density, slug/ft^3
μ	viscosity coefficient, lb sec/ft^2

Subscripts

a	results obtained from reference 18
eff	effective
l	results obtained from reference 19
1,2,...n	e coefficients in equation (A-1)
r	reference conditions in table A-2

Correlation Formulas

Many attempts were made to fit smooth curves through the desired property values obtained from references 5, 10, 18, and 19. Polynomials of all degrees up to 8 with coefficients determined by the method of least squares and the method of Tchebycheff were tried. Fourier series and generalized conics were also tried. In some cases it was found necessary to join as many as four sections of curves smoothly in series to obtain adequate correlations. An attempt was made to minimize possible discontinuities at the joints in segmented curves either by overlapping the sections and choosing a suitable point in this overlapped region to be the limit of the various curves (this was done for conics), or by matching the slope and property value of two adjoining curves at the same value of enthalpy (this was done for polynomials). The curves presented in this paper are the best results, from the methods attempted, for obtaining accurate and smoothly varying property values as functions of enthalpy.

Although various methods of correlation are used, it is convenient to express the correlation of all properties at a specific pressure level by the general formula

$$a + by + cxy + dy^2 + e_1x + e_2x^2 + e_3x^3 \ldots e_nx^n = 0 \qquad \text{(A-1)}$$

where the independent variable x is the enthalpy ratio h/h_r and the dependent variable y is the appropriate gas property. It is seen that if the coefficients $e_3 \ldots e_n$ are zero, the equation is that of a general

conic with inclined axis, and if the coefficients c and d are zero, the equation is that of a polynomial of degree n.

To facilitate the use of equation (A-1), the coefficients for the various properties at the pressure levels considered are presented in table A-1. This table shows the type of correlating function used (general conic or polynomial of degree n) for each property; the upper and lower enthalpy limits for the validity of each section of the correlation curve; and, for those properties fit by a general conic, the sign of the appropriate root is also given.

The overall limits of validity of these correlation formulas for each property correspond to a temperature range of approximately 1,000 to 15,000 K. For convenience, each property is referenced to a standard condition. The pressure is referenced to sea-level conditions. The reference conditions of all other properties correspond to their values at satellite enthalpy ($h_r = 3.125 \times 10^8$ ft^2/sec^2 or 12,474 Btu/lb) at each pressure level. The reference conditions are listed in table A-2.

Discussion of Results

The thermodynamic and transport properties as obtained from the correlation formulas presented in this report and the properties they represent from references 5, 10, 18, and 19 are compared in figures A-1–A-5. In general, the agreement is good. The analytical expressions should provide property values with sufficient accuracy for most machine calculations. In the remainder of this discussion, consideration is given to certain features of the correlations.

In figure A-3 where the ratio of the density-viscosity product to the Prandtl number is correlated, no attempt was made to fit the minor variation in the property values which occurred at low enthalpies (near $h/h_r = 0.3$). It was felt that the effect of this variation would be negligible in comparison to the effects of the overall variation. The peak in each curve corresponds to the onset of ionization. The correlation is seen to be very good in the ionization regime.

To study the effects of energy transport by gaseous radiation, the Planck mean mass absorption coefficient is useful. It has been calculated from theory in reference 19 and has been obtained by a combination of theory and experiment in reference 18. The two references are in reasonable, but not close, agreement. The results of both are correlated in figure A-5.

First, the absorption coefficient of reference 19 as correlated for all pressure levels is shown in figure A-5(a). The fit is fair except for the point at $h/h_r \approx 3.9$ for 1 atm. pressure. The high point at each pressure level corresponds to 15,000 K and was obtained by a graphical and logarithmic interpolation of results in reference 19 at 12,000 and 18,000 K.

The correlation of the absorption coefficient at individual pressure levels is shown in figures A-5(b)–(e), corresponding to the results of reference 19 and in figure A-5(f)–(i), corresponding to the results of reference 18. Except for figure A-5(f), the correlation is satisfactory. No attempt was made to fit figure A-5(f) because of the lack of a point defining the middle range of the properties.

Finally, it is instructive to go back and examine the thermal conductivity used in the Prandtl number of figure A-3. This is especially pertinent because the current lack of agreement between the stagnation point convective heat-transfer rates in references 20 and 21 may be attributed to the thermal conductivity of ionized air.

In the present paper, the thermal conductivity used in the Prandtl number includes the effects of energy transfer by both molecular collisions and diffusion of molecular species (ref. 5). The thermal conductivity calculated for air by Hansen (ref. 5) agrees quite well with experimental results at temperatures up to 5,000 K as reported by Peng and Ahtye (ref. 22). At higher temperatures, Hansen's results can be compared with the conductivity deduced experimentally for nitrogen by Maecker (ref. 23). In this comparison, shown in figure A-6, agreement is fairly good and the relative magnitudes of conductivities of the two gases are as expected (see refs. 22 and 24). Results of King (ref. 25) for the thermal conductivity of pure nitrogen agree very well with those of Maecker (see fig. 7-13).

Thus, thermodynamic properties and transport property parameters have been correlated as a function of enthalpy at four pressure levels. In general, the correlation formulas represent the properties quite accurately. Although the formulas are lengthy, they can be evaluated very rapidly by digital computers. For example, a property represented by an eighth-degree polynomial can be evaluated at 1,000 points in approximately 0.7 sec on an IBM 7090 data processing machine. This is one to two orders of magnitude faster than having this machine look up the same number of points in a table. The formulas are expected to be useful for flow-field computation on digital computers.

TABLE A-1.- COEFFICIENTS

Property, γ	Pressure level, atm	Type of curve	x limits for curve		a	b	c	d	c_1	c_2	c_3	c_4	c_5	c_6	c_7	c_8	Root of quadratic
			Lower	Upper													
$\frac{p_t}{p}$	10^{-1}	(a)	0.03608	5.4273	0.06592768	-1	0	0	1.505904	-1.165208	0.9343309	-0.3375398	0.05518693	-0.003330603	0	0	
	10^{0}	(a)	0.03608	3.9643	0.007398195	-1	0	0	2.109765	-2.739214	2.364413	-0.8556323	0.1007640	0.009547003	-0.002160125	0	
	10^{1}	(b)	0.03608	2.6736	0.01948670	-1	0	0	1.829233	-2.967630	7.119123	-11.11281	9.714190	-4.594607	1.105638	-0.1064150	
	10^{2}	(a)	0.03608	2.1589	0.01732455	-1	0	0	1.333830	-0.9134607	0.5819779	-0.3583186	0.1964153	-0.04129094	0	0	
$\frac{\beta L}{\rho \mu_t}$	10^{-1}	(c)	0.03608	5.4273	7.999610	-5.624454	-2.135941	1	-1.005803	-0.04987680	0	0	0	0	0	0	-
	10^{0}	(c)	0.03608	3.9643	2.967720	-4.336691	12.84509	1	-15.59082	3.058515	0	0	0	0	0	0	+
	10^{1}	(c)	0.03608	2.6736	-13.99580	-1.443177	89.74126	1	-89.68862	15.39430	0	0	0	0	0	0	+
	10^{2}	(c)	0.03608	2.1589	0.1344780	-4.118392	28.04161	1	-30.05294	4.841396	0	0	0	0	0	0	+
$\rho\mu Pr_t$	10^{-1}	(c)	0.03608	1.4	15.16116	-7.702875	2.738838	1	-19.90980	7.949521	0	0	0	0	0	0	-
$\rho\mu_t Pr$		(c)	1.4	1.6	-0.9378620	1	-0.5666152	0	0.8101086	-0.2057187	0	0	0	0	0	0	
		(c)	1.6	1.835	25.02171	-9.583479	3.787318	1	-19.55076	3.657150	0	0	0	0	0	0	+
		(c)	1.835	5.4273	-5.528132	1	1.029237	0	0.0006060	0.0629130	0	0	0	0	0	0	
	10^{0}	(c)	0.03608	0.45	-4.674994	1	12.72930	0	-19.98398	9.350414	0	0	0	0	0	0	-
		(c)	0.45	1.6	108.2544	-45.80435	23.90831	1	-130.1215	42.30918	0	0	0	0	0	0	
		(c)	1.55	2.35	-33.45746	8.832652	-7.821374	1	30.56290	-4.802969	0	0	0	0	0	0	
		(c)	2.35	3.9643	-3.994343	1	0.3894629	0	0.5779776	-0.03073380	0	0	0	0	0	0	-
	10^{1}	(c)	0.03608	1.0	14.04183	-7.002485	-24.87600	1	41.25561	-25.31620	0	0	0	0	0	0	+
		(c)	0.80	1.64	-172.8071	72.84828	-39.60441	1	203.8301	-64.21053	0	0	0	0	0	0	-
		(c)	1.6	2.6736	-17.96045	6.135884	-5.637358	1	15.14080	-1.694240	0	0	0	0	0	0	+
	10^{2}	(c)	0.03608	0.68	8.065993	-6.511489	50.27557	1	-109.8963	59.75427	0	0	0	0	0	0	
		(c)	0.68	1.5	-2.468844	1	0.3340534	0	1.417372	-0.3146546	0	0	0	0	0	0	+
		(c)	1.5	1.81	-24.14852	16.07877	-9.454224	1	22.63899	-5.168076	0	0	0	0	0	0	+
		(c)	1.78	2.16	-17.93436	9.928599	-7.072455	1	11.35373	-1.983110	0	0	0	0	0	0	-
$\frac{T}{T_t}$	10^{-1}	(a)	0.03608	0.08	-0.07161016	-1	0	0	7.599990	-33.45280	0	0	0	0	0	0	
	10^{0}	(a)	0.08	5.4273	0.1364769	-1	0	0	2.411026	-3.378803	2.901134	-1.302484	0.3106245	-0.03751842	0.0018102816	0	
		(a)	0.03608	2.54	0.01726946	-1	0	0	3.500558	-6.042997	5.382014	2.327105	0.4793450	-0.03780220	0	0	
		(c)	2.54	3.9643	1.243210	-1	0	0	0.2121646	0	0	0	0	0	0	0	
	10^{1}	(a)	0.03608	2.6736	0.05331397	-1	0	0	2.455306	-2.249730	0.2666849	0.8472206	0.4429167	0.0644144	0	0	
	10^{2}	(a)	0.03608	2.1589	0.03401435	-1	0	0	2.412343	-2.467107	1.219690	-0.2029401	0	0	0	0	
$\left(\frac{K_x}{K_{P_t/l}}\right)$	10^{-1}	(c)	0.03608	5.4273	0	68.85393	-33.18305	1	-37.97243	6.520246	0	0	0	0	0	0	+
	10^{0}	(c)	0.03608	3.9643	0	28.01277	-18.74220	1	-15.02563	7.682671	0	0	0	0	0	0	+
	10^{1}	(c)	0.03608	2.6734	0	133.9065	-51.91449	1	-27.90829	-49.49101	0	0	0	0	0	0	+
	10^{2}	(c)	0.03608	2.1589	0	23.19744	-15.39758	1	-12.22303	7.645397	0	0	0	0	0	0	+
	All levels	(c)	0.03608	5.4273	0	75.18458	-33.43958	1	-24.53630	-13.84419	0	0	0	0	0	0	+
$\left(\frac{K_L}{K_{P_t/\mu}}\right)$	10^{-1}	(c)	0.03608	5.4273	0	0	0	0	0	0	0	0	0	0	0	0	
	10^{0}	(c)	0.03608	3.9643	0	49.33526	-35.56380	1	-15.28951	8.139395	0	0	0	0	0	0	+
	10^{1}	(c)	0.03608	2.6736	0	80.99429	-39.79852	1	1.248875	-39.13508	0	0	0	0	0	0	+
	10^{2}	(c)	0.03608	2.1589	0	1634.040	-689.9332	1	-305.7013	234.0838	0	0	0	0	0	0	+

[a]Polynomial (least squares)
[b]Polynomial (Tchebycheff)
[c]Conic

TABLE A-2.– REFERENCE CONDITIONS

Pressure level, atm	h_r, ft^2/sec^2	ρ_r, $slug/ft^3$	$\rho_r\mu_r$, $lb^2\ sec^3/ft^6$	$Pr_r/\rho_r\mu_r$, $ft^6/lb^2\ sec^3$	T_r, K	$(K_{p_r})_l$, $ft^2/slug$	$(K_{p_r})_a$, $ft^2/slug$
10^{-1}	3.125×10^{8}	0.6271×10^{-5}	1.8254×10^{-11}	0.4777×10^{11}	6400	1.66×10^{1}	2.42×10^{1}
10^{0}	3.125×10^{8}	0.5700×10^{-4}	1.8065×10^{-10}	0.4694×10^{10}	7200	6.68×10^{1}	9.68×10^{1}
10^{1}	3.125×10^{8}	0.5185×10^{-3}	1.7754×10^{-9}	0.4613×10^{9}	8150	2.11×10^{2}	3.87×10^{2}
10^{2}	3.125×10^{8}	0.4697×10^{-2}	1.7556×10^{-8}	0.4460×10^{8}	9350	8.62×10^{2}	1.82×10^{3}

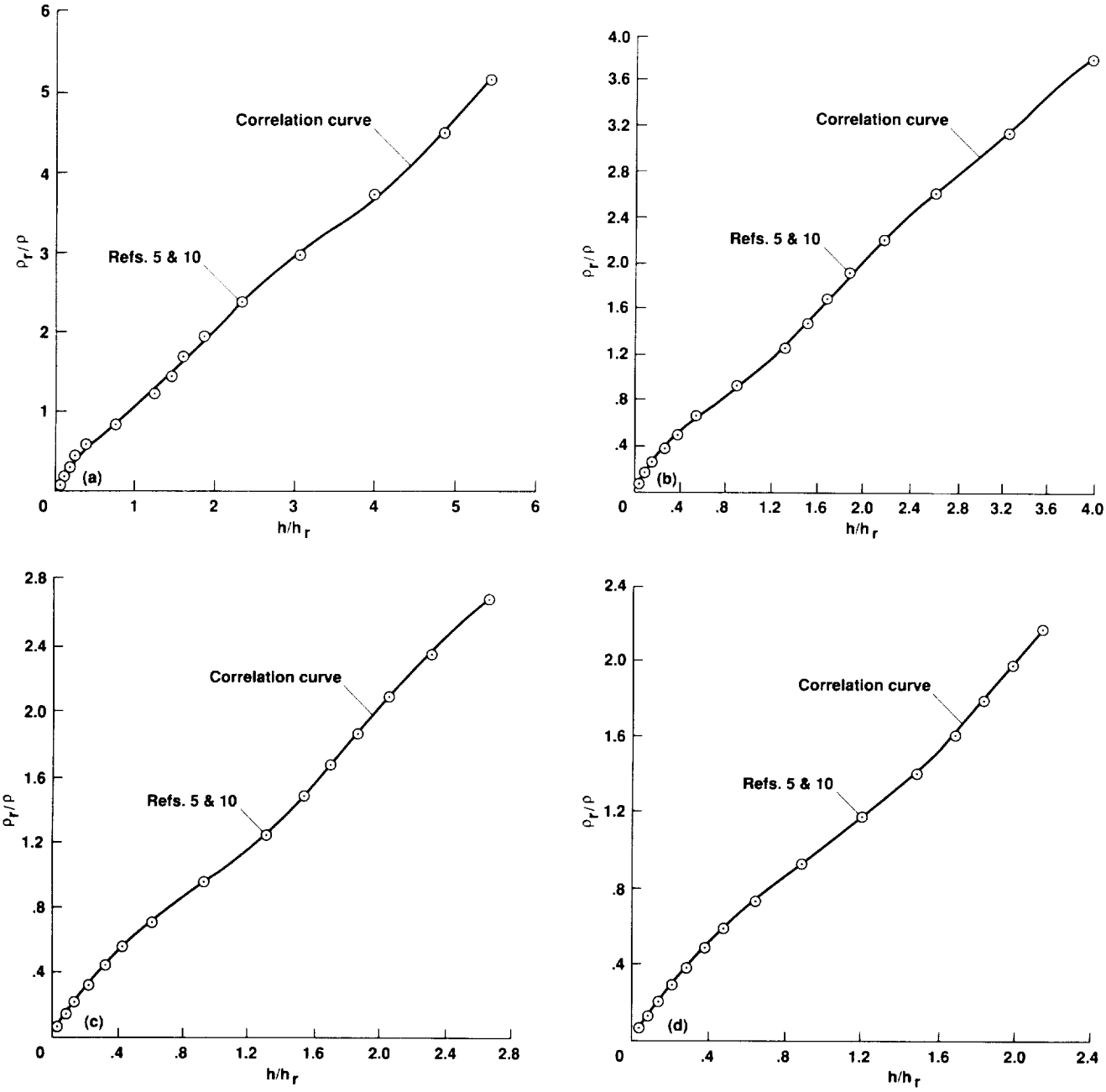

Figure A-1.– Density correlation. (a) p = 10^{-1} atm; (b) p = 1 atm; (c) p = 10 atm; (d) p = 100 atm.

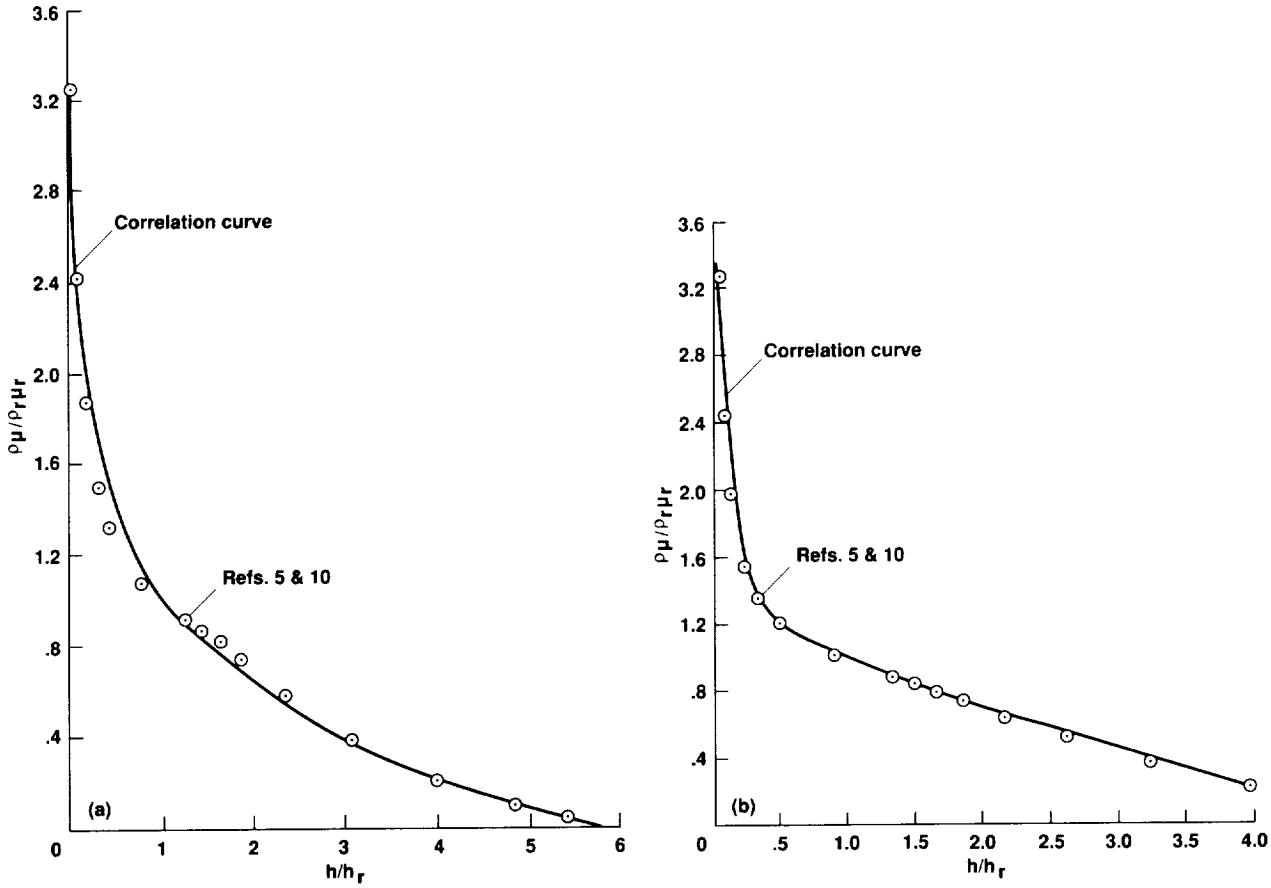

Figure A-2.– Density-viscosity parameter correlation. (a) p = 10^{-1} atm; (b) p = 1 atm.

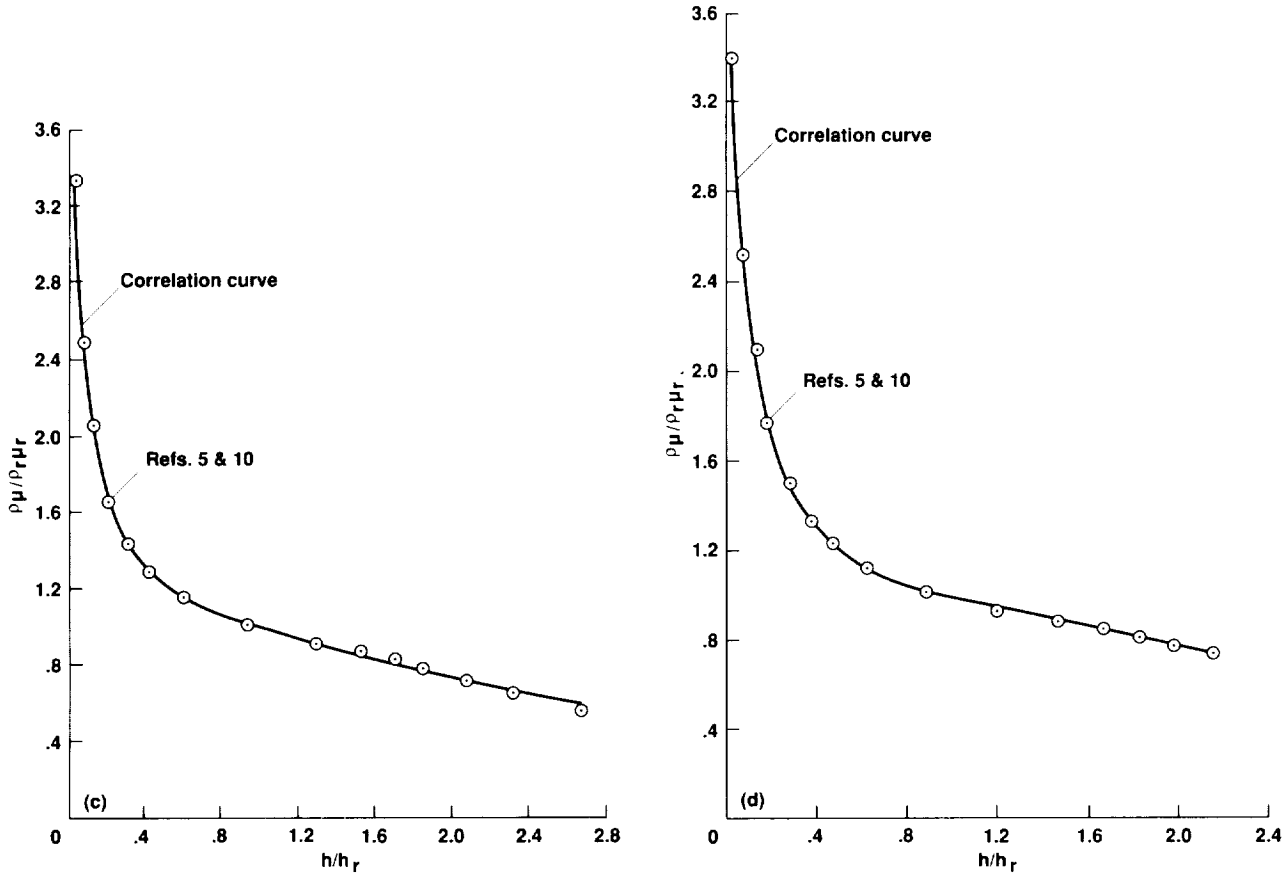

Figure A-2.– Concluded. (c) p = 10 atm; (d) p = 100 atm.

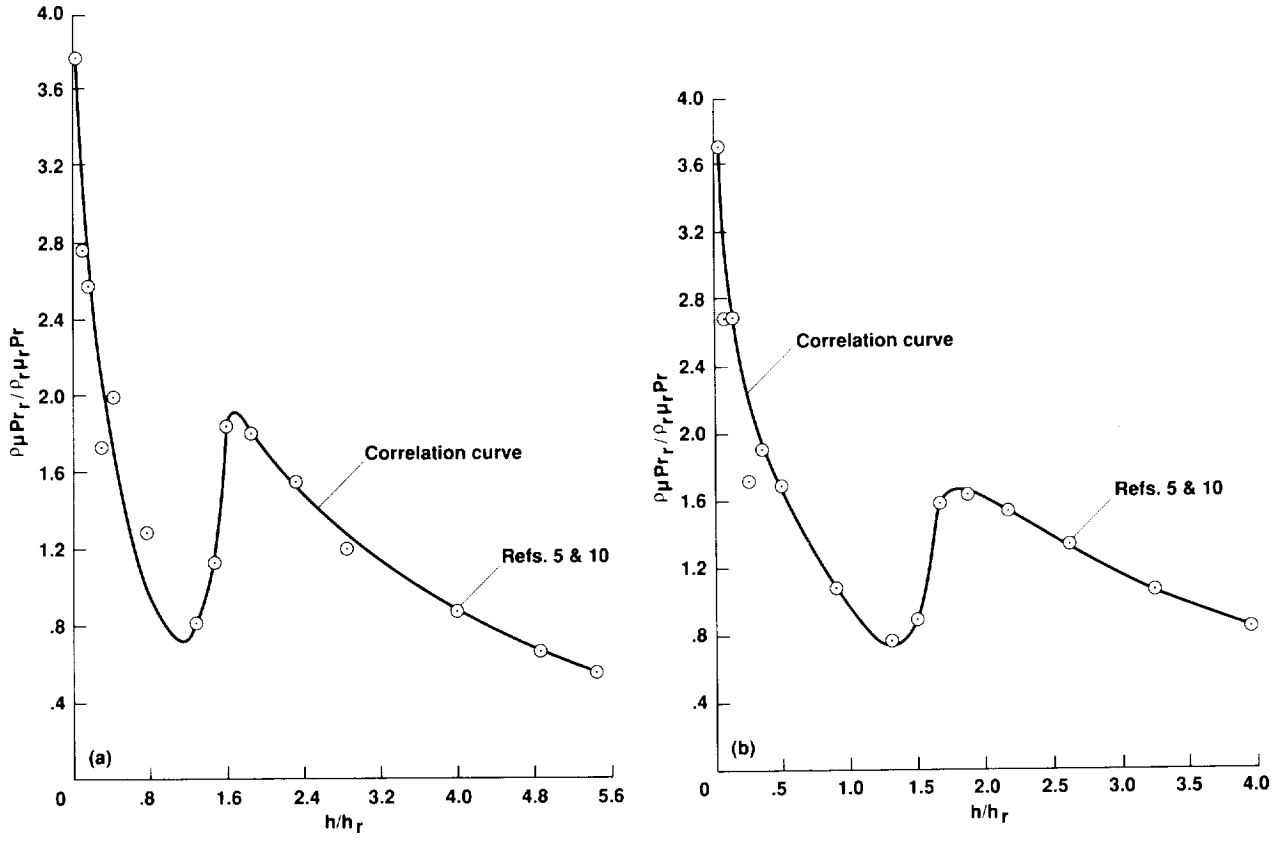

Figure A-3.– Density-viscosity Prandtl number parameter correlation. (a) p = 10^{-1} atm; (b) p = 1 atm.

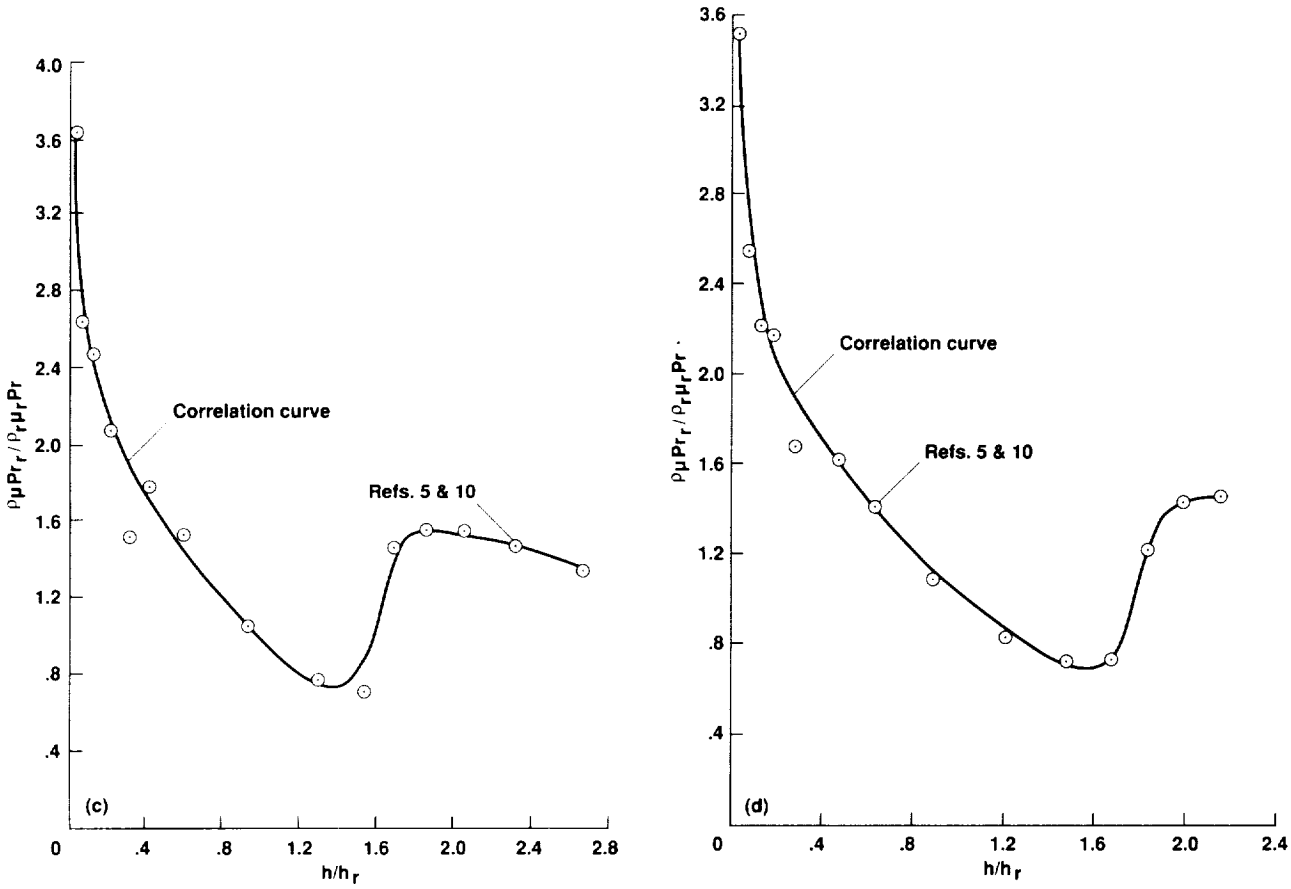

Figure A-3.– Concluded. (c) p = 10 atm; (d) p = 100 atm.

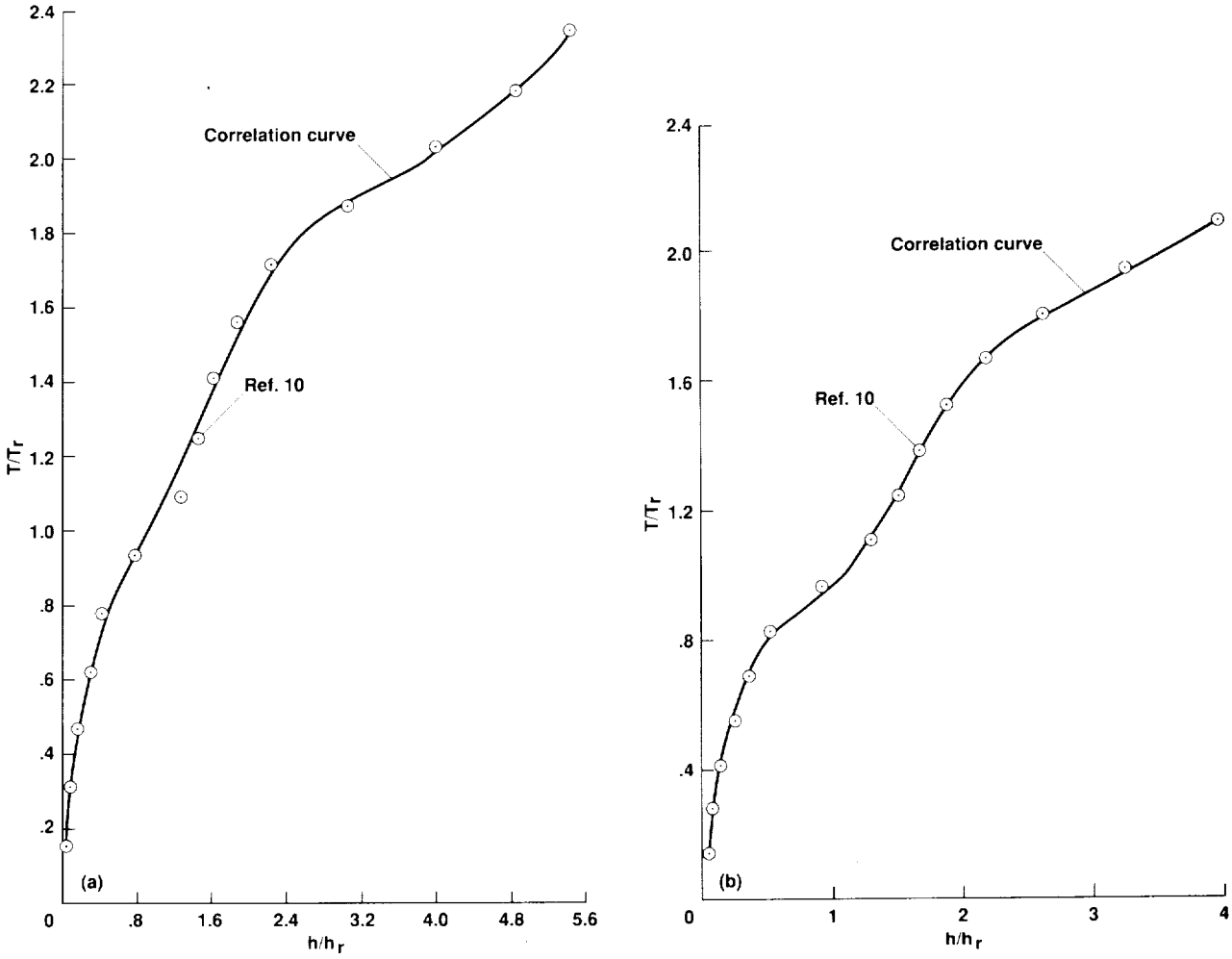

Figure A-4.– Temperature correlation. (a) p = 10^{-1} atm; (b) p = 1 atm.

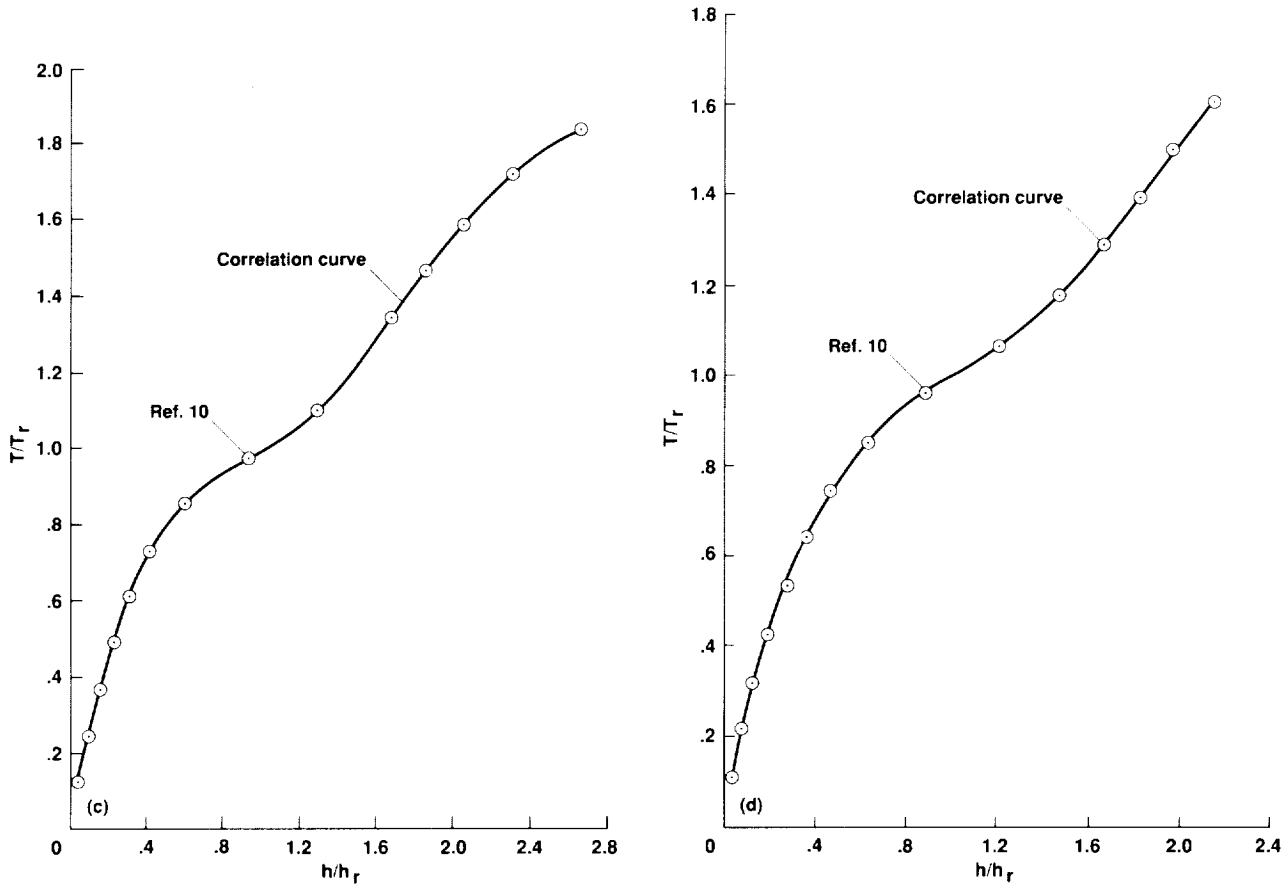

Figure A-4.– Concluded. (c) p = 10 atm; (d) p = 100 atm.

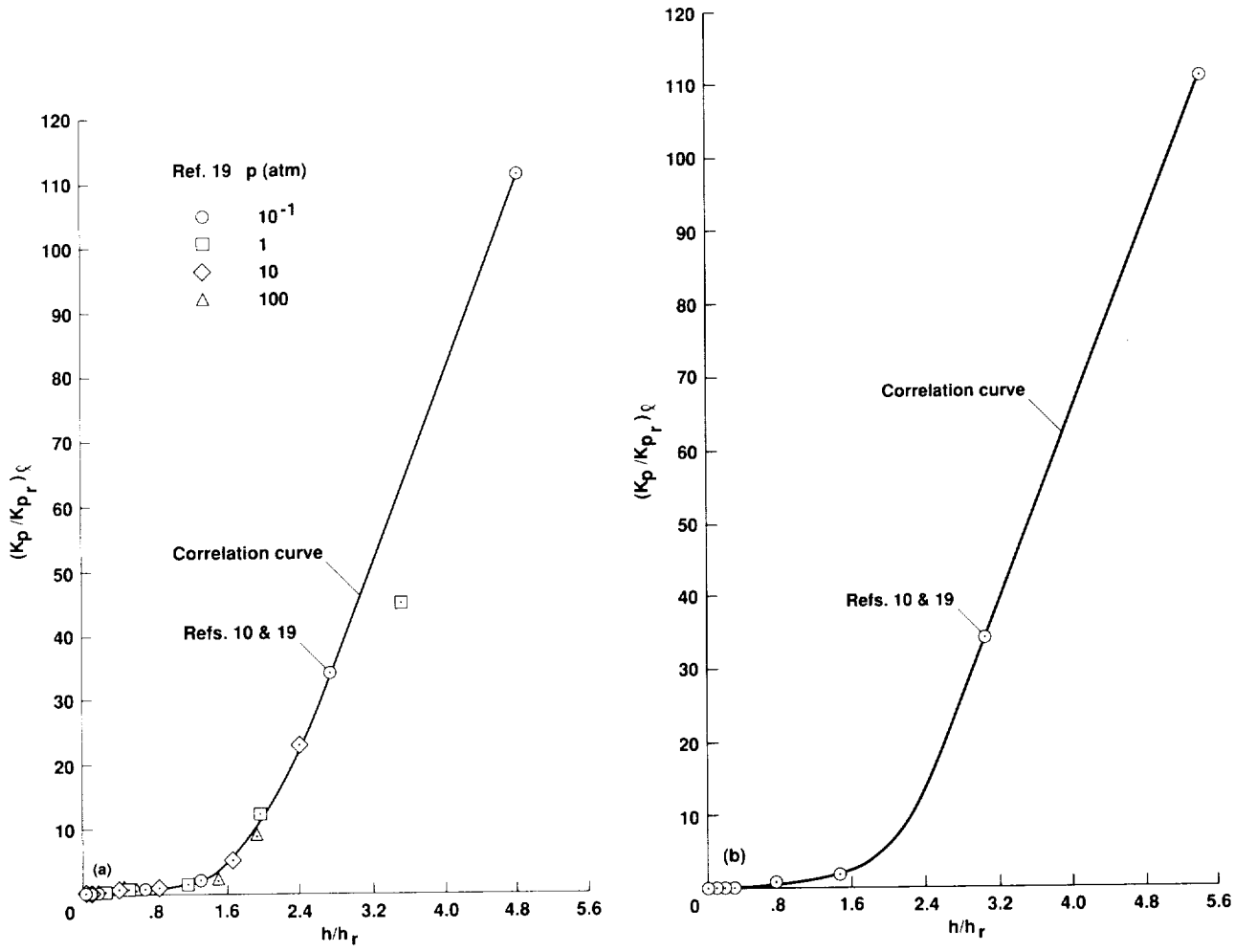

Figure A-5.– Planck mean-mass absorption coefficient correlation. (a) All pressures; (b) p = 10^{-1} atm.

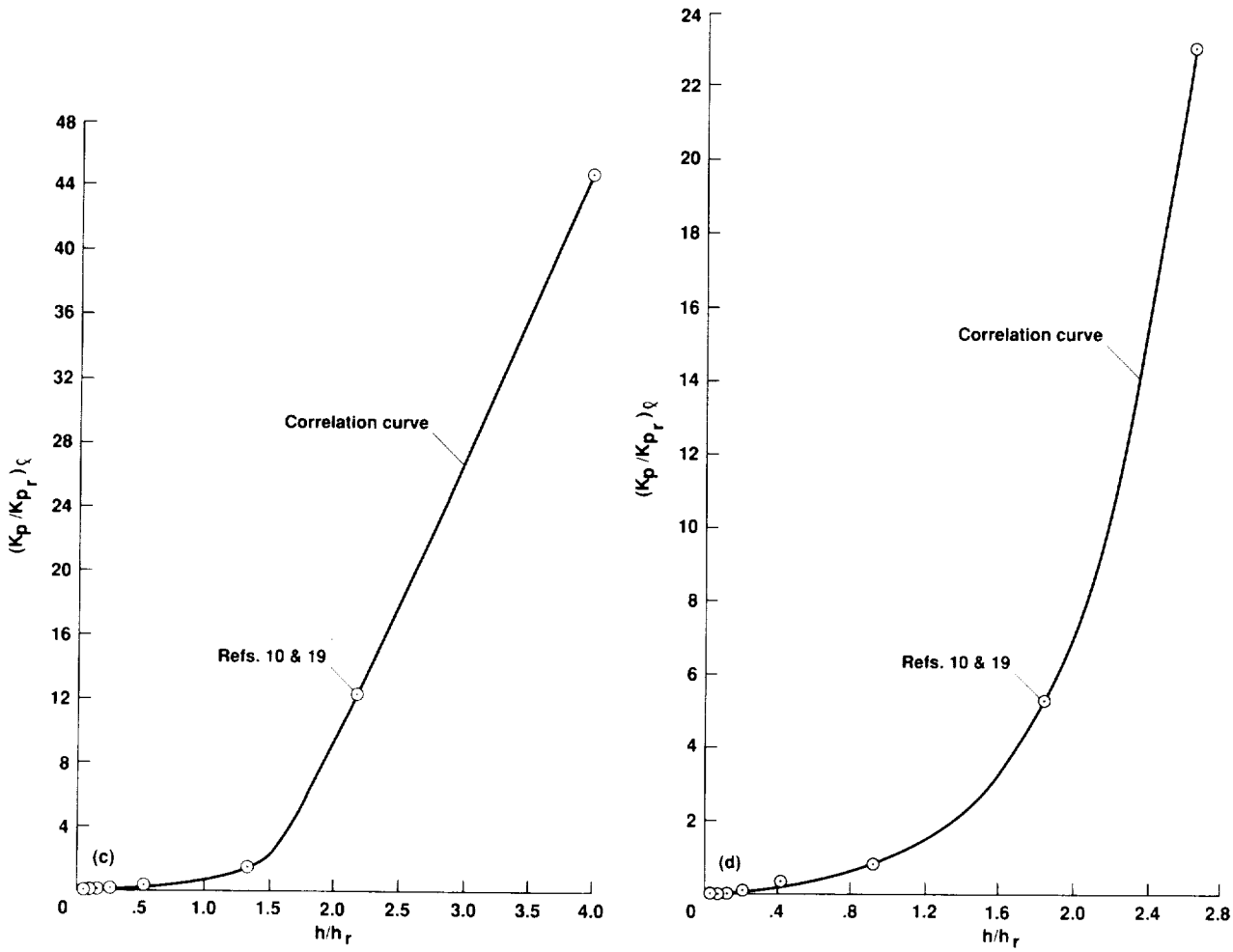

Figure A-5.– Continued. (c) p = 1 atm; (d) p = 10 atm.

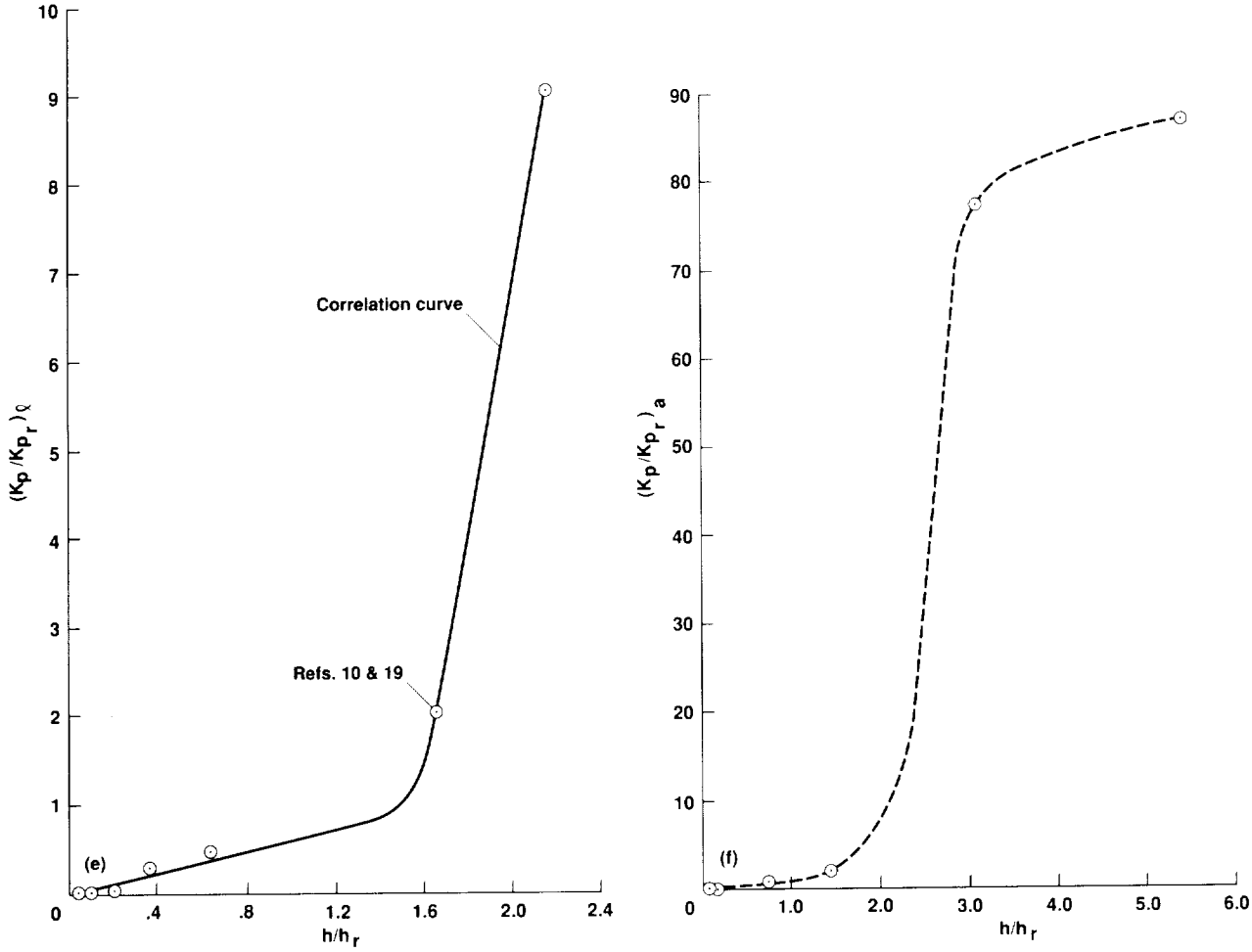

Figure A-5.– Continued. (e) p = 100 atm; (f) p = 10^{-1} atm.

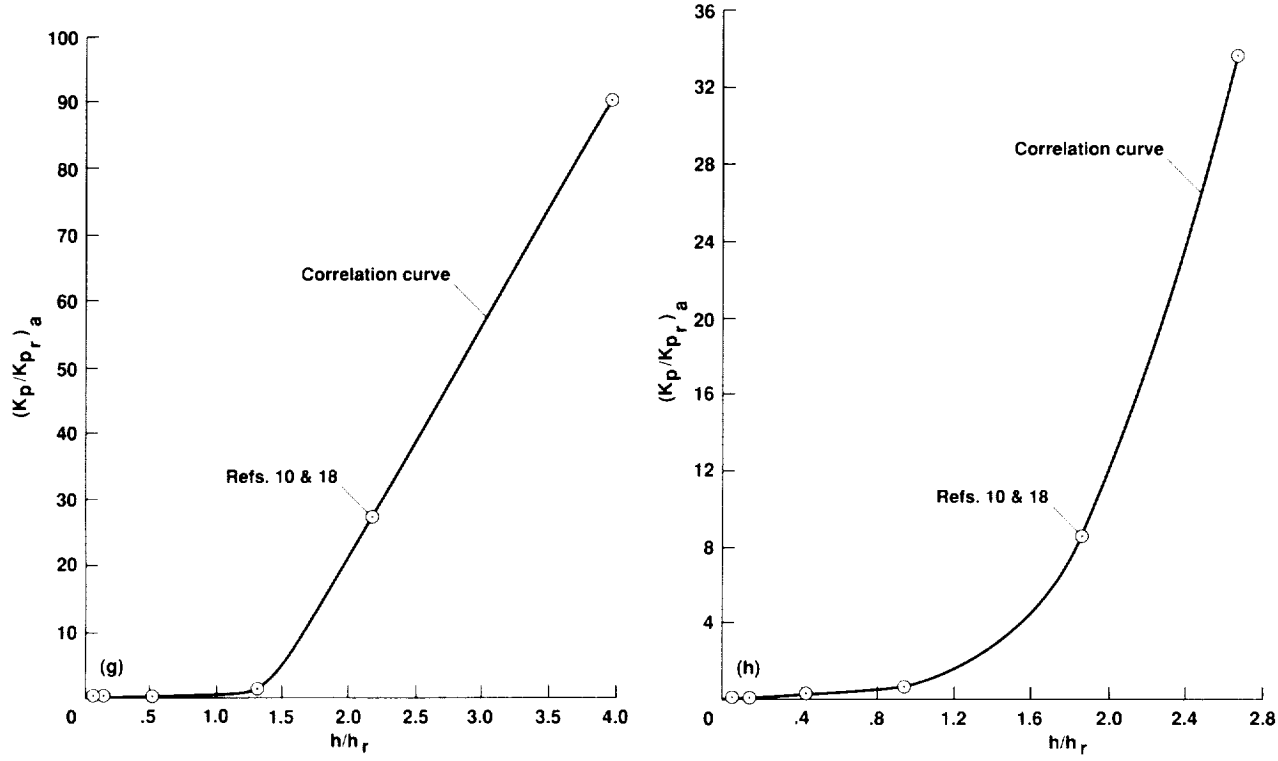

Figure A-5.– Continued. (g) p = 1 atm; (h) p = 10 atm.

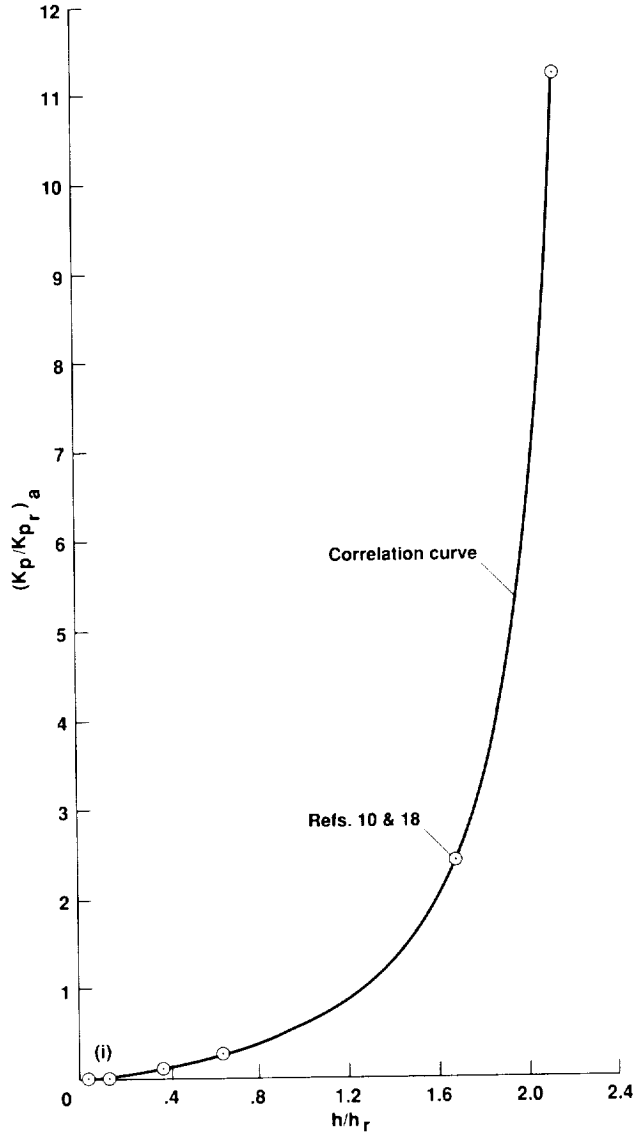

Figure A-5.– Concluded. (i) p = 100 atm.

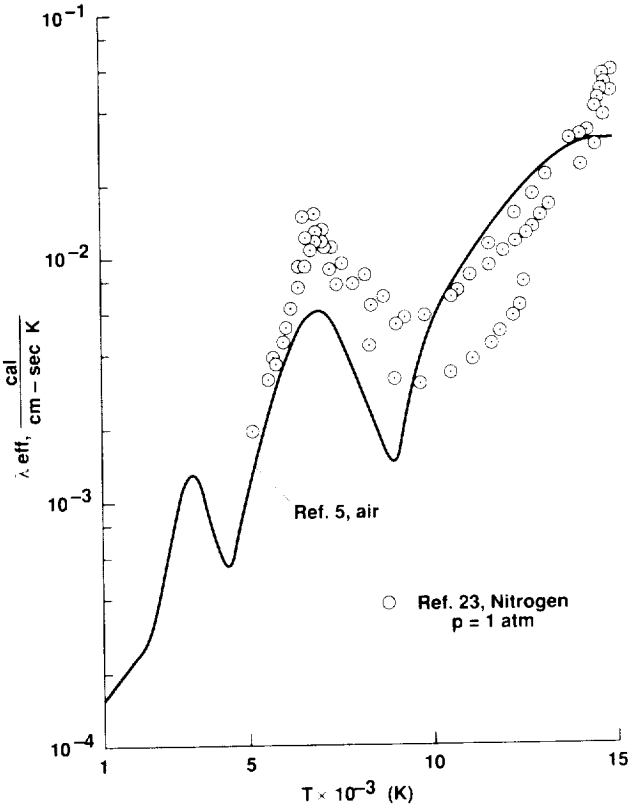

Figure A-6.– Thermal conductivity—comparison of experiment and theory.

REFERENCES

1. Ahtye, W. F.: A Critical Evaluation of Methods for Calculating Transport Coefficients of Partially and Fully Ionized Gases, NASA TN D-26111, 1965.

2. Hirschfelder, J. O.; Curtiss, C. F.; and Bird, R. B.: Molecular Theory of Gases and Liquids. Wiley, 1954.

3. Bird, R. B.; Stewart, W. E.; and Lightfoot, E. N.: Transport Phenomena. Wiley, 1960.

4. Chapman, S.; and Cowling, T. G.: Mathematical Theory of Non-Uniform Gases. Second ed., Cambridge Univ. Press, 1951.

5. Hansen, C. F.: Approximations for the Thermodynamic and Transport Properties of High Temperature Air. NASA TR R-50, 1959.

6. Lees, L.: Convective Heat Transfer with Mass Addition and Chemical Reactions. Presented at AGARD Combustion and Propulsion Colloquium, NATO Palermo, Sicily, 1958 (GALCIT Pub. 451), Pergamon Press, 1958.

7. Lees, L.: Ablation in Hypersonic Flows. Presented at Seventh Anglo-American Aeronautical Conf., New York, 1959 (GALCIT Pub. 481), Pergamon Press, 1959.

8. Kendall, R.; Rindal, R.; and Bartlett, R.: Thermochemical Ablation, Thermophysics and Temperature Control of Spacecraft and Entry Vehicles, G. P. Heller, ed., Progress in Astronautics and Aeronautics, Vol. 64, Martin Summerfield, Series Editor, 1966.

9. Yos, J. M.: Transport Properties of Nitrogen, Hydrogen, Oxygen, and Air to 30,000K, AVCO Rep. RAD TM 63-7, 1963.

10. Moeckel, W. E.; and Weston, K. C.: Composition and Thermodynamic Properties of Air in Chemical Equilibrium. NACA TN-4265, 1958.

11. Viegas, J. R.; and Howe, J. T.: Thermodynamic and Transport Property Correlation Formulas for Equilibrium Air from 1,000K to 15,000K. NASA TM D-1429, 1962.

12. Howe, J. T.; and Viegas, J. R.: Solutions of the Ionized Radiating Shock Layer, Including Reabsorption and Foreign Species Effects, and Stagnation Region Heat Transfer. NASA TR R-159, 1963.

13. Howe, J. T.; and Sheaffer, Y. S.: Effects of Uncertainties in the Thermal Conductivity of Air on Convective Heat Transfer for Stagnation Temperature up to 30,000 K. NASA TN D-2678, 1965.

14. Meador, W. E.; and Staton, L. D.: Electrical and Thermal Properties of Plasmas. Phys. Fluids, vol. 8, no. 9, Sept. 1965, pp. 1694-1703.

15. Howe, J. T.; and Sheaffer, Y. S.: Role of Charge Separation and Pressure Diffusion in the Gascap of Entry Objects. AIAA J., vol. 7, no. 10, Oct. 1969, pp. 1971-1977.

16. Cohen, Nathaniel B.: Correlation Formulas and Tables of Density and Some Transport Properties of Equilibrium Dissociating Air for Use in Solutions of the Boundary-Layer Equations. NASA TN D-194, 1960.

17. Yoshikawa, Kenneth K.; and Wick, Bradford H.: Radiative Heat Transfer During Atmosphere Entry at Parabolic Velocity. NASA TN D-1074, 1961.

18. Kivel, B.; and Bailey, K.: Tables of Radiation From High Temperature Air. Avco-Everett Research Laboratory. Res. Rep. 21, 1957.

19. Armstrong, B. H.; Sokoloff, J.; Nicholls, R. W.; Holland, D. H.; and Meyerott, R. E.: Radiative Properties of High Temperature Air. J. Quant. Spectros. Radiative Transfer, vol. 1, no. 2, Nov. 1961, pp. 143-162.

20. Scala, Sinclaire M.; and Warren, Walter R.: Hypervelocity Stagnation Point Heat Transfer. General Electric, Space Sciences Laboratory, R61SD185, 1961.

21. Pallone, Adrian; and Van Tassel, William: Stagnation Point Heat Transfer for Air in the Ionization Regime. ARS J., vol. 32, no. 3, Mar. 1962, p. 436.

22. Peng, Tzy-Cheng; and Ahtye, Warren F.: Experimental and Theoretical Study of Heat Conduction for Air Up to 5000°K. NASA TN D-687, 1961.

23. Maecker, H.: Thermal and Electrical Conductivity of Nitrogen Up to 15,000°K by Arc Measurements. Presented at Meeting on Properties of Gases at High Temperature, AGARD, Aachen, Sept. 21-23, 1959.

24. Ahtye, W. F.; and Peng, Tzy-Cheng: Approximations for the Thermodynamic and Transport Properties of High-Temperature Nitrogen With Shock-Tube Applications. NASA TN D-1303, 1962.

25. King, L. A.: Theoretical Calculation of Arc Temperatures in Different Gases. Colloquium Spectroscopicum Internationale VI (Amsterdam, 1956), pp. 152-161 (London: Pergamon Press, 1957). (Based on E.R.A. Report Ref. G/XT-155.)

CHAPTER 6

RADIATIVE TRANSFER; RADIATING SHOCK LAYER

In the development of terms that appear in the governing flow-field equations of Chapter 4, we come to the final formulation, that of radiative transfer. In a gas mixture at high temperature, various atomic and molecular processes cause the gas to emit and absorb radiant energy. As we said at the outset, we will not delve into the internal events of these species—that is a subject in its own right. Aside from a superficial description of these internal processes, we will confine our attention to the transfer of radiation in and through this gas mixture and assume that the coefficients we need to quantify emission and absorption of radiation are available to us. The physical processes have to do with the transition from one energy level to another in a gas species accompanied by the emission or absorption of radiation (a photon of radiant energy at a particular wavelength or frequency); emission if the species drops to a lower energy state, or absorption if it is excited to a higher energy level. Thus there are rotational, vibrational, and electronic states of molecules and atoms that are affected. Moreover, for electron processes, there are free-free, free-bound, and bound-bound processes which correspond to a trajectory change of a passing electron, capture of a free electron, or the transition of an electron from one orbit to another within a species, respectively. These various processes give rise to photons in specific parts of the electromagnetic spectrum, including spectral lines, bands, and continuum radiation. The details of the physical processes are beyond the scope of this monograph.

There are two phenomena that will be neglected because they are not important to the application to hypervelocity flight. First is the internal energy of radiation on the macroscopic level. The phenomenon of the instantaneous presence of photons of radiant energy in a volume of gas does not affect the internal energy of the gas at temperatures that concern us (up to 20000 to 30000 K). Secondly, radiation pressure will be neglected for our application. It is important for very large regions of very hot gas, but can be neglected in the equations of motion for present purposes. These two phenomena are discussed in references 1 and 2.

The phenomenon of radiative transfer in a hot gas cap is illustrated in figure 6-1, which shows a disk that is 10 in. in diameter mounted normal to a hypervelocity test stream of air. The air in which the model is immersed is heated by an electric arc discharged into the air upstream of the model, after which the air is passed through an aerodynamic nozzle having an exit diameter of 3.5 ft. The electric arc used can operate at 60 MW to produce enthalpy levels up to 20,000 Btu/lb_m on a continuous basis, and can accommodate models up to 20 in. in diameter. The test conditions for this figure correspond to a less severe environment intended to simulate flight at an altitude of 63 km and at a speed of 4.3 km/sec (recall that orbital speed is about 7 km/sec near Earth). The gas between the bow shock wave and the disk is luminous in the figure because it is emitting and absorbing radiation, some of which escapes the gas cap. (This figure is by courtesy of Warren Winovich and John Balboni of NASA Ames Research Center.)

Thus the figure illustrates the phenomenon which we intend to describe. Our objective in this chapter is to provide expressions for the radiative heating rate, $\vec{q}_r$, and the term, div $\vec{q}_r$, used in the differential equations that describe the flow field about a body in hypervelocity flight (eq. (3) of Chapter 4, the energy equation). Eventually, we will solve the set of coupled integro-differential equations.

For present purposes, a more detailed development of that which follows can be found in references by Chandrasekhar (ref. 3), or a very readable account by Kourganoff (ref. 2), wherein a very

Figure 6-1.– Radiating gas cap.

Some Definitions

detailed treatment of the development can be found, including some subtleties that are not elaborated upon in this monograph.

As shown in figure 6-2, let P be a fixed point in an absorbing and emitting gas mixture and let S be a fixed line through P. Let $d\sigma$ be an element of area containing P and let γ be the angle between S and the normal Y' to $d\sigma$.

The amount of radiant energy flowing through $d\sigma$, in a specified frequency interval $(\nu, \nu + d\nu)$, in a direction making an angle γ with the normal to $d\sigma$, within an elementary solid angle $d\omega'$ about the direction S, in time dt, is

$$dE_\nu = I_\nu \cos\gamma \, d\sigma \, d\omega' \, d\nu \, dt \tag{1}$$

It follows that the spectral intensity I_ν can be defined as the energy flowing at the point P in the direction S, per unit of time, of frequency interval, of solid angle, and of surface area normal to S (what is fundamental is not $d\sigma$, but its projection $d\sigma \cdot \cos\gamma$). In the general case,

$$I_\nu = I_\nu(P,S,t) \tag{2}$$

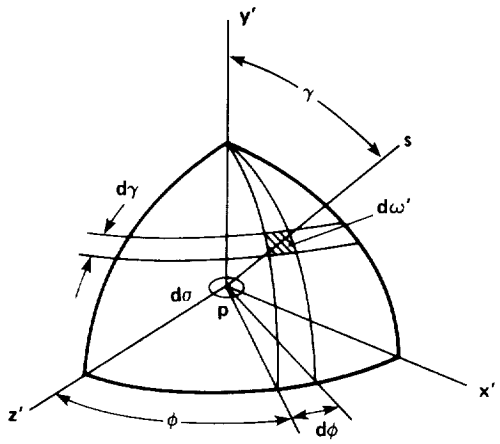

Figure 6-2.– Radiation coordinates.

It may be noted that for all S directions that make an angle γ with Y' the solid angle $d\omega$ is $(2\pi \sin \gamma \cdot d\gamma)$. The differential spectral radiation flux due to contributions from one S direction making an angle γ with the normal Y' is

$$dF_\nu = \frac{dE_\nu}{d\sigma\, dt\, d\nu} = I_\nu \cos \gamma\, d\omega' \tag{3}$$

Summing over all S directions making an angle γ with the normal Y' (replace $d\omega'$ by $d\omega$) and over all angles γ yields the directional spectral radiation flux

$$F_\nu = \int_{\gamma=0}^{\pi} I_\nu \cos \gamma (2\pi \sin \gamma\, d\gamma) = 2\pi \int_{\gamma=0}^{\pi} I_\nu \cos \gamma \sin \gamma\, d\gamma \tag{4}$$

The interaction between radiation and the gas is expressed in terms of an absorption coefficient and an emission coefficient. With reference to figure 6-3, the intensity I_ν in the direction S becomes $I_\nu + \delta I_\nu$ along S' by interaction between the radiation and the matter dm contained in the volume $d\sigma\, ds$. Experiment and theory show that

$$\frac{\delta I_\nu(s)}{I_\nu} = -K_\nu \rho\, ds = -\mu_\nu\, ds \tag{5}$$

where K_ν is the mass spectral absorption coefficient,[1] and radiative scattering phenomena are neglected.

Similarly, an element of mass dm sends in directions confined to an elementary solid angle $d\omega'$, in the frequency interval $(\nu + d\nu)$ and in time dt, an amount of radiant energy equal to

$$de_\nu = J_\nu\, dm\, d\nu\, d\omega'\, dt \tag{6}$$

[1] In the strict sense, the absorption coefficient, K_ν, deals with the Lagrangian loss of photons (ref. 2, pp. 4-5).

and is composed of that energy truly emitted by (created by) and that scattered into (from all directions) by dm (J_ν is the mass spectral emission coefficient).

Denoting the intensity of black radiation of frequency ν and temperature by $B_\nu(T)$, the local thermodynamic equilibrium (LTE) assumption is one of Kirchoff's laws

$$J_\nu = r_\nu^2 B_\nu(T) K_\nu \tag{7}$$

where r_ν is the index of refraction of the medium. For simplicity, we restrict ourselves to media for which $r_\nu = 1$. Thus

$$J_\nu = K_\nu \cdot B_\nu(T) \tag{8}$$

for LTE. The explicit form for the function $B_\nu(T)$ is given by quantum statistics, and is called Planck's law:

$$B_\nu(T) = \frac{2h\nu^3}{c^2}\left(\frac{1}{e^{h\nu/kT} - 1}\right) \tag{9}$$

where c is light speed, h is the Planck constant, and $B_\nu(T)$ is also called the "source function."

The Equation of Transfer

So far, we have adopted a partially Lagrangian point of view and, by means of the absorption coefficient and the emission coefficient, have examined what happens to certain photons. From the Eulerian point of view, the variations in the intensity of the photons near a given point are now examined.

Accordingly, consider the small cylinder element (shown in fig. 6-3) of cross section $d\sigma$ and length ds in the medium, and the radiant energies which cross the two faces normally in a time dt and in directions confined to a solid angle $d\omega'$.

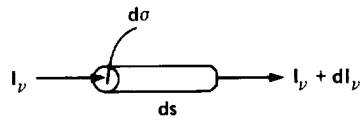

Figure 6-3.– Volume element of gas oriented in the S direction.

The energies *in* and *out* are

$$dE_{\nu_{in}} = I_\nu \, d\sigma \, d\omega' \, d\nu \, dt \tag{10}$$

$$dE_{\nu_{out}} = (I_\nu + dI_\nu) d\sigma \, d\omega' \, d\nu \, dt \tag{11}$$

The energy balance can be written by use of equations (6) and (5)

$$-(dE_{\nu_{in}} - dE_{\nu_{out}}) = J_\nu \, dm \, d\nu \, d\omega' \, dt - (K_\nu I_\nu \rho \, ds)(d\sigma \, d\omega' \, d\nu \, dt) \tag{12}$$

Noting that

$$dm = \rho \, ds \, d\sigma \tag{13}$$

we substitute equations (10) and (11) into equation (12)

$$dI_\nu \, d\nu \, d\sigma \, d\omega' \, dt = J_\nu \rho \, ds \, d\sigma \, d\nu \, d\omega' \, dt - K_\nu I_\nu \rho \, ds \, d\sigma \, d\nu \, d\omega' \, dt \tag{14}$$

This yields a first expression of the equation of transfer in the S-direction

$$-\frac{1}{\rho K_\nu}\frac{dI_\nu(s)}{ds} = I_\nu(s) - \frac{J_\nu}{K_\nu} \tag{15}$$

which for LTE becomes

$$-\frac{1}{\rho K_\nu}\frac{dI_\nu(s)}{ds} = I_\nu(s) - B_\nu(T) \tag{16}$$

Plane-Parallel Radiating Layer of Gas

For our purposes, a blunt stagnation region or a stellar atmosphere is considered to be stratified in homogeneous plane-parallel layers in such a way that a single variable (geometrical depth y) is sufficient for the specification of a layer of the atmosphere. The atmosphere is supposed to be in *strict radiative equilibrium*, i.e., it is assumed that the heat interchanged by convection and conduction is negligible compared with that interchanged by radiation.

We shall therefore introduce the geometrical depth y and the direction parameter $w = \cos\theta$ (see fig. 6-4).

$$dy = ds \cos\gamma = ds \cos(\pi - \theta) = -ds \cos\theta \tag{17}$$

$$ds = -\frac{dy}{\cos\theta} = -dy \sec\theta \equiv -\frac{1}{w}dy \tag{18}$$

$$w = \frac{1}{\sec\theta} = \cos\theta = -\cos\gamma \tag{19}$$

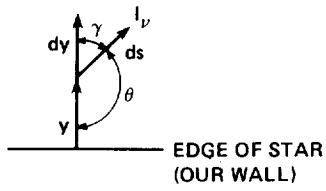

Figure 6-4.– "Plane-parallel" radiating gas.

As before, the assumption of local thermodynamic equilibrium, $J_\nu/K_\nu = B_\nu(T)$, is made (eq. 8). Thus we obtain the modified equation of transfer in any S-direction in terms of y, by use of equation (16)

$$\frac{w}{\rho K_\nu}\frac{dI_\nu}{dy} = I_\nu - B_\nu(T) \tag{20}$$

where

$$I_\nu = I_\nu(w,y)\,; \quad \rho = \rho(y)\,; \quad K_\nu = K_\nu(y)\,; \quad T = T(y) \tag{21}$$

The Intensity I_ν Expressed as a function of B_ν and the Optical Depth

We introduce the function τ_ν called the spectral optical depth

$$\tau_\nu = \int_0^y \rho K_\nu \, dy \tag{22}$$

thus, the element of optical depth

$$d\tau_\nu = \rho K_\nu \, dy \tag{23}$$

represents the relative weakening of the intensity transmitted, normally, by the corresponding layer of the geometrical thickness dy. Then equation (20) becomes

$$w\frac{dI_\nu}{d\tau_\nu} = I_\nu - B_\nu(T) \tag{24}$$

where

$$I_\nu = I_\nu(\tau_\nu, w) \tag{25}$$

We first want the solution of the homogeneous equation

$$\frac{dI_\nu}{I_\nu} = \frac{1}{w}d\tau_\nu \tag{26}$$

This is

$$I_\nu = C\exp\left(\frac{\tau_\nu}{w}\right) \tag{27}$$

where C is a constant. The particular integral of the nonhomogeneous equation is obtained by substituting equation (27) into equation (24) (where C is regarded as a function of τ_ν). From equation (27),

$$\frac{dI_\nu}{d\tau_\nu} = C\frac{1}{w}\exp\left(\frac{\tau_\nu}{w}\right) + \frac{dC}{d\tau_\nu}\exp\left(\frac{\tau_\nu}{w}\right) \tag{28}$$

Thus

$$C\exp\left(\frac{\tau_\nu}{w}\right) + w\frac{dC}{d\tau_\nu}\exp\left(\frac{\tau_\nu}{w}\right) = C\exp\left(\frac{\tau_\nu}{w}\right) - B_\nu(T) \tag{29}$$

finally, we have the relation

$$\frac{dC}{d\tau_\nu} = -\frac{B_\nu(T)}{w\exp\left(\frac{\tau_\nu}{w}\right)} \tag{30}$$

Integrating equation (30) gives us C as

$$C = -\int_c^{\tau_\nu} B_\nu(T)\exp\left(-\frac{t}{w}\right)\frac{dt}{w} \tag{31}$$

where the variable t replaces τ_ν.

From equations (27) and (31), we deduce the relation we were looking for:

$$I_\nu = -\exp\left(\frac{\tau_\nu}{w}\right)\int_c^{\tau_\nu} B_\nu\exp\left(-\frac{t}{w}\right)\frac{dt}{w} = -\int_c^{\tau_\nu} B_\nu\exp\left(-\frac{t-\tau_\nu}{w}\right)\frac{dt}{w} \tag{32}$$

Intensity Direction Convention and the Radiative Flux Expression

The determination of the constant C brings in the distinction between I_ν^+ (toward the wall), and I_ν^- (away from the wall).

We define I_ν^+ for $0 \le w \le 1$ by switching limits, changing sign, and allowing $C \to \infty$; thus for rays directed toward the wall from layers between τ_ν and ∞, from equation (32)

$$I_n^+ = \int_{\tau_\nu}^{\infty} B_\nu(T)\exp\left(-\frac{t-\tau_\nu}{w}\right)\frac{dt}{w} \tag{33}$$

Moreover, we know from equation (22) that at the surface ($\tau_\nu = 0$), rays directed away from the wall are from equation (32) and our convention

$$\bar{I}_{\nu 0} = -\int_c^0 B_\nu(T) \exp\left(-\frac{t}{w}\right)\frac{dt}{w} \tag{34}$$

But at τ_ν, the rays directed away from the wall are from equation (32).

$$\bar{I}_\nu = -\int_c^{\tau_\nu} B_\nu(T) \exp\left(-\frac{t-\tau_\nu}{w}\right)\frac{dt}{w} = -\int_0^{\tau_\nu} - \int_c^0 \tag{35}$$

therefore, at τ_ν, $\bar{I}_\nu$ is the sum of the contributions from the source functions corresponding to the layers below τ_ν, each weakened according to its optical distance $(\tau_\nu - t)$ from location τ_ν, and of the surface term $\bar{I}_{\nu 0}$.

Writing the last integral of equation (35) first, the expression for rays directed away from the wall at the location τ_ν is (by use of eq. (32))

$$\bar{I}_\nu(\tau_\nu) = (\bar{I}_{\nu 0}) \exp\left(\frac{\tau_\nu}{w}\right) - \int_0^{\tau_\nu} B_\nu(T) \exp\left(-\frac{t-\tau_\nu}{w}\right)\frac{dt}{w} \tag{36}$$

Recall from equation (4) that

$$F_\nu = 2\pi \int_{\gamma=0}^{\pi} I_\nu \cos\gamma \sin\gamma \, d\gamma = 2\pi \int_0^{\pi/2} (\bar{I}_\nu)\cos\gamma \sin\gamma \, d\gamma + 2\pi \int_{\pi/2}^{\pi} (\bar{I}_\nu^+)\cos\gamma \sin\gamma \, d\gamma \tag{37}$$

where positive F_ν is in the $+y$ direction. But

$$\cos\gamma = -w, \qquad \sin\gamma \, d\gamma = dw \tag{38}$$

and

$$\cos\gamma \sin\gamma \, d\gamma = -w \, dw \tag{39}$$

Substituting into equation (37) using equations (36) and (33) and noting that when $\gamma = 0$, $w = -1$, yields

$$F_\nu = -2\pi \int_{-1}^{0} \left[(\bar{I}_{\nu 0}) \exp\left(\frac{\tau_\nu}{w}\right) - \int_0^{\tau_\nu} B_\nu(T) \exp\left(-\frac{t-\tau_\nu}{w}\right)\frac{dt}{w} \right] w\, dw$$

$$- 2\pi \int_0^1 \left[\int_{\tau_\nu}^{\infty} B_\nu(T) \exp\left(-\frac{t-\tau_\nu}{w}\right)\frac{dt}{w} \right] w\, dw \qquad (40)$$

Define m by

$$m = \frac{1}{w}, \quad dw = -\frac{dm}{m^2}, \quad w\, dw = -\frac{dm}{m^3} \qquad (41)$$

Thus when

$$w = \pm 1 \Rightarrow m = \pm 1 \qquad (42)$$

$$w = 0^{\pm} \Rightarrow m = \pm\infty \qquad (43)$$

Correspondingly, substitute m for w and change the limits in equation (40),

$$F_\nu = -2\pi \int_{-1}^{-\infty} \left\{ (\bar{I}_{\nu 0}) \frac{\exp(\tau_\nu m)}{m^3} - \int_0^{\tau_\nu} \frac{B_\nu(T)\exp[-(t-\tau_\nu)(m)]}{m^2} dt \right\} (-dm)$$

$$-2\pi \int_{+\infty}^{1} \left\{ \int_{\tau_\nu}^{+\infty} \frac{B_\nu(T)\exp[-(t-\tau_\nu)(m)]}{m^2} dt \right\} (-dm) \qquad (44)$$

where the first integral originates at the wall, the second integral is flux outbound from the gas between the wall and τ_ν, and the last integral is inbound flux from the gas between τ_ν and ∞; and the entire expression gives the net spectral flux at the location τ_ν. Interchange the order of integration, integrating over m first, noting that $B_\nu(T)$ is not a function of m,

$$F_\nu = 2\pi \int_{-1}^{-\infty} (\bar{I}_{\nu 0}) \frac{\exp(\tau_\nu m)}{m^3} dm - 2\pi \int_0^{\tau_\nu} B_\nu(T) \left\{ \int_{-1}^{-\infty} \frac{\exp[-(t-\tau_\nu)(m)]}{m^3} dm \right\} dt$$

$$+ 2\pi \int_{\tau_\nu}^{+\infty} B_\nu(T) \left\{ \int_{+\infty}^{1} \frac{\exp[-(t-\tau_\nu)(m)]}{m^2} dm \right\} dt \qquad (45)$$

We introduce integro-exponential functions of order n (an integer), which are defined by

$$E_n(\zeta) = \int_1^{\infty} \frac{\exp(-\zeta m)}{m^n} dm \tag{46}$$

In the integrals of equation (45), we replace m by $-m$ and dm by $-dm$, which yields

$$\int_{-1}^{-\infty} (\bar{I}_{\nu 0}) \frac{\exp(\tau_\nu m)}{m^3} dm = \int_1^{+\infty} (\bar{I}_{\nu 0}) \frac{\exp(-\tau_\nu m)}{m^3} dm \tag{47}$$

and

$$\int_{-1}^{-\infty} \frac{\exp(-(t - \tau_\nu)m)}{m^2} dm = -\int_1^{+\infty} \frac{\exp[-(\tau_\nu - t)(m)]}{m^2} dm = -E_2(\tau_\nu - t) \tag{48}$$

We rewrite equation (45) as

$$F_\nu = 2\pi \int_1^{+\infty} (\bar{I}_{\nu 0}) \frac{\exp(-\tau_\nu m)}{m^3} dm + 2\pi \int_0^{\tau_\nu} B_\nu(T) E_2(\tau_\nu - t) dt - 2\pi \int_{\tau_\nu}^{+\infty} B_\nu(T) E_2(t - \tau_\nu) d\tau \tag{49}$$

We define the radiosity of the wall (which is assumed to be diffuse, i.e., the intensity does not depend on the direction)

$$J_{\nu 0} = \pi I_\nu(0) \tag{50}$$

Then, the first term of equation (49) becomes

$$2\pi \int_1^{+\infty} (\bar{I}_{\nu 0}) \frac{\exp(-\tau_\nu m)}{m^3} dm = 2J_{\nu 0} E_3(\tau_\nu) \tag{51}$$

We now assume that the wall is opaque with emissivity $\varepsilon_{\nu w}$ and reflectivity $R_{\nu w}$.

$$J_{\nu_0} = \varepsilon_{\nu_w}\pi B_\nu(T_w) + R_{\nu_w} 2\pi \underbrace{\int_0^{+\infty} B_\nu(T)\, E_2(t)dt}_{\text{last integral of equation (49) with } \tau_\nu = 0} \tag{52}$$

Substitute equation (52) into equation (51), then into equation (49) integrated over ν, with the notation

$$q_r = \int_0^\infty F_\nu \, d\nu \tag{53}$$

we find at τ_ν, the radiative flux is

$$q_r = \underbrace{\int_0^\infty 2\pi\varepsilon_{\nu_w} B_\nu(T_w) E_3(\tau_\nu) d\nu}_{\text{wall emission}} + \underbrace{\int_0^\infty 2R_{\nu_w} E_3(\tau_\nu) \left[\int_0^\infty 2\pi B_\nu(T)\, E_2(t)dt \right] d\nu}_{\text{wall reflection}}$$

$$+ 2\pi \int_0^\infty \underbrace{\int_0^{\tau_\nu} B_\nu(T)\, E_2(\tau_\nu - t)dt\, d\nu}_{\text{gas layer below } \tau_\nu} - 2\pi \int_0^\infty \underbrace{\int_{\tau_\nu}^\infty B_\nu(T)\, E_2(t - \tau_\nu)dt\, d\nu}_{\text{gas layer above } \tau_\nu} \tag{54}$$

That is, for a plane-parallel atmosphere, equation (54) is the radiative flux at $\tau_\nu(y)$ in the +y-direction. Note that this expression contains double integrals over space and frequency. Results of this spectral treatment will be shown in Chapter 9.

Grey Gas, Grey Surface

The grey gas assumption implies that the radiation is not a function of wavelength, i.e., properties such as K_ν and I_ν are independent of the frequency. The grey surface assumption yields $\varepsilon_{\nu_w} = \varepsilon_w$ (which here represents the grey surface emissivity), and $R_{\nu_w} = R_w$ (which here represents the grey surface reflectivity). Thus to simplify our development to a grey radiation problem,

$$B(T) = \int_0^\infty B_\nu(T) d\nu \tag{55}$$

Then the grey flux in the +y-direction is (where K and τ are independent of frequency, ν, and t is a dummy $\tau(y)$)

$$q_r(y) = 2\pi\varepsilon_w B(T_w)E_3(\tau) + 4\pi R_w E_3(\tau)\int_0^\infty B(t)\,E_2(t)dt$$

$$+ 2\pi\int_0^\tau B(t)\,E_2(\tau - t)dt - 2\pi\int_0^\infty B(t)\,E_2(t - \tau)dt \tag{56}$$

where

$$B(T) = B(t) \tag{57}$$

The divergence of the radiative flux is

$$\text{div}\,\underline{q}_r = \frac{\partial}{\partial y} q_r(y) \tag{58}$$

Recall that

$$\tau = \int_0^y \rho K\,dy \tag{59}$$

(where the K to be used will be the Planck mean mass absorption coefficient defined by Eq. (73), and correlated in the appendix of Chapter 5) and

$$d\tau = \rho K\,dy\,, \quad \frac{d}{dy} = \rho K\frac{d}{d\tau} \tag{60}$$

We differentiate E_2 and E_3, by use of equation (46) to obtain

$$\frac{dE_2(\tau - t)}{d\tau} = -E_1(\tau - t) \tag{61}$$

$$\frac{dE_2(t - \tau)}{d\tau} = E_1(t - \tau) \tag{62}$$

$$\frac{dE_3(\tau)}{d\tau} = -E_2(\tau) \tag{63}$$

We now differentiate equation (56) with respect to y, using equation (60), and assuming that the wall is black, $\varepsilon_w = 1$, and $R_w = 0$. First write

$$q_r(y) = 2\pi B(T_w)E_3(\tau) + 2\pi\int_0^{\tau} B(t)\,E_2(\tau - t)dt - 2\pi\int_{\tau}^{\infty} B(t)\,E_2(t - \tau)dt \tag{64}$$

$$\frac{\partial q_r}{\partial y} = \frac{\partial q_r}{\partial \tau}\cdot\frac{\partial \tau}{\partial y} = 2\pi\rho K\left\{-B(T_w)E_2(\tau) + \left[B(\tau)E_2(0) + \int_0^{\tau} B(t)\,\frac{dE_2(\tau - t)}{d\tau}\,dt\right]\right.$$

$$\left. -\left[-B(\tau)E_2(0) + \int_{\tau}^{\infty} B(t)\,E_2(t - \tau)dt\right]\right\} \tag{65}$$

Using equations (60)–(63) and $E_n(0) = 1/(n - 1)$ (for $n > 1$),

$$\frac{\partial q_r}{\partial y} = 2\pi\rho K\left[-B(T_w)E_2(\tau) + 2B(\tau) - \int_0^{\tau} B(t)\,E_1(\tau - t)dt - \int_{\tau}^{\infty} B(t)\,E_1(t - \tau)dt\right] \tag{66}$$

Combining the integrals,

$$\frac{\partial q_r}{\partial y} = 2\pi\rho K\left[-B(T_w)E_2(\tau) + 2B(\tau) - \int_0^{\infty} B(t)\,E_1(|t - \tau|)dt\right] \tag{67}$$

Finally, we use Stefan's Law, $\pi B(T) = \sigma T^4$ (where σ is the Stefan-Boltzmann constant) and the fact that there is no radiation originating beyond $\tau = \tau_s$ (at the shock):

$$\frac{\partial q_r}{\partial y} = \text{div}\,\underline{q}_r = 2\sigma\rho K\left[-T_w^4E_2(\tau) + 2T^4 - \int_0^{\tau_s \text{ or } \infty} T^4(t)\,E_1(|t - \tau|)dt\right] \tag{68}$$

Equation (68) is the term to be used in equation (3) of Chapter 4.

Transparent Gas Approximation for the Emission of Radiation

It is convenient for emitting gases which absorb little, or for purposes of making radiation estimates, to consider the extreme case of a transparent gas (fig. 6-5).

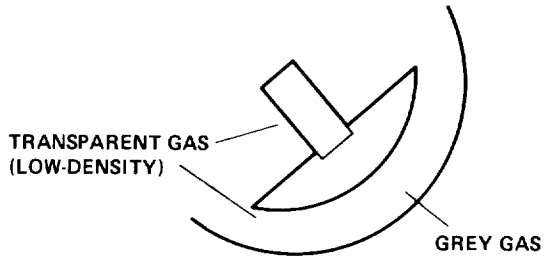

Figure 6-5.– Transparent emitting gas cap.

The radiative emission rate per unit mass, per unit time, in the frequency interval $(\nu,\nu + d\nu)$, within the solid angle $d\omega'$, is

$$de_\nu = J_\nu \, dm \, d\nu \, d\omega' \, dt = J_\nu \rho \, dV \, d\nu \, d\omega' \, dt \tag{69}$$

or

$$\frac{de_\nu}{dV \, dt} = J_\nu \rho \, d\nu \, d\omega' \tag{70}$$

In all 4π steradians, the gas emits radiation at the rate per unit volume

$$4\pi J_\nu \rho \, d\nu \tag{71}$$

Over all the frequencies, the emission rate per unit volume is

$$E_t = 4\pi\rho \int_0^\infty J_\nu \, d\nu = 4\pi\rho \int_0^\infty K_\nu B_\nu(T) d\nu \tag{72}$$

We define the Planck mean mass "absorption" coefficient as

$$K_p = \frac{\int_0^\infty K_\nu B_\nu \, d\nu}{\int_0^\infty B_\nu \, d\nu} = \frac{\pi \int_0^\infty K_\nu B_\nu \, d\nu}{\sigma T^4} \tag{73}$$

Correlated tabular values are presented in the appendix to Chapter 5. Then the energy emission per unit volume is

$$E_t = 4\sigma T^4 K_p \rho \equiv \text{div } \underline{q}_r \quad \text{(transparent gas)} \tag{74}$$

In the one-dimensional approximation, half the radiation is toward the wall and half is directed away from the wall, thus

$$q_r(y) = \frac{1}{2}\int_0^y E_t(y')dy' - \frac{1}{2}\int_y^\delta E_t(y')dy' + \sigma T_w^4 \tag{75}$$

where the last term is the outward emission from a radiatively black wall. At the wall, the flux is

$$q_r(0) = \sigma T_w^4 - \frac{1}{2}\int_0^\delta E_t(y)dy \tag{76}$$

and if the wall emission is neglected,

$$q_r(0) = -\frac{1}{2}\int_0^\delta E_t(y)dy \tag{77}$$

A combination of shock-tube experiments and theory by Kivel and Bailey (ref. 4) estimated the radiant emission rates per unit volume of air as a function of temperature and density. The air was assumed to be in chemical equilibrium with the corresponding chemical species concentrations. These results were correlated by Howe (ref. 5) in the form

$$\text{div } q_r = E_t = cT^d\left(\frac{\rho}{\rho_0}\right)^{nT^a} \tag{78}$$

The correlation is shown by the solid lines in figure 6-6, where the dashed curves are the results from reference 4. The ordinate is in terms of $E_t/2$ because it was used to estimate the heating rate to the wall. Thus $E_t/2$ multiplied by $-\delta$ is an estimate of the radiative heating to the wall from a transparent gas at uniform temperature in accord with equation (77). The correlation expression (eq. (78)) was received with more graciousness than it deserved (ref. 6, p. 398).

The Nearly Opaque Gas Approximation for the Transmission of Radiation

The other extreme, with respect to the transparent gas approximation, is the strongly absorbing gas that is nearly opaque. The latter approximation leads to a flux-divergence term in the energy equation which has the appearance of a radiation "diffusion" term, rather than the complete integral radiative-transfer expression. The corresponding differential equation is much more appealing than the full integro-differential equation. The approximation is called the Rosseland diffusion approximation. Although it appears in the literature, and a terse description of its derivation can be found in reference 7, I am unaware of a meaningful derivation in the literature. Thus a brief derivation is given in what follows (see fig. 6-7).

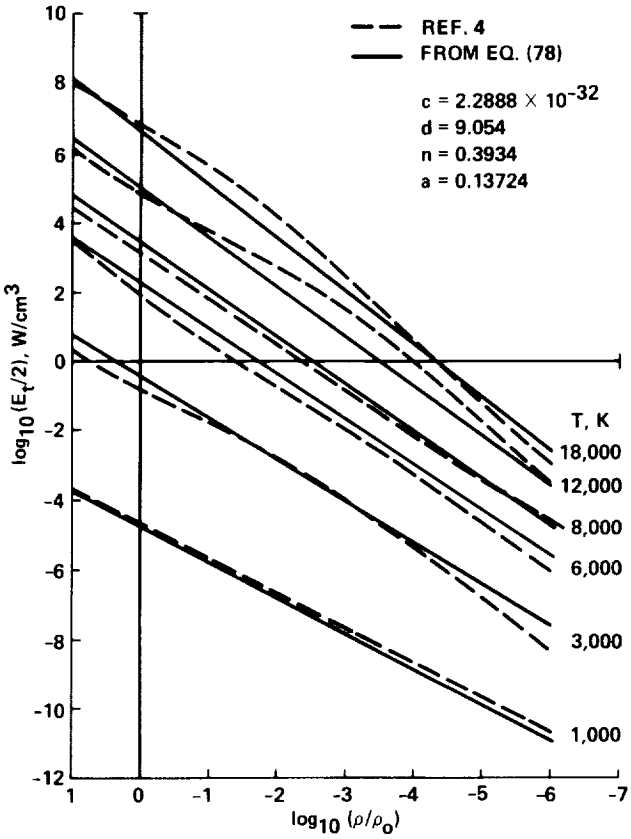

Figure 6-6.– Correlation of radiative emission rate for equilibrium air.

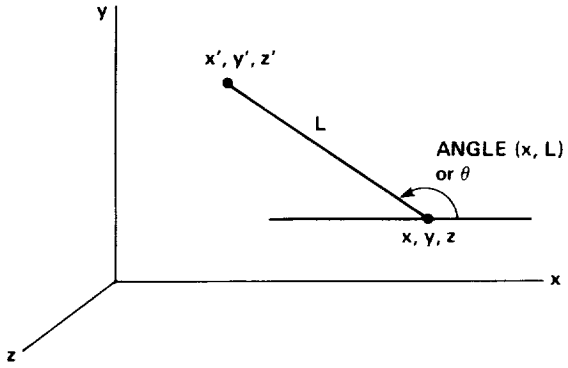

Figure 6-7.– Three-dimensional orthogonal coordinates.

For any point in the gas that does not "see" the wall, the first two terms of equation (54) can be omitted. For present purposes, consider the gas in a three-dimensional, orthogonal coordinate system shown in figure 6-7. Any point x,y,z, receives a portion of the radiation emitted from other locations x',y',z' a distance L away. We have defined $\mu_\nu = \rho K_\nu$ (eq. (5)), and J_ν (eq. 7), the mass spectral emission coefficient, or its equivalent $K_\nu B_\nu(T)$ (eq. (8)). It is now convenient to define

$$\bar{B}_\nu = 4\pi\mu_\nu B_\nu \tag{79}$$

which is the spectral energy emission rate per unit volume. Thus in the absence of radiative scattering, the x component of the spectral flux at x,y,z which originated at x',y',z' is

$$F_{x_\nu}(x,y,z) = -\int\int\int_{-\infty}^{\infty}\left[\frac{\bar{B}_\nu(x',y',z')}{4\pi L^2}\right]\cos(x,L)\exp\left(-\int_0^L \mu_\nu\, dL'\right)dx'\,dy'\,dz' \tag{80}$$

where the brackets are the intensity at radius L without absorption, the cosine term gives the x component, and the exponential factor accounts for absorption. Also

$$\cos(x,L) = \frac{(x'-x)}{L} \tag{81}$$

and as mentioned above

$$\exp\left(-\int_0^L \mu_\nu\, dL\right) \tag{82}$$

is the absorption along the path L. For this special case of strong absorption, we assume that the temperature varies slowly spacewise, and that radiative equilibrium exists locally. The local energy density of radiation at the frequency ν is characterized by a black body at the temperature T and is (see ref. 2, eq. (2.8))

$$u_\nu = \frac{8\pi h\nu^3}{\left\{c^3\left[\exp(h\nu/kT)-1\right]\right\}} \tag{83}$$

The energy absorbed at that frequency per unit volume per unit time is

$$cu_\nu\mu_\nu \tag{84}$$

which is equal to the rate of energy emission locally. Thus

$$\bar{B}_\nu = cu_\nu\mu_\nu \tag{85}$$

Assume that along a path length $1/\mu_\nu$, $u_\nu\mu_\nu$ changes little for all frequencies, so that equation (85) characterizes T(x',y',z') locally. The variation of μ_ν is small with distance, and μ_ν is kept constant in the integrals of equations (80) and (82). Substitute equations (85) and (81) into equation (80) to obtain

$$F_{x_\nu}(x,y,z) = -c\mu_\nu \iiint_{-\infty}^{\infty} \frac{u_\nu(x',y',z')}{4\pi L^2} \frac{(x'-x)}{L} e^{-\mu_\nu L}\, dx'\, dy'\, dz' \tag{86}$$

Expand u_ν in a taylor series

$$u_\nu(x',y',z') = u_\nu(x,y,z) + \left(\frac{\partial u_\nu}{\partial x}\right)_{x,y,z}(x'-x) + \left(\frac{\partial u_\nu}{\partial y}\right)_{x,y,z}(y'-y) + \left(\frac{\partial u_\nu}{\partial z}\right)_{x,y,z}(z'-z) \tag{87}$$

Substitute equation (87) into equation (86) to obtain

$$F_{x_\nu}(x,y,z) = -c\mu_\nu \iiint_{-\infty}^{\infty} \Bigg[\underline{u_\nu(x,y,z)} + \left(\frac{\partial u_\nu}{\partial x}\right)_{x,y,z}(x'-x) + \underline{\left(\frac{\partial u_\nu}{\partial y}\right)_{x,y,z}}(y'-y)$$

$$+ \underline{\left(\frac{\partial u_\nu}{\partial z}\right)_{x,y,z}}(z'-z) \Bigg] \frac{(x'-x)}{L} \exp(-\mu_\nu L) \left(\frac{dx'\, dy'\, dz'}{4\pi L^2}\right) \tag{88}$$

The terms that are underscored integrate to zero because they are antisymmetric with respect to $(x'-x)$, etc. Thus

$$F_{x_\nu}(x,y,z) = -c\,\mu_\nu \left(\frac{\partial u_n}{\partial x}\right)_{x,y,z} \iiint_{-\infty}^{\infty} \frac{(x'-x)^2 \exp(-\mu_\nu L)}{4\pi L^3}\, dx'\, dy'\, dz' \tag{89}$$

Since

$$\cos(x,L) \equiv \cos\theta = \frac{(x'-x)}{L} \tag{90}$$

this becomes

$$F_{x_\nu} = -c\mu_\nu \left(\frac{\partial u_\nu}{\partial x}\right)_{x,y,z} \iiint_{-\infty}^{\infty} \frac{\cos^2\theta}{4\pi L} e^{-\mu_\nu L}\, dx'\, dy'\, dz' \tag{91}$$

Now replace the volume element $dx'\, dy'\, dz'$ by an element in spherical coordinates centered at x,y,z as shown in figure 6-8. Thus the volume element is

$$(L\sin\theta\, d\phi)(L\, d\theta)dL = L^2 \sin\theta\, d\theta\, d\phi\, dL \tag{92}$$

and

$$F_{x_\nu}(x,y,z) = -c\,\mu_\nu \left(\frac{\partial u_\nu}{\partial x}\right)_{x,y,z} \int_{L=0}^{\infty} \int_{\theta=0}^{\pi} \int_{\phi=0}^{2\pi} \frac{\cos^2\theta\, e^{-\mu_\nu L}}{4\pi L} L^2 \sin\theta\, d\theta\, d\phi\, dL \tag{93}$$

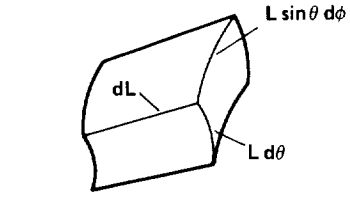

VOLUME: $(L \sin\theta\, d\phi)(L\, d\theta)\, dL$
OR $L^2 \sin\theta\, d\theta\, d\phi\, dL$

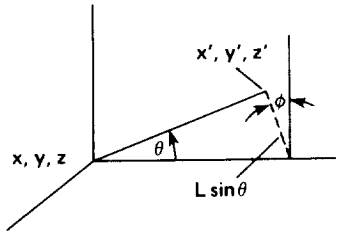

Figure 6-8.– Spherical coordinates and volume element.

We integrate with respect to θ first, and then with respect to ϕ.

$$F_{x_\nu}(x,y,z) = -c\mu_\nu \left(\frac{\partial u_\nu}{\partial x}\right)_{x,y,z} \int_{L=0}^{\infty} \int_{\phi=0}^{2\pi} \left(-\frac{\cos^3\theta}{3}\right)_0^{\pi} \frac{e^{-\mu_\nu L}}{4\pi} L\, d\phi\, dL$$

$$= \frac{-c\mu_\nu}{3} \left(\frac{\partial u_\nu}{\partial x}\right)_{x,y,z} \int_{L=0}^{\infty} e^{-\mu_\nu L} L\, dL \tag{94}$$

and finally

$$F_{x_\nu}(x,y,z) = \frac{-c\mu_\nu}{3} \left(\frac{\partial u_\nu}{\partial x}\right)_{x,y,z} \left(\frac{1}{\mu_\nu^2}\right) = -\frac{c}{3\mu_\nu} \left(\frac{\partial u_\nu}{\partial x}\right)_{x,y,z} \tag{95}$$

Since u_ν is a function of T alone

$$F_{x_\nu}(x,y,z) = -\frac{c}{3\mu_\nu}\frac{du_\nu}{dT}\frac{\partial T}{\partial x} \tag{96}$$

Thus the total flux component in the x direction is

$$F_x = \int_0^\infty F_{x_\nu}\, d\nu = -\frac{c}{3}\int_0^\infty \left(\frac{1}{\mu_\nu}\frac{du_\nu}{dT}\right) d\nu \frac{\partial T}{\partial x} \tag{97}$$

Rosseland defined the "mean free path," λ_R, such that

$$F_x = -\frac{c}{3}\lambda_R \frac{\partial E_{rad}}{\partial x} \tag{98}$$

or since

$$E_{rad} \equiv \frac{4\sigma}{c}T^4 = \int_0^\infty u_\nu\, d\nu \tag{99}$$

where σ is the Stefan-Boltzmann constant. Then

$$F_x = -\frac{16\,\sigma}{3}\lambda_R T^3 \frac{\partial T}{\partial x} \tag{100}$$

The y component is obtained by replacing x by y, and the divergence of F_y or q_{r_y} is simply $(\partial/\partial y)(q_{r_y})$. Of course, λ_R can be derived from standard tables of data by the expression obtained by combining equations (97), (99), and (100)

$$\lambda_R = \frac{\displaystyle\int_0^\infty \frac{1}{\mu_\nu}\frac{du_\nu}{dT}\, d\nu}{\displaystyle\int_0^\infty \frac{du_\nu}{dT}\, d\nu} \tag{101}$$

and has the units of length. The approximation is somewhat limited in flow-field computations because it tends to break down near the surface of the vehicle where temperature is diminished to the extent that λ_R becomes large; that is, the gas becomes less opaque. It could be terminated arbitrarily at a distance from the surface that is some factor of λ_R.

Before proceeding to use radiative-transfer expressions in the flow-field differential equations, it should be noted that in the treatment which follows, the gas will be assumed to be grey. That is, the dependence on wavelength will not be included. That is for convenience and not because of necessity.

As a practical matter, a single integral over physical space rather than a double integral which includes wavelength appears in the integro-differential equation for energy. The latter integral could be included with a modest increase in complexity. Our treatment uses the Planck mean mass absorption coefficient, equation (73), where K_ν weighted by B_ν was integrated over the entire spectrum, which smoothes out any strong or weak absorption effects. It is simply denoted by $\dot{K}$ in the next chapter. Another approximation which considers portions of the spectrum to be transparent, and other parts to be strongly absorbed (ref. 8, for example) is sometimes called the "picket fence" approximation. It is a simple spectral form and is easy to use; it may be particularly useful for ablation products which, although cold, absorb strongly in some portion of the spectrum.

Having mentioned spectral features, it is useful to mention some terms that have been used in this chapter; that is, a single photon of radiation at a particular frequency or wavelength

$$\Delta E = h\nu = \frac{hc}{\lambda} \tag{102}$$

here Planck's constant is

$$h = 6.6252\times10^{-27} \text{ erg sec} \tag{103}$$

The speed of light is c, and $hc = 1.9862\times10^{-12}$ erg μ. An angstrom is 10^{-8} cm or 10^{-4} μ. Thus the units of a photon can be shown to be ergs, or can be expressed in terms of electron volts, a unit of energy corresponding to a particular wavelength. We should also mention the particular wavelength corresponding to the peak in the black-body function B_ν. The peak is a function of temperature and the expression is called Wein's Law

$$\lambda_m = 2890/T \quad \text{(micrometers)} \tag{104}$$

Thus for a temperature of 14000 K,

$$\lambda_m = 2890/1.4\times10^4 = 0.206\,\mu\text{m} \tag{105}$$

and the photon energy can be calculated to be 6 EV at that wavelength by use of equation (102).

REFERENCES

1. Lighthill, M. J.: Dynamics of a Dissociating Gas, Part 2. J. Fluid Mech., vol. 8, pt. 2, June 1960.

2. Kourganoff, V.: Basic Methods in Transfer Problems. Clarendon Press, 1952.

3. Chandrasekhar, S.: Radiative Transfer. Clarendon Press, 1950.

4. Kivel, B.; and Bailey, K.: Tables of Radiation from High Temperature Air. AVCO-Everett Res. Lab. Res. Rep. 21, Dec. 1957.

5. Howe, J. T.: Radiation Emission Effects of the Equilibrium Boundary Layer in the Stagnation Region. NASA TN D-1031, 1961.

6. Penner, S. S.; and Olfe, D. B.: Radiation and Reentry. Academic Press, 1968, pp. 398.

7. Bethe, H. A.; Fuchs, K.; Hirschfelder, J. O.; Magee, J. L.; Peierls, E.; and von Neumann, J.: Blast Wave. Report L.A. 2,000, Los Alamos Scientific Laboratories, 1947.

8. Howe, J. T.; and Sheaffer, Y. S.: Spectral Radiative Transfer Approximations for Multicomponent Gas Mixtures. J. Quant. Spectrosc. Radiat. Trans., vol. 7, Pergamon Press, 1967, pp. 695-701.

CHAPTER 7

SOLUTIONS OF THE RADIATING SHOCK LAYER

The differential equations listed in Chapter 4 can now be solved. Air in the hot flow field is assumed to be in chemical equilibrium. The structure of the flow field will be shown, and quantities derived from the solutions will show radiative and convective heating as well as the effects of transpiration or mass addition. What follows is largely drawn from Howe and Viegas (ref. 1). Thus the equations for the nonadiabatic shock layer in the stagnation region of bluff bodies are solved for flight speeds up to 50,000 ft/sec in air. The effects of energy transport by conduction, diffusion of dissociated and ionized species, and gaseous radiation (with reabsorption) are included in the analysis. The effects of a foreign species on the radiant energy transfer in the shock layer are also investigated. Convective and radiative heat-transfer rates in the stagnation region of the body are obtained from the solutions and are compared with the results of others. Coupling between the two modes of heat transfer is examined. A simplified method for predicting the effect of radiative transport on convective heat transfer is discussed. Shock standoff distance determined from the solutions is presented and compared with the results of other investigations. Results indicate that coupling among the energy-transfer processes may reduce the heat transfer by as much as 50%.

At flight velocities above about 30,000 ft/sec, two phenomena may importantly affect the aerodynamic heating rate in the stagnation region of bluff bodies. The first of these is the ionization of the dissociated air, which may affect heat transfer because it increases the total thermal conductivity of the air. The second phenomenon is the emission and absorption of radiant energy by the air in the gas cap, which for large blunt bodies may impose a much larger heating load than convective processes do.

Each phenomenon has been treated separately by others. The effects of ionization on convective heat transfer have been examined in boundary-layer analyses by Hoshizaki (ref. 2), Cohen (ref. 3), and Pallone and Van Tassel (ref. 4) for equilibrium air; Adams (ref. 5) for frozen flow; and Scala (ref. 6) for equilibrium nitrogen. All of these investigations except reference 6 predict that ionization will have a modest influence on convective heat transfer. Stagnation-region heating caused by radiative emission from the isoenergetic equilibrium shock layer has been studied by Kivel (ref. 7).

At higher flight speeds, it can be expected that a coupling exists between convective and radiative heat transfer, and that the coupling is more pronounced for larger bodies. For example, the convective heat transfer to the stagnation surface can be expected to be diminished if the shock-layer enthalpy is diminished by radiant emission. Also, if radiation produces enthalpy gradients in the shock layer, thermal conduction and diffusion of species may become important in that region.

As noted previously, for purposes of analysis it has been customary to separate the flow field in the stagnation region of blunt bodies into a viscous nonadiabatic boundary layer and an inviscid isoenergetic shock layer. The present analysis, however, treats the entire shock layer and includes all three energy-transport processes (radiation, conduction, and diffusion), as well as momentum transport by viscosity, and the solutions extend from the vehicle surface to the bow shock wave. The analysis is formulated in this way in order to study the coupling between the radiation and the convection.

The effects of mass transfer from the body surface to the flow field are also considered insofar as they affect energy transport by radiation. In this regard, some of the simplifying assumptions of a previous study (ref. 8) are relaxed. In that analysis, the hot air in the shock layer was permitted only to emit

radiation, while the cold foreign species near the body was permitted only to absorb radiation. Another specialization of that analysis was that both the shock layer and the foreign species in the boundary layer were required to be at almost a black condition insofar as radiation phenomena were concerned. That situation may never be realized for flight in the Earth's atmosphere, and the results may be quite different if it is not. In the present analysis, all of these restrictions are lifted. The air and the foreign species are each permitted to both emit and absorb radiation and neither is required to be black.

ANALYSIS

Regime of Analysis

The flight regime in which the analysis is valid is presented in order to support some of the assumptions which will follow, and to relate the analysis to specific space missions. The regime is shown as the shaded area in figure 7-1. The upper boundary of the regime is that of equilibrium flow and appears as the heavy curve, taken from reference 7, and its extension to higher velocity. The boundary shown is for a 5-ft nose radius; for a 1-ft nose radius it would move down roughly 40,000 ft in altitude. The boundary on the lower right of the figure corresponds to a temperature of 15,000 K behind a normal shock. It is only a limit in that transport properties are presently not correlated at higher temperatures. Representative entry trajectories from references 7 and 9 (where results of ref. 10 are used in conjunction with ref. 9) enter the figure from the top. The ballistic coefficient is (m/C_DA) and the lift/drag ratio is L/D. Curves for several estimated (ref. 11) values of the ratio of radiative to convective heat transfer for a 5-ft nose radius are shown to indicate the relative importance of each. Estimated values of the same ratio for a 1-ft nose radius would be about 10% of those shown. The heavy vertical curve is the approximate ionization boundary. Results will be presented from just to the left of the vertical ionization curve to about 50,000 ft/sec flight speed at shock-layer pressure levels of 0.1 to 10 atm.

Differential Equations

The flow model for the analysis is as before (fig. 7-2). It is also patterned after that shown in reference 12. The velocity components u,v at the point x,y are parallel and normal to the body surface, respectively. The coordinate x is a measure of distance along the body surface only, the distance of the point x,y from the surface is y, and from the body axis (for $x/R \ll 1$)

$$r(x,y) = \mathcal{H}x \tag{1}$$

where

$$\mathcal{H} = 1 + (y/R) \tag{2}$$

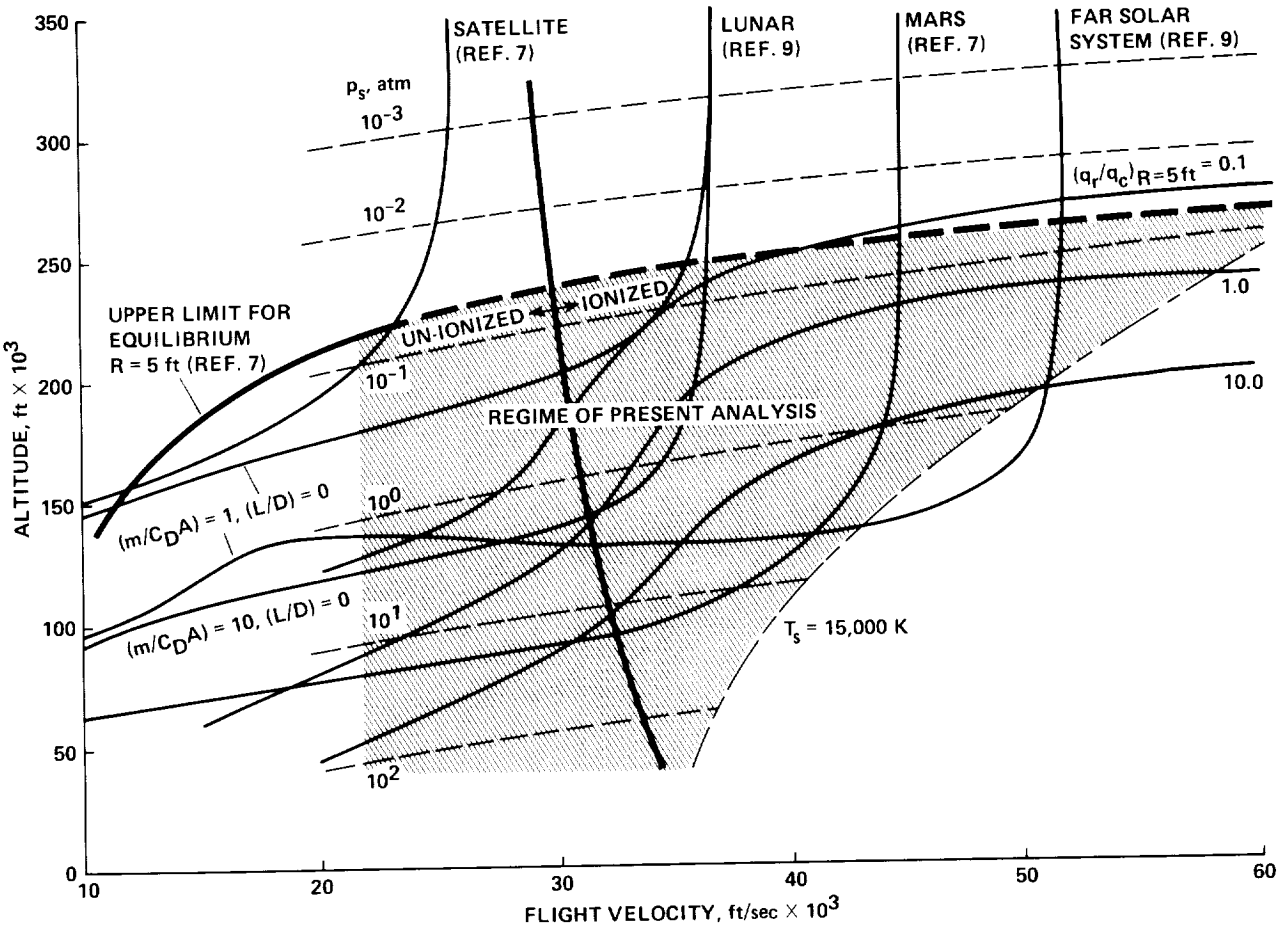

Figure 7-1.– Flight regime.

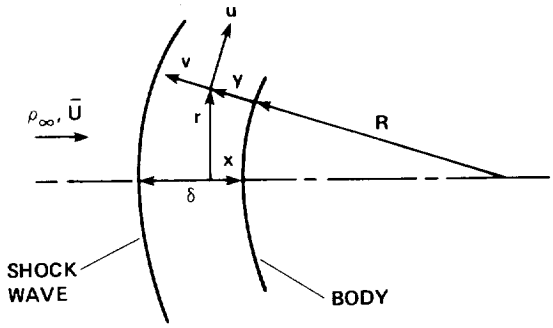

Figure 7-2.– Flow model.

The Navier-Stokes equations for a thin shock layer ($\delta/R \ll 1$) for $x \sim R$ were reduced by an order of magnitude analysis in reference 13 (which was completely reformulated as described in Chapter 6 to assess specific limitations and effects). In the present analysis, these equations are reduced still further by an order of magnitude analysis where it is assumed that $x \sim \delta$, restricting the results to the stagnation region. In addition to the transport of energy by ordinary conduction, considered in reference 13, transport by diffusion of reacting species and by gaseous radiation is included. For the radiative

transfer the assumptions of a grey gas, black surface, and plane-parallel shock layer are made. Detailed discussion of these assumptions is given in Chapter 6 and in references 14-16. The resulting set of equations for conservation of mass, x and y momentum expressions, and conservation of energy are, respectively,

$$\frac{\partial}{\partial x}(\rho u r^j) + \frac{\partial}{\partial y}(\mathcal{H}\rho v r^j) = 0 \tag{3}$$

$$\rho u \frac{\partial u}{\partial x} + \mathcal{H}\rho v \frac{\partial u}{\partial y} = -\frac{\partial p}{\partial x} + \mathcal{H}\frac{\partial}{\partial y}\left(\mu \frac{\partial u}{\partial y}\right) \tag{4}$$

$$\frac{\partial p}{\partial y} = \frac{\rho u^2}{R} + \sum_{i=1}^{\nu} n_i Y_i \tag{5}$$

$$\rho u \frac{\partial H}{\partial x} + \mathcal{H}\rho v \frac{\partial H}{\partial y} = \mathcal{H}\frac{\partial}{\partial y}\left(k \frac{\partial T}{\partial y} + \rho \sum_{i,j} D_{ij} h_i \frac{\partial c_i}{\partial y}\right)$$

$$+ \mathcal{H}\rho K\left[\int_0^{t_s} 2\sigma T^4(t)\, E_1(|t - \tau|)dt - 4\sigma T^4 + 2\sigma T_w^4 E_2(\tau)\right] \tag{6}$$

where

$$H = h + \frac{u^2 + v^2}{2} \tag{7}$$

$$h = \sum_{i=1}^{\nu} c_i h_i \tag{8}$$

$$h_i(T) = \int_0^T c_{p_i}\, dT + h_i^o \tag{9}$$

$$\tau = \int_0^y \rho K\, dy \tag{10}$$

and

$$E_n(\zeta) = \int_1^\infty \frac{e^{-\zeta\omega}}{\omega^n} d\omega \tag{11}$$

The boundary conditions for equations (3)-(6) are at $y = 0$:

$$u = 0\,, \quad v = v_w\,, \quad H = H_w = h_w \tag{12}$$

at $y = \delta$:

$$\left.\begin{aligned} u &= u_s = \frac{\overline{U}x}{R} \\ v &= v_s = -\varepsilon\overline{U} \\ p &= p_s = \rho_\infty \overline{U^2}(1-\varepsilon) \\ H &= H_s = \frac{\overline{U^2}}{2} \end{aligned}\right\} \tag{13}$$

where

$$\varepsilon = \frac{\rho_\infty}{\rho_s} \tag{14}$$

For flow near a blunt stagnation region in the absence of electric fields, it is convenient (although not imperative) to eliminate equation (5) entirely and replace it with

$$\frac{\partial p}{\partial y} = 0 \tag{15}$$

The advantages of using equation (15) are not only that it results in a saving of computation time but, primarily, it permits a simplification in the energy equation (6). That is, conduction and diffusion processes in the multicomponent mixture of reacting species (including effects of ionizing reactions) can be combined in the manner described by reference 17. Thus the transport of energy by diffusion of reacting species can be represented by a "reaction conductivity," as formulated by reference 18, which summed with the translational thermal conductivity yields a total effective thermal conductivity. As a result, the energy equation (6) becomes[1]

[1]It is noted that for a binary mixture of atoms and molecules, in which diffusion and conduction effects are accounted for separately, the same equation (16) would result if the Lewis number were assumed to be unity (not assumed here) and the equivalent Prandtl number were replaced by the frozen Prandtl number.

$$\rho u \frac{\partial H}{\partial x} + \mathcal{H} \rho v \frac{\partial H}{\partial y} = \mathcal{H} \frac{\partial}{\partial y}\left(\frac{\mu}{Pr} \frac{\partial h}{\partial y}\right)$$

$$+ \mathcal{H} \rho K \left[\int_0^{t_s} 2\sigma T^4(t)\, E_1(|t - \tau|)dt - 4\sigma T^4 + 2\sigma T_w^4 E_2(\tau) \right] \tag{16}$$

where Pr contains the effective thermal conductivity as presented in reference 19 and Chapter 5.

The integro-differential equations to be solved are now equations (3), (4), (15), and (16) subject to boundary conditions (12) and (13). Before proceeding with the transformation and solution to these equations, it is pertinent to mention the additional equations and assumptions required for studying effects of foreign species on radiative transport.

Foreign species effects.– Ideally, it is desirable to study the effects of a foreign species on both thermodynamic and transport properties in order to obtain the effect on heat transfer. However, there are two major difficulties associated with such a study. These are, first, that the chemical behavior of the mixture of air and ablated gas is usually not known and, second, that the radiative emission properties of the reacting foreign species and its products are not known. For these reasons, some simplifications are introduced that are applicable to this portion of the analysis only. In particular, attention will be focused on the gross effects of the foreign species on radiative properties alone to the exclusion of its effects on other transport properties; that is, transport properties of the foreign gas are taken to be identical to those of air, except for the radiation absorption coefficient. In spite of this, a considerable amount of generality is retained as being intrinsic in the formulation of the problem.[2] The diffusion equation applicable to the foreign species is

$$\rho u \frac{\partial c_f}{\partial x} + \mathcal{H} \rho v \frac{\partial c_f}{\partial y} = \mathcal{H} \frac{\partial}{\partial y}\left(\rho D_f \frac{\partial c_f}{\partial y}\right) \tag{17}$$

where c_f is either the local mass fraction of an inert foreign species or is the pseudo mass fraction (refs. 20 and 21) of a reacting foreign species (which accounts for both the pure form and its local combination in reaction products). The symbol D_f represents the "diffusion coefficient" of the "foreign" species relative to air.

The boundary condition at the surface is obtained from a mass balance, making the assumption that the air does not diffuse into the surface, and is at $y = 0$

$$\left(\frac{\partial c_f}{\partial y}\right)_w = -\frac{v_w}{D_{f_w}}(1 - c_{f_w}) \tag{18}$$

and at the shock, the boundary condition is at $y = \delta$

[2]For gas mixtures without ionization or light-gas elements, Lees (ref. 20) shows that it is often possible to lump all chemical species, including foreign reacting species, into two components insofar as diffusion transport is concerned. He shows that as long as the resulting Lewis number is approximately unity, heat-transfer conclusions are independent of the reaction flow model employed, of magnitude of reaction rates, and of any restrictions on the momentum equation. In the present work, the bulk of the foreign gas will be near the relatively cold wall where at least the air is not ionized and we can appropriate the generality of the Lees result for this portion of the analysis.

$$c_f = 0 \tag{19}$$

The influence of the foreign gas on radiative transfer is obtained by its influence on the Planck mean mass absorption coefficient K (which will be defined subsequently), which can be expressed for the mixture of gases as

$$K = (1 - c_f)K_{air} + c_f K_f \tag{20}$$

This is a good representation if the foreign species retains its identity (is inert) and its spectral characteristics are similar to those of air. It is noted that both K_{air} and K_f are functions of temperature and their partial pressures so that equation (20) can be written

$$K = K_{air}(p_{air}, T)\left\{1 + c_f\left[\frac{K_f(p_f, T)}{K_{air}(p_{air}, T)} - 1\right]\right\} \tag{21}$$

Equation (21) indicates the need for either knowing or specifying considerable detail about the radiant properties of the foreign species as well as those of air. Although the latter is known, the former is not, so we adopt a simpler approach. We simply inquire as to the overall effect of a foreign gas that is more absorbing or less absorbing than air and say

$$K = K_{air}(p_s, T)[1 + c_f(\alpha - 1)] \tag{22}$$

Expressing K in this way takes advantage of the fact that $K_{air}(p_s, T)$ has been correlated at several pressure levels in reference 22, by use of experimental data obtained by reference 23. The significance of α is obtained by a combination of equations (21) and (22)

$$\alpha = 1 + \frac{1}{c_f}\left[\frac{K_{air}(p_{air}, T)}{K_{air}(p_s, T)}(1 - c_f) + c_f\frac{K_f(p_f, T)}{K_{air}(p_s, T)} - 1\right]$$

For strong injection of foreign gas,

$$c_{f_w} \to 1\,, \quad p_{f_w} \to p_s$$

and at the wall

$$\alpha = \left[\frac{K_f(p_s, T)}{K_{air}(p_s, T)}\right]_w \tag{23}$$

Thus we consider α to represent in an approximate way the ratio of the absorption coefficient of the foreign gas to that of air at the shock-layer pressure and wall temperature. Expressing K in the approximate form of equation (22) retains all significant absorption phenomena; that is, when $\alpha = 1$, $K = K_{air}(p_s, T)$. When c_f is 1, $K = \alpha K_{air}(p_s, T)$. When c_f is zero, $K = K_{air}(p_s, T)$. Finally, when $\alpha = 0$ (injection of a nonradiating gas), K is given by the approximation $K = (1 - c_f)K_{air}(p_s, T)$.

Having coupled the energy equation (16) to the foreign gas diffusion equation (17) by use of equation (22) to obtain the influence of a foreign species on radiative transport in the gas, we proceed to transform all of the differential equations and their boundary conditions.

Transformations

Examination of equations (3), (4), (15), and (16) shows that except for the factor $\mathcal{H}$ appearing in all the equations, and the radiation term in equation (16), the equations are like the usual ones for a compressible laminar boundary layer. Correspondingly, we modify the usual boundary-layer transformations to include the effect of $\mathcal{H}$[3] The transforms used to change x and y to ξ and η as independent variables are

$$\xi(x) = \int_0^x \rho_s \mu_s \left(\frac{r}{\mathcal{H}}\right)^{2j} u_s \, dx \tag{24}$$

and

$$\eta(x,y) = \frac{u_s}{\sqrt{2\xi}} \left(\frac{r}{\mathcal{H}}\right)^{j} \int_0^y \mathcal{H}^j \rho \, dy \tag{25}$$

A stream function is defined such that

$$\frac{\partial \psi}{\partial y} = \rho u r^j , \quad \frac{\partial \psi}{\partial x} = -\mathcal{H} \rho v r^j \tag{26}$$

which satisfies the continuity equation (3). Other definitions are

$$f(\xi,\eta) = \frac{\psi}{\sqrt{2\xi}} \tag{27}$$

$$g(\xi,\eta) = \frac{H}{H_s} \tag{28}$$

$$\overline{T} = \frac{T}{T_s} \tag{29}$$

$$\overline{K} = \frac{K}{K_s} \tag{30}$$

[3]An alternate approach in which the continuity equation is reduced further is presented in reference 12, pp. 390-393.

$$\varphi = \frac{\rho\mu\mathcal{H}^j}{\rho_s\mu_s\mathcal{H}_s^j} \tag{31}$$

Then, from equations (25)-(27),

$$\frac{u}{u_s} = \frac{\partial f}{\partial \eta} \tag{32}$$

Applying the transforms and definitions to equations (4) and (16), noting that $(u^2 + v^2)/2 \ll H$ in the stagnation region, yields

$$\frac{\partial}{\partial\eta}\left(\varphi\frac{\partial^2 f}{\partial\eta^2}\right) + f\frac{\partial^2 f}{\partial\eta^2} = 2\xi\left\{\frac{1}{u_s}\frac{\partial u_s}{\partial\xi}\left[\left(\frac{\partial f}{\partial\eta}\right)^2 - 2\frac{\rho_\infty}{\rho}(1-\varepsilon)\right] + \frac{\partial f}{\partial\eta}\frac{\partial^2 f}{\partial\eta\partial\xi} - \frac{\partial^2 f}{\partial\eta^2}\frac{\partial f}{\partial\xi}\right\} \tag{33}$$

and

$$\frac{\partial}{\partial\eta}\left(\frac{\varphi}{Pr}\frac{\partial g}{\partial\eta}\right) + f\frac{\partial g}{\partial\eta} = -\left[\frac{4R\sigma T_s^4 K_s}{(j+1)\bar{U}^3}\right]\bar{K}\left[\int_0^{t_s}\bar{T}^4(t)\,E_1(|t-\tau|)dt - 2\bar{T}^4 + \bar{T}_w^4 E_2(\tau)\right]$$
$$-2\xi\left(\frac{\partial f}{\partial\xi}\frac{\partial g}{\partial\eta} - \frac{\partial f}{\partial\eta}\frac{\partial g}{\partial\xi}\right) \tag{34}$$

Finally, in order to reduce these equations further, it is assumed that

$$\rho_s\mu_s = \text{constant} \tag{35}$$

and that similarity exists; that is, all dependent variables are functions of η alone. Equations (33) and (34) become

$$(\varphi f'')' + ff'' = \frac{1}{(j+1)}\left[(f')^2 - 2\frac{\rho_\infty}{\rho}(1-\varepsilon)\right] \tag{36}$$

and

$$\left(\frac{\varphi}{Pr}g'\right)' + fg' = -\left[\frac{4R\sigma T_s^4 K_s}{(j+1)\bar{U}^3}\right]\bar{K}\left[\int_0^{\tau_s}\bar{T}^4(t)\,E_1(|t-\tau|)dt - 2\bar{T}^4 + \bar{T}_w^4 E_2(\tau)\right]$$
$$= Q \tag{37}$$[4]

In order to relate τ to η conveniently, it is assumed that $\rho = \rho(y)$ and thus from equations (10) and (25)

[4]For the case in which the flow field is emitting radiation, but is transparent to radiation, the right side of equation (37) is expressed differently. That case is treated briefly subsequently. Except where stated to the contrary, the integral expression for radiative transport as shown in equation (37) was used throughout the analysis.

$$\tau = \beta \int_0^{\eta} \bar{K}\, d\eta \tag{38}$$

where

$$\beta = K_s \sqrt{\frac{\rho_s \mu_s R}{\bar{U}(j+1)}} \tag{39}$$

The boundary conditions, equations (12) and (13), become at $\eta = 0$

$$\left.\begin{aligned} f = f_w &= -\rho_w v_w \sqrt{\frac{R}{\rho_s \mu_s \bar{U}(j+1)}} \\ f' &= 0 \\ g = g_w &= \frac{2h_w}{\bar{U}^2} \end{aligned}\right\} \tag{40}$$

at $\eta = \eta_s$,

$$\left.\begin{aligned} f = f_s &= \rho_\infty \sqrt{\frac{R\bar{U}}{\rho_s \mu_s (j+1)}} \\ f' = f_s &= 1 \\ g = g_s &= 1 \end{aligned}\right\} \tag{41}$$

It is noted that four boundary conditions involving f are employed on a third-order momentum equation, equation (36). The necessity for this is that the shock wave location, or η_s is actually determined where the above equations for f_s and f'_s are simultaneously satisfied. The diffusion equation (17) is transformed in like manner and becomes

$$\left(\frac{\varphi}{Sc} c'_f\right)' + f c'_f = 0 \tag{42}$$

Its boundary conditions are from equations (18) and (19) at $\eta = 0$

$$c'_f = c'_{f_w} = \left(\frac{Sc}{\varphi}\right)_w f_w (1 - c_{f_w}) \tag{43}$$

where Sc is the Schmidt number $\mu/\rho D_f$. At $\eta = \eta_s$

$$c_f = c_{f_s} = 0 \tag{44}$$

The equations to be solved are (36) and (37) (and (42) if foreign species effects are considered), subject to boundary conditions (40) and (41) (as well as (43) and (44)). Heat transfer to the surface and shock standoff distance are derived from the solutions of the equations. They are discussed in the next section.

Standoff Distance and Heat Transfer

The shock standoff distance, obtained from equations (25), (26), and (41), is simply

$$\delta = \sqrt{\frac{R\rho_s\mu_s}{\overline{U}(j+1)}} \int_0^{\eta_s} \frac{d\eta}{\rho} \tag{45}$$

Subsequently, it will be compared with the approximation given by Hayes (ref. 24) which is

$$\delta = \frac{R\varepsilon}{1 + \sqrt{2\varepsilon}} \tag{46}$$

The total heat-transfer rate at the stagnation surface is

$$q_T = q_c + q_r \tag{47}$$

where the convective heat-transfer rate is

$$q_c = -\left(\frac{\mu}{Pr}\frac{\partial h}{\partial y}\right)_w = \left(\frac{\varphi}{Pr}\right)_w \frac{\overline{U}^{5/2}}{2} \sqrt{\frac{\rho_s\mu_s(j+1)}{R}}\, g'_w \tag{48}$$

and the net radiative heat transfer at the surface is (for a black surface)

$$q_r = \sigma T_s^4 \left[\overline{T}_w^4 - 2\int_0^{t_s} \overline{T}^4(t)\, E_2(t)dt \right] \tag{49}$$

Equations (47)-(49) can be combined to yield the total heat-transfer expression

$$q_T = -\left(\frac{\varphi}{Pr}\right)_w \frac{U^{5/2}}{2} \sqrt{\frac{\rho_s\mu_s(j+1)}{R}}\, g'(0) + \sigma T_s^4 \left[\overline{T}_w^4 - 2\int_0^{t_s} \overline{T}^4(t)\, E_2(t)dt \right] \tag{50}$$

The radiation flux from the hot gas cap to the wall, q_g, is represented by the integral in equations (49) and (50). For the case of a transparent isothermal gas cap, this integral, with the aid of equation (10), and the fact that in this instance $E_2(t) \approx 1$ and $\bar{T} \approx 1$ becomes

$$q_g = -2\sigma T_s^4 \int_0^\delta \bar{T}^4 E_2(t)\, \rho_s K_s\, dy = -2\sigma T_s^4 \rho_s K_s \delta \tag{51}$$

The total energy emission rate per unit volume of gas is shown by reference 16 (p. 31) to be

$$E_t = 4\pi\rho \int_0^\infty B_\nu K_\nu\, d\nu \tag{52}$$[5]

The definition of the Planck mean mass absorption coefficient is

$$K \equiv \frac{4\pi \int_0^\infty B_\nu K_\nu\, d\nu}{4\pi \int_0^\infty B_\nu\, d\nu} = \frac{E_t}{4\sigma T^4 \rho} \tag{53}$$

From equations (51) and (52) the transparent isoenergetic gas-cap radiation is

$$q_g = -\frac{E_t \delta}{2} \tag{54}$$

This expression can be compared with that used in reference 11 for the plane-parallel isoenergetic transparent gas cap represented in figure 7-3. The elemental volume dV is emitting energy at the rate of E_t per unit volume. The rate at which energy is received by the wall area dA from the gas volume dV is

$$dq_g dA = -\left(\frac{E_t dV}{4\pi}\right)\left(\frac{dA \cos\theta}{l^2}\right)$$

where the first set of parentheses is the energy emission rate per unit solid angle from dV, and the second set is the solid angle subtended by the wall area dA. Expressing the volume element dV in

[5]It is useful to note that E_t for equilibrium air can be obtained from reference 23 by the relationship $E_t = 2\sigma T^4(\varepsilon/L)$, where ε/L (the emissivity per unit depth of gas) is the terminology of the reference and not of this chapter.

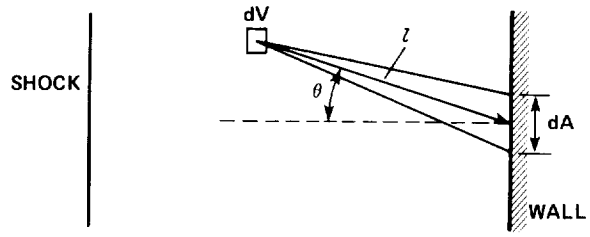

Figure 7-3.– Isoenergetic transparent gas cap.

spherical coordinates with the origin at dA, and integrating overall gas space yields the net radiant heating rate per unit wall area[6]

$$q_g = -\frac{E_t \delta}{2}$$

which is the same as equation (54).

Having formulated the problem and expressed quantities of interest to be derived from its solution, it is instructive to mention some features of the method of solution.

Solution of the Equations

In this section we will first discuss some of the information needed to initiate the solutions. Then the sequence of steps used in the numerical integration will be described in a general way. Additional information pertaining to the evaluation of the radiative flux term in the energy equation will be presented in an appendix.

The differential equations (36) and (37) subject to boundary conditions, equations (40) and (41), can be integrated if the transport properties φ, φ/Pr, and $\overline{K}$ and the thermodynamic properties ρ and T are known as functions of enthalpy at constant pressure. Except where noted, these are obtained from reference 22. In that reference, the transport and thermodynamic properties of Hansen (ref. 19) and Moeckel and Weston (ref. 25) for equilibrium air to 15,000 K were represented by correlation formulas.

---

[6]If, instead of the plane-parallel assumption, it is assumed that the body and shock are concentric hemispheres, equation (52) becomes

$$q_g = \frac{E_t \delta}{2}\left(\frac{\delta}{R}\right)^{-1}\gamma\left[\frac{1}{2} - \frac{\gamma^{1/2}}{3} + \frac{\gamma}{8} - \frac{\gamma^2}{48} + 0(\gamma^3)\right]$$

where $\gamma = [(\delta/R) + 2](\delta/R)$. For $\delta/R \ll 1$, the expression is

$$q_g \doteq \frac{E_t \delta}{2}\left[1 - \frac{2\sqrt{2}}{3}\left(\frac{\delta}{R}\right)^{1/2}\right]$$

which reduces to the plane-parallel case for $\delta/R \to 0$. Thus it can be seen that for the case of $\delta/R \approx 0.04$, equation (54) overestimates the radiant flux by approximately 15%. From this we see that the assumption of a plane-parallel gas cap is good for the transparent case, and is expected to be better yet for reabsorption.

The Planck mean mass absorption coefficient for equilibrium air obtained from reference 23 was also expressed by correlation formulas in reference 22. In passing, it is noted that since $\mathcal{H} \approx 1$ everywhere, $\varphi \approx \rho\mu/\rho_s\mu_s$. However, the derivative of φ is also used and must contain the derivative of $\mathcal{H}$; thus,

$$\varphi' \approx \left(\frac{\rho\mu}{\rho_s\mu_s}\right)' + \frac{j}{\rho}\sqrt{\frac{\rho\mu_s}{\overline{UR}(j+1)}}\left(\frac{\rho\mu}{\rho_s\mu_s}\right) \tag{55}$$

Obviously, the derivative of φ/Pr must also contain the derivative of $\mathcal{H}$.

The functions $E_1(\zeta)$ and $E_2(\zeta)$ are also needed in the solution of equation (37) and in the radiant heat-transfer equations (49) and (50). These can be obtained from the tables of reference 26 in fairly coarse intervals of ζ or (as in the present work) can be generated from the exponential integral tables of reference 27 in very fine intervals noting that

$$E_1(\zeta) = -E_i(-\zeta) \tag{56}$$

where the E_i designates the exponential integral and is not to be confused with $E_1 \ldots E_n$ defined by equation (11). The function $E_2(\zeta)$ and subsequently $E_3(\zeta)$ is generated from equation (56) by the recurrence formula for $n > 1$

$$E_n(\zeta) = \frac{1}{n-1}\left[e^{-\zeta} - \zeta E_{n-1}(\zeta)\right] \tag{57}$$

The procedure for solving the differential equations begins with the assumption of profiles of φ, φ/Pr, ρ^{-1}, and Q as functions of η, where Q is the entire right side of equation (37). Equation (36) is then integrated numerically using the Adams-Moulton predictor-corrector variable step integration scheme (ref. 28). The solution is obtained by iteration to find the value of $f''(0)$ that makes the resulting solution satisfy the first two boundary conditions (41). The solution of equation (36) is used to solve equation (37) directly without iteration by evaluating the integrated form of equation (37), which is obtained as follows. The energy equation (37) can be rewritten:

$$\left(\frac{\varphi}{Pr}\cdot g'\right)' + \left(\frac{\varphi}{Pr}\cdot g'\right) f\frac{Pr}{\varphi} = Q(\eta) \tag{58}$$

Let

$$\alpha = \frac{\varphi}{Pr}\cdot g' \tag{59}$$

Equation (58) becomes

$$\frac{d\alpha}{d\eta} + \alpha f\frac{Pr}{\varphi} - Q(\eta) = 0 \tag{60}$$

An integrating factor θ is defined by

$$\theta = e^{\int_0^{\eta} f(Pr/\varphi)ds}, \quad \theta' = e^{\int_0^{\eta} f(Pr/\varphi)ds} \cdot f\frac{Pr}{\varphi} = \theta \cdot \left(f\frac{Pr}{\varphi}\right) \tag{61}$$

Multiply equation (60) by θ,

$$\theta \cdot \frac{d\alpha}{d\eta} + \alpha f\frac{Pr}{\varphi} \cdot \theta - \theta \cdot Q(\eta) = 0 \tag{62}$$

Then

$$\frac{d\alpha\theta}{d\eta} = \theta \cdot Q(\eta) \tag{63}$$

and

$$\alpha\theta = \int \theta Q(\eta)d\eta + \text{const.} \tag{64}$$

$$\frac{Pr}{\varphi} \cdot g' \cdot e^{\int_0^{\eta} f(Pr/\varphi)ds} = \int_0^{\eta_s} Q(\eta)e^{\int_0^{s} f(Pr/\varphi)dw} \cdot ds + \text{const.} \tag{65}$$

At $\eta = 0$, $g' = g'_w$ yet unknown. Say

$$\text{const.} = \left(\frac{\varphi}{Pr}\right)_w \cdot g'_w \tag{66}$$

Substitute equation (66) into equation (65) to obtain

$$g'(\eta) = \frac{dg}{d\eta} = \frac{1}{\varphi/Pr \cdot e^{\int_0^{\eta} f(Pr/\varphi)\cdot ds}} \cdot \left[\left(\frac{\varphi}{Pr}\right)_w g'_w + \int_0^{\eta} Q(\eta)\, e^{\int_0^{s} f(Pr/\varphi)\cdot d\omega} \cdot ds\right] \tag{67}$$

We integrate again with, at $\eta = 0$, $g = g_w$:

$$g(\eta) = g_w + \left(\frac{\varphi}{Pr}\right)_w \cdot g'_w \cdot \int_0^{\eta} \frac{ds}{(\varphi/Pr) \cdot e^{\int_0^s f(\varphi/Pr)d\omega}}$$

$$+ \int_0^{\eta} \frac{1}{(\varphi/Pr) \cdot e^{\int_0^s f(Pr/\varphi)d\omega}} \left[\int_0^s Q(\eta) e^{\int_0^{\omega} f(Pr/\varphi)dz} \cdot d\omega \right] ds \qquad (68)$$

which is the solution of the transformed energy equation. To evaluate g'_w, let $\eta = \eta_s$ in equation (68) and use the boundary condition that $g(\eta_s) = 1$ and solve for g'_w, which is

$$g'_w = \frac{1}{(\varphi/Pr)_w \int_0^{\eta_s} \frac{d\eta}{(\varphi/Pr) e^{\int_0^{\eta} f(Pr/\varphi)ds}}}$$

$$\times \left\{ 1 - g_w - \int_0^{\eta_s} \frac{1}{(\varphi/Pr) e^{\int_0^{\eta} f(Pr/\varphi)ds}} \left[\int_0^{\eta} Q e^{\int_0^s f(Pr/\phi)d\omega} \right] d\eta \right\} \qquad (69)$$

If a foreign species is considered, equation (43) is used to integrate equation (42), with the result

$$c_f(\eta) = c_{f_w} + f_w(1 - c_{f_w}) \int_0^{\eta} \frac{Sc}{\varphi} e^{-\int_0^{\omega} (Sc/\varphi) f \, d\omega} \, ds \qquad (70)$$

which is evaluated as before without iteration so that c_{f_w} is selected to make $c_f(\eta_s)$ equal to zero in accord with equation (44), thus

$$c_{f_w} = \frac{1}{\left\{1 - 1/\left[f_w \int_0^{\eta_s} \frac{Sc}{\varphi} e^{-\int_0^{\omega} (Sc/\varphi) f \, ds} \, d\omega\right]\right\}} \tag{71}$$

The resulting profiles of $g(\eta)$, $g'(\eta)$, and $c_f(\eta)$ are used to calculate new profiles of φ, φ/Pr, ρ^{-1}, $\overline{T}$, and $\overline{K}$. The corresponding profiles of Q are calculated as described in the appendix. Using the new profiles, the next major iteration is begun by seeking a new solution of equation (36) and so on. The procedure is repeated until $f''(0)$ does not change from one major iteration to the next, at which point δ, q_r, and q_T are calculated from the solution of the differential equations using equations (45), (49), and (50). The method of evaluating equation (49) is presented in the appendix.

RESULTS OF THE ANALYSIS

The solutions of the integro-differential equations, including the resulting fluid flow and property profiles across the shock layer, are presented for a variety of flight conditions. Then heat-transfer results and shock standoff distance are shown and discussed. Finally, results with mass transfer are presented and their significance with regard to heat transfer is discussed.

Solutions

Nonionized regime– In presenting solutions of the differential equations, results for flight in the nonionized regime (but near the ionization boundary in fig. 7-1) are examined first in order to evaluate the present analysis in the light of known phenomena. It is pointed out that for the low-speed case presented (fig. 7-4 only) two specializations have been introduced in the differential equations. These are (1) the fluid in the gas cap emits, but is transparent to radiation, and (2) conduction and diffusion effectors are separated (and thus the frozen Prandtl number is assumed to be 0.72, and the Lewis number is unity in keeping with footnote 1). Both specializations are valid where they are used. The consequence of the first one is that the integral radiation term in the energy equation (37) is replaced by

$$Q = \left[\frac{2R}{(j+1)\overline{U}^3}\right]\frac{E_t}{\rho} \tag{72}$$

where $E_t(p,T)$ is obtained from reference 23.

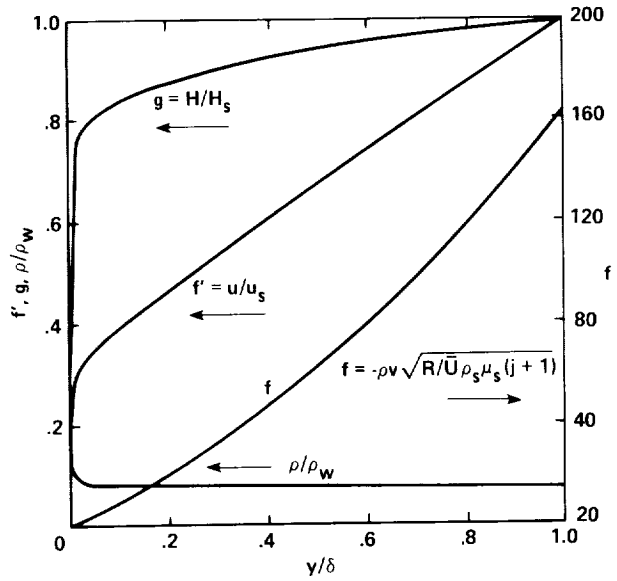

Figure 7-4.– Flow-field solutions for $\bar{U}$ = 32,000 ft/sec at 110,000 ft altitude; p_s = 10 atm, R = 5 ft.

A solution is shown in figure 7-4 for flight at 32,000 ft/sec at an altitude of 110,000 ft (p_s = 10 atm) for a body having a 5-ft nose radius. It was obtained by setting $\varphi = 1$ in the flow equations. When φ was allowed to vary in accord with the computation of $\rho\mu$ by the correlation formulas of reference 17 for dissociated nonionized air, the resulting profiles could hardly be distinguished from those shown for $\varphi = 1$. The standoff distance was the same in either case ($\delta/R = 0.0409$) and was about 3% below the value estimated by Hayes' method (ref. 24). Although the radiative heat transfer was unaffected by the assumption $\varphi = 1$, the convective heat transfer (which is presented subsequently) was approximately 15% lower for the $\varphi = 1$ case, an effect that has been observed and discussed in references 20 and 29, and was as expected.

The structure of the flow field indicated by the f and f' profiles is that of a momentum boundary layer with constant external vorticity. The thermal structure indicated by the g profile is somewhat like that of a thickened thermal boundary layer—much like that of reference 30.

The above comments apply generally to solutions obtained in the nonionized regime. At lower shock-layer pressure levels, the standoff distance was still closer to Hayes' estimate and the flow-field structure was even more like that of a boundary layer joined to an isoenergetic shock layer.

Thus, in every respect, the present results, for which the flow field is not separated into a boundary layer and inviscid flow field, agree with results obtained when the flow field was so divided. The use of equation (15) instead of equation (5) and, further, the agreement of the present results with those obtained previously justify the use of equation (15) instead of equation (5). We thus conclude that the y momentum equation (5) is not important in the stagnation region flow field for the high Reynolds number regime. Having established the validity of the present method, we now apply it at higher flight speeds. Henceforth we revert to our previous formulation and avoid "frozen" specific heat and Prandtl number, but use the effective thermal conductivity instead.

Ionized regime– In the ionized regime, results are presented with and without radiative transfer to show its effect on the solution. Properties, computed by the use of reference 22, include the effects of ionization.

Flow-field profiles corresponding to flight at 50,000 ft/sec at 190,000 ft altitude (p_s = 1 atm) for R = 1 ft without radiative transport effects are shown in figure 7-5. Here the boundary-layer structure is less distinct than was exhibited at lower flight speed. Far from the wall, however ($y/\delta > 0.3$), the flow field is isoenergetic and has almost constant vorticity, as indicated by the nearly constant slope of the u/u_s curve. The transport property parameter $(\varphi/Pr)/(\varphi/Pr)_w$ is shown in the figure. Using the criterion of reference 22, it is noted that the region between the body and the peak in this parameter (essentially 3% of the standoff distance) is essentially not ionized.

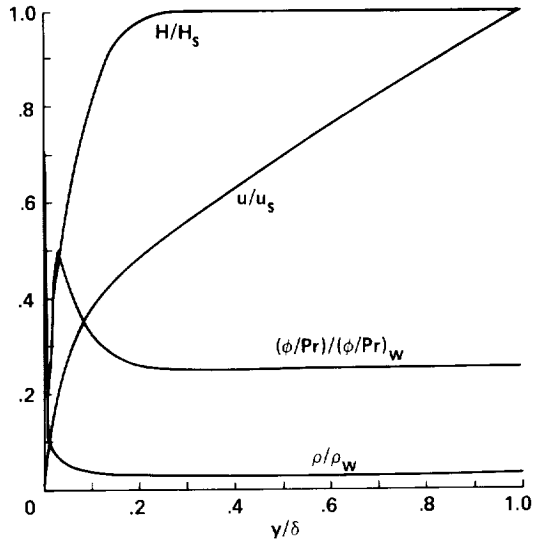

Figure 7-5.– Flow field with ionization but without radiation effects; $\overline{U}$ = 50,000 ft/sec at 190,000 ft altitude, R = 1 ft, p_s = 1 atm.

A solution at the same flight condition, but with radiative transport expressed by the integral form included in the energy equation (37), is shown in figure 7-6. The enthalpy level is substantially diminished from that of the previous figure because of the transport of energy by radiation. Here the thermal structure of the flow field is that of a very thick thermal boundary layer joined to a nonisoenergetic shock layer, and the question is raised as to the applicability of first-order boundary-layer theory at this flight condition. Some speculation on this question will be made subsequently.

The effect of increasing nose radius can be seen by comparing figure 7-7 with figure 7-6. In figure 7-7, the flow field is far from isoenergetic everywhere. This behavior will, of course, affect the convective heat transfer as will be shown subsequently.

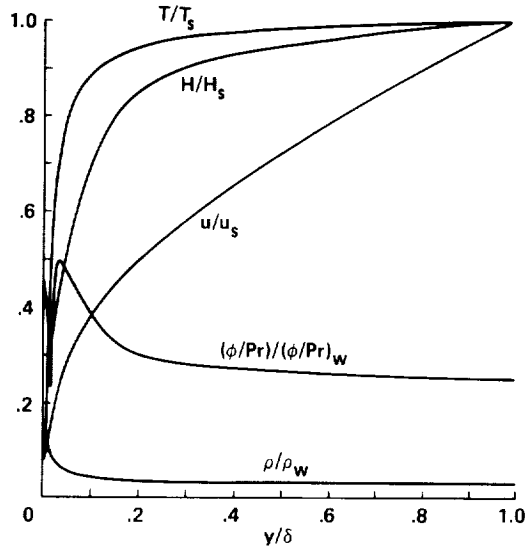

Figure 7-6.– Flow field with both ionization and radiation effects; $\overline{U}$ = 50,000 ft/sec at 190,000 ft altitude, R = 1 ft, p_s = 1 atm.

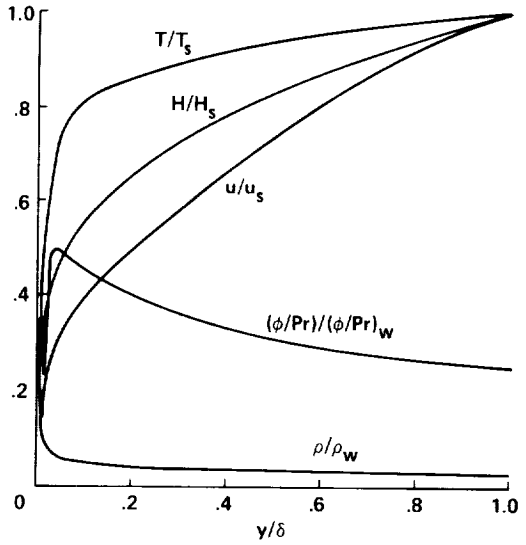

Figure 7-7.– Flow field for large nose radius; $\overline{U}$ = 50,000 ft/sec at 190,000 ft altitude, R = 5 ft, p_s = 1 atm.

Solutions at higher and lower pressure levels (10.0 and 0.1 atm) are shown in figures 7-8 and 7-9. Boundary-layer structure is, of course, more evident in the high-pressure profiles (fig. 7-8).

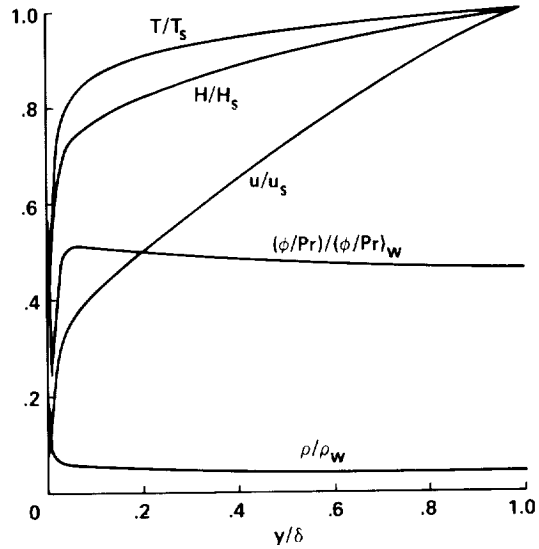

Figure 7-8.– Flow-field profiles for $\overline{U}$ = 40,000 ft/sec at 118,000 ft (p_S = 10 atm, R = 1 ft).

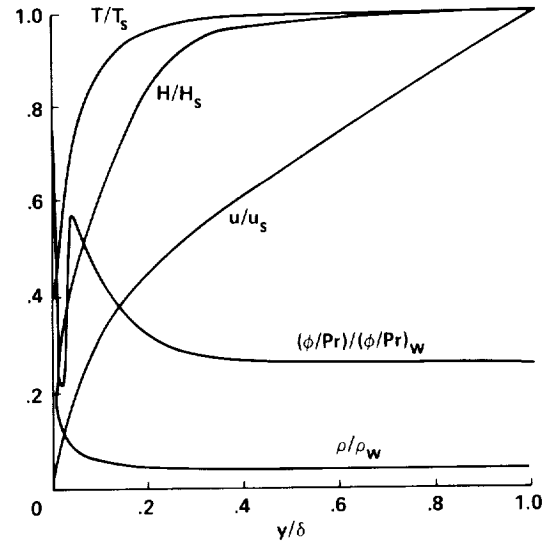

Figure 7-9.– Flow-field profiles for $\overline{U}$ = 50,000 ft/sec at 248,000 ft; p_S = 0.1 atm, R = 5 ft.

A solution with mass addition at the surface is shown in figure 7-10. The flight condition is the same as that for figure 7-6. A comparison of the two figures shows that the profiles for the injection case are shifted a small amount to the right for $0 < y/\delta \leq 0.5$, but coincide with the no-injection results for $y/\delta > 0.5$.

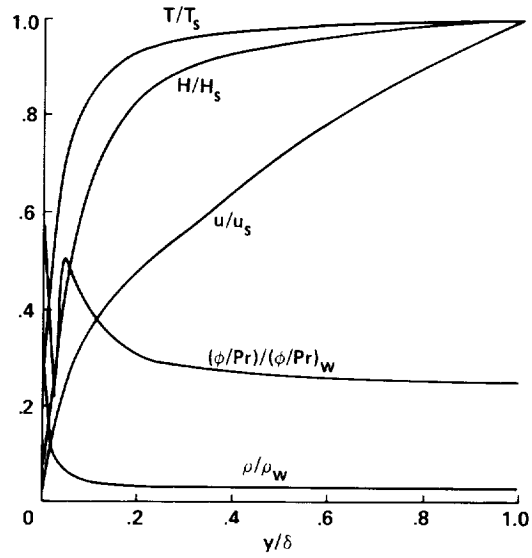

Figure 7-10.– Flow-field profiles with air injection at the wall; $\overline{U}$ = 50,000 ft/sec at 190,000 ft altitude, R = 1 ft, p_s = 1 atm, f_w = –0.4.

Although figure 7-10 is for air injection at the wall, the profiles (except for c_f) resemble those for a foreign gas, with α = 50, injected at the same mass-flow rate. The latter result is shown in figure 7-11. In general, the flow field is slightly cooler than that for air injection.

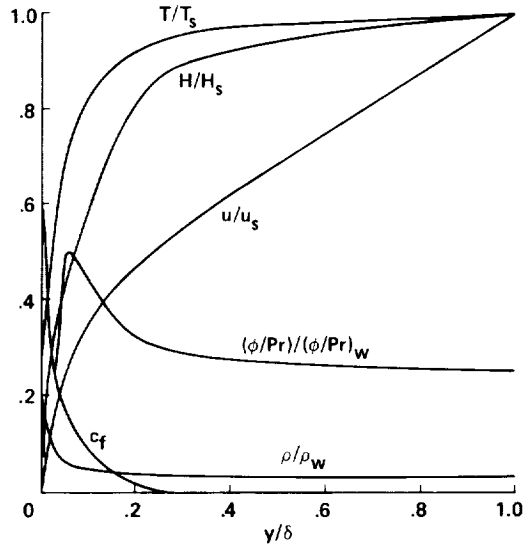

Figure 7-11.– Flow-field profiles with foreign gas injection at the wall; $\overline{U}$ = 50,000 ft/sec at 190,000 ft altitude, R = 1 ft, p_s = 1 atm, f_w = –0.4, α = 50.

A solution was attempted for a larger injection rate ($f_w = -0.7$), but it became unstable. Although the solution did not diverge indefinitely, the profiles oscillated, apparently within limits, with sufficient amplitude to render them invalid. Of course, for large injection rates (corresponding, for example, to high ablation rates caused by large heating rates), the flow field will become physically unstable.

Heat Transfer

Attention is now directed to the stagnation-region heat-transfer rates obtained from the solutions. Convective heat-transfer rates are presented and compared with those of others. The effect of radiative transport on convective heat transfer is shown. The conflicting theoretical (and experimental) results of various investigators for convective heat transfer mentioned earlier are discussed and an explanation is advanced for the differences. Radiant heat-transfer results are presented and compared with those calculated by use of the isoenergetic shock-layer assumption.

Convection– The results of convective heating analysis are presented in the form of reference 6 in figure 7-12(a). Results of references 2, 3, and 6 are shown for comparison. It is seen in figure 7-12(a) that if radiative transfer is neglected, the present result agrees well with the results of references 2 and 3. However, it (like the results of refs. 2, 3, 4, and 5) differs greatly from the results of reference 6 at high speed. The result of reference 29 is also shown for comparison, although ionization effects were not included in that analysis.

The computed results of Howe and Viegas and of Scala (ref. 6) are compared with experiments as shown in figure 7-12(b). The experiments of Warren (ref. 31) agree with the theory of Scala, while the experiments of references 2 and 31-34 are more in agreement with Howe and Viegas. Although the experimental discrepancy was never resolved (to my knowledge), the theoretical results were, as will be discussed subsequently.

When radiative transport effects are included in the differential equations, the convective heat transfer is diminished, as shown in figure 7-12(c), the effect being larger for larger nose radii and larger pressure levels. For $R = 5$ ft, $p_s = 1$ atm, and $U = 50{,}000$ ft/sec, the convective heating is less than 50% of what it would be if radiative transport were ignored[7] and is only 16% of the value predicted by the theory of reference 6.

Insofar as convective heat transfer is concerned, two questions are suggested. First, what is responsible for the difference between the results of reference 6 and those of other analyses when radiative transport is ignored? Second, is it possible to use the modified boundary-layer edge properties with existing boundary-layer results to predict the effects of radiative coupling on convective heat transfer?

Of course, some of the differences between the results of reference 6 and those of other analyses can be attributed to the assumed chemical state of the gas as well as to the method of formulating and solving the problem (comparison of several analyses is made in ref. 35). However, it is likely that the principal reason that reference 6 obtains much higher convective heating results than do other analyses lies in the transport properties.

---

[7]It is noted that although the dashed line labeled "present result without radiation coupling" in figure 7-12(b) is shown to be for $p_s = 1$ atm and $R = 1$ ft, it is not very sensitive to changes in pressure level and nose radius and can be used as a basis for comparison for all R and p_s.

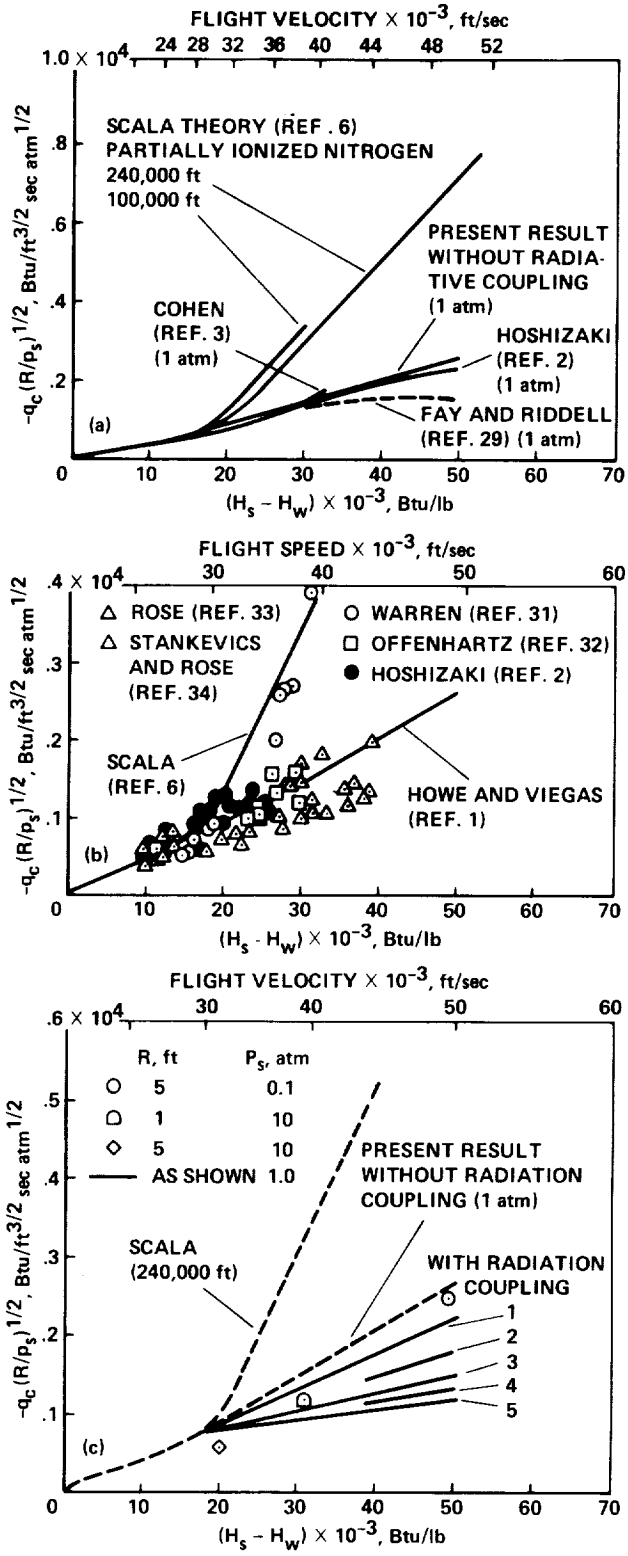

Figure 7-12.– Comparison of convective heat-transfer rates. (a) Radiative transport neglected in flow equations. (b) Convective heating—comparison with experiment. (c) Effects of radiative transport in flow equations.

Significantly, references 2-4 and the present analysis all use the transport properties of Hansen (ref. 19), but reference 6 does not. A comparison of the thermodynamic and transport properties of reference 6 with those of reference 19 yields the following result. The properties of viscosity, frozen specific heat, frozen thermal conductivity, and frozen Prandtl number generally agree within a few percent except at high temperatures, where viscosity differs by approximately a factor of 2, which also shows up in the frozen Prandtl number.[8] However, when the binary diffusion coefficients of reference 6 are put into the form of an equivalent reaction conductivity and added to the thermal conductivity, the result is very different from Hansen's total effective conductivity at high temperatures as shown in figure 7-13. At 5000 K, the value deduced from reference 6 agrees well with Hansen's value. At 10,000 K, the former is greater than the latter by a factor of about 25; and at 13,000 K, by a factor of about 20.

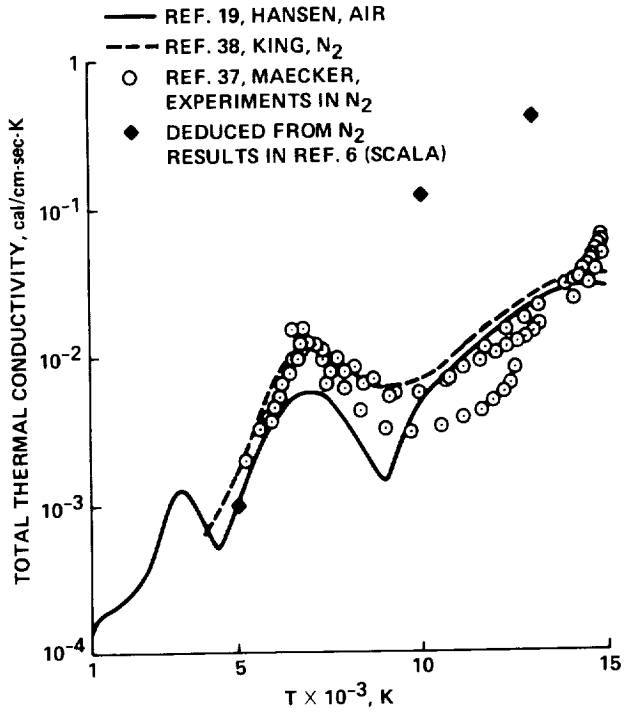

Figure 7-13.– Total thermal conductivity comparison; p = 1 atm.

Thus, it is likely that the difference between the convective heat-transfer results of reference 6 and those using Hansen's properties can be attributed to the reaction conductivity (or to the equivalent diffusion coefficients or their corresponding cross sections). Some experimental values of total thermal conductivity in nitrogen obtained from reference 37 are shown in figure 7-13. They are in substantial agreement with both the curve obtained from reference 38 for N_2 and Hansen's curve (ref. 19) for air, but do not agree with the values deduced from reference 6. However, more experimental work on conductivity, diffusion coefficients, or cross sections is required before the problem can be completely settled.

[8]According to a private communication from Scala, the viscosity in reference 6 is off by a factor of 2 because of an error in reference 36, but when viscosity is corrected, there is no appreciable change in the convective heat-transfer result of reference 6.

Turning to the second question, it is noted that convective heat transfer has been correlated by means of the driving enthalpy across the boundary layer and other outer-edge boundary-layer properties (refs. 2, 3, and 29). The question is, can the reduction in convective heat transfer due to radiative coupling be accounted for by simply making the driving enthalpy $(H_e - H_w)$ less than $(H_s - H_w)$ by an amount corresponding to the radiant energy emitted from an isoenergetic shock layer? The result is not encouraging; even for a small nose radius where coupling is expected to be relatively small, the approximation gives an erroneous result. For example, the driving enthalpy (and thus the estimated convective heat transfer) for a body with a 1-ft nose radius flying at 50,000 ft/sec at 190,000 ft altitude would be diminished by about 8% because of this radiant emission, but the actual convective heat transfer calculated by the method of this paper is diminished by about 15% from the case where radiative transport is neglected (as seen in figure 7-12(b)). Furthermore, the comparison is still worse if the change in boundary-layer edge properties corresponding to the diminished driving enthalpy is taken into account. Then the estimated convective heat transfer would increase by 5% in contrast to the actual decrease of 15% because $\rho_e\mu_e$ increases as H_e decreases.[9] The situation is much worse for larger nose radii.

It is speculated that this failure of simple boundary-layer theory may be attributed to failure to match gradients of the flow properties at the outer edge of the boundary layer.

Radiation– Studies of radiant heat transfer from the isoenergetic transparent shock layer have been made in references 7 and 11. Our purpose here is to indicate how the radiant heat transfer may be altered if transport processes are considered, and if the transparent gas assumption of those references is relaxed.

The effect can be seen by comparing the solid line with the dashed line in figure 7-14. It is seen that for larger nose radii at 50,000-ft/sec flight speed with $p_s = 1$ atm, the radiant heat transfer is actually about half what would be predicted for an isoenergetic transparent shock layer. It is noted that a similar effect was obtained for the convective heat transfer at this flight condition. Thus the coupling of transport processes reduces the convective heat transfer, and the fact that the shock layer is not isoenergetic reduces radiative heat transfer by large amounts at severe flight conditions.

The ratio of actual radiative heat transfer to that which would be predicted by an isoenergetic transparent shock layer assumption[10] is shown in figure 7-15 for several flight conditions. Interestingly enough, the ratio drops off more rapidly at 40,000 ft/sec than it does at 50,000 ft/sec (for $p_s = 1$ atm). It can be shown by a detailed comparison of the two solutions for $R = 1$ ft (which is beyond the scope of this chapter) that the result can be attributed to real-gas properties.

---

[9]It is assumed for illustrative purposes that (after Cohen, ref. 3) $q_c \propto (H_e - H_w)(\rho_e\mu_e)^{0.43}$.

[10]Both q_r and q_r^* are the radiant heating rate to the wall less that emitted by the wall. Equation (49) is used to compute q_r while equations (49) and (51) are used to obtain q_r^* for an isoenergetic transparent flow field. The result is $q_r^* = \sigma T_s^4(\overline{T}_w^4 - 2\delta\rho_s K_s)$.

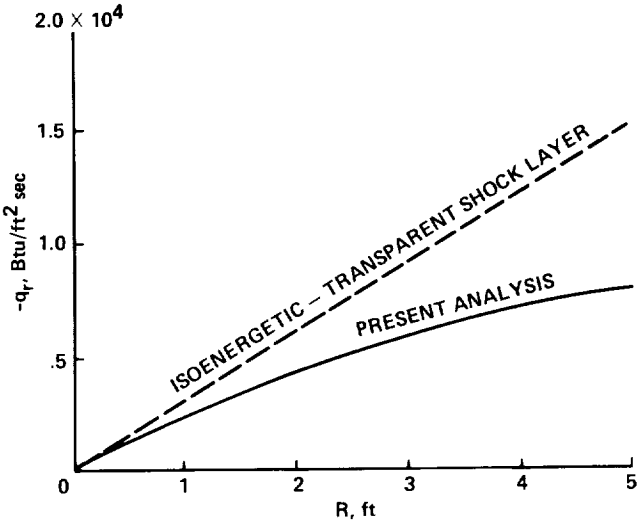

Figure 7-14.– Effect of nose radius on radiative heat transfer; $\bar{U}$ = 50,000 ft/sec at 190,000 ft altitude, p_s = 1 atm.

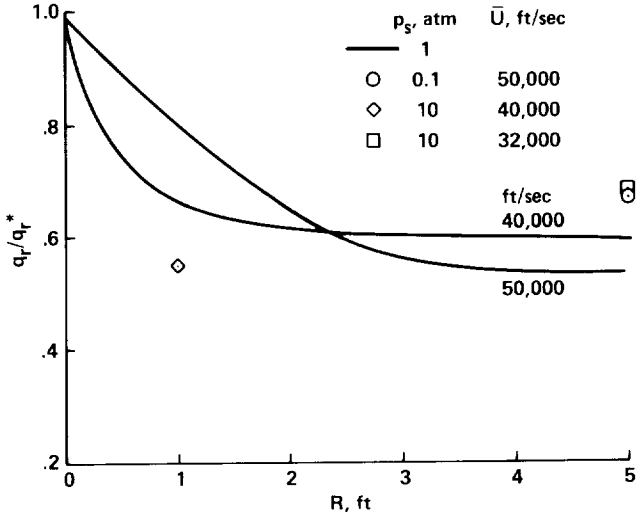

Figure 7-15.– Comparison of radiative heat-transfer results to those of isoenergetic shock layer (T_w = 1500 K).

Heat-transfer correlation– Attempts to correlate the convective heat-transfer results shown in figure 7-12(c) in a simple way have not been successful. However, net radiative heat transfer (radiation flux incident on the wall less that emitted by the wall) has been correlated by the expression

$$\frac{-q_r\sqrt{R/R_{ref}}}{\rho_\infty \bar{U}(H_s - H_w)(\bar{U}/\bar{U}_{ref})^{5/4}} = -0.0024 + 0.053\rho_s K_s R\,\frac{p_{ref}}{p_s} \tag{73}$$

where R_{ref}, $\bar{U}_{ref}$, and p_{ref} are 1 ft, 10^4 ft/sec, and 2117 lb/ft^2, respectively. The correlation is shown in figure 7-16, and includes results for flight speeds between 30,000 and 50,000 ft/sec, nose radii between

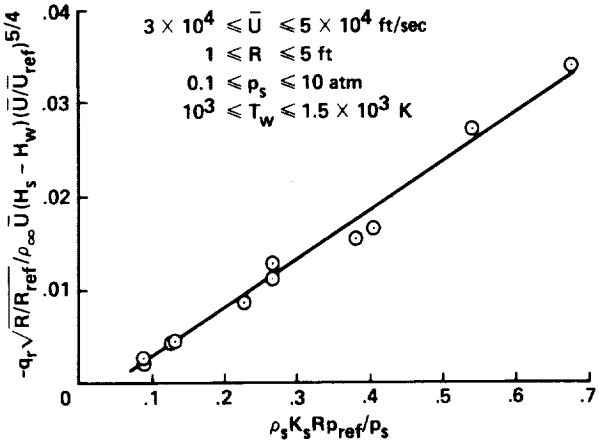

Figure 7-16.– Correlation of radiative heat transfer.

1 and 5 ft, and shock-layer pressure levels between 0.1 and 10.0 atm, at wall temperatures of 1000 to 1500 K.

If it is noted that $p_s \approx \rho_\infty \bar{U}^2$ and $(H_s - H_w) \approx \bar{U}^2/2$, the expression for net radiant stagnation-region heating rate becomes

$$-q_r = \rho_\infty \bar{U}^{1/4}\left(C_1 \frac{\bar{U}^4}{\sqrt{R}} + C_2 \frac{K_s}{\varepsilon}\sqrt{R}\,\bar{U}^2\right) \tag{74}$$

where $C_1 = -0.12\times10^{-7}$ sec$^{5/4}$ ft$^{-3/4}$, C_2 is 0.561×10^{-3} sec$^{5/4}$ lb ft$^{-11/4}$, and the units for q_r are ft lb/ft^2 sec.

Some approximate heating generalizations– Importantly, in the absence of mass addition we may say that size or nose radius, R, affects heating in the following ways: (1) convective heating varies inversely with $\sqrt{R}$ without radiative coupling (figs. 7-12(a) and (b)), (2) radiative heating varies directly with R for the isoenergetic case where the shock layer is transparent (fig. 7-14), and radiative heating at the wall varies approximately as $\sqrt{R}$ when the radiative transfer is fully coupled to the flow field (fig. 7-14 and eq. (74)—when the last term dominates). These notions will be useful in Chapter 8 where the powerful effects of mass addition on heating are examined in detail.

Effect of mass addition on heat transfer– When air is injected from the surface into the flow field (corresponding to the solution shown in fig. 7-10), the convective heat transfer is only about 65% of that when there is no injection (solution shown in fig. 7-7), but the radiative heat transfer is about 106% of the no-injection value. The increase in radiation is caused by a 5% increase in shock standoff distance because of the mass addition into the flow field.

If a foreign gas that is approximately 50 times as strong an absorber and emitter of radiation as air is injected into the flow field, the convective heat-transfer result for the foreign gas injection is about 86% of that for air injection. The decrease in convective heat transfer is accompanied by an increase in radiative heat transfer of about 7%. Standoff distance for the foreign injection is approximately 10% less

than that for air injection, possibly because the increased radiant emission for the former cools the shock layer and increases the density slightly.

It is interesting to note that injection of a gas that is 50 times as strong an emitter as air increases the radiant heat transfer by only 14% over the no-injection case for this flight condition. The reason is, of course, that most of the mass of foreign gas is in the cold part of the flow field, as can be seen from the profiles of ρ/ρ_w, c_f, and $\bar{T}$ in figure 7-11.

Shock Standoff Distance

In the absence of mass transfer at the body surface, there appears to be very little effect of transport phenomena on shock standoff distance at flight speeds up to 50,000 ft/sec for the cases considered. For example, at a speed of 40,000 ft/sec for $p_s = 1$ atm, δ/R varies from 0.0467 to 0.0468 for all nose radii, with or without radiative transport in the flow equations. These values are very near the 0.0472 predicted by Hayes' method (ref. 24).

The standoff distance for a flight speed of 50,000 ft/sec without mass addition is shown in figure 7-17. The open symbol is the present result without radiative transport considered and is about 7% above Hayes' estimates. With radiative transport, the present result lies from 3% about to 11% below the estimate of Hayes.

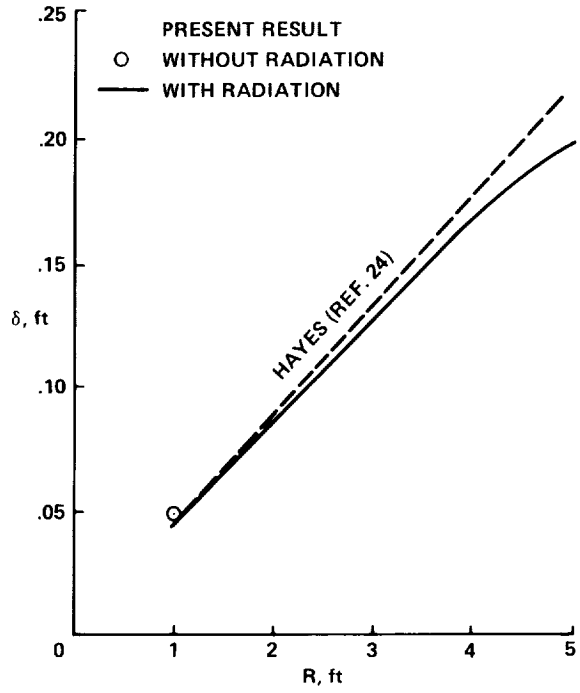

Figure 7-17.– Shock standoff distance; $\bar{U} = 50{,}000$ ft/sec, $p_s = 1$ atm.

It is expected that energy transport will diminish the standoff distance because it tends to cool the flow field and raise the density. The present results indicate that this is the case. It appears in figure 7-17 that as nose radius increases above 4 ft, and radiant transfer becomes more severe, the standoff distance tends to grow less rapidly with R. Although results are not available, it may be that there is a

strong transport phenomena effect on standoff distance for very large radii (R > 5 ft) at severe flight conditions.

Finally, for the cases of moderate rates of air injection[11] at the surface, the standoff distance increased approximately 5% above the no-injection case, while for a strongly absorbing gas ($\alpha = 50$) injected at the same rate, the standoff distance was about 6% below the no-injection value.

SUMMARY

In this chapter the derivation has been used for solving the entire flow field in the stagnation region of bluff bodies where the flow field cannot readily be separated into a shock layer and a boundary layer. The method has been tested wherever possible to establish its validity. At flight speeds of about 30,000 ft/sec it has reproduced known results in terms of heat transfer, standoff distance, viscous effects, and flow-field structure. At higher speeds (in the ionized flow regime), it has reproduced known heat-transfer and standoff results when radiative transfer effects were neglected. The method has been applied to study the effects of coupling between radiative and convective transport as well as the effects of mass addition on energy transport. A number of general conclusions may be drawn. For high-speed flight in the equilibrium regime (flight speeds of the order of escape speed and higher for shock-layer pressure levels of about 1 atm and higher) strong coupling among the various modes of energy transport exists. The prediction of convective heat transfer without including radiative coupling effects overestimates convective heating by a factor of about 2 for flight at 50,000 ft/sec for R = 5 ft. Similarly, the prediction of radiative heat transfer by the isoenergetic approximation overestimates radiative heating by a factor of about 2 for the same flight condition.

It is interesting to note that coupling between convective and radiative heat transfer generally reduces the convective heating rate more than can be accounted for by considering the fact that the driving enthalpy for convective heating has been diminished by the emission of radiant energy from the shock layer. The conclusion is that the combination of all modes of transport in the entire flow field is important in determining convective heat transfer at the wall.

Without mass addition at the body surface, only about 7% to 3% of the flow field is free from ionization at flight speeds from 40,000 ft/sec to 50,000 ft/sec for $p_s = 1$ atm. This, of course, is the region near the cold wall. Its extent appears to be about doubled when a gas that does not ionize more readily than air is injected (at moderate rates).

Injection of a foreign gas that is 50 times as strong an emitter of radiant energy as air increases the radiant heat transfer by only 14% while diminishing the convective heat transfer by about 45% compared with the no-injection case (for $\bar{U} = 50{,}000$ ft/sec, $p_s = 1$ atm, R = 1 ft). The total heat transfer was diminished by about 14%. The radiant heating increase is small because the bulk of the foreign gas remains near the cold wall. Very little foreign gas gets into that part of the flow field where the air is ionized.

Finally, these results of real-gas effects were obtained by use of what the author believes are currently the most reasonable values of real-gas properties. The results are considered to be quantitative to

[11] A moderate injection rate is one low enough not to upset the stability of the flow field. The limiting rate corresponds roughly to that which would just "blow off" the laminar boundary layer (refs. 8 and 39).

the extent that the gas properties are quantitative. In any event, the phenomenological effects shown in the results are considered to be qualitatively correct.

APPENDIX

EVALUATION OF RADIATION INTEGRALS

The term Q in the energy equation (37) that accounts for the emission and absorption of radiant energy is

$$Q = \frac{-4R\sigma T_s^4 K_s}{(j+1)\bar{U}^3}\bar{K}\left[\int_0^{\tau_s} \bar{T}^4(t)\,E_1(|t-\tau|)dt - 2\bar{T}^4 + \bar{T}_w^4 E_2(\tau)\right] \tag{A1}$$

The expression must be evaluated at every point in the flow field between the body and the shock.

The terms in the brackets can be expressed as a finite series if the curve $\bar{T}^4(t)$ is replaced by M straight-line segments in equal intervals ($\Delta t = \tau_s/M$) of τ and the result is integrated. The brackets then become

$$\left[\int_0^{\tau_s} \bar{T}^4(t)\,E_1(|t-\tau|)dt - 2\bar{T}^4 + \bar{T}_w^4 E_2(\tau)\right]$$

$$= -\left\{E_2(t_s-\tau) + \frac{1}{\Delta t}\sum_{i=0}^{M-1}(\bar{T}_{i+1}^4 - \bar{T}_i^4)[E_3(|t_{i+1}-\tau_j|) - E_3(|t_i-\tau_j|)]\right\} \tag{A2}$$

The series is evaluated at a constant τ (starting with $\tau = 0$), with the dummy variable t ranging from $t = 0$ to t_s. This leads to one value of Q corresponding to that τ_j (or to η, which is related to τ by eq. (38)). Then τ_j is increased by $\Delta\tau$ and the entire process is repeated until $\tau = \tau_s$. The method can be illustrated in detail by use of table A1.

At the end of each integration of the energy equation (37), new profiles of the various thermodynamic and transport properties (including $\bar{T}$ and $\bar{K}$) and the optical depth τ are obtained as functions of η from the new profiles of g. The resulting optical depth at the shock $\tau_s = t_s$ (= 0.10 for purposes of illustration in the table) is divided into M (= 10 in the table) equal intervals in τ and t so that $\tau_0 = 0 \ldots \tau_j = j\Delta \ldots \tau_M = \tau_s = M\Delta$ and $t_0 = 0 \ldots t_i = i\Delta t \ldots t_M = t_s = M\Delta t$. A table of $\bar{T}_i^4$, $\bar{T}_{i+1}^4 - \bar{T}_i^4$ and, for each value of t, a table of $E_3(|t_i - \tau|)$ corresponding to t_i is formed. Now it is easy to see the application of the table for evaluating the right side of equation (A2). The term $E_2(t_s - \tau_j)$ is evaluated by use of the table and the recurrence formula (57). The series is evaluated at each τ_j (for example, 0.02) using column 3 and the column corresponding to τ_j (column 7).

Because of the symmetry of the table $E_3(|t_i - \tau|)$ about its diagonal, the table can be reduced to only two columns of E_3 values. It is noted that the column corresponding to τ_j differs from that of τ_{j-1} only in that the former is shifted downward one step and the top value in the τ_j column is the ith value in the $\tau_j = 0$ column. Thus, using the $\tau_j = 0$ column as a master column plus one working τ_j column makes it possible to generate the next working column. In that way, only 2(M + 1) values of E_3 need be retained in the digital computer memory instead of $(M + 1)^2$ values. A very large saving in memory space is achieved for large values of M.

In similar fashion, the integral in the heat-transfer equation (50) can be replaced by a finite series

$$2\int_0^{\tau_s} \overline{T}^4(t)\, E_2(t)dt - \overline{T}_w^4 = -2\left\{ E_3(t_s) + \frac{1}{\Delta t} \sum_{i=0}^{M-1} (\overline{T}_{i+1}^4 - \overline{T}_i^4)[\, E_4(t_{i+1}) - E_4(t_i)] \right\} \qquad \text{(A3)}$$

Here, $\tau = 0$ and the series can be evaluated by a one-column table of $E_4(t_i)$.

TABLE A1.– NUMERICAL METHOD FOR SOLVING THE RADIATIVE TRANSFER INTEGRAL

			$E_3(\lvert t_i - \tau_j \rvert)$											
1	2	3	4	5	6	7	8	9	10	11	12	13	14	15
i	$\bar{T}_i^4$	$\bar{T}_{i+1}^4 - \bar{T}_i^4$	t_i \ τ_j	0	0.01	0.02	0.03	0.04	0.05	0.06	0.07	0.08	0.09	0.10
0	$\bar{T}_0^4$	$\bar{T}_1^4 - \bar{T}_0^4$	0	0.500	0.490	0.481	0.472	0.463	0.455	0.477	0.439	0.431	0.424	0.416
1	$\bar{T}_1^4$	$\bar{T}_2^4 - \bar{T}_1^4$	.01	.490	.500	.490	.481	.472	.463	.455	.447	.439	.431	.424
2	$\bar{T}_2^4$	↓	.02	.481	.490	.500	.490	.481	.472	.463	.455	.447	.439	.431
3	↓	↓	.03	.472	.481	.490	↓	↓	↓	↓	↓	↓	↓	.439
4			.04	.463	.472	.481								.447
5			.05	.455	.463	.472								.455
6			.06	.447	.455	.463								.463
7			.07	.439	.447	.455								.472
8			.08	.431	.439	.447								.481
M–1			.09	.424	.431	.439								.490
M			.10	.416	.424	.431	.439	.447	.455	.463	.472	.481	.490	.500

REFERENCES

1. Howe, J. T.; and Viegas, J. R.: Solutions of the Ionized Radiating Shock Layer, Including Reabsorption and Foreign Species Effects, and Stagnation Region Heat Transfer. NASA TR R-159, 1963.

2. Hoshizaki, H.: Heat Transfer in Planetary Atmospheres at Super-Satellite Speeds. ARS Paper 2173-61, American Rocket Society, ARS J., vol. 32, Oct. 1961, pp. 1544-1551.

3. Cohen, Nathaniel B.: Boundary-Layer Similar Solutions and Correlation Equations for Laminar Heat-Transfer Distribution in Equilibrium Air at Velocities up to 41,000 Feet per Second. NASA TR R-118, 1961.

4. Pallone, A.; and Van Tassel, W.: Stagnation Point Heat Transfer for Air in the Ionization Regime. ARS J., vol. 32, no. 3, March 1962, pp. 436-437.

5. Adams, Mac C.: A Look at the Heat Transfer Problem at Super Satellite Speeds. ARS Paper 1556-60, American Rocket Society, New York, Dec. 1960.

6. Scala, Sinclaire M.; and Warren, Walter R.: Hypervelocity Stagnation Point Heat Transfer. R61SD185, Space Sciences Lab., General Electric, Oct. 1961.

7. Kivel, Bennett: Radiation from Hot Air and Its Effect on Stagnation-Point Heating. J. Aero. Sci., vol. 28, no. 2, Feb. 1961, pp. 96-102.

8. Howe, John Thomas: Shielding of Partially Reflecting Stagnation Surfaces Against Radiation by Transpiration of an Absorbing Gas. NASA TR R-95, 1961.

9. Chapman, Dean R.: An Analysis of the Corridor and Guidance Requirements for Supercircular Entry into Planetary Atmospheres. NASA TR R-55, 1959.

10. Chapman, Dean R.; and Kapphahn, Arline K.: Tables of Z Functions for Atmosphere Entry Analyses. NASA TR R-106, 1961.

11. Yoshikawa, Kenneth K.; and Wick, Bradford H.: Radiative Heat Transfer During Atmosphere Entry at Parabolic Velocity. NASA TN D-1074, 1961.

12. Hayes, Wallace D.; and Probstein, Ronald F.: Hypersonic Flow Theory. Academic Press, 1959.

13. Ho, Hung-Ta; and Probstein, Ronald F.: The Compressible Viscous Layer in Rarefied Hypersonic Flow. ARL TN 60-132, Div. of Eng., Brown University, Aug. 1960.

14. Goulard, Robert; and Goulard, Madeline: Energy Transfer in the Couette Flow of a Radiant and Chemically Reacting Gas. Heat Transfer and Fluid Mechanics Institute, Stanford Univ. Press, 1959.

15. Tellep, D. M.; and Edwards, D. K.: Paper II: Radiant-Energy Transfer in Gaseous Flows. Volume I, Part 1—Fluid Mechanics, General Research in Flight Sciences, Jan. 1959-Jan. 1960. LMSD-288139, Missiles and Space Div., Lockheed Aircraft Corp., Jan. 1960.

16. Kourganoff, V.: Basic Methods in Transfer Problems. Clarendon Press, 1952.

17. Cohen, Nathaniel B.: Correlation Formulas and Tables of Density and Some Transport Properties of Equilibrium Dissociating Air for Use in Solutions of the Boundary-Layer Equations. NASA TN D-194, 1960.

18. Butler, James N.; and Brokaw, Richard S.: Thermal Conductivity of Gas Mixtures in Chemical Equilibrium. J. Chem. Phys., vol. 26, no. 6, June 1957, pp. 1636-1643.

19. Hansen, C. Frederick: Approximations for the Thermodynamic and Transport Properties of High-Temperature Air. NASA TR R-50, 1959.

20. Lees, Lester: Convective Heat Transfer with Mass Addition and Chemical Reactions. Paper presented at Third Combustion and Propulsion Colloquium, AGARD, NATO, Palermo, Sicily, 1958. Pergamon Press, 1958. (GALCIT Pub. 451.)

21. Dennison, M. R.; and Dooley, D. A.: Combustion in the Laminary Boundary Layer of Chemically Active Sublimators. Pub No. U-110, Aeronutronic Systems, Inc., Glendale, Calif., Sept. 23, 1957.

22. Viegas, John R.; and Howe, John T.: Thermodynamic and Transport Property Correlation Formulas for Equilibrium Air from 1000 K to 15,000 K. NASA TN D-1429, 1962.

23. Kivel, B.; and Bailey, K.: Tables of Radiation from High Temperature Air. Res. Rep. 21, AVCO Research Lab., Dec. 1957.

24. Hayes, Wallace D.: Some Aspects of Hypersonic Flow. The Ramo-Wooldridge Corp., Jan. 4, 1955.

25. Moeckel, W. E.; and Weston, Kenneth D.: Composition and Thermodynamic Properties of Air in Chemical Equilibrium. NACA TN 4265, 1958.

26. Case, K. M.; DeHoffman, F.; and Placzek, G.: Introduction to the Theory of Neutron Diffusion. Vol. 1, Los Alamos Scientific Lab., June 1953.

27. Anon: Tables of Sine, Cosine, and Exponential Integrals. Vol. I, National Bureau of Standards Computation Lab., 1940.

28. Hildebrand, F. B.: Introduction to Numerical Analysis. McGraw-Hill Book Co., 1956.

29. Fay, J. A.; and Riddell, F. R.: Theory of Stagnation Point Heat Transfer in Dissociated Air. J. Aero. Sci., vol. 25, no. 2, Feb. 1958, pp. 73-85 and 121.

30. Howe, John Thomas: Radiation Emission Effects of the Equilibrium Boundary Layer in the Stagnation Region. NASA TN D-1031, 1961.

31. Warren, W. R.; Rogers, D. A.; and Harris, C. J.: The Development of an Electrically Heated, Shock Driven Test Facility. Second Symposium on Hypervelocity Techniques, Denver, 1962.

32. Offenhartz, E.; Weisblatt, H.; and Flagg, R. F.: Stagnation Point Heat Transfer Measurements at Super Satellite Speeds. J. Roy. Aero. Soc., vol. 66, no. 613, January 1962, p. 54.

33. Rose, P. H.; and Stark, W. I.: Stagnation Point Heat-Transfer Measurements in Dissociated Air. J. Aero. Sci., vol. 25, no. 2, Feb. 1958, pp. 86-97.

34. Stankevics, J. O. A.; and Rose, P. H.: Measurements of Stagnation Point Heat Transfer in Partially Ionized Air. Paper presented at IAS Meeting, January 1963.

35. Fay, J. A.: Hypersonic Heat Transfer in the Air Laminar Boundary Layer. Paper presented at the AGARD Hypersonic Specialists' Conference, Brussels, Belgium, April 3-6, 1962.

36. Hirschfelder, Joseph O.; Curtiss, Charles F.; and Bird, R. Byron: Molecular Theory of Gases and Liquids. John Wiley and Sons, 1954.

37. Maecker, H.: Thermal and Electrical Conductivity of Nitrogen up to 15,000 K by Arc Measurements. Presented at Meeting on Properties of Gases at High Temperature, AGARD, Aachen, Sept. 21-23, 1959.

38. King, L. A.: Theoretical Calculation of Arc Temperatures in Different Gases. Proceedings of the Sixth International Conference on Spectroscopy, Amsterdam, 1956. Pergamon Press, 1957.

39. Emmons, H. W.; and Leigh, D.: Tabulation of the Blasius Function with Blowing and Suction. Div. of Appl. Sci., Harvard Univ., Nov. 1953. (Combustion Aerodynamics Lab. Interim Tech. Rep. 9.)

CHAPTER 8

HYPERVELOCITY FLOW FIELDS WHICH HIGHLIGHT THE EFFECTS OF MASS ADDITION

INTRODUCTION

In this chapter, many solutions of the viscous shock layer equations with mass addition are obtained. As before, flow-field equations include the effects of heat conduction, diffusion of reacting species, and emission and absorption of gaseous radiation for dissociated and partially ionized air in chemical equilibrium. Convective and radiative heating rates with mass addition are obtained from the solutions. Algebraic equations are derived for predicting the nose radius that minimizes total heating rates at a given flight speed and shock-layer pressure level. Values for the corresponding natural ablation rate, both the intrinsic and the effective heat of ablation, the ratio of radiative to convective heating rate, surface shear stress, and shock-wave standoff distance are given. The effects of ablated gases that radiate more strongly than air are examined. Rules for scaling flow-field structure with mass addition are discussed. Solutions without mass addition at low Reynolds numbers where external vorticity, energy depletion, and flow energy limiting are important are compared with existing theory and experiments. This chapter is largely the text of a report originally published as reference 1.

The study of mass addition in the stagnation region is of interest because any object, blunt or pointed, which enters the atmosphere at high speed will generally have a blunted stagnation region as the material suffers thermal erosion. Interest is further enhanced because the aerodynamic heating rate is likely to be a maximum in the stagnation region.

The hot, thin gas cap over the forward surface of an object entering a planetary atmosphere is the host to a myriad of interrelated physical phenomena. The study of the gas cap is especially cumbersome if the flow field is a mixture of air and foreign species which were added to the flow because the surface is ablating. The knowledge of mass addition effects at speeds below which ionization and gaseous radiation effects may be neglected is highly developed from both the flow-field and materials points of view. (A small part of the extensive literature on the subject will be brought into the discussion subsequently where appropriate.) On the other hand, mass addition at speeds greater than 30,000 ft/sec for which the gas cap is both ionized and radiating has received comparatively little attention.

The present purpose is to examine the effects of mass addition at flight speeds greater than 30,000 ft/sec as it influences and is influenced by some of the many other phenomena, parameters, and physical properties of the gas cap. To this end we consider mass addition in the general sense, transpiration, and in the special sense, ablation.

For mass addition in general, we particularly want to know its influence on convective heating. Is heat blockage as effective at the higher speeds as it is at the lower speeds? Do the existing correlation formulas obtained for lower speeds apply at hypervelocity?

With respect to ablation, we are especially interested in finding the conditions for which the total heating rate at a given flight condition and given material is minimized, for two reasons. First, minimum heating of itself is intrinsically advantageous. Second, it gives one ideal situation in terms of nose radius and ablation rate at each flight condition for which we can examine some of the other questions of

interest, thus affording some economy in the range in which other parameters need to be varied. We obtain an appreciation of what may be achieved under advantageous conditions.

Other questions have to do with the effect of mass addition on related quantities. For example, we may expect that mass addition will alter the flow-field structure and change the standoff distance. At once the question arises: what is the effect of altered standoff distance on radiative heating? Moreover, the species added to the flow field may be expected to radiate differently from air. The question is,: how important might this effect be? Some ablating materials suffer from lack of physical strength, so we are interested in the magnitude of viscous shear stresses at the surface and how they compare with pressure stresses. We are, of course, concerned with the relative importance of radiative to convective heating because it bears on the type of surface useful for heat-shielding, and it indicates where improvements in our knowledge are more important—in gaseous radiation emission properties or in total thermal conductivity of the gas. Ablation rates and effective heat of ablation are important to determine at speeds greater than 30,000 ft/sec.

Because much of the experimental work on mass addition is performed in ground-based facilities for which both the entry object and the environment must be modeled, we wish to examine the problem of scaling mass addition effects.

Finally, because of interest in pointed or very slightly blunted entry bodies, low Reynolds number (based on nose radius) effects or external vorticity effects have become important. This problem will be examined briefly.

GENERAL FEATURES OF SOLUTIONS

In this study we are concerned with both the structure of the stagnation-region flow field (which will be obtained from solutions of the flow-field equations) and with quantities derived from flow-field solutions. The details of the method of solution of the flow-field equations are contained in Chapter 7 and in references 1 and 2.

Briefly, the conservation equations for mass, momentum, and energy are solved in the stagnation region of blunt bodies from the body surface to the shock wave. Momentum transport by viscosity and energy transport by conduction, diffusion of reacting species, and emission and absorption of radiation are included in the integro-differential equations.

The thermodynamic and transport properties (radiative transfer sometimes excepted as discussed subsequently) of the mixture of air and injected gases are assumed to be those of partially dissociated and ionized air in chemical equilibrium (ref. 2). This assumption should lead to reasonable results even if the injected gases become ionized, if the ablation products are nitrogen, oxygen, and carbon compounds, the reason being the similarities among these species and their compounds. That is, the atomic weights of monatomic species are nearly alike, as are the molecular weights of diatomic species. Moreover, the dissociation energy of CO_2 is close to that of O_2; that of CN like that of NO; and CO like N_2; while CO, N, and O all have nearly the same first ionization potential (which is not radically different from that of C). Actually, the bulk of the injected species will be near the wall of the body where the temperature and degree of ionization are suppressed, and the argument of Lees (refs. 3 and 4) may be employed. For nonionized gas mixtures, Lees has shown that it is not necessary to understand the extraordinarily complicated details of the chemical interaction between the atmospheric gas components

and the vaporized surface material insofar as convective energy transport is concerned as long as the molecular weights and collision cross sections of the injected gas and air are of comparable size, or that the ratio of mass diffusivity to thermal diffusivity (Lewis number) of the mixture is near unity.

On the other hand, radiative transport by the mixture of injected vapor and air may be significantly different from that of air alone. This behavior is allowed for in the governing equations by including a quantity proportional to the injected species concentration in the Planck mean mass absorption coefficient expression and a diffusion equation to account for this species. In the results to be presented, radiation from injected gases is specified to be like that of air except where stated to the contrary.

The results of the analysis have been tested against those by others where possible in order to establish the validity of the method. In reference 2 it was shown that the calculated structure of the flow field exhibits both an isoenergetic shock layer and a boundary layer in the low speed (such that energy depletion by radiation is negligible), high Reynolds number regime as it should. The analysis reproduced the well-known effects on convective heating of the assumption $\rho\mu = \text{const}$ when $\rho\mu$ was artificially set constant. The shock standoff distances predicted by this method agree with those predicted by other methods (e.g., ref. 5). When radiation coupling is negligible, it produces convective heating results at high speeds (up to 50,000 ft/sec) that agree with the boundary-layer results of references 6 and 7, which use the same transport properties. It will be seen subsequently that in the low Reynolds number regime the method leads to flow fields which exhibit the expected shock-layer vorticity structure and the corresponding enhanced surface shear stress and convective heating rates. One additional test of the method is shown in figure 8-1. The solid lines are enthalpy profiles across the flow field for the nose radii and flight conditions noted, and the symbols are the results of K. K. Yoshikawa (ref. 8), corresponding to the one-dimensional flow of radiating air behind the shock wave. It is seen that both analyses show that the shock layer is nonisoenergetic and both give the same results for that half of the flow field nearest the shock. The present analysis shows lower enthalpy and larger enthalpy

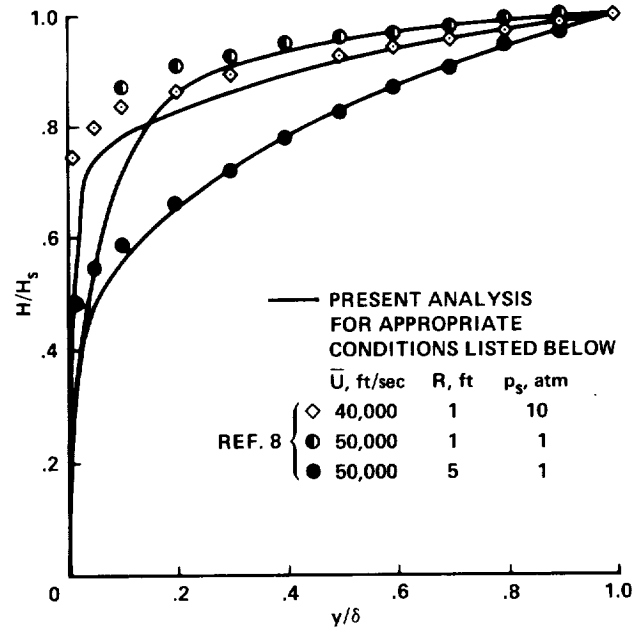

Figure 8-1.– Comparison of enthalpy profiles with those of reference 8.

gradients as a result of convective transport in that half of the flow field near the body, because neither a body nor energy transport by conduction was included in the one-dimensional analysis of reference 8.

Before mass addition effects are discussed, a brief comment should be made regarding terminology. Throughout the rest of the paper, comments relating to mass addition and injected gases, in general, apply to both forced mass addition (transpiration) and natural mass addition (thermal erosion or ablation). When our comments are specialized to thermal erosion only, the word ablation will be used.

EFFECTS OF MASS ADDITION ON HEATING RATES

Radiative Heating

Mass addition can affect radiative heating in two ways: by altering the temperature and structure of the flow field and by adding species which radiate differently from air. However, results of numerous flow-field solutions[1] with mass addition show that (except for a combination of low Reynolds number and strong injection of gases which radiate more strongly than air, discussed subsequently) radiative heating is much less affected by mass addition than is convective heating.

Mass addition of gases like air tends to thicken the shock layer, thus tending to enhance radiative heating, but it also tends to cool the flow field—inhibiting radiative heating. In almost all of the solutions, the net effect of injection of a species which radiates like air was to increase radiative heating modestly. For example, for a flight speed of 50,000 ft/sec, a nose radius of 0.25 ft, a shock-layer pressure level of 1 atm, and a surface mass flux of 13% of the free-stream mass flux ($f_w = -1.5$), the radiative heating was enhanced about 24%.

Moreover, it was shown in figure 9 of reference 2 that for high Reynolds number, the bulk of the injected species remains close to the vehicle surface where the temperature is low compared with that behind the shock wave. Thus the radiant flux at the surface is enhanced only 7% by a gas which emits 50 times as strongly as air injected at the same rate ($f_w = -0.4$, or mass addition rate 2% of the free-stream mass flux; same flight condition as above with R = 1 ft).

On the other hand, it will be shown subsequently (in the discussion of fig. 18) that if the Reynolds number is low, injected species will also be present in the hot part of the flow field and need not radiate much more strongly than air in order to have an appreciable effect on radiative heating.

Convective Heating

Convective heating is very strongly influenced by mass addition. In the flight regime for which air is dissociated but not ionized, many studies (ref. 9) have employed a linear approximation relating ψ (the ratio of convective heating with mass addition to that without) to the product of mass addition rate and driving enthalpy divided by the convective heating without mass addition. The linear ψ was based upon an empirical correlation of experimental and theoretical transpiration results from references 10-12. Swann (ref. 13) and Swann and Pittman (ref. 14) obtained a quadratic expression for ψ in

[1]All of the results of this section of the paper correspond to wall temperatures between 1500 and 3000 K.

terms of the above variables by an empirical fit of the results of ideal gas boundary-layer solutions of Beckwith (ref. 15).

In the present analysis, the influence of mass addition on convective heating was obtained from the results of the ionized radiating flow-field solutions (both q_c and q_{c_0}, which are convective heating with mass addition and without, respectively, were obtained from the solutions). The parameter ψ for speeds of 40,000 and 50,000 ft/sec is shown in figure 8-2 as a function of f_w, the dimensionless stream function at the wall. The quantity f_w is proportional to the mass addition rate by the relation

$$\dot{m}_w = \rho_w v_w = -f_w \sqrt{\frac{\rho_s \mu_s \bar{U}(j+1)}{R}} \tag{1}$$

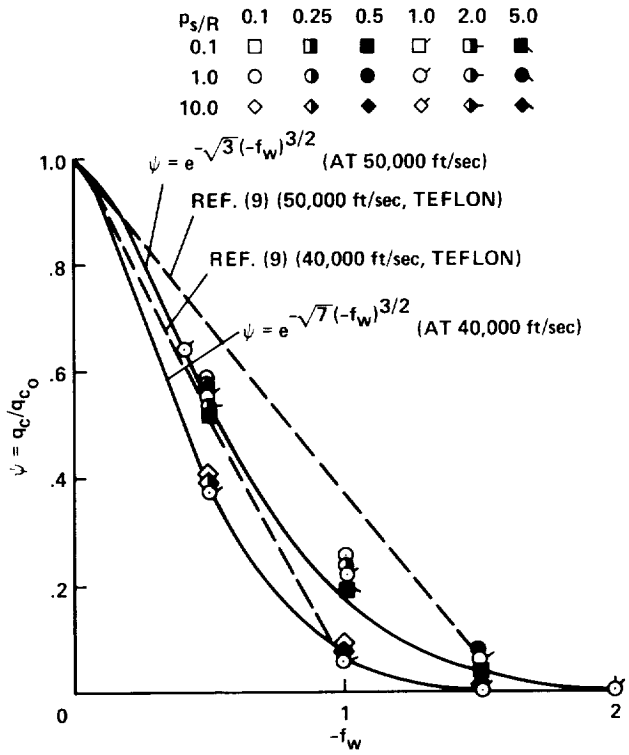

Figure 8-2.– Separate correlations of results of blowing on convection at $\bar{U}$ = 40,000 and 50,000 ft/sec.

For the moment, attention is directed to the solid curves of the figure. (The dashed lines are an application of the linear ψ approximation and will be discussed in a subsequent section of this chapter.) Each solid line correlates results for one flight speed, various nose radii, and various shock-layer pressure levels, as can be seen from a comparison with the plotted symbols. Each of these curves is represented by the exponential[2]

[2]Some experiments by Vojvodich, Pope, and Dickey of Ames Research Center at conditions corresponding to subsatellite speed indicate that ψ for strong ablation of some materials may approach an asymptote different from zero, possibly of the order of 10^{-1} (this effect was remarked upon in ref. 16). An appropriate form of ψ for that case would be

$$\psi = e^{-b(-f_w)^n} \tag{2}$$

where b is a function of flight velocity alone and n is 3/2. Similar curves can be constructed for other flight velocities. Note that a given f_w is less effective in retarding convective heating at higher speeds.

We can correlate results over a wide range of conditions by expressing b as a function of $\overline{U}$, where $\overline{U}$ is flight velocity in units of 10,000 ft/sec. That is, results of 36 mass addition solutions for nose radii[3] ranging from 0.01 to 5 ft, flight speeds from 30,000 to 50,000 ft/sec, and shock-layer pressure levels from 0.1 to 10 atm are correlated in figure 8-3 by use of equation (2) with

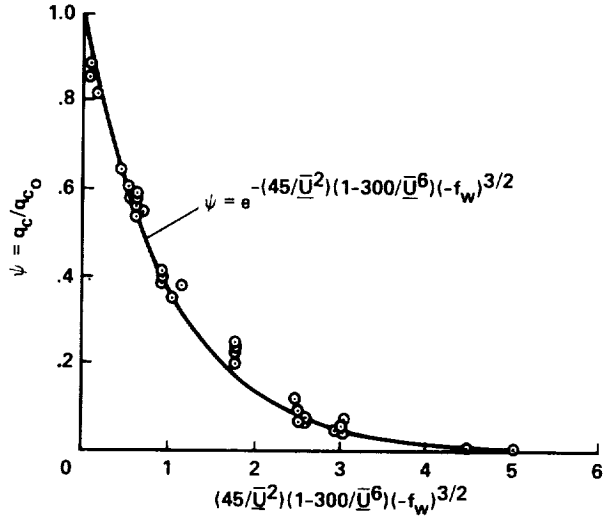

Figure 8-3.– General correlation of result of blowing on convection. (The points are identified in table I.)

$\psi = a + (1 - a)e^{-b(-fw)^n}$, where a is the value of the asymptote. The asymptote does not appear to be caused by wall temperature effects alone. In the examples of figures 2 and 3, no asymptote other than zero could be distinguished, even though wall temperature was changed from 1500 to 3000 K. For example, at 40,000-ft/sec flight speed, 1-atm shock-layer pressure level, 1-ft nose radius, and $f_w = -1.0$, both q_c and q_{c_o} changed as T_w was changed from 1500 to 3000 K, but their ratio ψ remained the same to four decimal places, 0.0626. It is conceivable that molecular weight of surface vapors may have something to do with the asymptote. For example, the vaporization temperature of Teflon is low enough that surface vapors may have a molecular weight of 100 rather than that between 16 and 30 for the air injection (or for that matter, 15 for vaporizing phenolic nylon) under consideration. This large a disparity in molecular weight may be significant and would tend to raise ψ for the higher molecular weight gas. The presence of an asymptote for ablation is expected for other reasons; that is, if $\psi \to 0$, $q_c \to 0$. For test models that are small, q_r is also negligible. Thus in the extreme, the heating which causes ablation vanishes and some asymptotic value of ψ or finite value of q_c is necessary to initiate ablation.

[3]Two points should be mentioned in connection with the small nose radii. First, the correlation holds for examples for which there is strong vorticity in the entire flow field as long as q_{c_o} also includes the external vorticity effect. Second, the chemical equilibrium assumption is somewhat in doubt for the small nose radii, a point which will be discussed subsequently.

TABLE I.– CONDITIONS FOR POINTS SHOWN IN FIGURES 8-3 AND 8-4

Group	Point	p_s, atm	$\overline{U}$	R, ft	$-f_w$	Comments
1	1	1.0	4.1	0.01	0.1	
	2	1.0	4.1	1.0	.1	
	3	1.0	5.0	1.0	.2	
2	4	1.0	5.0	1.0	.4	
	5	1.0	5.0	1.0	.45	
	6	1.0	5.0	.1	.5	
	7	1.0	5.0	.25	.5	
	8	1.0	5.0	.5	.5	
	9	1.0	5.0	1.0	.5	
	10	1.0	5.0	2.0	.5	
	11	.1	5.0	5.0	.5	
3	12	10.0	4.0	.1	.5	
	13	10.0	4.0	.25	.5	
	14	1.0	4.0	1.0	.5	
	15	1.0	3.0	1.0	.5	
	16	1.0	5.0	1.0	.75	
4	17	1.0	5.0	.1	1.0	17 and 18 appear as one point on figures 8-3 and 8-4
	18	1.0	5.0	.25	1.0	
	19	1.0	5.0	.5	1.0	
	20	1.0	5.0	1.0	1.0	
	21	.1	5.0	5.0	1.0	
5	22	1.0	5.0	1.0	1.25	
	23	1.0	4.1	.01	1.0	
	24	1.0	4.1	1.0	1.0	
	25	10.0	4.0	.1	1.0	25 and 26 appear as one point on figures 8-3 and 8-4
	26	10.0	4.0	.25	1.0	
	27	1.0	4.0	1.0	1.0	
6	28	1.0	3.0	1.0	1.0	
	29	1.0	5.0	.1	1.5	29 and 30 appear as one point on figures 8-3 and 8-4
	30	1.0	5.0	.25	1.5	
	31	1.0	5.0	.5	1.5	31 and 32 appear as one point on figures 8-3 and 8-4
	32	1.0	5.0	1.0	1.5	
	33	.1	5.0	5.0	1.5	
7	34	10.0	4.0	.25	1.5	34 and 35 appear as one point on figures 8-3 and 8-4
	35	1.0	4.0	1.0	1.5	
8	36	1.0	5.0	1.0	2.0	

$$b = \frac{45}{\bar{U}^2}\left(1 - \frac{300}{\bar{U}^6}\right) \tag{3}$$

and n = 3/2. This formula is useful for extrapolation to flight speeds above 50,000 ft/sec, but cannot be used for speeds much below 30,000 ft/sec because it changes sign at about 26,000 ft/sec. The same mass addition solution results are correlated by letting

$$b = 0.706 + 1.6\bar{U} - 0.28\bar{U}^2 \tag{4}$$

and n = 3/2. The result is shown in figure 8-4. This formula can be used to extrapolate to speeds below 30,000 ft/sec, but cannot be used for speeds much above 50,000 ft/sec, because it changes sign at about 61,000 ft/sec.

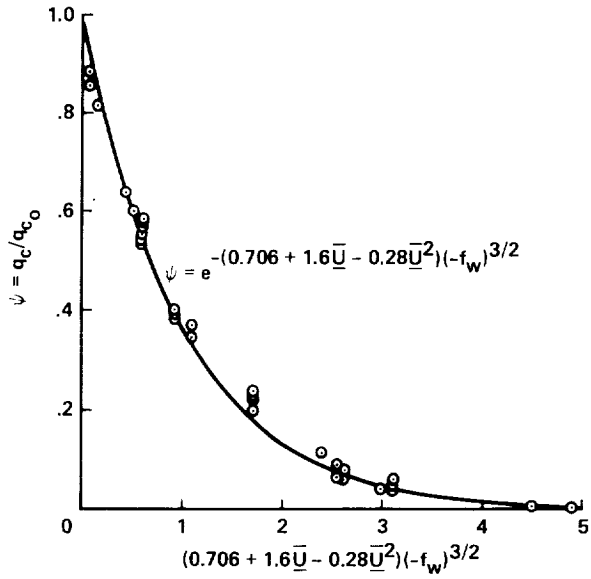

Figure 8-4.– General correlation of result of blowing on convection. (The points are identified in table I.)

The flight condition, nose radius, and value of f_w for each point shown in figures 8-3 and 8-4 are listed in table I. Groups of points are numbered consecutively from left to right on the figure. Points within a group are numbered consecutively from top to bottom.

These same results are also compared in figure 8-5 with the linear ψ approximation of reference 9 and quadratic ψ approximation of reference 14. The points on the figure correspond to our solutions listed in table II, where now the points are simply numbered from left to right in figure 8-5. In the figure, if the constant 0.49 in the linear approximation corresponding to Teflon (which would be 0.5 for phenolic nylon (ref. 9)) is changed to 0.6 (mentioned by ref. 9 as obtained from refs. 10-12), the fit is improved for the initial part of the data out to about $H_s m/(-q_{c_o})$ equal to unity. Clearly, however, it cannot be made to fit the results beyond unity.

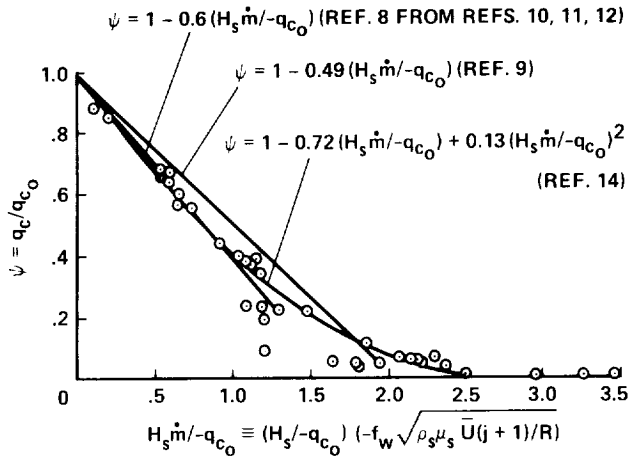

Figure 8-5.– Present results compared with other correlation formulas. (The points are identified in table II.)

The quadratic expression of reference 14 fits the present result well for $H_s\dot{m}/(-q_{c_o})$ equal to unity also, but not beyond. That approximation is set to zero when $H_s\dot{m}/(-q_{c_o})$ is 2.5. However, three points are shown to the right of 2.5 for which $\psi \neq 0$. Subsequently, during the examination of special conditions which minimize total heating rate, it will be important to have a simple correlation which must differ from zero at the high mass addition rates, for if ψ were zero, the radius which minimizes total heating would be that which minimizes radiative heating, namely, zero. The exponential correlation (eq. (2)) will be especially useful in that regard.

The two approximations were obtained from relatively low-speed results for which the air was either dissociated or inert, and it is not surprising to see that they do not fit the present results which include (among other differences) thermodynamic and transport properties of partially ionized air and are extended to higher values of $H_s\dot{m}/(-q_{c_o})$.

The simple expression, equation (2), describing the effects of mass addition on convective heating at high speeds can now be applied with other information to the special case of mass addition by ablation.

TABLE II.– CONDITIONS FOR POINTS SHOWN IN FIGURE 8-5

Point	p_s, atm	$\overline{U}$	R, ft	$-f_w$
1	1	4.1	0.01	0.1
2	1	4.1	1	.1
3	1	5	1	.2
4	1	5	.1	.5
5	1	5	1	.4
6	1	5	.25	.5
7	.1	5	5	.5
8	1	5	.5	.5
9	1	5	1	.45
10	1	5	1	.5
11	1	5	2	.5
12	10	4	.1	.5
13	1	4	1	.5
14	1	5	.1	1
15	1	5	1	.75
16	10	4	.25	.5
17	1	3	1	.5
18	1	5	.25	1
19	1	4	.01	1
20	.1	5	5	1
21	1	5	.5	1
22	1	5	1	1
23	1	5	.1	1.5
24	1	5	.25	1.5
25	.1	5	5	1.5
26	1	5	1	1.25
27	1	5	.5	1.5
28	10	4	.1	1
29	1	4.1	1	1
30	1	4	1	1
31	1	5	1	1.5
32	10	4	.25	1
33	1	3	1	1
34	1	5	1	2
35	1	4	1	1.5
36	10	4	.25	1.5

ABLATION

General Relations for Ablation Quantities

Subliming ablators are attractive for heat protection because of heat absorption due to vaporization and the heat blockage effect in the boundary layer. Moreover, high-temperature subliming ablators have still another asset—the rejection of heat by reradiation.

On the other hand, at conditions corresponding to subsatellite speeds, subliming ablators have at least one liability from the heat-rejection point of view. A theoretical study of Scala (ref. 17) shows that reactions between air and a graphite surface impose a significant heat load on the vehicle. Theoretical studies by Hartnett and Eckert (ref. 18) and Cohen, Bromberg, and Lipkis (ref. 19) show enhanced convective heating caused by gas-phase reactions between air and ablated vapors. Experimental results of Vojvodich and Pope (ref. 20) confirm that both heterogeneous and homogeneous combustion between air and charring ablators impose a heat load comparable to the net convective heating ($q_{c_0}\psi$) at low levels of shock-layer pressure (10^{-3} to 10^{-2} atm) and driving enthalpies up to about 8000 Btu/lb_m. However, they show that the relative importance of combustion diminishes with increasing driving enthalpy and increasing pressure level. Very likely, the reason for diminished importance of surface reactions between air and ablation material is that higher injection rates prevent air from reaching the surface at the more extreme conditions. An analogous phenomenon was studied theoretically by Chung (ref. 21) in which he showed that heterogeneous recombination reactions are inhibited by air transpiration at a cold wall, preventing dissociated shock-layer air from reaching the surface. Further, the relative importance of energy release by gas phase reactions between air and injected species is diminished, probably because of the increased energy release by recombination reactions of air components themselves at the more severe conditions.

Thus we assume that at the higher levels of shock-layer pressure (10^{-1} to 10 atm) and higher enthalpies (20,000 to 50,000 Btu/lb_m) with which the present study is concerned, one need not sort out gas-phase combustion reactions from other recombination reactions. So, we appropriate Lees' argument mentioned previously and neglect the details of the combustion reactions, but consider for practical purposes that their effects are included implicitly in q_c, the convective heating results.

At high flight speeds, radiative heating must be included with convective heating as causing ablation. The ablation rate for a given vaporizing material is related to the actual total heating flux, q_T, by (see eq. (45) in Chapter 4)

$$\rho_w v_w = \dot{m}_w = -q_T/\left(h_{m_w} - h_{m_{interior}}\right) \tag{5}$$

where v_w is the mass average velocity at the wall, h_{m_w} is the enthalpy of the material gases at the wall, $h_{m_{interior}}$ is the enthalpy of the unheated solid, and the minus sign arises from the convention that positive flux is outward from the surface (that is, q means flux; it will be represented by a negative number if the wall is receiving heat). Now we define the intrinsic heat of ablation as

$$h_a = h_{m_w} - h_{m_{interior}} \tag{6}$$

The definition of the mass averaged velocity, v_w, applied at the wall can be written

$$\dot{m}_w = \rho_w v_w = (\rho_{air} v_{air})_w + (\rho_m v_m)_w \tag{7}$$

where v_{air} and v_m are the absolute velocities of the air and material gases. In order for air not to penetrate the surface, $(\rho_{air} v_{air})_w = 0$. Then combining equations (5)-(7) yields

$$-q_T = \dot{m} h_a \tag{8}$$

where the subscript w has been dropped from $\dot{m}$. Moreover, $\dot{m}$ refers only to ablated species.

Let q_r be the net radiative heat flux accepted by the wall. It is a combination of the accepted incident radiative flux from the gas and the reradiated flux from the wall; thus

$$q_r = q_{r_g} + \varepsilon_w \sigma T_w^4 \tag{9}$$

where ε_w is the surface emissivity, and σ is the Stefan-Boltzmann constant. (See also eqs. (56) and (64) of Chapter 6, and eq. (49) of Chapter 7.)

To express q_T in a simple way, assume that (1) there is no coupling between radiative and convective heating rates (a very reasonable assumption for the application to moderate sized bodies made subsequently) and (2) q_{r_g} is not a strong function of $-f_w$ or mass addition rate (which will be verified for conditions of special interest in the next section), and that (3)

$$q_{r_g} = -\alpha_w B R \tag{10}$$

where B is a constant for a given flight condition and α_w is the surface absorption coefficient. Numerical solutions indicate that, for purposes of the estimates in this section, equation (10) is a good approximation even though the flow field is nonisoenergetic, as long as B is obtained from the nonisoenergetic solutions at a given flight condition. Because no coupling is assumed, we can use the simple, no-blowing, convective-heating correlation (which, by the way, excludes external vorticity effects) of Hoshizaki (ref. 6), which can be put in the form

$$\frac{q_c}{\psi} = q_{c_o} = -4.03\times10^{-5}(2\varepsilon)^{1/4}\overline{U}^{0.19}(H_s - H_w)\sqrt{\frac{p_s}{R}} \tag{11}$$

where the units on 4.03×10^{-5} are $(lb_f)^{1/2}$ sec/ft$^{3/2}$ and the units on q_{c_o} are lb_f/ft^2 sec. Combining equations (2), (5), and (9)-(11) leads to an expression for total heating rate

$$-q_T = \alpha_w B R - \varepsilon_w T_w^4 + 4.03\times10^{-5}(2\varepsilon)^{1/4}\overline{U}^{0.19}(H_w - H_w)\sqrt{\frac{p_s}{R}}\, e^{-b(-f_w)^n} \tag{12}$$

It is convenient to define

$$
\left.
\begin{aligned}
A &\equiv \frac{\alpha_w B}{h_a \sqrt{\rho_s \mu_s \bar{U}(j+1)}} \\
C &\equiv \frac{4.03\times10^{-5}(2\varepsilon)^{1/4}\bar{U}^{0.19}(H_s - H_w)\sqrt{p_s}}{h_a \sqrt{\rho_s \mu_s \bar{U}(j+1)}} \\
D &\equiv \frac{\sigma \varepsilon_w}{h_a \sqrt{\rho_s \mu_s \bar{U}(j+1)}}
\end{aligned}
\right\} \tag{13}
$$

In terms of these quantities, equation (12) becomes

$$
-q_T = h_a \sqrt{\rho_s \mu_s \bar{U}(j+1)} \left[AR + \frac{C}{\sqrt{R}} e^{-b(-f_w)^n} - DT_w^4 \right] \tag{14}
$$

Now if equations (1), (5), and (8)-(11) are combined, a transcendental expression is obtained for the natural blowing rate parameter f_w in terms of R, the flight conditions, and material properties:

$$
-f_w = AR^{3/2} + Ce^{-b(-f_w)^n} - DR^{1/2} T_w^4 \tag{15}
$$

Another quantity of interest is the effective heat of ablation (where the subscript o means without mass addition).

$$
h_{eff} = \frac{-q_{T_o}}{\dot{m}} = -\frac{(q_{c_o} + q_{r_o})}{\dot{m}} \tag{16}
$$

If we assume

$$
q_{r_o} \approx q_r \tag{17}
$$

which is approximately true for the moderate ablation rates which will concern us in this and the next section (and will be demonstrated at the end of the next section), it is simple to show that

$$
\frac{q_T}{q_{T_o}} = 1 - \left[1 - e^{-b(-f_w)^n} \right] \frac{q_{c_o}}{q_{T_o}} \tag{18}
$$

Combining equations (8), (13), (16), and (18) leads to

$$
h_{eff} = h_a \left\{ 1 + \frac{C}{(-f_w)} \left[1 - e^{-b(-f_w)^n} \right] \right\} \tag{19}
$$

where $-f_w$ is obtained from equation (15).

Now it is instructive to specialize some of these ablation relationships still further—to the case of convection only.

Ablation Due to Convection Only

For flight speeds greater than satellite entry speed, both radiative and convective heating are important in determining ablation rates, even for small nose radii (which will be shown subsequently). However, if for the moment convection is assumed to be the only heating mode, and both radiation and reradiation are excluded, we are led to some interesting comparisons. For these conditions, both equations (15) and (19) reduce to simpler forms; thus

$$-f_w e^{b(-f_w)^n} = C \tag{20}$$

and

$$\frac{h_{eff}}{h_a} = e^{b(-f_w)^n} = \frac{1}{\psi} \tag{21}$$

respectively. So we see that for the convective case, both the ablation rate in terms of f_w (eq. (20)) and effective heat of ablation (eq. (21)) for a given material are independent of nose radius and ambient density (or pressure level), but depend only on flight speed (because b is a function of $\overline{U}$ alone (eq. (4)) and C is essentially a function of $\overline{U}$ because in equation (13)

$$(H_s - H_w)\sqrt{p_s/\rho_s\mu_s} \approx (\overline{U}^3/2)\sqrt{\rho_\infty/\rho_s\mu_s}$$

and the last square root is a very weak function of ambient density. Lees (ref. 22) and Bethe and Adams (ref. 23) reached a similar conclusion for melting and glassy ablators at subsatellite speeds; that is, velocity is the important parameter.

It is interesting to compare this f_w and h_{eff} result obtained from ψ that is exponential with respect to $(-f_w)^n$ (eq. (2)) with those obtained from ψ that is linear with respect to $(-f_w)$ of reference 9. The ψ of that paper written in terms of f_w by use of equation (1) is

$$\psi = 1 - \beta\frac{(-f_w)(H_s - H_w)}{q_{c_o}}\sqrt{\frac{\rho_s\mu_s\overline{U}(j+1)}{R}} \tag{22}$$

where β is a constant for a given wall material. The corresponding f_w for convection only (for that paper) obtained from equation (11) is

$$-f_w = \frac{4.03\times10^{-5}(2\epsilon)^{1/4}\overline{U}^{0.19}(H_s - H_w)}{[h_a + \beta(H_s - H_w)]}\sqrt{\frac{p_s}{\rho_s\mu_s\overline{U}(j+1)}} \tag{23}$$

or

$$-f_w = \frac{C}{1 + (\beta/h_a)(H_s - H_w)} \tag{24}$$

while h_{eff} for the linear ψ would be

$$\frac{h_{eff}}{h_a} = 1 + \frac{\beta}{h_a}(H_s - H_w) \tag{25}$$

The comparison of the natural f_w for Teflon as predicted by the two results (eqs. (20) or (22) in (24)) is shown in figure 8-6 (using $\beta = 0.49$ and $h_a = 2.38 \times 10^7$ ft^2/sec^2 from reference 9 for Teflon).[4] It is seen that the two results are in close agreement and that both depend strongly on velocity, but not on pressure. Similarly, the results of h_{eff}/h_a as a function of velocity are in close agreement for convection only (using eqs. (21) and (25)) as shown in figure 8-7.

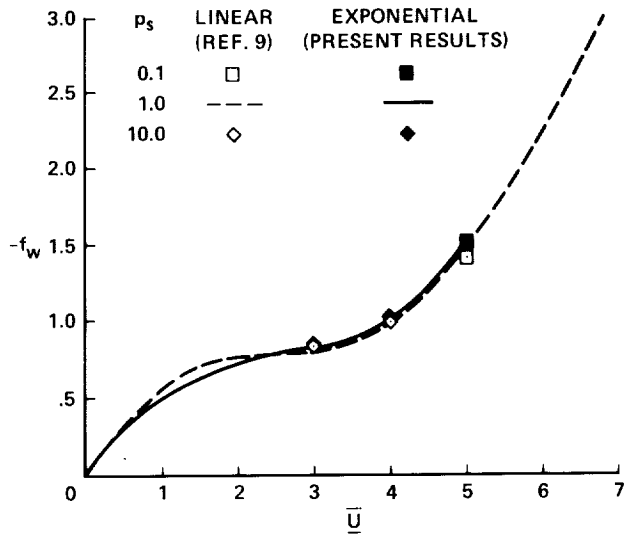

Figure 8-6.– Wall blowing parameter for natural ablation of Teflon at stagnation region—convection only.

[4]In this application and throughout the rest of this chapter, the values of b and n for a given flight condition were obtained by passing equation (2) through results from the two flow-field solutions having the highest values of $-f_w$. Numerically, b and n are slightly different from equations (3) and (4) for b and 3/2 for n obtained for the general correlation.

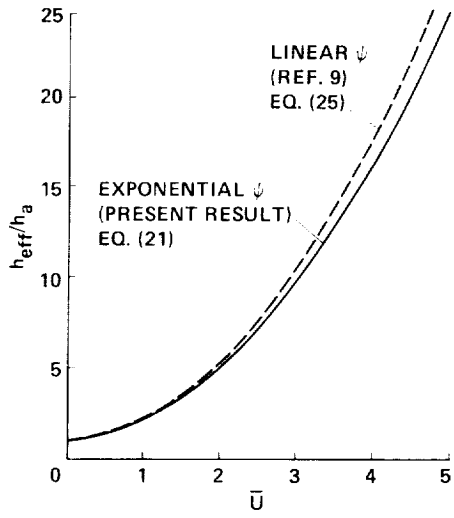

Figure 8-7.– Effective heat of ablation of Teflon (convection only).

The agreement between the two methods might indicate that $e^{b(-f_w)^n}$ of equations (20) and (21) equals $1 + (\beta/h_a)(H_s - H_w)$. At first glance one might suspect that these natural blowing rates are small enough to be on the initial part of the ψ curve where the exponential can be replaced by the first two terms of its series. It turns out that this is not the case, as can be seen in figure 8-2. The solid curves and dashed lines correspond to the exponential and linear ψ (to eqs. (2) and (22)), respectively, for the flight speeds shown. Although agreement between the solid curve and dashed line is better at the lower speeds, in neither case is the solid curve well represented by the dashed line except at the one point where they intersect. That intersection just happens to occur very near the natural value of f_w in each case. Thus the apparent agreement in the results does not imply any general agreement in the function ψ but, rather, is considered to be fortuitous.

Now we turn again to the case of ablation caused by both radiative and convective heating to examine some special conditions. In this way we can acquire some notions of the behavior of various phenomena under definable favorable conditions.

Conditions at Minimum Heating Rate With Ablation

Because of the many combinations of variables, parameters, and phenomena associated with the ablation problem, it is convenient to seek an optimum condition, in terms of minimizing total heating rate or total mass loss rate of a given material at each flight condition, and then present some of the other quantities of interest correspondingly. In this way we can acquire some notions of the behavior of various phenomena under definable favorable conditions.

Nose radius and ablation rate for minimum heating rate– Equation (14) shows that at a given flight condition, convective heating rate becomes large with small R whereas radiative heating rate becomes large at large R.[5] Thus there is an intermediate value of R for which total heating rate is a minimum. This is illustrated graphically for one flight condition in figure 8-8. The family of solid light curves is calculated by the use of equation (12) for specified values of f_w, and represents approximately

[5]See "Approximate heating generalizations" following figure 7-16 for further discussion.

the flow-field solution results. The family of dashed curves is calculated for Teflon by use of equations (8) and (1), also for specified values of f_w (the physical properties used for Teflon and phenolic nylon are listed in table III). The intersection of a line of each family corresponding to one value of f_w denotes a combination of q_T, R, and f_w that satisfies both the flow-field results and the material behavior. The heavy solid curve is the locus of such intersections. Its minimum gives the optimum nose radius R*, which minimizes total heating rate (and total ablation rate) for Teflon for this flight condition. Thus R* is 0.109 ft and the ablation rate is given by $-f_w = 1.94$ in this example. The right branch of the heavy curve shows an interesting result. That is, for a nose radius half again as large as R*, convective heating has been essentially eliminated by strong ablation, and therefore q_T increases linearly with R and is independent of ablation rate ($-f_w = 3$ line coincides with $-f_w = \infty$), as it should be for radiative heating only, according to the approximation of equation (10). Correspondingly, ablation is caused by radiative heating alone and its rate must be increasing in proportion to q_T, and thus R, in accord with equation (8). This points out the potential importance of reflecting ablative surfaces for heat protection for radii greater than R*.

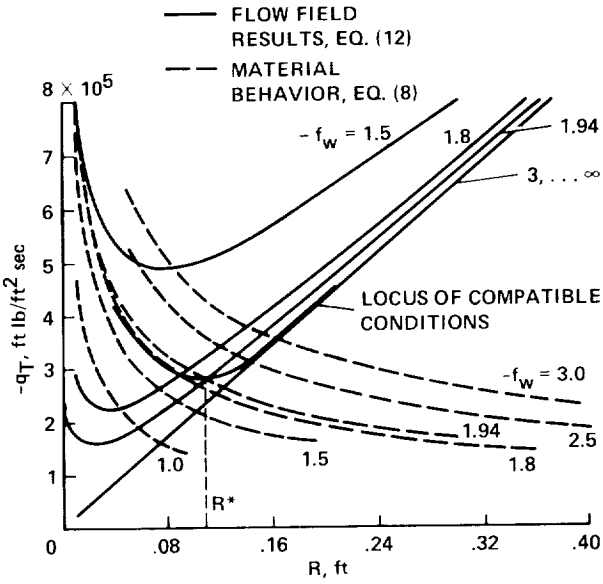

Figure 8-8.– Optimum nose radius for Teflon at $\overline{U}$ = 50,000 ft/sec, p_s = 1 atm ($\alpha_w = \varepsilon_w = 1$).

Analytically, R* and f_w for a specific material and flight condition are obtained as follows. The partial derivative of q_T with respect to R (obtained by differentiation of eq. (14) noting that f_w is a function of R by eq. (15)) is set to zero. After some algebra, the expression

$$f_w + \frac{Ce^{-b(-f_w)^n}}{2}[bn(-f_w)^n + 3] - DT_w^4 R^{1/2} = 0 \qquad (26)$$

is obtained. The simultaneous solution of equations (15) and (26) yields the optimum nose radius and natural ablation rate (f_w) for a given material and flight condition.

It can be noted that for no reradiation ($DT_w^4 R^{1/2}$ negligible), equation (26) is uncoupled from equation (15) and the former can be solved directly for f_w after which the latter can be used to obtain the optimum R. Thus we obtain the result that f_w is independent of the radiative properties of the gas expressed by A in equation (13). Although f_w depends only on the convective heating properties of

the gas (expressed by C in eq. (13) which appears in eq. (26)), it differs from the f_w for convection only (eq. (20)) for the following reasons. If equation (15) is satisfied by $AR^{3/2} \neq 0$ by use of the f_w obtained from equation (26), it cannot be satisfied for $AR^{3/2} = 0$ by the same f_w. Moreover, if radiation is zero, we cannot use equation (26) to calculate f_w, but must revert to equation (20).

TABLE III.– PROPERTIES OF ABLATING SURFACES[a]

Material	h_a, ft^2/sec^2	T_w, K	ε_ω	α_ω
Teflon[b]	2.38×10^7 (9)	1000	1 and 0.5	1 and 0.5
Phenolic nylon	3.755×10^7 (9)	3700 (50)	0.6 (50)	0.6 (50)

[a]Values in the table are estimates made from information in the references shown in parentheses.

[b]The temperature shown for Teflon is higher than the 800°F (or 700 K) given by reference 9. However, it is of no consequence because reradiation from the higher temperature is still negligible. It should be noted that in applying our ψ results to Teflon, we have not made any allowance for the presence of a finite asymptote (see footnote 2). If indeed a finite asymptote does exist at hypervelocity, we must consider our Teflon results to apply instead to a material which has the properties shown above but which does not have a finite ψ asymptote.

For radiation different from zero but negligible reradiation, h_{eff} is independent of the radiative flux because f_w used in equation (19) is independent of radiative properties. The same is true for ψ because of equation (2). On the other hand, the optimum R obtained from equation (15) depends on the radiative properties. Of course, $\dot{m}$ depends on the radiative properties because it depends on R (eq. (1)), and the same is true for both q_c (eq. (11)) and q_r (eqs. (9) and (10)).

The optimum nose radius with convection, radiation, and reradiation obtained from equations (15) and (26) is shown as a function of flight speed in figure 8-9 for Teflon and phenolic nylon. It can be seen that the optimum nose radius diminishes with increasing shock-layer pressure at a given flight speed. On the other hand, the optimum nose radius increases as flight speed is diminished, shock-layer pressure level being constant. These trends can be related to actual entry trajectories, by noting (ref. 2, fig. 1) that typical trajectories consist of essentially a path of increasing shock-layer pressure at constant velocity followed by a path of diminishing velocity at constant pressure. Now if the major heating occurs at constant velocity (the case of plunging probes), total heating rates could be minimized only by artificially tailoring the nose shape (for example, by pushing concentric rods of progressively smaller radii out the front of the vehicle in a programmed sequence—a refinement of a suggestion by H. J. Allen (ref. 24)). On the other hand, if the major heating occurs at constant shock-layer pressure (typical of g-limited entry), the problem of minimizing total heating rates is simplified because R grows by ablation naturally in the direction of the growing optimum.

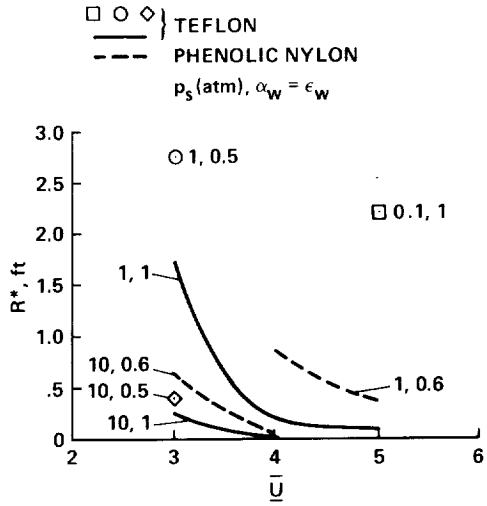

Figure 8-9.– Optimum nose radius for ablation.

The wall absorptivity, α_w, is important to both charring and noncharring ablators because it influences the amount of radiant heat accepted from the gas cap and thus R*. In figure 8-9, if α_w is diminished by 50% for Teflon (noncharring), R* is increased by about 50%.

The wall emissivity, ε_w, is important to high-temperature charring ablators for which reradiation is an important heat-rejection mechanism. For phenolic nylon, reradiation is partly responsible for a larger optimum nose radius than that of Teflon (for which reradiation is negligible because of its low vaporization temperature)—by about a factor of 3 in the speed range 40,000-50,000 ft/sec, as can be seen in the figure. The phenolic nylon calculation for $p_s = 1$ atm was not extended to lower speed because of the uncertain wall temperature; that is, the wall temperature becomes a function of the heating rate at less severe heating conditions.

The ablation rate, in terms of f_w, corresponding to optimum heating rate conditions is shown as a function of flight speed for various pressure levels and absorptivities for Teflon and phenolic nylon in figure 8-10. The heavy lines and symbols represent minimized total heating-rate conditions, while the light lines represent the result for convection only (shown previously in fig. 8-6 for Teflon). It is important to point out that the difference between the total-heating heavy lines and convective-heating light lines does not represent the contribution of radiative heating. When minimum total heating rate is considered, there is a complete rearrangement of convective and radiative contributions. The result is that the radiative contribution is usually larger (sometimes much larger) than the convective contribution (which will be demonstrated subsequently in fig. 8-15). The result of the sum of the two readjusted heating components on f_w is shown by the heavy lines in figure 8-10.

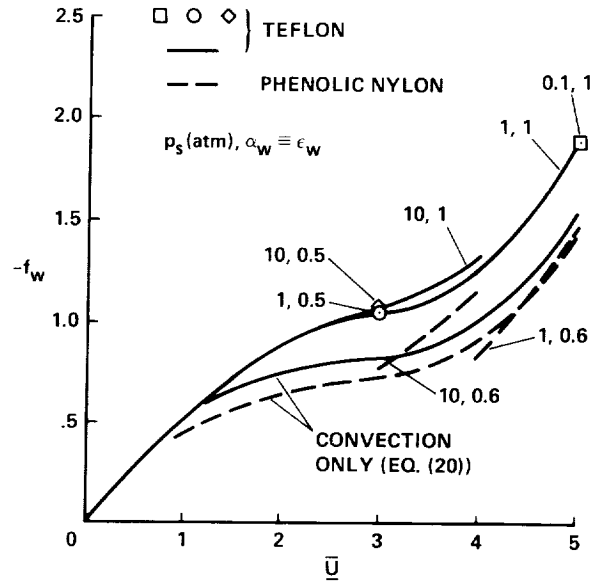

Figure 8-10.– Blasius wall-blowing parameter corresponding to ablation with optimum nose radius.

It is especially interesting to note that for Teflon, optimum f_w is a very weak function of both absorptivity and pressure level. This will have consequences in figure 8-12, where it will be remarked upon.

The ratio of the surface mass flux to free-stream mass flux is related to f_w by the Reynolds number. Thus

$$\frac{\dot{m}}{\rho_\infty \bar{U}} = -f_w \sqrt{\frac{(j+1)}{\varepsilon Re}} \tag{27}$$

where Re is the Reynolds number $\rho_\infty \bar{U} R/\mu_s$. It should be mentioned that $\varepsilon^{1/2}$ is almost invariant with flight speed (between 30,000 and 50,000 ft/sec) at a given level of shock-layer pressure. It only varies at the worst from 0.233 to 0.278 as pressure level changes from 0.1 atm to 10.0 atm.

The mass flux ratio of Teflon is presented in figure 8-11 for optimum conditions. The location of the point corresponding to 0.1 atm indicates that relationships at optimum conditions are not systematic in a simple way. The surface mass flux varies from 2.5 to 25% of the free-stream mass flux between 30,000 and 50,000 ft/sec. Some approximate calculations show that it is reasonable to extrapolate this result to 70,000 ft/sec. The result is that the mass flux ratio is still less than 0.5 for optimum conditions. This is in sharp contrast to the values in excess of unity for entry of some meteors for which the nose radius is very different from R* (Přibram meteor, for example, which likely has a radius of the order of a meter, ref. 25).

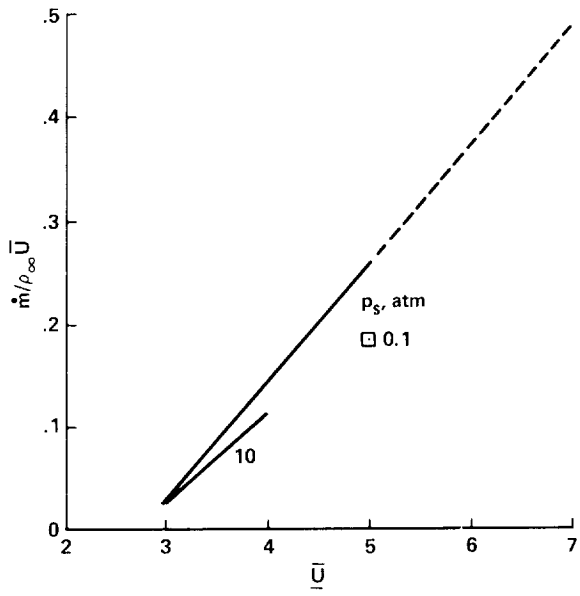

Figure 8-11.– Mass addition ratio for optimum conditions (Teflon, $\alpha_w = 1$).

In fact, it is apparent from the present optimum results for $\overline{U} = 50{,}000$ ft/sec and $p_s = 1$ atm that if nose radius is increased from the optimum of 0.109 to only 0.5 ft, the mass loss ratio will exceed unity as a result of radiative heating alone.

Now that we have the nose radius which minimizes total heating rate, and the corresponding ablation rate, we can examine several other interesting quantities corresponding to these conditions.

Effective heat of ablation– The ratio of the effective heat of ablation to the intrinsic heat of ablation is calculated by use of equation (19) and is presented in figure 8-12. The ratio depends strongly on velocity, but is relatively insensitive to pressure level (altitude) and, for the case of Teflon, surface absorptivity. The last is a consequence of the insensitivity of f_w to α_w shown in figure 8-10, and the fact that h_{eff} is very strongly dependent on f_w in equation (19). The ratio h_{eff}/h_a subject to combined radiative and convective heating is less than that obtained from convection alone, which can be seen by comparing figure 8-12 with figure 8-7.

In spite of the fact that h_{eff}/h_a in figure 8-12 is smaller for phenolic nylon than for Teflon, the actual h_{eff} for phenolic nylon is larger. At 50,000 ft/sec, the ratio of effective heat of ablation of phenolic nylon to that of Teflon is 1.13, which includes the reradiation effects. (It should also be remembered that the phenolic nylon is not ablating as rapidly as Teflon for these optimum conditions.)

Effect of mass addition on standoff distance– The ratio of standoff distance with optimum mass addition (and nose radius) to that without mass addition, δ_o, was obtained by solving the flow-field equations using values of R^* and f_w obtained from figures 8-9 and 8-10. The result is shown in figure 8-13 for Teflon. For speeds below 30,000 ft/sec, where mass addition rates are low (3% of free-stream mass flux, fig. 8-11), the standoff distance with blowing is actually less than that without blowing (ratio is about 0.94). This interesting effect occurs at very low mass addition rates over a broad flight range and may be attributable to a cooling effect that increases the flow-field density (and diminishes standoff distance) more than enough to overcome the space required for the increase in mass flow in the

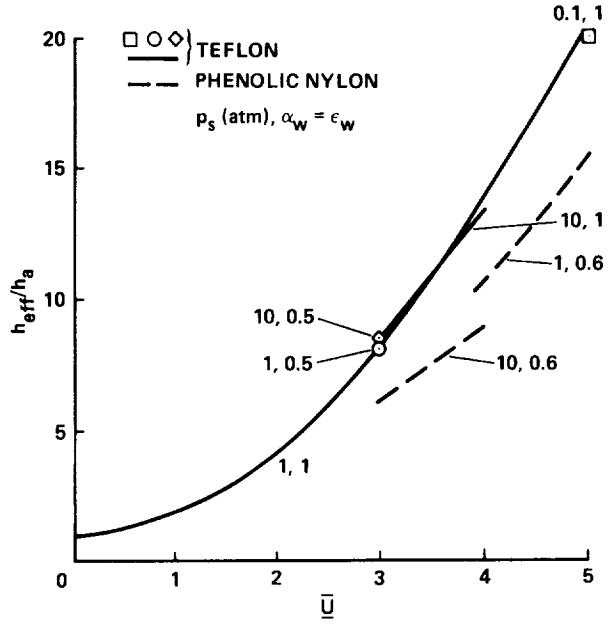

Figure 8-12.– Effective heat of ablation corresponding to natural ablation for optimum conditions.

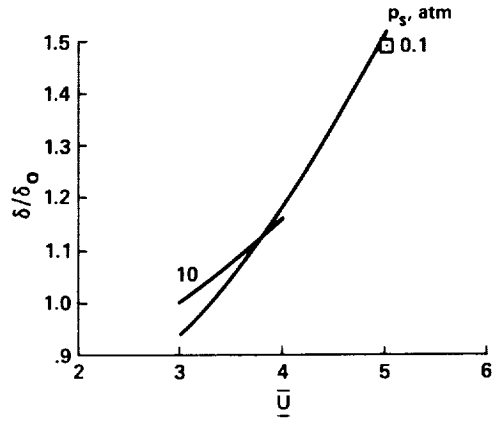

Figure 8-13.– Ratio of standoff distance with blowing to that without blowing for optimum conditions (Teflon, $\alpha_w = 1$).

flow field. At higher speeds, and thus higher ablation rates, the standoff distance is enhanced by ablation. It is seen that for optimum conditions, the shock layer is thickened by about 50% at a speed of 50,000 ft/sec.

Effect of mass addition on radiative heating– Mass addition can influence gaseous radiative heating flux in two ways: (1) by altering the standoff distance and temperature distribution in the flow field (it should be mentioned that gaseous radiation reabsorption is negligible in the regime being considered), and (2) by adding chemical species to the flow field which radiate differently from air. To examine the first effect, due to alteration of flow-field structure, the foreign species was assumed to

radiate like air. The resulting incident gaseous radiant flux at the wall as obtained from flow-field solutions corresponding to the optimum R^* and f_w of Teflon is compared with the no-ablation value in figure 8-14. In the flight regime studied, the maximum effect of the ablation on radiant flux is an increase of about 17% for these optimum conditions. This is in sharp contrast with the very large effects on convective heating presented earlier and supports the approximations of equations (10) and (17). For example, for a flight condition in which radiative flux was changed 17%, ablation diminished the convective flux by two orders of magnitude (to 0.8% of its nonablation value).

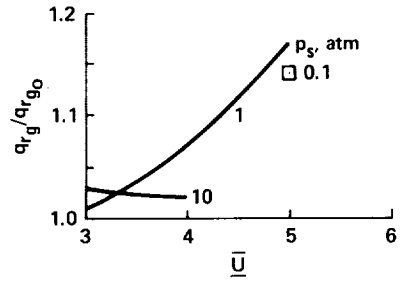

Figure 8-14.– Ratio of incident gaseous radiation flux with ablation to that without ablation at optimum conditions (Teflon, $\alpha_w = 1$).

To examine the second effect, that of introducing species which radiate differently from air, α (the rate of absorption in the foreign species relative to that of air (Chapter 7)) was specified to be different from unity. Briefly, the result is that if a foreign gas that radiates twice as strongly as air ($\alpha = 2$) is introduced at the same rate, the radiative flux is enhanced at the most by only 5% over the air value. If the foreign gas radiates 10 times as strongly as air ($\alpha = 10$), the radiative flux is enhanced at the most by about 50% over its airlike value. Finally, the influence of these radiative properties that differ from those used in estimating optimum conditions on the optimum conditions themselves is as discussed previously. That is, to the extent that reradiation is negligible, there is no effect on f_w and h_{eff}. However, the effect on R^* is to reduce it by a factor of $1.5^{-2/3}$ (or 0.76) and the effect on $\dot{m}$ is to increase it by a factor of $1.5^{1/3}$ (or 1.14) at the worst by virtue of equations (15) and (1), respectively.

Comparison of radiative and convective heating– The ratio of the radiative to convective heating rate was obtained from solutions of the flow-field equations in which R^* and f_w corresponded to minimum heating conditions for Teflon. The result is that radiation exceeds convection by a factor of from 2 to 9 as shown in figure 8-15. The importance of convection increases as the level of shock-layer pressure is increased. For phenolic nylon, the results are almost the same without reradiation. That is, q_{r_g}/q_c is greater than unity. However, because of reradiation, the ratio q_r/q_c is less than unity except at high pressures ($p_s = 10$ atm). In any event, the gaseous radiant flux incident on the wall is considerably larger than the convective flux for either Teflon or phenolic nylon at optimum conditions.

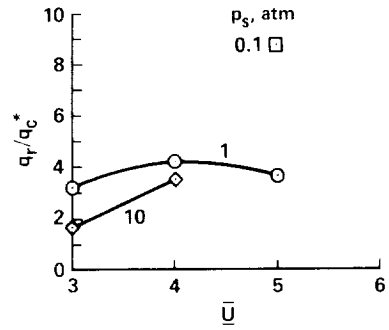

Figure 8-15.– Comparison of radiative and convective heating at optimum conditions (Teflon, $\alpha_w = 1$).

Effect of mass addition on surface shear stress– In figure 8-16, the surface shear stress divided by distance from the stagnation point is shown as a function of flight speed for various pressure levels for Teflon at optimum conditions. It was obtained from the flow-field solutions by use of the relationship

$$\frac{\tau_w}{x} = \varphi_w \left(\frac{\bar{U}}{R}\right)^{3/2} \sqrt{(j+1)\rho_s \mu_s}\, f'_w \tag{28}$$

which can be derived by use of the transforms in Chapter 7. Generally, wall shear stress increases with velocity and shock-layer pressure level. For reasonable values of x, the shear stress is not excessive (even at $p_s = 10$ atm, the surface shear stress per foot is of the order of standard atmospheric pressure per foot for optimum conditions, and the optimum size is considerably less than a foot). The shear stress for phenolic nylon would be slightly larger than that for Teflon because the mass addition rate for the former is lower at a given flight condition.

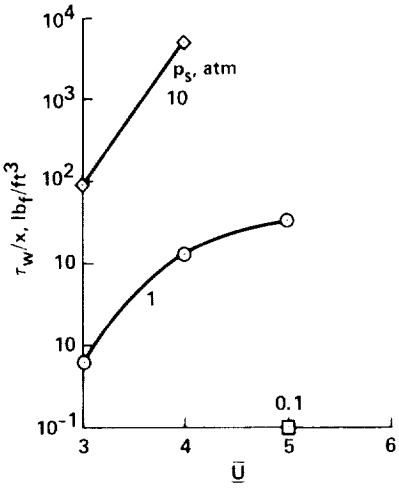

Figure 8-16.– Stagnation region shear stress at optimum conditions (Teflon, $\alpha_w = 1.0$).

Of course, without mass addition, the shear stress would be considerably higher. The ratio of wall shear stress with mass addition to that without mass addition is shown in figure 8-17 for Teflon under optimum conditions. It is noted that the ratio is only 0.035 at $\bar{U}$ = 50,000 ft/sec and $p_s = 1$ atm.

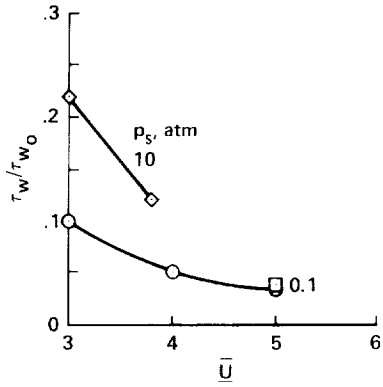

Figure 8-17.– Ratio of stagnation region shear stress with ablation to that without ablation at optimum conditions (Teflon, $\alpha_w = 1$).

Comments on validity– Our optimum-condition considerations have led to results of small nose radii for which the assumption of a flow field in chemical equilibrium may be doubtful. In spite of the fact that the chemistry and some of the thermodynamic and transport properties may be grossly in error for nonequilibrium flow fields, the basic structure of the flow field (velocity and enthalpy profiles) is not expected to be seriously in error. The reason is twofold: First, the analysis in the appendix of reference 26 shows that in the absence of transport phenomena, the enthalpy profile is almost unaffected by large departures from chemical equilibrium. Second, the velocity and enthalpy profile results of reference 27, which include both chemical nonequilibrium and transport phenomena, do not differ in a significant way from those of reference 2 or this chapter for chemical equilibrium (excluding low Reynolds number results).

Moreover, the convective heating is not likely to be very much in error because the wall is expected to be catalytic, and thus nonequilibrium convective heating would be essentially the same as that for equilibrium since recombination would occur at or near the wall in either case.

We have noted that at the minimum heating condition, radiative heating dominates. Our radiative heating estimates could be in error for several reasons. Although the neglect of nonequilibrium radiation is a potential source of error for the small optimum nose radii, the present estimate is that it is not an important effect as gaged by the results of reference 28. We have already noted that there is some change in radiative heating caused by flow-field distortion and the presence of foreign species which radiate differently from air. Moreover, there is still considerable uncertainty in the radiative properties of air itself (the radiative properties of air given by ref. 29 may be high by a factor of 2 according to ref. 30) and in the absorptivities and emissivities of the surface material.

The effect of underestimating the radiative properties on optimum conditions has been noted in the section on effect of mass addition on radiative heating. Briefly, we now examine the effect of overestimating radiative properties by a factor of 2. As before, f_w, h_{eff}, and ψ are unchanged (for a material which does not reradiate importantly). But R^* is enhanced by about 60%, so m and q_c are diminished by a factor $1.6^{-1/2}$ (or 0.79) by virtue of equations (1) and (11). So both q_r and q_c change, but in such a way that f_w is constant. The error in radiative properties by a factor of 2 has a large effect on R^* (60%); only a 20% effect on q_c and m; and no effect on f_w, h_{eff}, and ψ.

Thus, in spite of the many uncertainties in the flow-field chemistry and in our knowledge of gas properties, the results of the minimized heating-rate study remain meaningful.

MASS ADDITION AND SCALING

To a large extent, experimental studies of high-speed planetary entry problems consist of exposing models to a simulated entry environment in a test facility, such as an arc-heated wind tunnel, a shock tube, or a ballistic range. Experimental results are then scaled to the actual flight conditions by one means or another.

Strictly speaking, we cannot expect to scale flow-field profiles at all because thermodynamic and transport properties used in the flow equations do not scale. However, in this portion of this chapter, we will examine briefly how to scale dimensionless foreign-species profiles approximately for forced mass addition (transpiration) and then specialize the result to natural mass addition (ablation).

Scaling With Arbitrary Mass Addition

It is well known that in order to scale stagnation-region flow fields in general, the Reynolds number should be fixed. In order to scale foreign-species concentration profiles, the mass addition rate must also be fixed. Or, because of the Reynolds number factor in the expression relating f_w and $\dot{m}/\rho_\infty \bar{U}$ (and in view of the small variation in $\varepsilon^{1/2}$ noted earlier), we may simply say that in order to scale mass addition effects, both f_w and $\dot{m}/\rho_\infty \bar{U}$ must be fixed. We will illustrate this by use of flow-field solutions.

The main points of the demonstration are briefly as follows. In figures 18-21, solutions corresponding to the conditions shown in table IV are presented in which either, but not both, f_w or $\dot{m}/\rho_\infty \bar{U}$ is the same between pairs of examples (assuming that these quantities can be varied at will). These results can be compared with those for which both f_w and $\dot{m}/\rho_\infty \bar{U}$ (or Re) are constant, shown in figures 8-22 through 8-25.

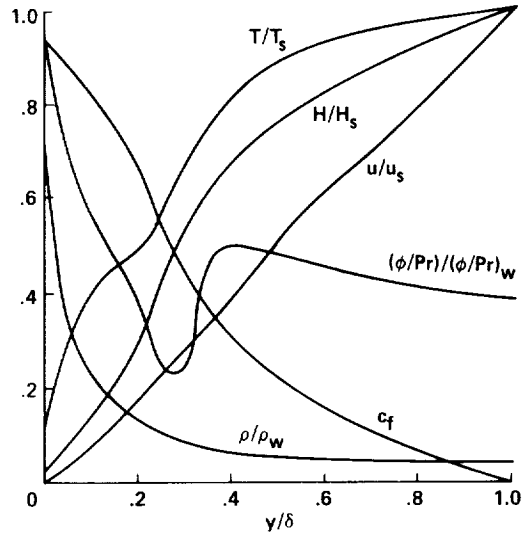

Figure 8-18.– Flow-field profiles; $\bar{U}$ = 41,000 ft/sec, p_s = 1 atm, R = 0.01 ft, $f_w = -1$.

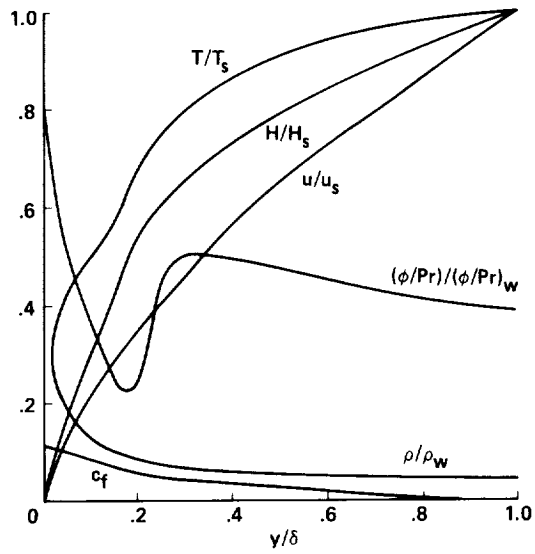

Figure 8-19.– Flow-field profiles; $\overline{U}$ = 41,000 ft/sec, p_s = 1 atm, R = 0.01 ft, f_w = –0.1.

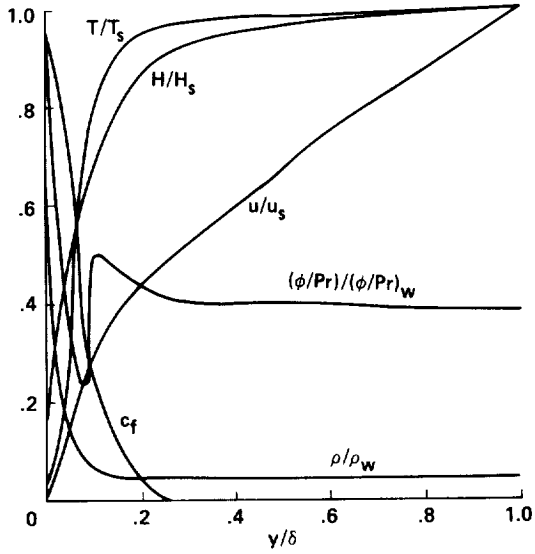

Figure 8-20.– Flow-field profiles; $\overline{U}$ = 41,000 ft/sec, p_s = 1 atm, R = 1 ft, f_w = –1.

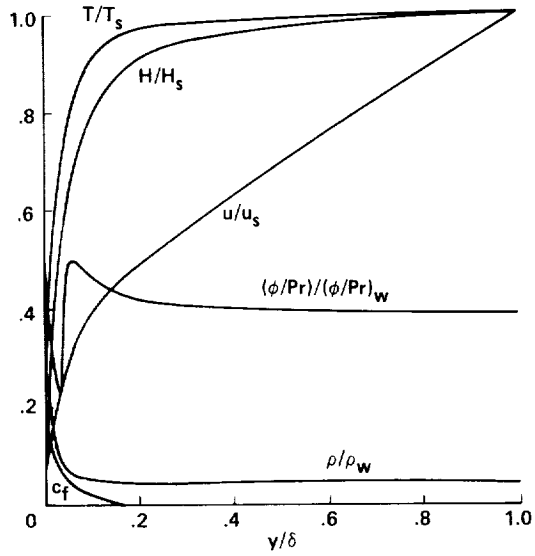

Figure 8-21.– Flow-field profiles; $\overline{U}$ = 41,000 ft/sec, p_S = 1 atm, R = 1 ft, f_w = –0.1.

TABLE IV.– SCALING FOREIGN-SPECIES EXAMPLES

Figure	$\overline{U}\times10^{-4}$, ft/sec	p_S, atm	$-f_w$	$\dot{m}/\rho_\infty\overline{U}$	R, ft	Re
18	4.1	1	1.0	0.5	0.01	1.14×10^2
19	4.1	1	.1	.05	.01	1.14×10^2
20	4.1	1	1.0	.05	1.0	1.14×10^4
21	4.1	1	.1	.005	1.0	1.14×10^4
22	3	1	.3	.05	.063	1.19×10^3
23	4.1	10	.3	.05	.011	1.05×10^3
24	4.1	1	.3	.05	.1	1.14×10^3
25	5	1	.3	.05	.074	1.26×10^3

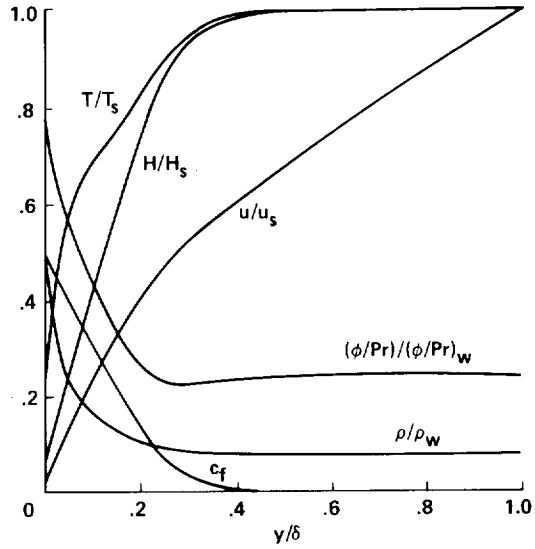

Figure 8-22.– Flow-field profiles; $\overline{U}$ = 30,000 ft/sec, p_s = 1 atm, R = 0.063 ft, f_w = –0.3.

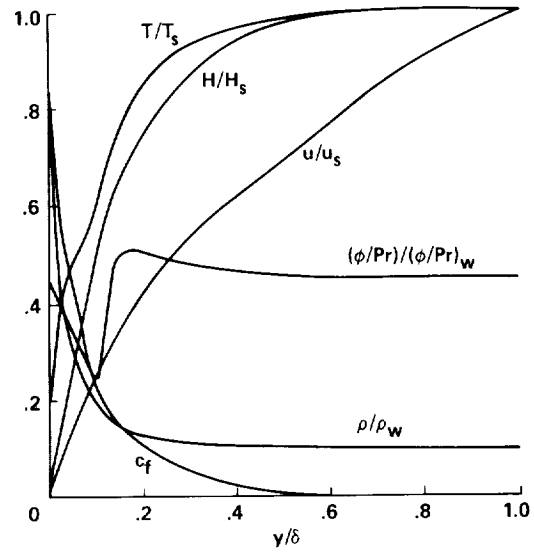

Figure 8-23.– Flow-field profiles; $\overline{U}$ = 41,000 ft/sec, p_s = 10 atm, R = 0.011 ft, f_w = –0.3.

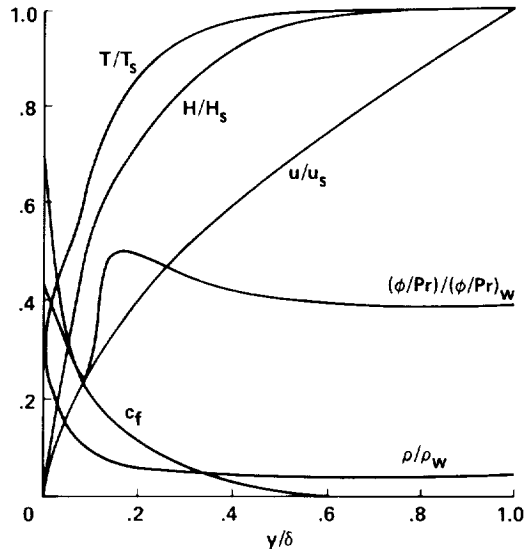

Figure 8-24.– Flow-field profiles; $\overline{U}$ = 41,000 ft/sec, p_s = 1 atm, R = 0.1 ft, f_w = –0.3.

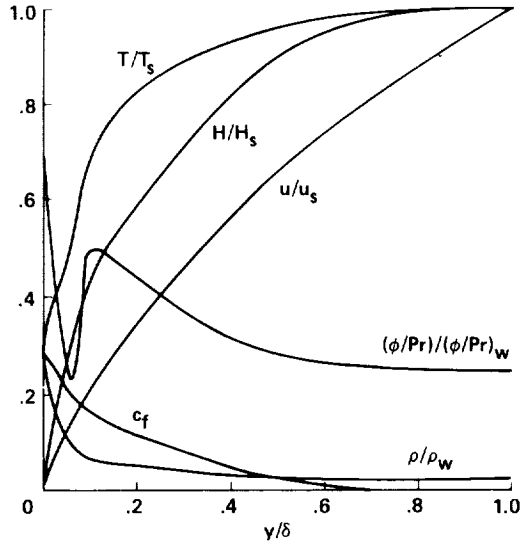

Figure 8-25.– Flow-field profiles; $\overline{U}$ = 50,000 ft/sec, p_s = 1 atm, R = 0.074 ft, f_w = –0.3.

The foreign-species profiles corresponding to these two groups of figures are summarized in figures 8-26(a) and (b), respectively. Obviously, the concentration profiles resulting from fixing only one of the parameters do not scale, as can be seen in figure 8-26(a). The figure shows that f_w essentially controls the foreign-species concentration at the wall, while Reynolds number determines its penetration into the flow field. Thus, if both f_w and Re (or $\dot{m}/\rho_\infty U$) are fixed, scaling should be much improved, as is evidenced by the c_f profiles summarized in figure 8-26(b). Moreover, since fixing f_w and $\dot{m}/\rho_\infty U$ essentially preserves the Reynolds number (the slight variations in Re in table IV are caused by variations in $\epsilon^{1/2}$ in eq. (27)), the velocity profiles of the second set (figs. 8-22 through 8-25) are scaled;

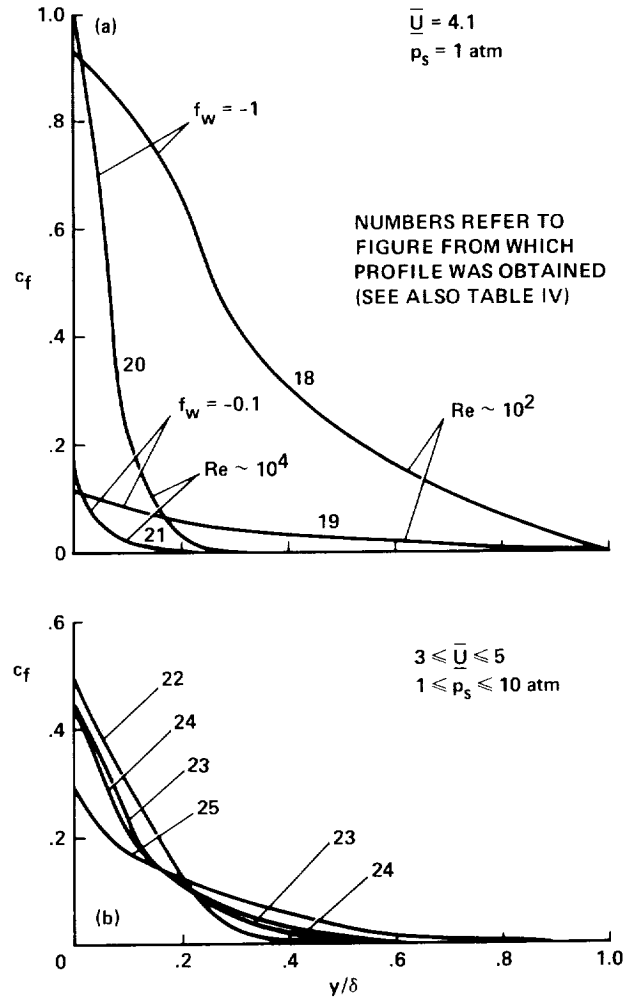

Figure 8-26.– Foreign-species concentration profiles. (a) Either f_w or $\dot{m}/\rho_\infty \bar{U}$ fixed. (b) Both f_w (= –0.3) and $\dot{m}/\rho_\infty \bar{U}$ (= 0.05) fixed.

where in the first set (figs. 8-18 through 8-21) they are not. Finally, the enthalpy profiles of the first set exhibit less similarity than those of the second set. The latter are summarized in figure 8-27.

There are additional features of some of the solutions mentioned above which, although secondary to the argument, are worth comment. In figure 8-18, for a flight condition of $\bar{U}$ = 41,000 ft/sec and p_s = 1 atm, a nose radius of 0.01 ft, and a blowing rate f_w = –1.0, both momentum (associated with u/u_s profile) and thermal (associated with H/H_s profile) boundary layers are conspicuously absent. Indeed, the vorticity (slope of u/u_s curve) is approximately constant throughout the flow field. Interestingly, the flow field is far from isoenergetic everywhere; not because of enthalpy depletion by radiation but, rather, by convection. The mass addition rate at the surface is half the free-stream mass flux (table IV), and standoff distance is 90% higher than the no-blowing value (this is the most extreme result we have in both regards). The foreign species completely permeates the flow field, which is important from the point of view of the relative importance of air and ablation species radiation. In this regard, results show that the incident gaseous radiant-heating flux at the wall is enhanced by 49% over the no-blowing value if air is the injected gas (because of the thickened shock layer), but is enhanced by

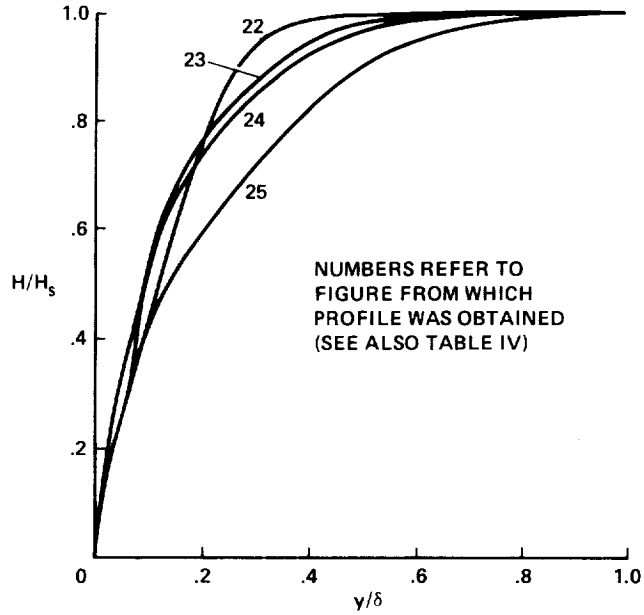

Figure 8-27.– Comparison of enthalpy profiles for both f_w (= –0.3) and $\dot{m}/\rho_\infty \bar{U}$ (= 0.05) fixed.

93% over the no-blowing value if a species that is three times as strong an absorber and emitter as air ($\alpha = 3$) is injected at the same rate. If the mass addition rate is diminished by a factor 1/10, the principal effect is to greatly diminish the foreign-species concentration (fig. 19). However, the foreign species still permeates the entire flow field because Re is moderately low ($\sim 10^2$).

Now if we increase body size (going from figs. 8-19 and 8-20), the result is that we regain the structure of both a momentum and a thermal boundary layer (i.e., there are large changes in u/u_s and H/H_s near the wall). The foreign species vanishes at only a third of the distance from the wall to the shock in spite of the fact that its concentration at the wall is an order of magnitude larger than that of figure 8-19 and the mass addition rate is the same. These are all the effects of going to a larger Reynolds number ($\sim 10^4$ in table IV), and they underscore the importance of preserving (at least approximately) the Reynolds number in scaling mass addition effects.

Now we specialize the scaling discussion to the ablation case.

Scaling With Ablation

Although it is generally not possible (and sometimes not desirable) to simulate or scale all of the pertinent parameters in the laboratory, it is nevertheless worth examining the extent to which mass addition can be scaled in the presence of conduction, gas and surface radiation, and ablation.

Conduction, radiation, and reradiation– The expression for the material f_w as obtained from equations (15) and (13) can be written

$$-f_w = \frac{1}{h_a}\sqrt{\frac{Re}{\varepsilon(j+1)}}\left[\alpha_w B(\bar{U},\rho_s)\frac{R}{\rho_s\bar{U}}\right.$$

$$\left. + 2.015\times10^{-5}(2\varepsilon)^{1/4}\bar{U}^{0.19}\bar{U}^2\sqrt{\frac{\varepsilon}{\rho_s R}}\,e^{-b(-f_w)^n} - \frac{\sigma\varepsilon_w T_w^4}{\rho_s\bar{U}}\right] \tag{29}$$

We confine our attention to one material and assume that h_a, α_w, ε_w, and T_w are constant and, moreover, that ε and $\bar{U}^{0.19}$ are almost constant. Then, in order to scale the flow-field concentration, we require (from the preceding section), that both f_w and $\dot{m}/\rho_\infty U$ be fixed; or, alternatively, we require that both f_w and Re be fixed. From equation (29) these can be fixed if the brackets in equation (29) are fixed. Conceivably, one could find a range of flight conditions and nose radii for which the bracket and f_w within the bracket are fixed. The constancy of the bracket would then constitute a somewhat unappealing scaling law. It could be specialized to a set of simple laws, namely that

$$\frac{RB(\bar{U},\rho_s)}{\rho_s\bar{U}}, \quad \frac{\bar{U}^2}{\sqrt{\rho_s R}}e^{-b(-f_w)^n}, \quad \text{and} \quad \frac{1}{\rho_s\bar{U}}$$

are individually constant, where these pertain to radiative, convective, and surface reradiative transport, respectively. If convective heating is negligible, we can scale by keeping $\rho_s U$ and R fixed between model and prototype.

Note that, in general, we cannot have constant-velocity scaling with this set of simple laws; that is, ρ_s and (because $b = b(\bar{U})$) R must be individually constant so that there is no hope of scaling either flow field or model to achieve foreign-species scaling. Even if we neglect either radiative or convective heating, we cannot have constant-velocity scaling because of the surface reradiative term.

Radiation only– If this is the only energy transfer mode, scaling can be accomplished if f_w and Re are constant, which requires that $BR/\rho_s U$ be constant. Or the last can be replaced by constant BR^2/μ_s because the Reynolds number is fixed. For scaling at constant velocity, BR/ρ_s must be constant.

Convection only– This situation is especially applicable to ground-based tests with noncharring ablation models in arc-heated wind tunnels and ballistic ranges. If this heating mode is assumed to prevail also for the prototype at actual flight conditions (as was the case for the mass addition calculation of ref. 31), the scaling law requires that either $\left(\bar{U}^2/\sqrt{\rho_s R}\right)e^{-b(-f_w)^n}$ or $\left(\bar{U}^{5/2}/\sqrt{\mu_s}\right)e^{-b(-f_w)^n}$ be constant (as well as constant Re and thus constant f_w). For constant-velocity scaling, the requirement is simply that $\sqrt{\mu_s}$ be constant (along with Re). Since $\sqrt{\mu_s}$ is a weak function of altitude for constant velocity, the conclusion is that $\dot{m}/\rho_\infty U$ is constant and the foreign-species profiles are scaled simply if Re is preserved. T. N. Canning and G. Chapman of Ames Research Center have advanced the former conclusion ($\dot{m}/\rho_\infty U$ constant for constant Re) based on phenomenological arguments under the same constraints (simulated shape, Reynolds number, velocity, and noncharring material (no reradiation)), and for convection only.

In short, then, ablation scaling (by simple rules) in terms of ratio of mass flux at the wall to that in the free-stream and foreign-species concentration profile can best be achieved for very special heating conditions. Constant-velocity scaling cannot be achieved for materials which reradiate importantly.

Low Reynolds Number Effects Without Mass Addition

It is common to study mass addition effects on convective heat transfer by use of the effective heat of ablation and a heating rate corresponding to no mass addition. For large Reynolds number (no shock-layer vorticity) and high speeds (up to 50,000 ft/sec), the convective heating rate without mass addition is quite well known by both experiment (refs. 6 and 32-35) and theory (refs. 2, 6, 36, and 37). Moreover, a number of investigators have studied the regime of Mach numbers up to 8, where Reynolds numbers are low enough that shock-layer vorticity affects the convective heating rate for no mass addition (refs. 38-44). Van Dyke (refs. 45 and 46) has studied the vorticity effect up to infinite Mach number without real gas effects. Hoshizaki (ref. 47) has examined the vorticity effect for the incompressible shock layer. Our intent is to examine briefly the external vorticity (or low Reynolds number) effect on wall shear stress and convective heat transfer at high speed using real gas properties.[6]

Surface shear stress– The present flow-field analysis is a single-layer analysis in which the equations are solved from the body to the shock. A very simple comparison of the single-layer result with the no-vorticity, two-layer (boundary layer plus inviscid shock layer) result for surface shear stress can be made as follows.

The single-layer shear stress has been expressed by equation (28). It is simple to show for the two-layer, no-vorticity analysis for a cold wall (ref. 2, for example) that

$$\left(\frac{\tau_w}{x}\right)_{\text{no vort}} = \left(\frac{\overline{U}}{R}\right)^{3/2} \frac{(2\varepsilon)^{3/4}\sqrt{\rho_w \mu_w (j+1)}\, F''_w}{2\sqrt{2}} \tag{30}$$

where F''_w is the value at the wall corresponding to the solution of the Blasius equation for no mass addition, and is given by reference 48. The ratio of $\tau_w/\tau_{w_{\text{no vort}}}$ obtained by combining equations (28) and (30) is

$$\frac{\tau_w}{(\tau_w)_{\text{no vort}}} = \frac{2\sqrt{2}\,(\varphi_w)^{1/2}}{(2\varepsilon)^{3/4}} \frac{f''_w}{F''_w} \tag{31}$$

The result is shown in figure 8-28 in which the ratio is plotted as a function of Reynolds number of the form used by reference 39. As would be expected, shear stress increases over its no-vorticity value as Reynolds number decreases. At a given Reynolds number, the effect is enhanced by increasing speed and decreasing pressure.

Convective heat-transfer rate– The convective heat-transfer results for the same examples are shown in figure 8-29. For present purposes, $q_{c_{\text{no vort}}}$ was obtained by use of equation (11), which is the result of Hoshizaki (ref. 6). It can be noted that the convective heating result parallels the shear-stress result as would be expected.

[6]Because of a conflict which arises in the outer boundary conditions for very small Reynolds numbers, the results of this section and those of figures 8-18 and 8-19 are considered to be first approximations. The conflict is discussed and evaluated in an approximate way in the appendix.

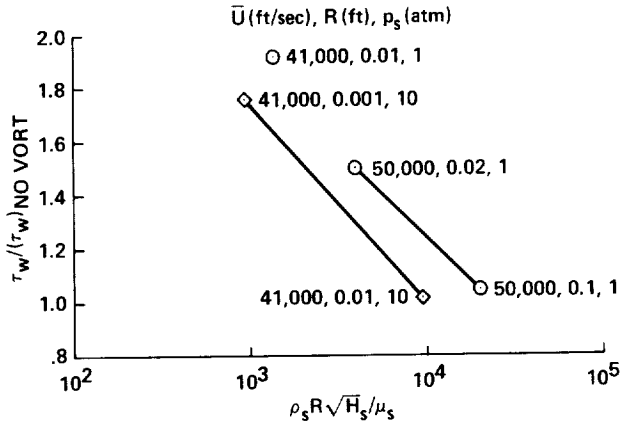

Figure 8-28.– Effect of Reynolds number on surface shear stress with no mass addition.

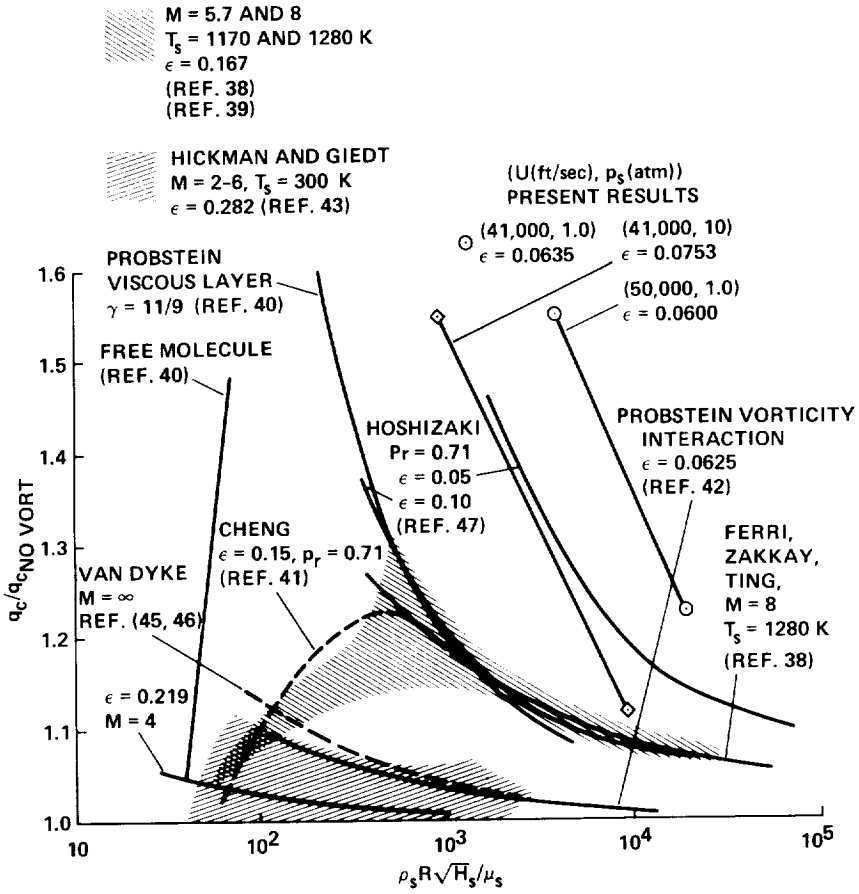

Figure 8-29.– Effect of Reynolds number on convective heat transfer with no mass addition.

The theoretical and experimental results of others (as obtained from refs. 39, 44, and 47) are shown for comparison. In each separate study the ratio of convective heating with vorticity to that

without is enhanced by an increase in speed or Mach number (M) or (for the case of ref. 47) ε at a given Reynolds number. Among the various studies, the ratio does not always increase with Mach number and there is some disagreement as to the reason (discussed in refs. 38, 44, and 46). The present results lie considerably higher than those of references 39, 41, 43, 45, and 46 as would be expected because of our comparatively high speed (or Mach number) and/or low ε.

Our results are close to the viscous layer results of Probstein (ref. 40) and Hoshizaki (ref. 47). The results of these three studies are all derived from flow-field analyses which employed the Navier-Stokes equations from the body to the shock wave. Both Probstein and Hoshizaki assumed constant density and Prandtl number. Our results lie above theirs for a given Reynolds number and ε, possibly because of our variable Prandtl number corresponding to higher speeds for which ionization occurs, and possibly because of compressibility effects near the cold wall. The slopes of our lines are alike and are much like those of Hoshizaki at lower Reynolds numbers. The vorticity results show that convective heating may be as much as 60% higher than the no-vorticity value and that the ratio of the two is enhanced by increased $\bar{U}$ or diminished p_s (or ε) at constant Reynolds number.

The ratio of convective heat-transfer rate to total free-stream energy flux for these same examples is shown as a function of Reynolds number in figure 8-30. The results of references 38 and 39 at Mach 5.7 and 8 are also shown. In each case the slanted line corresponds to the no-vorticity result. At a given Reynolds number, C_H, the ratio of convective heat transfer rate to the free-stream energy flux without vorticity increases with increasing speed. The symbols represent the present result and are attached to the appropriate no-vorticity line by a vertical line. Conservation of energy requires that C_H not be more than unity. Thus C_H of unity represents the flow energy limit. For the examples represented by the symbols, the convective heating was less than half the flow-energy limit at the most.

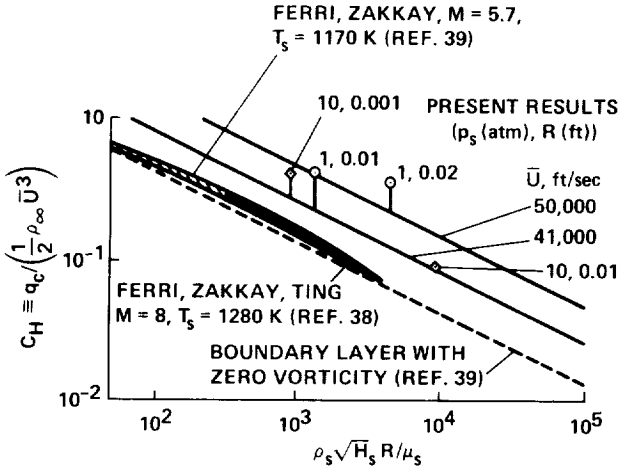

Figure 8-30.– Effect of Reynolds number on heat-transfer coefficient for no mass addition.

Finally, flow-field solutions for some of the nonablating small-body points of figures 8-28 through 8-30 are shown in figures 8-31 through 8-33. The trend toward increased vorticity near the wall relative to that near the shock, and toward a more nearly isoenergetic flow field behind the shock for higher pressure can be seen from comparison of figures 8-31 and 8-32.

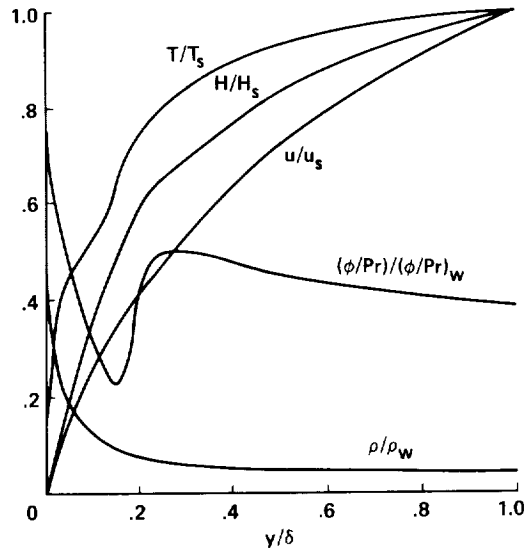

Figure 8-31.– Nonisoenergetic flow field with shock-layer vorticity for no mass addition ($\overline{U}$ = 41,000 ft/sec, p_s = 1 atm, R = 0.0104 ft).

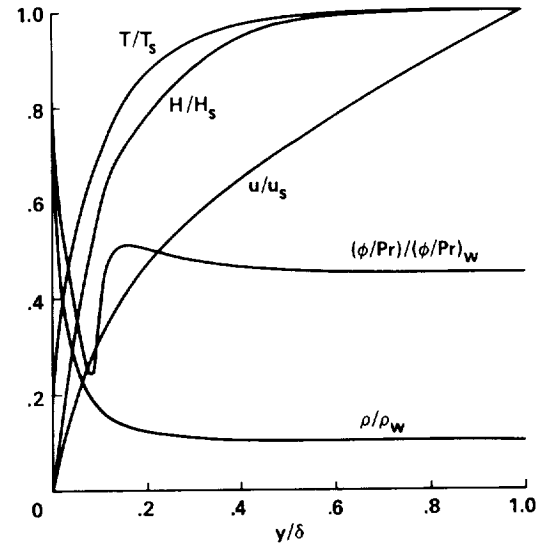

Figure 8-32.– Nonisoenergetic flow field with shock-layer vorticity for no mass addition ($\overline{U}$ = 41,000 ft/sec, p_s = 10 atm, R = 0.01 ft).

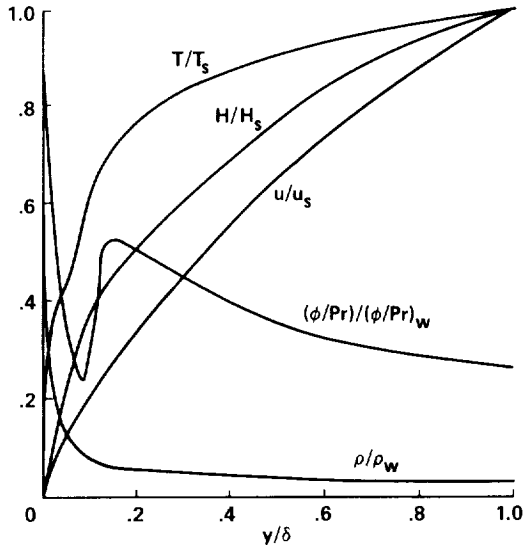

Figure 8-33.– Nonisoenergetic flow field with shock-layer vorticity for no mass addition ($\bar{U}$ = 50,000 ft/sec, p_s = 1 atm, R = 0.02 ft).

CONCLUDING REMARKS

The flow equations in the stagnation region of the shock layer of blunt bodies (including mass, momentum, and energy transport phenomena) have been solved for numerous examples at flight speeds up to 50,000 ft/sec in air. The thermodynamic and transport properties of dissociating ionizing air were used in the analysis.

Many results with mass addition (by transpiration or ablation) were obtained. It was shown that convective heating was more strongly affected by mass addition than was radiative heating for mass addition rates up to half the free-stream mass flux (excluding effects of radiation from ablation products). Convective heating results were correlated by a simple relation which shows that mass addition diminishes convective heating exponentially, where the argument of the exponential is a simple function of flight speed and Blasius-type wall stream function to the 3/2 power, $(-f_w)^{3/2}$. Results with mass addition for body nose radii between 0.01 and 5.0 ft, flight speeds from 30,000 and 50,000 ft/sec, wall temperatures from 1500 to 3000 K, shock-layer pressure levels from 0.1 to 10.0 atm, and surface mass addition rates up to half the free-stream mass flux were correlated by the simple expression.

Previous correlation formulas obtained from subsatellite speed results do not correlate the present higher speed convective heating results corresponding to high mass addition rates.

The results with mass addition were used to study ablation at hypervelocity for which convection, gaseous radiation, and surface reradiation were taken into account. At specified flight conditions (ranging in speed between 30,000 and 50,000 ft/sec and between 0.1- and 10.0-atm shock-layer pressure level) for a given ablator, the nose radius which minimizes total heating rate was determined. For this "optimum" nose radius, the following results were obtained.

1. The ablation rate in terms of the stream function at the wall depends only on the convective heating properties of the gas and is independent of the gaseous radiation properties if reradiation from the surface itself is negligible.

2. The ablation rate in terms of mass flux at the surface is not more than one-fourth the free-stream mass flux for the flight regime cited above and is not more than one-half the free-stream mass flux at a speed of 70,000 ft/sec.

3. The influence of mass addition on standoff distance is moderate, the distance being enhanced by not more than 50% over its no-ablation value.

4. The gaseous radiation flux incident on the surface is larger than the conduction flux by a factor of 2 to 9.

5. If the ablated vapors radiate like air, mass addition enhances the incident radiant flux at the surface by less than 20% over the no-ablation value.

6. If the ablated vapors radiate 10 times as strongly as air, mass addition enhances the incident radiant flux at the surface by less than 50% over the airlike value.

7. The surface viscous shear stress is low, generally not more than 5% of the surface pressure.

In order to scale mass addition effects in terms of dimensionless concentration profiles of the foreign species, it is necessary to match both Reynolds number and either the stream function at the wall or the ratio of the mass flux at the wall to that of the free stream.

Ablation rate and foreign-species concentration profiles can be scaled conveniently for very special heating conditions only. Constant-velocity scaling cannot be achieved for materials which reradiate importantly.

Finally, at low Reynolds numbers, the shock-layer vorticity enhances both shear stress and convective heating over the no-vorticity values, the effect being greater at higher speed and lower pressure.

APPENDIX

BOUNDARY CONDITIONS BEHIND BOW SHOCK WAVE FOR VERY SMALL NOSE RADII OR REYNOLDS NUMBER

The outer boundary condition employed for the energy equation is

$$H_s = \bar{U}^2/2 \tag{A1}$$

However, for nose radii small enough that a conductive heat flux exists just behind the shock, the boundary condition may be quite different from equation (A1) as follows.[7]

For simplicity, we consider only the normal portion of the shock wave and equate energy flux on each side of the shock. Thus,

$$\rho_\infty \bar{U}\left(h_\infty + \frac{\bar{U}^2}{2}\right) + \left(\frac{k}{c_p}\frac{dh}{dy}\right)_\infty = -\rho_s v_s\left(h_s + \frac{v_s^2}{2}\right) + \left(\frac{k}{c_p}\frac{dh}{dy}\right)_s \tag{A2}$$

where y and v are positive outward from the body. We employ the strong shock approximation

$$h_\infty \ll \frac{\bar{U}^2}{2} \tag{A3}$$

and assume

$$\left(\frac{dh}{dy}\right)_\infty = 0 \tag{A4}$$

From mass continuity,

$$-v_s = \varepsilon \bar{U} \tag{A5}$$

By use of equations (A2)-(A5)

$$H_s = \frac{\bar{U}^2}{2} - \frac{1}{\rho_\infty \bar{U}}\left(\frac{k}{c_p}\frac{dh}{dy}\right)_s \tag{A6}$$

So we see that H_s is always less than $\bar{U}^2/2$ by an amount that cannot be determined until the solution of the flow field behind the shock has been obtained and $(dh/dy)_s$ is known. The problem at once

[7]A similar difficulty exists with the outer boundary conditions on the momentum equation because of vorticity behind the shock, as noted in reference 47. One way out of these difficulties is to integrate through the shock wave and use the free stream as boundary conditions, as presented in reference 49. Even at that, many uncertainties in the shock wave (e.g., thermal and chemical relaxation phenomena) remain at these high velocities.

becomes one of iterating not only on the simultaneous differential equations, but on their boundary conditions as well.

We can estimate how much H_s differs from $\bar{U}^2/2$ by assuming

$$\frac{dh}{dy} = \frac{h_s - h_w}{\delta} \approx \frac{h_s}{\delta} \tag{A7}$$

Then H_s becomes

$$H_s = \frac{\bar{U}^2}{2} \frac{(1 + \varepsilon^2\gamma)}{(1 + \gamma)} \tag{A8}$$

where

$$\gamma = \frac{1}{\rho_\infty \bar{U}(\delta/R)R} \left(\frac{k}{c_p}\right)_s = \frac{Pr_s}{Re(\delta/R)} \tag{A9}$$

Since δ/R is not a strong function of $R, \bar{U}$, or p_s in the examples considered, γ is inversely proportional to the Reynolds number and directly proportional to the Prandtl number behind the shock wave. If $\gamma \ll 1$, we have the usual boundary condition $H_s = \bar{U}^2/2$. However, as Re gets smaller, that is,

if	then	
$\gamma \approx 1$	$H_s \approx \frac{\bar{U}^2}{4}$	
$\gamma \gg 1$	$H_s \approx \frac{\bar{U}^2}{2}\left(\frac{1}{\gamma} + \varepsilon^2\right)$	(A10)
$\varepsilon^2\gamma \gg 1$	$H_s \approx \frac{\bar{U}^2}{2}\varepsilon^2$	

In the limit the approximation tells us that H_s is much less than $\bar{U}^2/2$.

For the moment, we adopt the point of view that H_s was specified, and that the result of the corresponding solution might apply directly to a higher flight speed. That is, the true flight speed is larger than the assumed flight speed by the factor $\sqrt{(1 + \gamma)/(1 + \varepsilon^2\gamma)}$. For the results in question, shown in figure 8-29, the factor varies from 1.0 to 1.2.

However, we cannot make direct application to the higher speed because we then violate another boundary condition in which the smaller value of $\bar{U}$ was employed; namely, $\rho_s v_s = -\rho_\infty \bar{U}$. For these reasons, the present low Reynolds number results are considered to be first approximations.

REFERENCES

1. Howe, J. T.; and Sheaffer, Y. S.: Mass Addition in the Stagnation Region for Velocity up to 50,000 Feet per Second. NASA TR R-207, 1964.

2. Howe, J. T.; and Viegas, J. R.: Solutions of the Ionized Radiating Shock Layer Including Reabsorption and Foreign Species Effects and Stagnation Region Heat Transfer. NASA TR R-159, 1963.

3. Lees, L.: Convective heat Transfer With Mass Addition and Chemical Reactions. Presented at AGARD Combustion and Propulsion Colloquium, NATO, Palermo, Sicily, 1958 (GALCIT Pub. 451).

4. Lees, L.: Ablation in Hypersonic Flows. Paper presented at the Seventh Anglo-American Aeronautical Conference, New York, Oct. 5-7, 1959 (GALCIT Pub. 481).

5. Hayes, Wallace D.: Some Aspects of Hypersonic Flow. Ramo-Wooldridge Corp., Jan. 4, 1955.

6. Hoshizaki, H.: Heat Transfer in Planetary Atmospheres at Supersatellite Speeds. ARS paper 2173-61, ARS J., vol. 32, Oct. 1962, pp. 1544-5I.

7. Cohen, N. B.: Boundary-Layer Similar Solutions and Correlation Equations for Laminar Heat-Transfer Distribution in Equilibrium Air at Velocities up to 41,000 ft/sec. NASA TR R-188, 1961.

8. Yoshikawa, K. K.; and Chapman, D. R.: Radiative Heat Transfer and Absorption Behind a Hypersonic Normal Shock Wave. NASA TN D-1424, 1962.

9. Adams, Mac C.: Recent Advances in Ablation. ARS J., vol. 29, no. 9, Sept. 1959, pp. 625-632.

10. Georgiev, S.; Hidalgo, H.; and Adams, M. C.: On Ablation for the Recovery of Satellites. Res. Rep. 47, AVCO Res. Lab., March 1959.

11. Gross, J. J.; Masson, D. J.; and Gazley, C., Jr.: General Characteristics of Binary Boundary Layers With Application to Sublimation Cooling. Rand Rep. P-1371, 1958.

12. Stewart, J. D.: Transpiration Cooling: An Engineering Approach. General Electric Rep. MSVD-TIS-R 59SD338, May 1, 1959.

13. Swann, Robert T.: Effect of Thermal Radiation From a Hot Gas Layer on Heat of Ablation. J. Aero. Sci., vol. 28, no. 7, July 1961, pp. 582-583.

14. Swann, R. T.; and Pittman, C. M.: Numerical Analysis of the Transient Response of Advanced Thermal Protection Systems for Atmosphere Entry. NASA TN D-1370, 1962.

15. Beckwith, I. E.: Similar Solutions for the Compressible Boundary Layer on a Yawed Cylinder With Transpiration Cooling. NACA TN 4345, 1958.

16. Lundell, J. H.; Winovich, W.; and Wakefield, R. M.: Simulation of Convective and Radiative Entry Heating. Arthur M. Krill, ed., Advances in Hypervelocity Techniques Proc. Second Symposium on Hypervelocity Techniques. Plenum Press, New York, 1962, pp. 729-748.

17. Scala, S. M.: The Ablation of Graphite in Dissociated Air, Part I, Theory. IAS paper 62-154, 1962 (also General Electric Co. Missile and Space Division, R 62SD72, Sept. 1962).

18. Hartnett, J. P.; and Eckert, E. R. G.: Mass Transfer Cooling With Combustion in a Laminar Boundary Layer. Heat Transfer and Fluid Mechanics Institute, Univ. of Calif., Berkeley, 1958, Stanford U. Press, Stanford, Calif., 1958, pp. 54-68.

19. Cohen, C. B.; Bromberg, R.; and Lipkis, R. P.: Boundary Layers With Chemical Reactions Due to Mass Addition. Jet Propulsion, vol. 28, no. 10, Oct. 1958, pp. 659-668.

20. Vojvodich, N. S.; and Pope, R. B.: An Investigation of the Effect of Gas Composition on the Ablation Behavior of a Charring Material. Paper for ARS and MIT Conference on Physics of Entry Into Planetary Atmospheres (AIAA), Cambridge, Mass., Aug. 1963.

21. Chung, P. M.: Shielding Stagnation Surfaces of Finite Catalytic Activity by Air Injection in Hypersonic Flight. NASA TN D-27, 1959.

22. Lees, Lester: Similarity Parameters for Surface Melting of a Blunt Nosed Body in a High Velocity Gas Stream. ARS J., vol. 29, no. 5, May 1959, pp. 345-354.

23. Bethe, Hans A.; and Adams, Mac C.: A Theory for the Ablation of Glassy Materials. JAS, vol. 26, no. 6, June 1959, pp. 321-328 and p.350.

24. Allen, H. J.; Seiff, A.; and Winovich, W.: Aerodynamic Heating of Conical Entry Vehicles at Speeds in Excess of Earth Parabolic Speed. NASA TR R-185, 1963.

25. Allen, H. J.; and James, N.: Prospects for Obtaining Aerodynamic Heating Results From Analysis of Meteor Flight Data. NASA TN D-2069, 1964.

26. Howe, John T.; Viegas, John F.; and Sheaffer, Yvonne S.: Study of the Nonequilibrium Flow Field Behind Normal Shock Waves in Carbon Dioxide. NASA TN D-1885, 1963.

27. Chung, P. M.: Hypersonic Viscous Shock Layer of Nonequilibrium Dissociating Gas. NASA TR R-109, 1961.

28. Page, W. A.; and Arnold, J. O.: Shock Layer Radiation of Blunt Bodies at Reentry Velocities. NASA TR R-193, 1964.

29. Kivel, B.; and Bailey, K.: Tables of Radiation From High Temperature Air. Res. Rep. 21, AVCO Res. Lab., Dec. 1957.

30. Wick, Bradford H.: Radiative Heating of Vehicles Entering the Earth's Atmosphere. Paper presented to the Fluid Mechanics Panel of AGARD, Brussels, 1962.

31. Craig, Roger A.; and Davy, William C.: Thermal Radiation From Ablation Products Injected Into a Hypersonic Shock Layer. NASA TN D-1978, 1963.

32. Rose, P. H.; and Stark, W. I.: Stagnation Point Heat-Transfer Measurements in Dissociated Air. J. Aero. Sci., vol. 25, no. 2, Feb. 1958, pp. 86-97.

33. Stankevics, J. O.; and Rose, P. H.: Stagnation Point Heat Transfer in Partially Ionized Air. IAS Paper 63-61, 1963.

34. Compton, Dale L.; and Chapman, Gary T.: Two New Free-Flight Methods for Obtaining Convective Heat-Transfer Data. Paper presented at AIAA Testing Conference, March 1964.

35. Offenharty, E.; Weisblatt, H.; and Flagg, R. F.: Stagnation Point Heat Transfer Measurements at Supersatellite Speeds. J. Roy. Aero. Soc., vol. 66, no. 613, Jan. 1962, p. 53.

36. Fay, James A.: Hypersonic Heat Transfer in the Air Laminar Boundary Layer. Paper presented at Hypersonic specialists Conference, AGARD, Brussels, Belgium, Apr. 3-6, 1962.

37. Pallone, A.; and Van Tassell, W.: Stagnation Point Heat Transfer for Air in the Ionization Regime. ARS J., vol. 32, no. 3, March 1962, pp. 436-437.

38. Ferri, Antonio; Zakkay, Victor; and Ting, Lu: Blunt-Body Heat Transfer at Hypersonic Speed and Low Reynolds Numbers. J. Aero. Sci., vol. 28, no. 12, Dec. 1961, pp. 962-971 and p. 991.

39. Ferri, Antonio; and Zakkay, Victor: Measurements of Stagnation Point Heat Transfer at Low Reynolds Numbers. J. Aero. Sci., vol. 29, no. 2, July 1962, pp. 847-850.

40. Probstein, R. F.: Shock Wave and Flow Field Development in Hypersonic Reentry. Paper presented at the ARS Semiannual Meeting, Los Angeles, May 9-12, 1960, ARS Preprint 1110-60.

41. Cheng, H. K.: Hypersonic Shock-Layer Theory of the Stagnation Region at Low Reynolds Numbers. Proc. 1961 Heat Trans. and Fluid Mech. Inst. Stanford U. Press, Stanford, Calif., 1961, pp. 161-175.

42. Hayes, Wallace D.; and Probstein, Ronald F.: Hypersonic Flow Theory. Academic Press, Inc., New York, 1959, p. 372.

43. Hickman, R. S.; and Giedt, W. H.: Heat Transfer to a Hemisphere-Cylinder at Low Reynolds Numbers. AIAA J., vol. 1, no. 3, March 1963, pp. 665-672.

44. Tong, Henry; and Giedt, W. H.: Supersonic Stagnation Point Heat Transfer at Low Reynolds Numbers. AIAA J., vol. 2, 1964, pp. 185-186.

45. Van Dyke, Milton: Second-Order Compressible Boundary Layer Theory With Application to Blunt Bodies in Hypersonic Flow. Hypersonic Flow Res., Academic Press, Inc., New York, 1962, pp. 37-76.

46. Van Dyke, Milton: A Review and Extension of Second-Order Hypersonic Boundary-Layer Theory. Rarefied Gas Dynamics, vol. 2, Academic Press, Inc., New York, 1963, pp. 212-227.

47. Hoshizaki, H.: Shock Generated Vorticity Effects at Low Reynolds Numbers. Tech. Rep. LM SD-48381, Missile and Space Division, 1959.

48. Emmons, H. W.; and Leigh, D.: Tabulation of the Blasius Function with Blowing and Suction. Combustion Aerodynamics Lab., Interim Tech. Rep. 9, Harvard Univ., Nov. 1953.

49. Probstein, R. F.; and Kemp, N. H.: Viscous Aerodynamic Characteristics in Hypersonic Rarefied Gas Flow. J. Aero/Space Sci., vol. 27, March 1960, pp. 174-192.

50. Kratsch, K. M.; Hearne, L. F.; and McChesney, H. R.: Thermal Performance of Heat Shield Composites During Planetary Entry. Presented at AIAA-NASA National Meeting, Palo Alto, Calif., 1963.

CHAPTER 9

VERY SEVERE FLIGHT ENVIRONMENTS, THE JUPITER PROBE

Thus far we have learned something about hypervelocity flight in Earth's atmosphere. We have considered stagnation-region heating in considerable detail. The flow has been in chemical and thermodynamic equilibrium in the illustrations presented. We can now say that the apparent sterile formalism of kinetic theory and radiative transfer have been applied with some fidelity to real gas flow.

Flight in other planetary atmospheres has been studied: Mars, including return to Earth (ref. 1); Venus, Uranus, and Saturn (and its largest moon, Titan (ref. 2)); and the most severe entry environment that we have studied in detail—Jupiter (ref. 3). The last of these is the subject of this chapter.

Both convective and radiative heating rates for various hypervelocity flights (circles) and some facilities that were used to simulate those flight environments (squares) are shown in figure 9-1 of the AIAA Survey Paper presented in this chapter. Thus we see Apollo, Pioneer Venus, Space Shuttle, and the Jupiter Probe. The Jupiter entry is two orders of magnitude more severe in terms of heating than the Apollo flight. Correspondingly, the Giant Planet Probe Facility (GPPF) at NASA Ames Research Center is shown, which partially simulated the Jupiter Probe entry for a small body.

The Jupiter Probe is part of what is called the Galileo Mission. Although the probe has been designed and built, its launch has been delayed for lack of a launch vehicle. Nevertheless, it is instructive to examine the phenomenological events involved in the design of the probe destined to enter an environment that is an inferno.

It may be remarked at the outset that the heat-shield material for the probe was selected to be carbon phenolic. Although that choice was partially attributed to the writer, I preferred a heat shield that back-scattered radiation in the depths of the material (even though the surface was ablating) in this intense radiative environment. Indeed, that technology was well advanced, but it was not given serious consideration.

A descriptive survey of the effort constitutes the balance of this chapter, which was originally presented as AIAA Survey Paper 81-1068. References starting with reference 4 are those of that paper. The work is that of many people at NASA Ames Research Center, Langley Research Center, The Jet Propulsion Laboratory, the General Electric Co., the Acurex Corporation, and other organizations and people. It was a major technology effort. There is no reason to highlight the features, uncertainties, and difficulties of the supporting research and technology effort in advance, so we move directly into the text of the paper.

(Text of the)
SURVEY OF THE SUPPORTING RESEARCH AND TECHNOLOGY FOR THE THERMAL PROTECTION OF THE GALILEO PROBE[1]

Abstract

The Galileo Probe, which is scheduled to be launched in 1985[2] and to enter the hydrogen-helium atmosphere of Jupiter up to 1475 days later, presents thermal protection problems that are far more difficult than those experienced in previous planetary entry missions. The high entry speed of the probe will cause forebody heating rates orders of magnitude greater than those encountered in the Apollo and Pioneer Venus missions, severe afterbody heating from base-flow radiation, and thermo-chemical ablation rates for carbon phenolic that rival the free-stream mass flux. This paper presents a comprehensive survey of the experimental work and computational research that provide technological support for the probe's heat-shield design effort. The survey includes atmospheric modeling; both approximate and first-principle computations of flow fields and heat-shield material response; base heating; turbulence modeling; new computational techniques; experimental heating and materials studies; code validation efforts; and a set of "consensus" first-principle flow-field solutions through the entry maneuver, with predictions of the corresponding thermal-protection requirements.

Introduction

The Galileo Probe is scheduled to be launched sometime in 1985 and to enter Jupiter's atmosphere as many as 1475 days later. After entry, a parachute will be deployed, both the forebody and afterbody heat shields will be jettisoned, and scientific measurements will be made as the payload descends through the atmosphere. Because this entry severely tests our thermal-protection design capability, a significant research base—both experimental and analytical—has been formed in support of the probe heat-shield design effort. Since about July 1975 (ref. 4) the supporting research and technology base has involved Ames Research Center, Langley Research Center, and several contractors.

The high-speed entry (up to 48.2 km/sec relative to the hydrogen-helium atmosphere of Jupiter) is expected to lead to probe forebody heating rates that are hundreds of times greater than those of Apollo and 10 times the Pioneer Venus rates (fig. 9-1). The corresponding thermo-chemical ablation rate of the carbon phenolic heat shield is expected to rival the free-stream mass flux because of the intense radiative and convective heating from the hot turbulent gas cap that will envelop the probe. Moreover, for the cool dense model of the Jovian atmosphere, it is likely that radiative heating rates near the stagnation point will be so severe that the heat-shield material will undergo spallation as well as thermo-chemical ablation. It is calculated that the severe environment will cause the probe forebody to lose about one-third of its mass during the entry heating pulse. Not only is forebody heating a severe problem for the Jovian probe, but the afterbody will incur significant radiative heating from the wake region of the flow. As a result, it is necessary that the flow field and the heating rates about the entire probe, including the wake, be understood as thoroughly as possible in order for the design of the thermal protection systems to be as effective as practical.

---

[1]Written by J. T. Howe, W. C. Pitts, and J. H. Lundell, Ames Research Center, as AIAA Survey Paper 81-1068.

[2]The Galileo Probe was launched in October 1989.

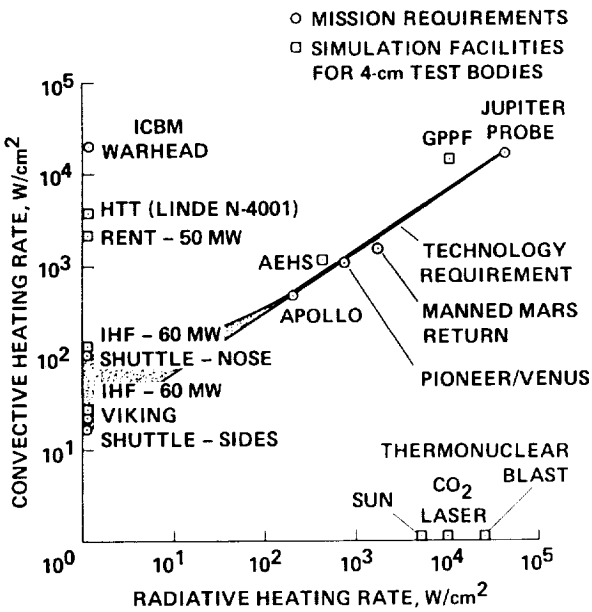

Figure 9-1.– Heating environments.

The flow environment and material response about the probe is beyond our previous capability to simulate experimentally, or to compute realistically. In recent years, new experimental facilities have been devised, constructed, and used to simulate some but not all of the features of the entry environment; indeed they cannot simulate the flow field in all respects. The Ames Giant Planet Probe Facility (GPPF) can produce heating rates that simulate the heating levels on the flank of the probe, and the Ames Gas Dynamic Laser Facility can simulate heating rates to the stagnation region of the probe and produce heating levels that cause spallation of the heat-shield material. These facilities will be discussed subsequently. Both the forebody and afterbody flow fields and radiative transfer have been studied in shock-tube facilities, and by firing free-flight models into a noble gas mixture to simulate Mach number and Reynolds number in order to observe forebody and wake flow-field structure. Moreover, various computational codes have been developed to predict the effects of a great many coupled physical phenomena in the flow field and in the heat-shield material.

A number of additional problems have been addressed to assess their effects on the probe heat shield. These include the composition and thermal structure of the atmosphere, probe shape, and targeting (initial entry) conditions. But some phenomena (such as spallation) that cannot readily be assessed by computational physical analysis must be investigated experimentally. The final objective of the comprehensive supporting research and technology effort is to provide an acceptable set of first-principle computational codes to be used as a standard for the more approximate design codes of others. To enhance confidence in the results of these first-principle, or benchmark, codes it is necessary to validate the codes experimentally, where possible, and to provide experimental corrections to account for phenomena that cannot be modeled in the codes.

Targeting, Atmospheric Modeling, and Trajectory Computations

Targeting for the entry probe has been at an altitude of 450 km at various latitudes near the Jovian equator. Effects of variations in the azimuthal angle (near equatorial), of the entry angle of the

probe, with respect to the planet, and of probe mass and configuration on thermal-protection requirements have been examined. That target altitude was fixed early in the study, because it corresponded to what was thought to be the "top" of the model atmosphere, according to reference 5. Subsequently, however, there were a number of other model atmospheres which differed both in thermal structure and in relative abundance of hydrogen and helium. The thermal structures of these different nominal atmospheres are shown in figure 9-2, which was adapted from an Acurex Corporation report. The original atmospheric model, which corresponded to that reported in reference 5, was composed of 85% hydrogen and 15% helium by volume. That was followed by the atmosphere shown by the solid line in figure 9-2; it was referred to as the Hunten model. That model had the thermal structure given by reference 6, but a composition of 89% hydrogen and 11% helium in accord with reference 7. This was followed by a nominal atmosphere model developed by G. Orton of the Jet Propulsion Laboratory which has the thermal structure shown in figure 9-2, and a composition of 89% hydrogen and 11% helium, as noted above.

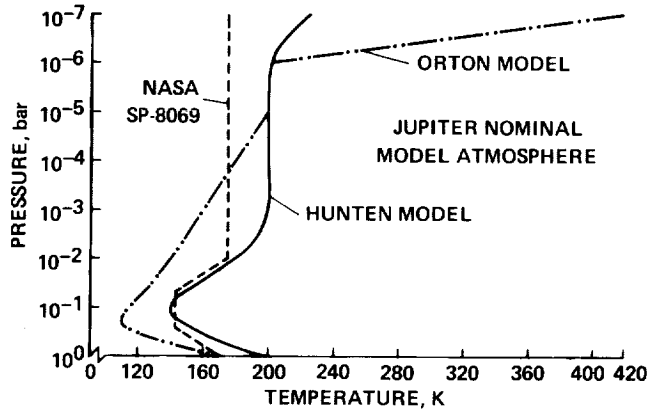

Figure 9-2.– Thermal structure for nominal model atmospheres of Jupiter.

The atmosphere was assumed to be in hydrostatic equilibrium. Hence, an ordinary differential equation could be solved for each model atmosphere composition and thermal structure to compute density-altitude profiles for each model. These computations were performed by M. J. Green, W. C. Davy, and D. Kirk of Ames Research Center. (Mr. Kirk and his co-workers also contributed to the Galileo SRT effort in the area of flight mechanics, which is not included in the scope of this paper.) A comparison of two sets of these atmospheres is shown in figure 9-3, in which the corresponding atmospheric composition is also shown. Thus for each atmosphere defined by a thermal structure there is a warm, nominal, and cool version, depending on the composition. The Orton cool and nominal model atmospheres are seen to be significantly higher than those of reference 5. (Subsequently, for the heavy (310-kg) probe study, a revised version of the Orton atmosphere was used.) Nevertheless, targeting was still specified at 450 km, and trajectories were calculated such that the probe would arrive at that altitude with the specified entry angle. Trajectories were calculated to include the effects of latitude, azimuthal angle, entry angle, and ballistic coefficient for each candidate probe shape, and to accommodate the fact that Jupiter is a rotating oblate spheroid.

ATMOSPHERIC MODEL	COMPOSITION H_2/H_e (VOL)	
	SP 8069	ORTON
WARM	96/4	100/0
NOMINAL	85/15	89/11
COOL	70/30	78/22

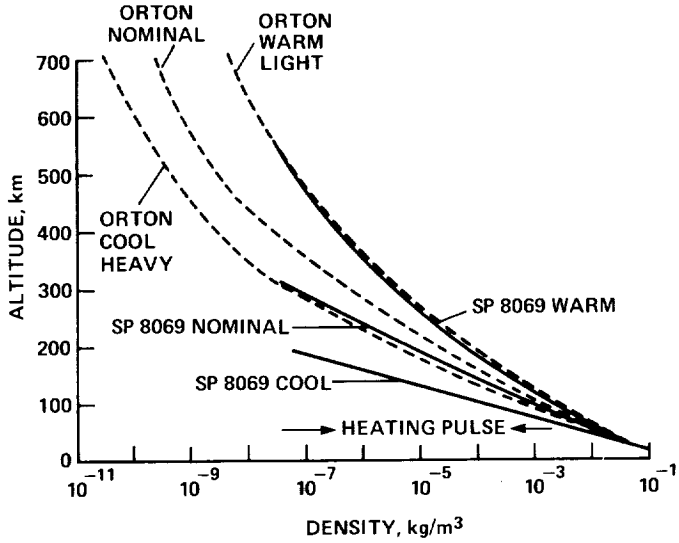

Figure 9-3.– Atmospheric models of Jupiter.

Entry was usually at quite shallow entry angles (5 to 11° inertial entry angle or 6.25 to 13.72° relative to the rotating atmosphere (ref. 8)) with flight in the posigrade direction to take advantage of the velocity of the rotating atmosphere (about 12 km/sec). In this way the velocity of the probe relative to the atmosphere was significantly diminished (from about 60 km/sec inertial to 48 km/sec relative) in order to reduce the heating rates and the weight of the thermal-protection system. Probe shapes were studied that varied from 35°-half-angle hyperboloid forebodies (ref. 9) to 60°-half-angle sphere cones (ref. 10) with a bluntness ratio of about 1/2. The baseline shape was a 45°-half-angle sphere cone with a nose radius of 0.31 m and a base radius of 0.62 m. The shape was modified slightly late in the study. The probe weight was increased during the course of the study as greater demands were placed upon the probe. Much of the early work was for 242-kg probe; later work was for 290-kg and 310-kg probes, as will be shown.

Flow About the Forebody and Heat-Shield Response

During the heating pulse the flow is determined over the forebody at a number of times through the trajectory. To provide a reference set of benchmark solutions, the physical phenomena illustrated in figure 9-4 (adapted from ref. 11) must be included in the analysis. Thus the flow equations include the transport of mass, momentum, energy, and species. The gases are hot and reacting, and emit thermal radiation which is incident on the heat shield. The radiative and convective heating cause the heat-shield surface to ablate at a rate that is sometimes comparable to the free-stream mass flux. The ablated gases mix with and react with the atmospheric gases, and enter into the radiative transfer in the shock layer. The gas mixture makes a transition from laminar to turbulent flow as it is swept around the body. To obtain the benchmark flow-field solutions, a quasi-steady-state ablation boundary condition is applied such that the ablation rate is simply related to the net heating to the wall. Subsequently, the heat shield is designed by applying the heating rates obtained from the flow field to a transient material-response

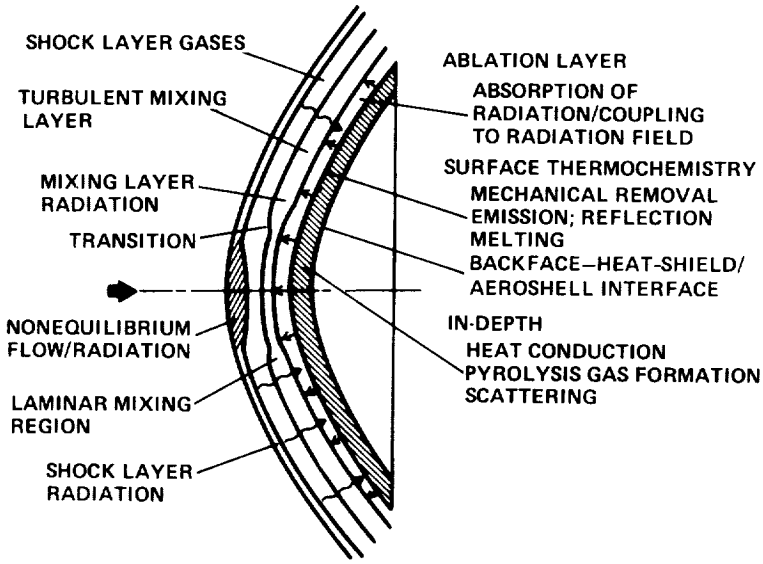

Figure 9-4.– Heat-shield and flow phenomenology.

analysis of a material of finite thickness; the latter material is receding and losing mass by thermochemical ablation of the surface char, and by the outgassing of the pyrolysis gases caused by the internal conduction of heat. The thickness of the heat shield is determined by a specified allowable temperature at its back surface.

A number of flow-field studies were performed early in the research effort, using either inviscid codes or various codes that employ correlations and physical estimates to assess the existing state-of-entry environment-prediction methods (ref. 10); and the extent and importance of atmospheric structures on radiative heating (ref. 8), radiative heating distributions (ref. 12), problems concerned with an atmospheric reconstruction experiment (ref. 13), and configuration effects on radiative heating (ref. 14).

Moreover, an extensive effort was made to acquire and refine the radiative properties of carbonaceous ablation gases both experimentally and theoretically (refs. 15-25). The detailed effect of these carbonaceous species is illustrated in figure 9-5, which was adapted from reference 26. Figure 9-5(a) shows the spectral radiative flux incident on the stagnation region of the entry probe near peak heating, and figure 9-5(b) shows the spectral flux incident on the surface. The difference between the two spectra represents absorption by spectral bands of the ablation gases, as shown in the figure. The spectral-property studies were used to provide input data primarily to the detailed benchmark flow-field codes, as mentioned previously.

Three primary benchwork codes, which were developed over an extended period of time, solve a coupled set of partial differential equations for the mass, momentum, energy, and elemental species transport between the forebody and shock wave. This set of equations was complicated by a radiative flux divergence term, which is a double integral over space and wavelength. The three codes—RASLE, HYVIS, and COLTS—were developed primarily by W. E. Nicolet, J. N. Moss, and A. J. Kumar, respectively. Briefly, RASLE (ref. 11) solves the equations simultaneously by a Newton-Raphson numerical technique; HYVIS solves the equations sequentially by iteration; and COLTS is a time-dependent version of HYVIS. The development of these codes cannot be described in detail here; in general, however, the laminar stagnation region shock layer was first solved by RASLE (ref. 27) and was used to provide ablation blocking corrections for more approximate codes used in a parametric

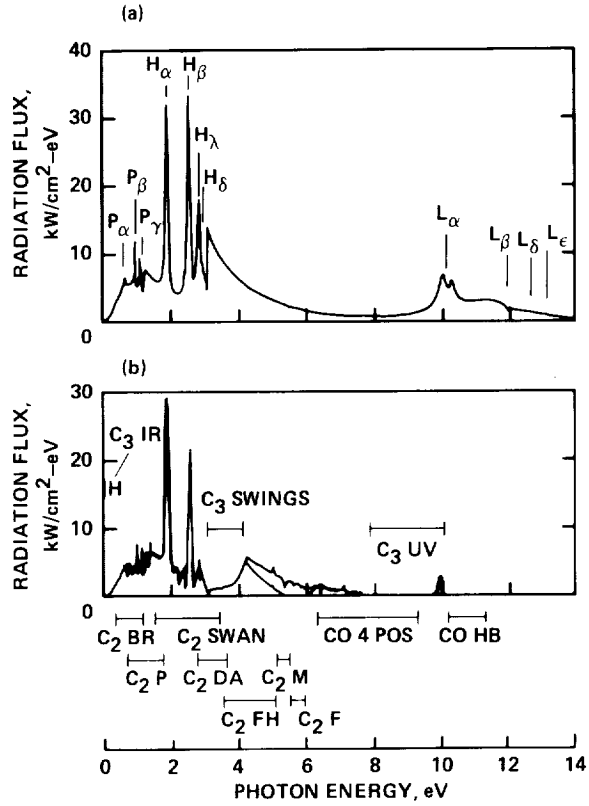

Figure 9-5.– Spectral flux attenuation by ablation species: Shock temperature = 16,090 K, pressure = 5.1 atm, 89% H_2, 11% He atmosphere, carbon phenolic heat shields. (a) Spectral flux incident on ablation area. (b) Spectral flux incident on wall.

study (ref. 28), in which comparisons with other parametric studies were made. These results were used in reference 29 to assess heat-shield requirements and were compared with the pioneering work of Tauber (ref. 30).

The HYVIS code was a pioneering code in several respects. The code produced laminar solutions about hyperboloids of revolution. The solutions were over the entire carbon phenolic forebody heat shield, and included coupled ablation as a quasi-steady-state boundary layer (ref. 31). Subsequently, the code also produced turbulent-flow solutions about both sphere-cones and hyperboloids with coupled ablation for carbon phenolic heat shields (ref. 32).

The RASLE code also computed turbulent flow over a sphere-cone heat shield at various points in an entry trajectory (ref. 33), and the results were compared with those of reference 29. The turbulence models for the two codes differed somewhat. HYVIS used a Prandtl mixing length near the wall and a Clauser-Klebanoff outer eddy viscosity; RASLE used an ordinary differential equation for the mixing length near the wall, selected partly on the basis of an experiment of reference 34 for a highly cooled wall, and a wake-like mixing length differential equation away from the wall. Surface radiative conditions for the two codes also differed, so that there were significant differences in the integrated mass loss obtained from results of the two codes through the trajectory, as shown in figure 9-6. The inertial entry angle was –9° in the nominal atmosphere. Results from the COLTS code (ref. 35) are also shown; in general, they agree with the results of HYVIS. It may be noted that HYVIS was able to obtain solutions at the beginning of the heat pulse and after peak heating, but not in between. RASLE solutions were

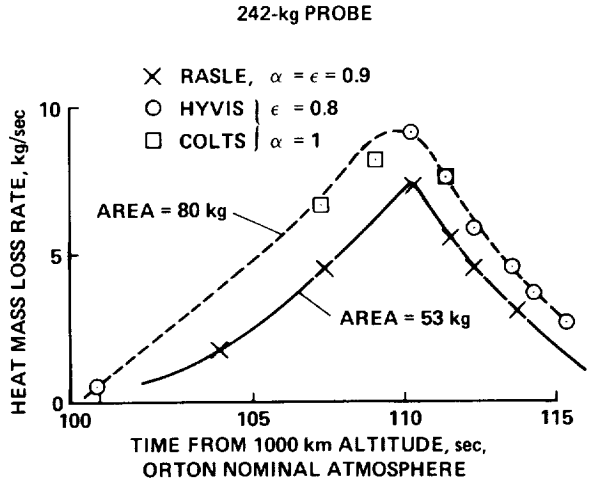

Figure 9-6.– Probe mass-loss-rate comparison for quasi-steady ablation of carbon phenolic.

obtained throughout the heating pulse. The COLTS code seems to have overcome some instabilities experienced by HYVIS and to have obtained two additional solutions on the upward part of the heating pulse.

A very detailed comparison of the results of these benchmark codes was performed at two times in the trajectory (ref. 36): 110.2 sec and 111.3 sec. Differences in physics, methods, boundary conditions, and "convergence" criteria were presented, and the effects were assessed. An attempt was made to reconcile results of the codes by making adjustments to correct for some differences. The work reported in reference 36 is a remarkable effort to sort out many coupled interrelated effects to determine those which are most significant. Global mass and energy conservation checks were made. Among three major contributors to differences in the results, the turbulence models are considered to be the most important, because of their effect on radiative transfer to the wall. Although the various turbulence models employed do not affect state profiles near the wall significantly, profiles remote from the wall are affected. Thus, temperature profiles away from the wall differ because of the turbulence model. Correspondingly, species profiles differ as well. Thus the species that emit and absorb radiation are distributed differently in differing thermal environments by the different turbulence models; the radiation emitted differs correspondingly. Because radiation is the most important phenomenon causing heat-shield ablation, the effect of turbulence modeling on radiative transfer is of primary importance. Results of this important paper (ref. 36) have affected subsequent benchmark solutions and contributed to a "consensus" set of benchmark solutions shown in part subsequently in this paper.

Turbulence modeling of a very hot, chemically reacting flow over a relative cool surface that is ablating at a rate comparable to the free-stream mass flux is very poorly understood. A comparison of several candidate turbulent models (including those cited above) has been made (ref. 37) in the context of a given flow-field code to isolate the effect of the model alone, and to rank the various models according to severity. It is clear that this is an important problem. Experiments must be devised that will make it possible to construct realistic turbulence models and to provide input data for those models.

As noted previously, the flow-field results shown in figure 9-6 are obtained by use of a quasi-steady-state ablation condition. The heat shield designed by the CMA code—using the net heating output from the RASLE code as input to the in-depth materials-response code—is shown in figure 9-7. The CMA code computes the transient thermal response of a charring ablating material of finite variable thickness, and includes the effects of temperature-dependent properties and in-depth pyrolysis. The

criteria that "design" the heat shield are the maximum allowable backface temperature of 700 K and the safety margins (shown in fig. 9-7). These margins are percentages of the ablated material that are added for safety purposes. The figure shows the initial and final shapes of this probe designed for entry into the nominal atmosphere. The mass loss (47 kg) is less than that shown in figure 9-6 (53 kg). The difference is affected by the heat storage in the transient, in-depth solution in only a minor way; this point will be discussed subsequently. When the heat shield with the safety margins defined by figure 9-7 is allowed to enter the cool dense atmosphere at an inertial entry angle of –11°, an additional thermal protection mass (22%) is required for survival, with no safety margin (ref. 38). These preliminary results are for a 242-kg probe and are illustrative only. Subsequently, we shall cite research that reconciles some of the differences among the benchmark codes and present results for a more recent heavier probe (310 kg).

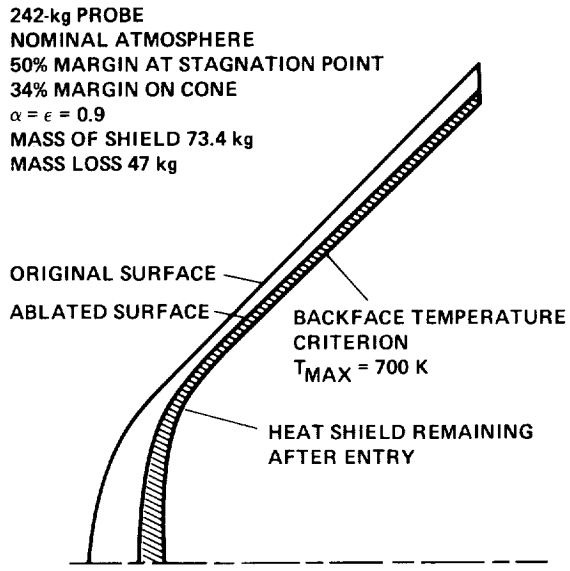

Figure 9-7.– Transient heat-shield response: carbon phenolic.

The codes that produced the results of figures 9-6 and 9-7 are based on first principles and are considered to be benchmark flow-field and material response codes. They might even be labeled "first-generation" benchmark codes, because new computational techniques are being devised and applied to this problem, as will be shown subsequently. However, even these first-generation benchmark codes are very costly to operate and are difficult and time-consuming to run—especially for broad parametric studies. Thus for engineering purposes, more flexible, more approximate codes are useful for economic reasons. Zoby et al. (ref. 39) have developed an approximate code that simulates inviscid radiating flow-field analysis by the use of analytic shock shapes and a 58-step radiative transfer model. Moreover, a code has been developed to predict laminar and turbulent convective heating of reactive and nonreactive gases about blunt reentry configurations for hypersonic flight (ref. 40). These approximate codes produce results that are in good agreement with more complicated codes, and are used extensively for parametric studies.

Flow about the Afterbody and Base Heating

Although the convective heating of the base regions is small (ref. 41), radiative heating is not. The significance of the base radiative heating was noted by Stephenson (ref. 42) in 1965 by measurements made of radiation from the wake of an ablating blunt body launched into air; the measurements were made as the body flew past the radiation sensors.

Park (ref. 43) developed a base flow-field model and derived the base radiative heating from the model. Observations from both ablating and nonablating free-flight tests were used to devise the flow-field model shown in figure 9-8. The main features of the flow field were an expansion about the shoulder; a recirculation region behind the body; and a wake which recompressed and formed a neck about 1.5 body diameters aft of the frustum, with a neck diameter between one-half and two-thirds of the body diameter. Method-of-characteristics solutions about the shoulder were matched to the recirculation region by a choice of base pressure that gave the observed turning angle. Physical reasoning led to a theoretical model of the recirculation, recompression, and neck-region flows. In the ablation case of interest, chemical and radiative modeling predicted that the most severe radiation would occur immediately behind the frustum, because of radiation from hydrogen and carbon atoms that were not in chemical equilibrium in the expansion region. At the base stagnation point, radiation is received from both the neck and recompression region, and the recirculation region—as shown in figure 9-9. These regions are probably in chemical equilibrium, and detailed spectral radiation computations from the hydrogen-carbon mixture produce the upper line corresponding to the ablation case. (It is interesting that the nonablating case gives almost comparable results—probably because the temperature is higher.) It is believed that the high base pressure obtained by the model is the most significant physical property that leads to the high base radiative heating. The effect of base pressure was examined and the radiative heating was found to vary as the square of the ratio of base-to-forward-stagnation-point pressure.

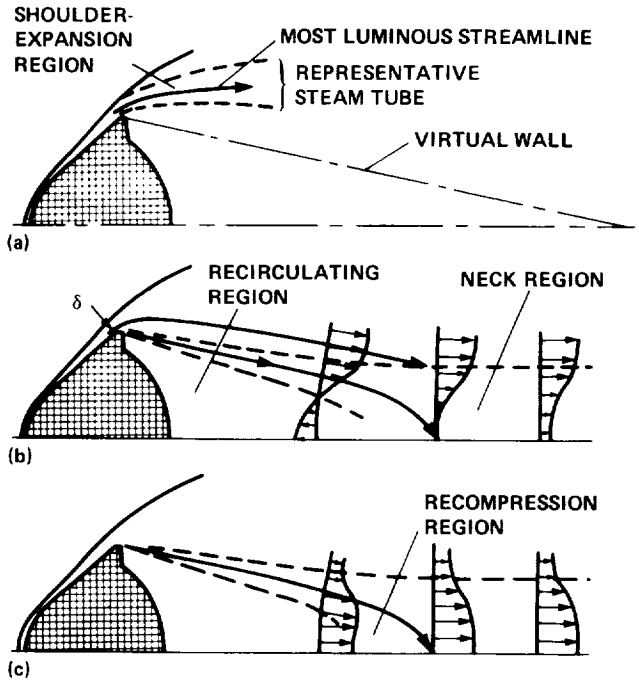

Figure 9-8.– Schematic of base-region flow field. (a) Shoulder region. (b) Velocity profiles. (c) Enthalpy profiles.

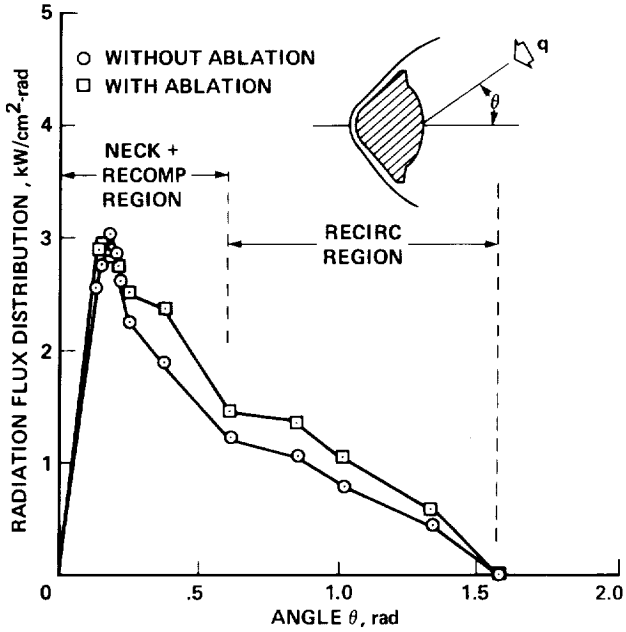

Figure 9-9.– Radiation at base stagnation point.

Experiments performed by instrumented nonablating models in shock tubes (ref. 44) showed that radiative heat fluxes are indeed significant, and the results were generally in agreement with those of reference 43. Comparison of the experimental and theoretical results was made with the early work reported in reference 42; agreement was generally good. It was determined that the ratio of base-to-front-stagnation radiative heat fluxes and pressure ratios for a Jovian probe are significant, and are in agreement with the theory of reference 43.

A summary of the work of references 43 and 44 is presented in reference 45. The work described in references 43-45 is for laminar flow. Work in progress in free-flight facilities addresses the turbulent-base-flow problem.

Second-Generation Flow-Field Codes

Although benchmark flow-field codes were being used extensively to produce forebody solutions with ever-increasing complexity and physical detail, it was apparent that the method was being strained to the utmost, and accuracy and convergence problems were becoming more severe (ref. 36). Moreover, afterbody solutions were becoming more important, and they were intimately related to forebody events (ref. 43). Thus efforts were initiated to develop a new method, one in which new coordinate systems and advanced numerical techniques would be used. A new code, CAGI (ref. 46), that was tailored to capture the major flow-field features of both the forebody and the afterbody, was developed. The code solved the unsteady compressible Navier-Stokes equations for two-dimensional axisymmetric three-dimensional flow. A finite-volume formulation was devised, rather than the usual finite-difference approximations of the differential equations. The finite-volume formulation maintains global conservation of mass, momentum, and energy over the computational volume in accord with specified fluxes at the volume boundaries. A mesh is constructed over the entire probe configuration; the mesh is flow-aligned over four principal regions—forebody shock-layer, base recirculation, outer inviscid wake, and inner inviscid wake (ref. 47). There is a singular coordinate mesh topology in the recompression

region. The computational code employed is an outgrowth of the basic factored implicit algorithm of references 48-52.

The first results of the code were presented in reference 46, where real-gas properties were modeled rigorously by a variable "gamma," which reduces to the ratio of specific heats for the case of a perfect gas. A "homogeneous sweep" algorithm was used in that study instead of the full-factored implicit algorithm. Results were presented in reference 46 for the case of flight at Mach 50; some results for mass addition along the forebody surface were included. Of particular interest is the flow-field structure about the entire bluff body and the corresponding computational mesh shown in figure 9-10 (actually adapted from ref. 47). The computed pressure distribution is shown in figure 9-11, and a comparison of the computed velocity vector field with an experimental shadowgraph by C. Park is shown in figure 9-12.

A chemically reactive gas module of the code was introduced (ref. 53) and solutions were obtained. The pressure distribution, and the temperature, enthalpy, compressibility, and species profiles were computed and compared with results of reference 9. There was generally good agreement between the results of the two studies.

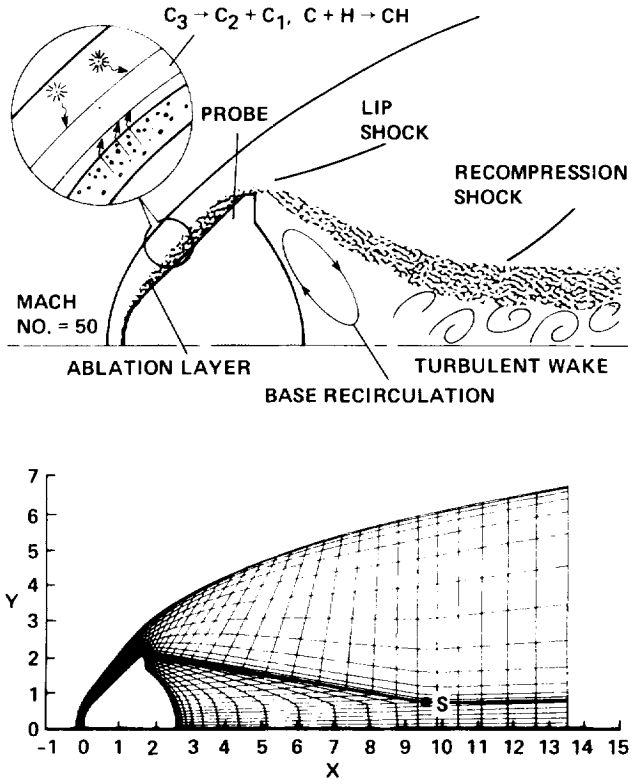

Figure 9-10.– Probe flow-field features and the computational grid.

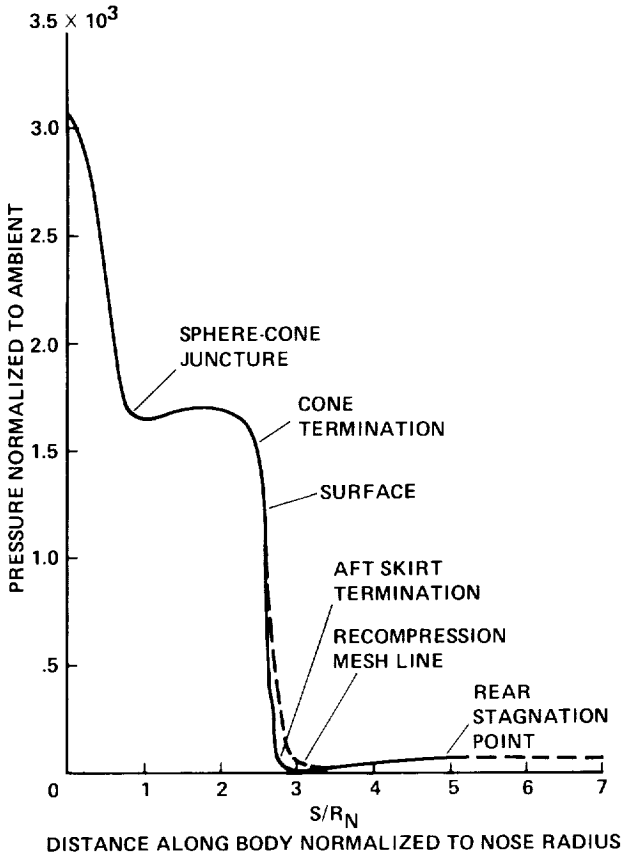

Figure 9-11.– Computed pressure distributions.

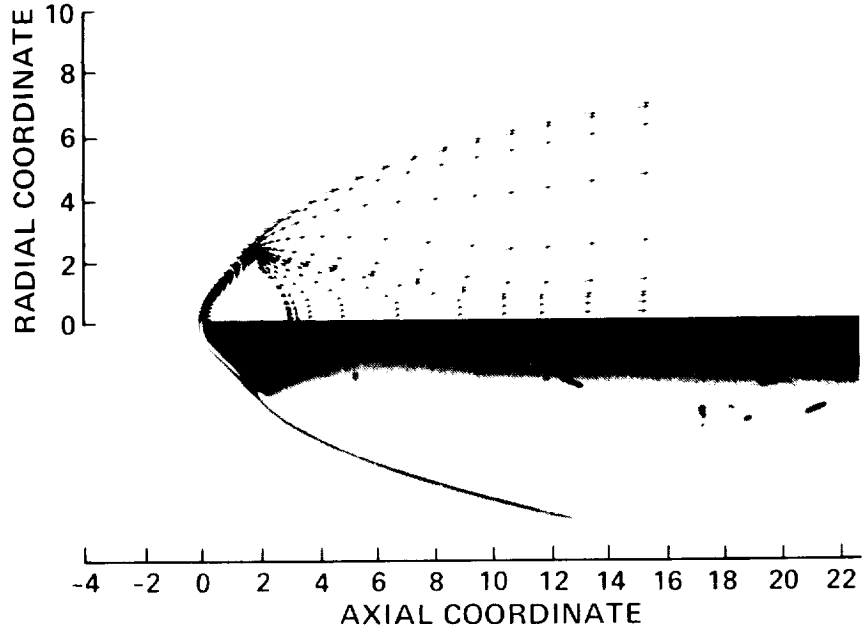

Figure 9-12.– Computed velocity field compared with free-flight shadowgraph.

Experimental Program

In addition to the analytical program, there is also an extensive experimental program on both the forebody and afterbody heat-shield materials. The objectives of the program are (1) to provide ground-based facilities that simulate the expected Jovian entry heating conditions as closely as possible and (2) to evaluate candidate materials in those facilities. The magnitude of the simulation problem is illustrated in figure 9-13, which shows the heating distribution over the forebody, at peak heating, for one of the early study versions of the entry probe. Note that the nonablating peak heating rate is greater than 40 kW/cm^2 at the stagnation point, but that it decreases to 8 kW/cm^2 at the rear end of the conical frustum. The convective heating is much more uniform over the forebody, decreasing from about 12 kW/cm^2 at the stagnation point to 9 kW/cm^2 on the frustum.

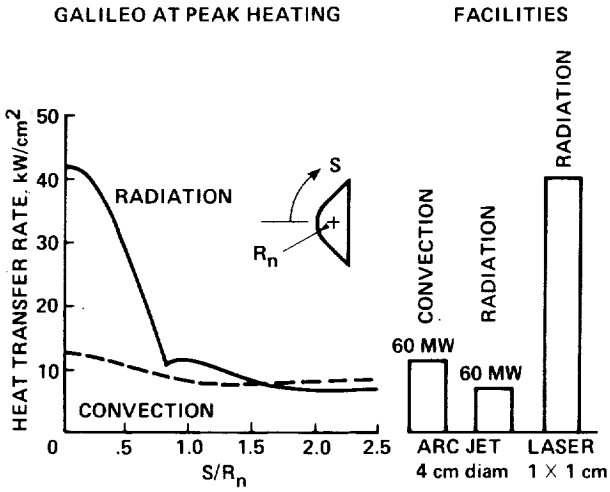

Figure 9-13.– Galileo peak-heating facilities.

The heating rate on the conical frustum, where 85% of the forebody heat-shield weight is located, is well simulated by the GPPF; the GPPF is illustrated in figure 9-14 and is described in detail in reference 54. In the arc heater, an equimolar mixture of hydrogen and helium is injected uniformly along the 4.32-m-long constrictor and heated to about 15,000 K by an electric arc, which terminates on external graphite electrodes. For the initial heat-shield test program, the facility was operated under the following conditions: power = 57.7 MW, current = 5.33 kA, flow rate = 0.12 kg/sec, bulk enthalpy = 185 MJ/kg, and model stagnation pressure = 2.2 atm. The combined convective and radiative heating rate measured by a 4-cm-diam. thin-shell tungsten calorimeter, with a radius of curvature of 20 cm, was 14.6 kW/cm^2. A radiometer of similar geometry was used to measure the radiative heating component, and the measured value was 6.0 kW/cm^2. By combining these two numbers and correcting for the reflectivity of the tungsten calorimeter cap, the applied convective heating rate was determined to be 12.0 kW/cm^2. These heating rates pertain to the model test position, which is 7 cm downstream of the 7-cm-diam. nozzle exit. The facility is equipped with four swing arms, so that a calorimeter, a pressure probe, and two ablation models can be inserted into the free jet stream during a given run. The ablation models are 4-cm-diam. flat-faced cylinders consisting of a concentrically wound carbon phenolic shroud and a 2-cm-diam. core on which recession and weight measurements are made.

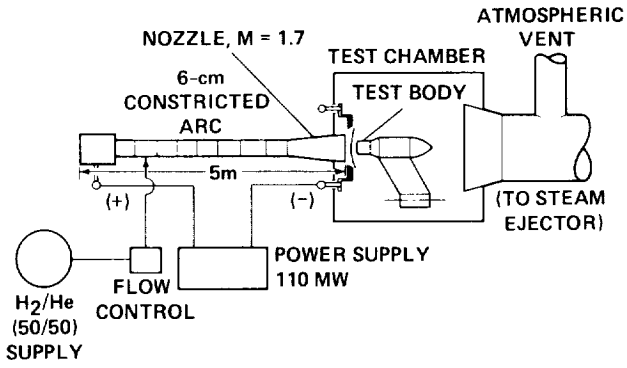

Figure 9-14.– Giant Planet Probe Facility.

Heat-shield materials studied to date include six versions of the carbon phenolic forebody materials, carbon-carbon composites, graphites, hyperpure silica reflective materials, and the nylon phenolic afterbody material. Only the work on one version of carbon phenolic and graphite will be discussed. In all the test programs, ATJS graphite is used as a control material against which the other materials are compared. It also serves as a check on the arc-jet repeatability. Results of some of the earliest tests on carbon phenolic and graphite are compared with theoretical calculations in the next section. In later work, all materials were tested at four different exposure times so that the steady-state ablation rates could be established. A comparison of the steady-state rates for chop-molded carbon phenolic (the nose-cap material) with those of the control material is shown in figure 9-15. For ATJS graphite, the steady-state mass-loss rate is 0.41 g/sec and the recession rate is 0.070 cm/sec. Corresponding values for carbon phenolic are 0.528 g/sec and 0.104 cm/sec. Thus, the carbon phenolic material has a mass-loss rate that is 28.8% higher than that of ATJS, and the recession rate is 48.6% higher than that of ATJS. The greater disparity in the recession rate is accounted for, in part, by the fact that the density of carbon phenolic is 1.45 g/cm^3 compared with 1.83 g/cm^3 for the graphite.

Of course, ablation performance is not the sole criterion for a heat-shield material. In addition to accommodating entry heating by ablation, the heat shield must protect the bond line between the shield and the structure from excessive temperatures. Thus, in addition to its ablative properties, the insulative properties of a heat-shield material are important. In flight, the superior insulation properties of carbon phenolic will tend to compensate for its somewhat poorer ablation performance.

Since the GPPF is not capable of producing radiative heating rates comparable to the peak values expected in flight, a gasdynamic laser (GDL) must be used to evaluate materials under these severe heating conditions. The facility, which is described in detail in reference 55, is a conventional combustion-driven laser which produces radiation at 10.6 μm by burning CO to produce CO_2 as the lasing medium. Although the lasing wavelength is significantly different from the UV and visible radiation expected in flight, the difference is not expected to be important, because the heat-shield materials are graybody absorbers. When the internal mirrors are freshly polished and aligned, the laser will produce an output power of 33 kW when room-temperature nitrogen is injected along with the CO and up to 45 kW when the nitrogen is heated to 1400 K by a gas-fired heat exchanger. Thus, when the output beam is focused to a 1.0-cm^2 spot, the peak radiative heating rate expected in flight (fig. 9-14) can be simulated.

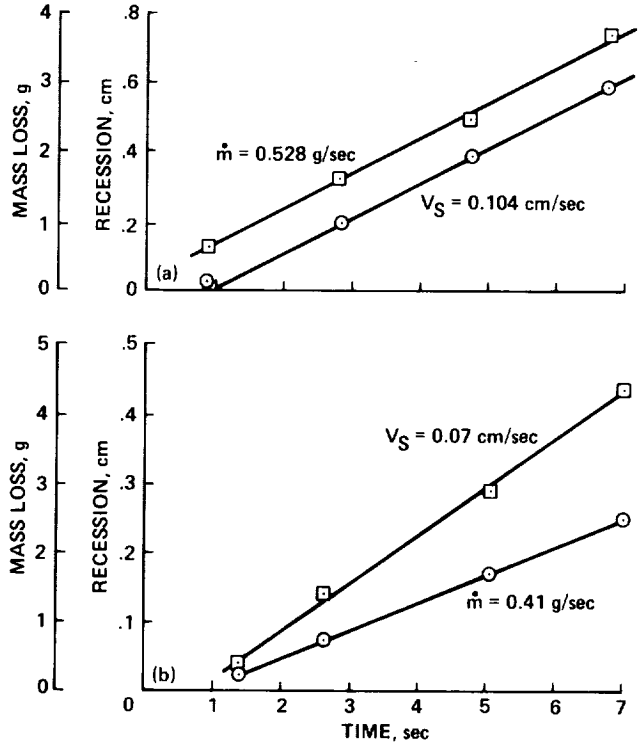

Figure 9-15.– Ablation results at 57.7 MW. (a) Carbon phenolic. (b) ATJS graphite.

Early in the laser testing (ref. 56), it was discovered that carbon phenolic tends to spall (fig. 9-16) when exposed to severe radiative heating. Although this phenomenon may be unique to laser testing, it must be assumed, to be conservative, that it will also occur during peak heating of the Galileo probe. In order to account for spallation in the heat-shield design, the phenomenon must be quantified; such tests were performed.

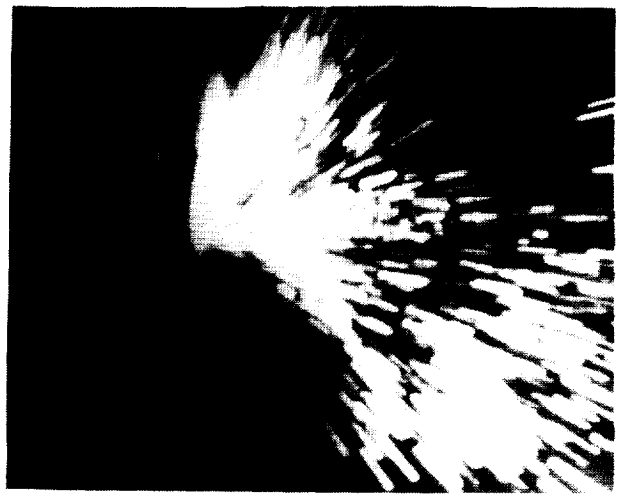

Figure 9-16.– Carbon phenolic spallation.

The experimental setup for these tests is illustrated in figure 9-17 and described in reference 57. The output beam of the GDL is collimated into an 8-cm diameter and then transformed into a spatially uniform 1.0-cm by 1.0-cm spot by means of a segmented mirror. This device consists of an eight-by-eight array of 1-cm by 1-cm polished molybdenum segments. Although the segments are optically flat, they are mounted on a curved, water-cooled substrate which gives the device a 1.0-m focal length. The mirror divides the incident beam into many 1-cm by 1-cm beams and superimposes them at the focal point. The focal image is then reimaged one-to-one, by a 1.5-m-focal-length mirror, into a canister in which the test specimen is mounted. The canister (fig. 9-18) is designed with suitable baffling so that the laser beam can enter, but the spalled particles cannot escape. An air jet in front of the specimen deflects the laser plume upward and allows the beam to reach the surface without significant absorption in the plume.

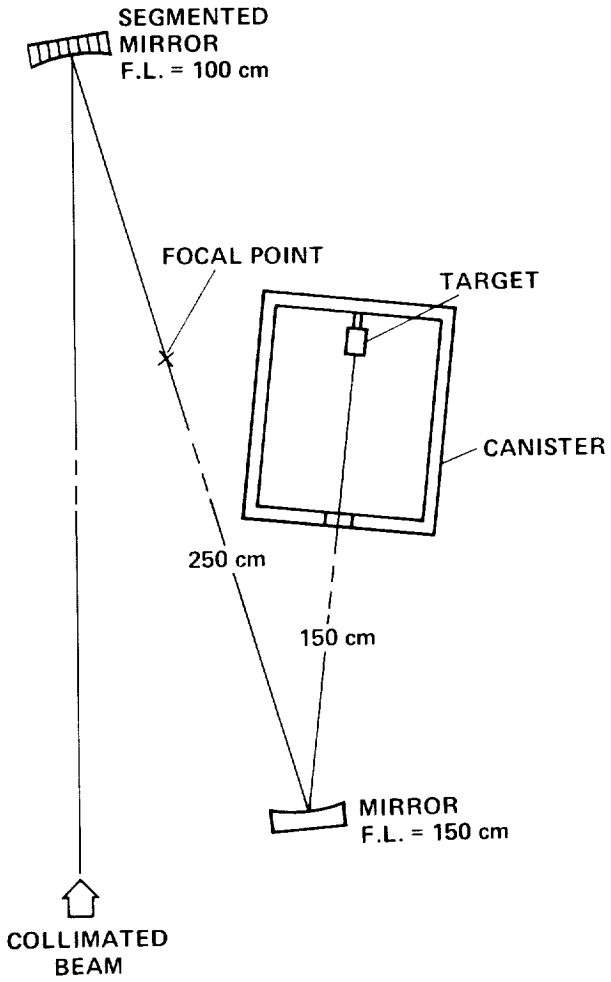

Figure 9-17.– Experimental setup for spallation tests.

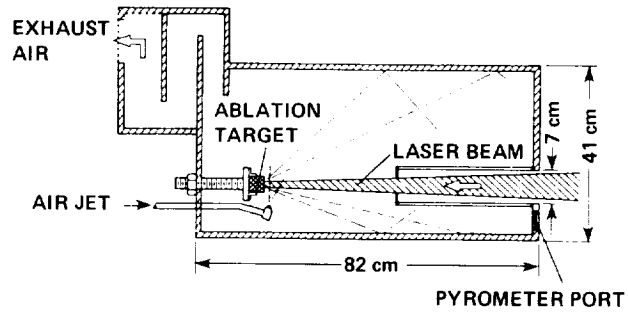

Figure 9-18.– Spallation canister.

Typical spallation results are shown in figure 9-19. The total mass loss is determined by weighing the sample (3 cm square by 5.1 cm long) before and after exposure, and the spallation mass loss is determined by collecting and weighing the particles in the bottom of the canister. At least three exposure times are used so that the steady-state total mass loss and spallation rates can be obtained. Note that for the data shown, 18.3% of the mass loss is by spallation at an intensity of 23 kW/cm^2. By repeating the test at a variety of intensities, a correlation of spallation fraction as a function of intensity will be developed. The calculated radiation history in flight will then be used in conjunction with the correlation to determine the total mass loss by spallation over the complete heating pulse and over the entire forebody heat shield.

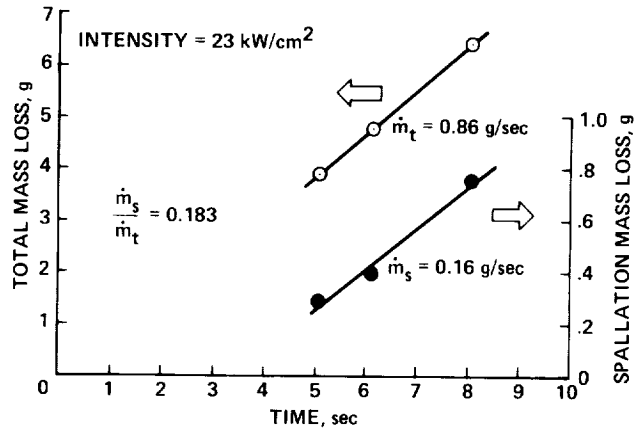

Figure 9-19.– Spallation results for carbon phenolic.

Because of the power limitations of the laser, the peak flight radiative rate cannot be simulated on a spot larger than 1 cm by 1 cm. Use of such a small spot size results in a hole being bored in the end of a square sample 3 cm by 3 cm in size, and may produce results that are unique to the test setup. To check for scale effects, future work will involve tests with a square segmented mirror 2 cm on a side, which will produce a square spot 2 cm on a side on the end of a square sample 2 cm on a side. Thus the test sample will be fully enveloped in the beam in a better simulation of the flight situation. Because of the power limitation, these tests will be limited to intensities of 10 kW/cm^2 or less. The results will be compared with the 10-kW/cm^2 results with the 1-cm segmented mirror to see whether there are significant differences between the two test techniques. Note that the intensity of 10 kW/cm^2, which can be achieved with the 2-cm mirror, is a good simulation of the maximum radiative rate expected on the conical frustum of the entry probe.

Code Validation

It has been noted that the computational studies that have been discussed push the limits of theoretical analysis, and that they were used to calculate material responses to environments that cannot be simulated fully in any existing experimental facility. Therefore, it is very difficult to validate these theoretical methods experimentally. The best efforts to do this to date were reported in references 58 and 59. We present here a very brief summary of some of the results presented in reference 59.

The data used for this code validation were obtained using the GPPF (ref. 54), wherein the equimolar mixture of hydrogen and helium gas was injected uniformly along the constricted arc (fig. 9-14), and was heated to about 15,000 K, as noted previously. The facility operating conditions for the data discussed below were as follows: arc power, 55 MW; arc current, 5330 A; mass flow rate, 0.118 kg/sec; pressure, 5 atm.

The models used for the test were 4-cm-diam. flat-faced cylinders. The flat face was 7 cm from the nozzle exit, and the exit was 7 cm in diameter. The heat flux to the models was measured using a thin-shell calorimeter; the calorimeter was also 4 cm in diameter, but it had a 20-cm radius of curvature on the front face. The models and calorimeter were mounted on separate rotating arms so that they could be swung alternately to the same position of the arc stream, as described previously.

Absorbed heat flux data from this test are compared with heat fluxes computed by the RASLE code in figure 9-20. The calculated values generally fall within the estimated $\pm 10\text{-MW/m}^2$ error bands of the calorimeter data. The RASLE solutions were obtained using a nonablating boundary condition for the tungsten surface of the calorimeter. The application of the RASLE code to these experimental conditions was not direct, primarily because the RASLE code is based on hypersonic approximations and the test Mach number was only 1.2. These approximations had to be modified for the subject analysis without significantly modifying the structure of the RASLE code. It was found convenient to obtain RASLE solutions for an equivalent sphere rather than the cylindrical models. From a parametric study (ref. 59), it was found that a 4-cm-diam. cylinder is equivalent, in terms of stagnation-point heat-transfer rate, to a spherical model with an 8-cm radius.

The response of the ablation models to the GPPF arc flow is shown in figure 9-21 for two materials. For the computed curves RASLE was used for the flow-field analysis and CMA for the material response. The agreement is good for the ATJS graphite, but the predicted recession is twice the measured recession for the carbon phenolic. As for the Jupiter entry conditions, the predicted convective heating was reduced to a negligible value by ablation products. The reason for the much better agreement for ATJS graphite than for carbon phenolic is not clear. One reason may be that the material properties were better known for the ATJS graphite than for the carbon phenolic. The question of material properties for carbon phenolic is under investigation.

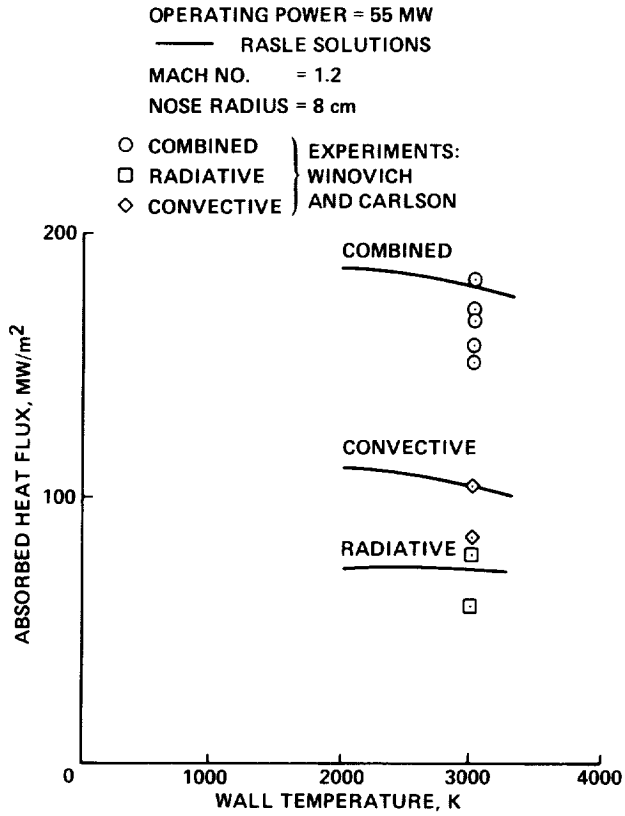

Figure 9-20.– Comparison of computed and measured absorbed calorimeter heating.

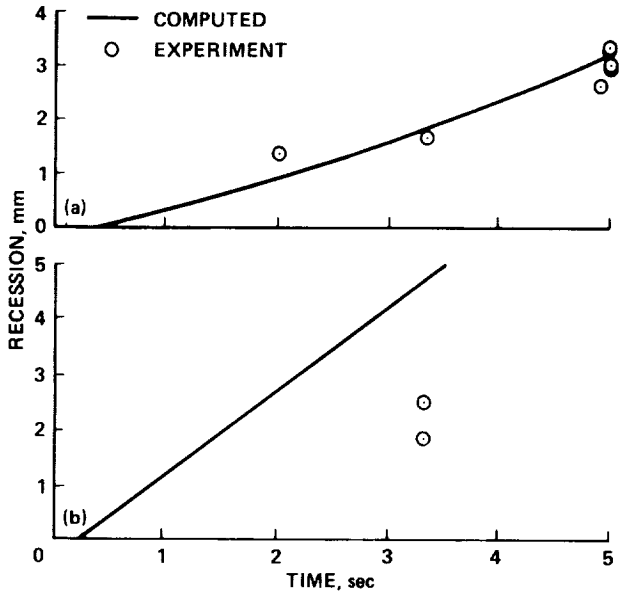

Figure 9-21.– Comparison of predicted and measured ablation tests in GPPF. (a) ATJS graphite. (b) Carbon phenolic.

Consensus Benchmark Flow-Field Solutions

To provide a set of solutions as a standard for calibrating other codes, a matrix of flight conditions for entry into the nominal Jovian atmosphere was specified, and forebody flow-field solutions were obtained by the COLTS and RASLE codes. The probe was a 44.25°-half-angle sphere-cone; it is described in reference 60. Two probe weights were studied: 290 kg and 310 kg. The results of the study are shown for the 310-kg probe in terms of mass loss rate at various times in the entry trajectory by the symbols in figure 9-22. It may be noted that there is consistently good agreement between COLTS and RASLE, except near the peak mass-loss rates at 50.3 and 51.5 sec. Examination of these results by J. N. Moss, W. E. Nicolet, A. Balakrishnan, W. C. Davy, M. J. Green, and J. T. Howe failed to resolve the differences near peak mass loss. Therefore, a "consensus" curve was agreed on; it is shown by the solid line in figure 9-22. The mass loss integrated over the trajectory is 101 kg. If the curve were drawn through the RASLE results (the square symbols), the result would be an additional 3 kg (approximate) of heat-shield mass. The integrated heat-shield mass loss is presented and discussed in references 60 and 61 for both the nominal and cool dense atmospheres.

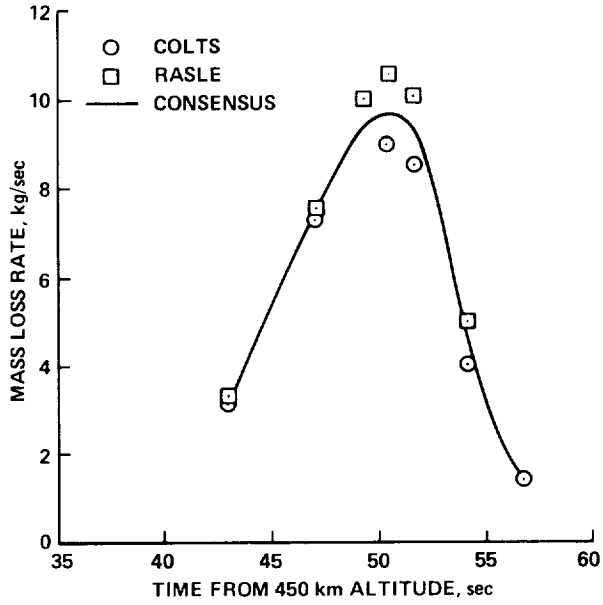

Figure 9-22.– 310-kg probe benchmark solution results: nominal Jovian atmosphere, nominal entry angle.

The distribution of mass-loss rate about the body at 47, 50.3, and 54.1 sec is shown in figure 9-23, which was adopted from references 60 and 62. The mass-loss rate distribution is shown nondimensionally, where local mass-loss rate was normalized by the product of instantaneous flight velocity and atmospheric density. At 47 sec, both the integrated mass-loss rate (fig. 9-22) and the mass-loss distribution about the body (fig. 9-23) are in good agreement. At 50.3 and 54.1 sec, both figures show a generally higher mass-loss rate by RASLE—especially on the conical frustum where most of the probe mass resides.

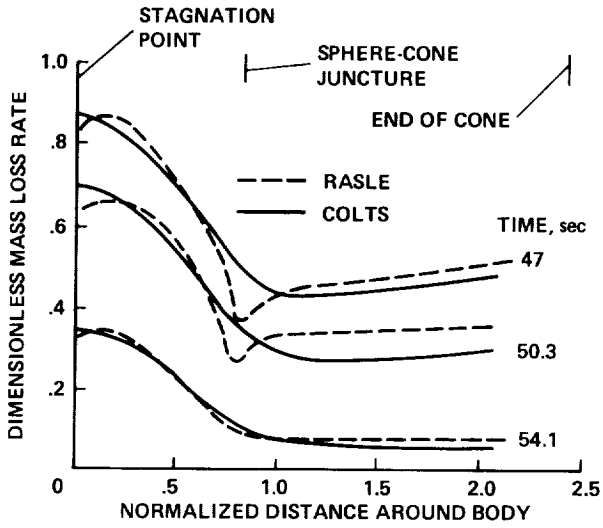

Figure 9-23.– Comparison of coupled carbon phenolic mass loss distributions about 310-kg probe: nominal atmosphere.

These consensus solutions had a quasi-steady-state ablation boundary condition. Moreover, by prior agreement, the radiative boundary condition was that the surface absorbed all of the flux incident upon it—a very severe condition.

In reference 61, the more severe surface heating-rate history derived from the RASLE flow-field results (ref. 60) were input into the CMA code, which is a transient material-response code for a pyrolyzing ablating material of finite thickness wherein material properties are temperature-dependent. An allowable bond-line temperature between the aeroshell and the heat shield was specified, and the required heat-shield thickness distribution was determined. For the nominal atmosphere, safety margins were added to account for uncertainties (such as spallation effects). Thus a heat-shield "design" from a benchmark material code was produced (fig. 9-24). Similar results were obtained for the cool dense atmosphere (without safety margins). The question of survivability of the nominal benchmark "design" in the cool dense entry environment was assessed in reference 61. Results of that paper suggest that for a thermochemically ablating heat shield with physical uncertainties that fall within the prescribed margin allowances, the 310-kg probe would survive the nominal Jovian atmosphere. Moreover, there appears to be a reasonable probability that the probe would survive off-nominal atmospheres without margin.

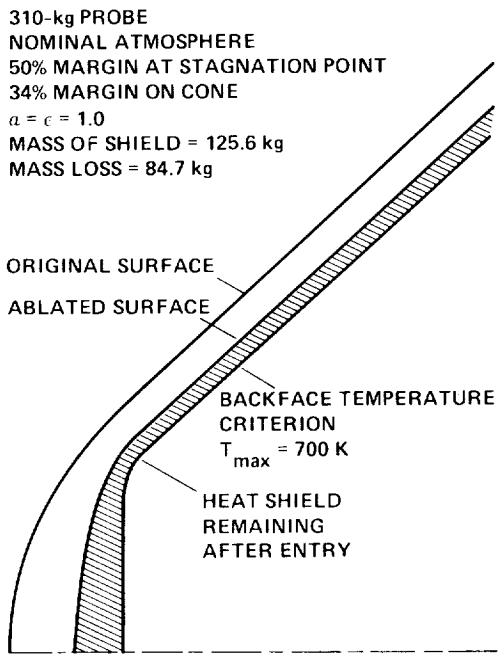

Figure 9-24.– Transient heat-shield response: carbon phenolic.

Conclusions

A supporting research and technology effort related to the entry of the Galileo probe into the Jovian atmosphere has been reported. Entry at various initial conditions into numerous model atmospheres by probes of various size and mass has been studied experimentally and computationally to determine both forebody and afterbody heating environments and forebody heat-shield requirements. Two kinds of codes were used: (1) codes that use engineering correlations and (2) benchmark codes that use basic modeled physical phenomena. Detailed comparisons of the benchmark flow-field codes have been performed, and they show that the turbulence modeling of a hot gas about a relatively cool probe that is massively ablating has important consequences and needs continued development. Ranking of various turbulence models according to severity has been performed.

For the first time in entry technology experience, both forebody and afterbody heating are severe. For that reason, a second-generation benchmark code that computes the flow over the entire probe and into the wake is being developed. The code uses very advanced computational fluid dynamic concepts and techniques. Initial results have been obtained for flow about the entire Galileo probe configuration, and some results have been obtained for flow of a reacting gas.

Experiments were performed in the GPPF to simulate probe flank heating levels, and with the gasdynamic laser to simulate stagnation-region heating for several materials. Spallation was studied and partially quantified in the gasdynamic laser. Efforts to validate the computer codes by tests in the GPPF were performed for several materials.

For the "heavy" Galileo probe, a set of consensus benchmark flow-field solutions has been obtained. Results that contributed to these solutions have been used in a benchmark material-response code to assess the prospects for survivability of the probe during entry into the atmosphere of Jupiter.

The overall effort has revealed areas for future entry technology research that will lead to understanding of phenomena that are currently uncertainly known and as a result are carried in the weight margin. These include turbulence modeling and mechanical spallation in particular.

REFERENCES

1. Tauber, M. E.; and Yang, L.: Performance Comparisons of Maneuvering Vehicles Returning from Orbit. Paper 87-2490 CP, AIAA Atmospheric Flight Conference, Monterey, August 1987.

2. Green, M. J.; Balakrishnan, A.; and Swenson, B. L.: Aerothermodynamic Environment for a Titan Probe with Deployable Decelerator. AIAA Paper 85-1063, Williamsburg, 1985.

3. Howe, J. T.; Pitts, W. C.; and Lundell, J. H.: Survey of the Supporting Research and Technology for Thermal Protection of the Galileo Probe. AIAA Paper 81-1068, Palo Alto, 1981.

4. Entry Probes in the Outer Solar System. Report of the Outer Planet Probe Science Study Group, D. M. Hunten, Chairman, NASA Ames Research Center, July 1975.

5. The Planet Jupiter. NASA SP-8069, 1971.

6. Hunten, D. M.: Atmospheres and Ionospheres. Jupiter Studies of the Interior, Magnetosphere, and Satellites, T. Gehrels, ed., Univ. Ariz. Press, 1975, p. 23.

7. Houck, J. R.; Pollack, J. B.; Schaak, D.; Reed, R. A.; and Summers, A.: Jupiter: Its Infrared Spectrum from 16 to 40 Micrometers. Science, vol. 189, 1975, pp. 720-722.

8. Sutton, K.; Jones, J. J.; and Powell, R. W.: Effects of Atmospheric Structure on Radiative Heating for Jupiter Entry Probe. Progress in Astronautics and Aeronautics, Vol. 64, Outer Planet Entry Heating and Thermal Protection, R. Viskanta, ed., 1979, pp. 3-21.

9. Moss, J. N.: A Study of the Aerothermal Entry Environment for the Galileo Probe. AIAA Paper 79-1081, 1979.

10. Sutton, K.; Moss, J. N.; Falaniga, R. A.; and Olstad, W. B.: Outer Planet Entry Probes Aerothermal Environment-Status of Prediction Methodology. AIAA Paper 75-1148, 1975.

11. Nicolet, W. E.; Waterland, L. R.; and Kendall, R. M.: Methods for Predicting Radiation Coupled Flowfields about Planetary Entry Probes. Progress in Astronautics and Aeronautics, Vol. 59, Aerodynamic Heating and Thermal Protection Systems, L. S. Fletcher, ed., 1978, pp. 120-136.

12. Sutton, K.: Radiative Heating About Outer Planet Entry Probes. AIAA Paper 75-183, 1975.

13. Walberg, G. D.; Jones, J. J.; Olstad, W. B.; Sutton, K.; Moss, J. N.; and Powell, R. W.: Mass Loss Shape Change and Real-Gas Aerodynamic Effects on a Jovian Atmospheric Probe. Acta Astronaut., vol. 4, Pergamon Press, 1977, pp. 555-575.

14. Sutton, K.; Jones, J. J.; and Powell, R. W.: Effect of Probe Configuration on Radiative Heating During Jupiter Entry. Progress in Astronautics and Aeronautics, Vol. 56, Thermophysics of Spacecraft and Outer Planet Entry Probes, A. M. Smith, ed., 1977, pp. 355-376.

15. Arnold, J. O.: A Shock Tube Determination of the Electronic Transition Moment of the C_2 (Swan) Bands. J. Quant. Spectros. Radiation Trans., vol. 8, no. 1781, 1968.

16. Cooper, D. M.; and Borucki, W. J.: Measurements of Hydrogen-Helium Radiation at Shock-Layer Temperatures Appropriate for Jupiter Entries. J. Quant. Spectros. Radiation Trans., vol. 13, no. 1047, 1973.

17. Cooper, D. M.: Absolute Measurements of the Electronic Transition Moments of Seven Band Systems of the C_2 Molecule. Ph.D. Thesis, York Univ., Toronto, 1974.

18. Cooper, D. M.; and Nicholls, R. W.: Measurements of the Electronic Transition Momenta of C_2 Band Systems. J. Quant. Spectros. Radiation Trans., vol. 15, no. 139, 1975.

19. Cooper, D. M.; and Langhoff, S. R.: Electronic Structure and Properties of the Lowest Lying States of CO. Thirty-Second Symposium on Molecular Spectroscopy, Ohio State Univ., Columbus, July 13-17, 1977.

20. Arnold, J. O.; and Langhoff, S. R.: A Theoretical Study of the Low-Lying Singlet States of C_3. Paper RD1, Thirty-Third Symposium on Molecular Spectroscopy, Columbus, OH, June 12-16, 1978.

21. Cooper, D. M.: A Theoretical Study of the Electronic Structure and Properties of Selected Triplet States of C_2. Presented at the American Conf. on Theoretical Chem., Boulder, CO, June 25-30, 1978.

22. Cooper, D. M.; and Jones, J. J.: An Experimental Determination of the Cross Section of the Swings Band System of C_3. J. Quant. Spectros. Radiation Trans., vol. 22, no. 2, 1979, pp. 201-208.

23. Treffers, R. R.; and Gilra, D. P.: The Vibrational Spectrum of C_3 in the 5-Micron Region. Astrophys. J., vol. 202, no. 839, 1975.

24. Prakash, S. G.; and Park, C.: Shock Tube Spectroscopy of C_3+C_2H Mixture in the 140-700nm Range. AIAA Paper 79-0094, Jan. 1979.

25. Cooper, D. M.: Theoretical Electronic Transition Moments for the Kallik-Ramsey, Fox-Herzberg, and Swan Systems of C_2. J. Quant. Spectros. Radiation Trans., vol. 26, no. 2, 1981.

26. Arnold, J. O.; Cooper, D. M.; Park, C.; and Prakash, S. G.: Line-by-Line Transport Calculations for Jupiter Entry Probes. Prog. Astronaut. Aeronaut., Vol. 69, Entry Heating and Thermal Protection, W. B. Olstad, ed., 1980, pp. 52-82.

27. Nicolet, W. E.: Radiative Heating Environments for Jovian Entry Conditions. Prog. Astronaut. Aeronaut., Vol. 49, Radiative Transfer and Thermal Control, A. M. Smith, ed., 1977, pp. 231-250.

28. Nicolet, W. E.; Morse, H. L.; and Vojvodich, N. S.: Outer Planet Probe Thermal Protection. Part I. Aerothermodynamics Environment. AIAA Paper 74-700, 1974.

29. Nicolet, W. E.; Howe, J. T.; and Mezines, S. A.: Outer Planet Probe Entry Thermal Protection. Part II. Heat Shielding Requirements. AIAA Paper 74-701, 1974.

30. Tauber, M. E.: Heat Protection for Atmospheric Entry into Saturn, Uranus and Neptune. Preprint AAS-7;-145, Seattle, 1971.

31. Moss, J. N.; Anderson, E. C.; and Boltz, C. W., Jr.: Aerothermal Environment for Jupiter Entry Probes. Prog. Astronaut. Aeronaut., Vol. 56, Thermophysics of Spacecraft and Outer Planet Entry Probes, A. M. Smith, ed., 1977, pp. 333-354.

32. Moss, J. N.; Anderson, E. C.; and Simmons, A. L.: The Impact of Turbulence on a Radiating Shock Layer with Coupled Ablation Injection. AIAA Paper 78-1186, 1978.

33. Nicolet, W. E.; and Balakrishnan, A.: Methods for Predicting Off-Stagnation Point Flow Fields for Planetary Entry Probes. Prog. Astronaut. Aeronaut., Vol. 69, Entry Heating and Thermal Protection, W. G. Olstad, ed., 1980, pp. 26-51.

34. Hopkins, R. A.; and Nerem, R. M.: An Experimental Investigation of Heat Transfer from a Highly Cooled Turbulent Boundary Layer. AIAA J., vol. 6, no. 10, Oct. 1968, p. 1912.

35. Kumar, A.; Graves, R. A.; Weilmuenster, K. J.; and Tiwari, S. N.: Laminar and Turbulent Flow Solutions with Radiation and Ablation Injection for Jovian Entry. AIAA Paper 80-0288, 1980.

36. Menees, G. P.: An Evaluation of Computer Codes for Simulating the Galileo Probe Aerothermal Entry Environment. AIAA Paper 81-1069, 1981.

37. Menees, G. P.; and Lombard, C. K.: The Effect of Modeled Turbulence on a Hypersonic Shock Layer with Massive Ablation Injection. AIAA Paper 81-1071, 1981.

38. Nicolet, W. E.; Davy, W. C.; and Wilson, J. F.: Galileo Probe Forebody Entry Thermal Protection: Aerothermal Environments and Heat Shielding Requirements. ASME Paper 80-ENAs-24, 1980.

39. Zoby, E. V.; Sutton, K.; Olstad, W. B.; and Moss, J. N.: An Approximate Inviscid Radiating Flowfield Analysis for Outer Planet Entry Probes. AIAA Paper 78-189, 1978.

40. Zoby, E. V.; Moss, J. N.; and Sutton, K.: Approximate Convective Heating Equations for Hypersonic Flow. AIAA Paper 79-1078, 1979.

41. Lockman, W. L.: Base Heating Measurements on Apollo Block 2 Command Module. J. Spacecraft Rockets, vol. 7 no. 1, Jan. 1970, pp. 93-95.

42. Stephenson, J. D.: Measurement of Optical Radiation from the Wake of Ablating Blunt Bodies in Flight at Speeds up to 10 km per Second. NASA TN D-2760, 1965.

43. Park, C.: Modeling of Radiative Heating in Base Region of Jovian Entry Probe. Prog. Astronaut. Aeronaut., Vol. 69, Entry Heating and Thermal Protection, W. G. Olstad, ed., 1980, pp. 124-147.

44. Shirai, H.; and Park, C.: Experimental Studies of Radiative Base Heating of a Jovian Entry Model. Prog. Astronaut. Aeronaut., Vol. 69, Entry Heating and Thermal Protection, W. B. Olstad, ed., 1980, pp. 148-171.

45. Park, C.: Problems of Radiative Base Heating. Paper 79-0919, AIAA/NASA Conf. on Adv. Technol. for Future Space Systems, Hampton, 1979.

46. Lombard, C. K.; Davy, W. C.: and Green, M. J.: Forebody and Base Region Real-Gas Flow in Severe Planetary Entry by a Factored Implicit Numerical Method. Part 1. Computational Fluid Dynamics, AIAA Paper 80-0065, 1980.

47. Lombard, C. K.; Lombard, M. P.; Menees, G. P.; and Yang, J. Y.: Some Aspects of Adapting Computational Mesh to Complex Flow Domains and Structures with Application to Blown Shock Layer and Base Flow. Presented at the Workshop on Numerical Grid Generation Techniques of Partial Differential Equations, NASA Langley Research Center, Oct. 1980.

48. Warming, R. F.; and Beam, R. M.: An Implicit Finite-Difference Algorithm for Hyperbolic Systems in Conservation-Law Form. J. Comp. Phys., vol. 22, 1976, pp. 87-110.

49. Beam, R. M.; and Warming, R. F.: An Implicit Factored Scheme for the Compressible Navier-Stokes Equations. AIAA Paper 77-645, 1977.

50. Warming, R. F.; and Beam, R. M.: On Construction and Application of Implicit Factored Schemes for Conservation Laws. SIAM-AMS Proc., vol. 11, 1977.

51. Briley, W. R.; and McDonald, H.: Solution of the Multidimensional Compressible Navier-Stokes Equations by a Generalized Implicit Method. J. Comp. Phys., vol. 24, 1977, pp. 372-397.

52. Briley, W. E.; and McDonald, H.: Solution of the Three-Dimensional Compressible Navier-Stokes Equations by an Implicit Technique. Proc. Fourth Intern. Conf. on Numerical Methods in Fluid Dynamics, Springer-Verlag, NY, 1975. (See also United Aircraft Research Laboratories Report M911363-6, 1973.)

53. Davy, W. C.; Lombard, C. K.; and Green, M. J.: Forebody and Base Region Real Gas Flow in Severe Planetary Entry by a Factored Implicit Numerical Method. Part II. Equilibrium Reactive Gas, AIAA Paper 81-0282, Jan. 1981.

54. Winovich, W.; and Carlson, W. C. A.: The Giant Planet Facility. Paper presented at the 25th Instrument Society of America Symposium, Anaheim, CA, May 1979.

55. Lundell, J. H.; Otten, L. J.; and Dickey, R. R.: The CO_2 Gasdynamic Laser as a High-Intensity Radiation Facility. Presented at the AIAA 13th Aerospace Sciences Meeting, Pasadena, CA, 1975.

56. Lundell, J. H.; and Dickey, R. R.: Response of Heat-Shield Materials to Intense Laser Radiation. Prog. Astronaut. Aeronaut., Vol. 64, Outer Planet Entry Heating and Thermal Protection, R. Viskanta, ed., AIAA, New York, 1979, pp. 193-209.

57. Dickey, R. R.; and Lundell, J. H.: A Technique for Evaluating the Jovian Entry-Probe Heat-Shield Material with a Gasdynamic Laser. Presented at the International Congress on Instrumentation in Aerospace Simulation Facilities, Monterey, CA, Sept. 24-26, 1979. (IEEE Publication 79 CH 1500-8 AES.)

58. Davy, W. C.; Menees, G. P.; Lundell, J. H.; and Dickey, R. R.: Hydrogen-Helium Ablation of Carbonaceous Material: Numerical Simulation and Experiment. Prog. Astronaut. Aeronaut., Vol. 64, Outer Planet Entry Heating and Thermal Protection, R. Viskanta, ed., AIAA, New York, 1979, pp. 228-244.

59. Green, M. J.; and Davy, W. C.: Numerical Simulation of Experiments in the Giant Planet Facility. Prog. Astronaut. Aeronaut., Vol. 69, Entry Heating and Thermal Protection, W. B. Olstad, ed., AIAA, New York, 1980, pp. 172-197.

60. Balakrishnan, A.; and Nicolet, W. E.: Galileo Probe Forebody Thermal Protection: Benchmark Heating Environment Calculations, AIAA Paper 81-1072, June 1981.

61. Green, M. J.; and Davy, W. C.: Galileo Probe Forebody Thermal Protection. AIAA Paper 81-1072, June 1981.

62. Moss, J. N.; and Kumar, A.: Significance of Turbulence and Transition Location on Radiative Heating and Ablation Injection. AIAA paper 81-0281, 1981.

CHAPTER 10

HYPERVELOCITY FLIGHT AT LOW DENSITY, NONEQUILIBRIUM FLOW

In figure 1-1 of chapter 1, near the center of the figure, a short double horizontal line at about 50-km altitude was labeled "thermochemical nonequilibrium." It was shown to illustrate that at high altitudes where gaseous molecules, atoms, etc., are less dense, collisional processes occur at diminished frequency. The practical significance is that the gas cap over a hypervelocity vehicle approaches thermodynamic and chemical equilibrium at a finite rate—it does not occur instantaneously. For early hypervelocity flight (e.g., Apollo), it was not necessary to understand this nonequilibrium regime in any detail—it was only necessary to be sure that a vehicle could safely pass through that high-altitude domain to lower altitudes where most of the deceleration and aerodynamic heating occurs. Nevertheless, we thought we understood the main features of the high-altitude flight—it was out of chemical equilibrium, and ways were devised to study flow fields that were relaxing chemically at a finite rate. However, in this decade, Park (ref. 1) and others deduced that the flow field is out of equilibrium thermodynamically as well. That is, the internal states of species are not equilibrated, and the gas may need to be characterized by more than one temperature locally (a translational temperature), as well as vibrational, rotational, and electronic temperatures. These temperatures equilibrate at finite rates that may need to be determined. Currently, there is intense activity aimed at achieving an understanding of thermochemical nonequilibrium because a new class of hypervelocity aeromaneuvering vehicles will function in that high-altitude regime. That regime is depicted by the "u"-shaped area centered at about 9 km/sec in figure 10-1, which may extend far to the right to include very high enthalpy hypervelocity flight on

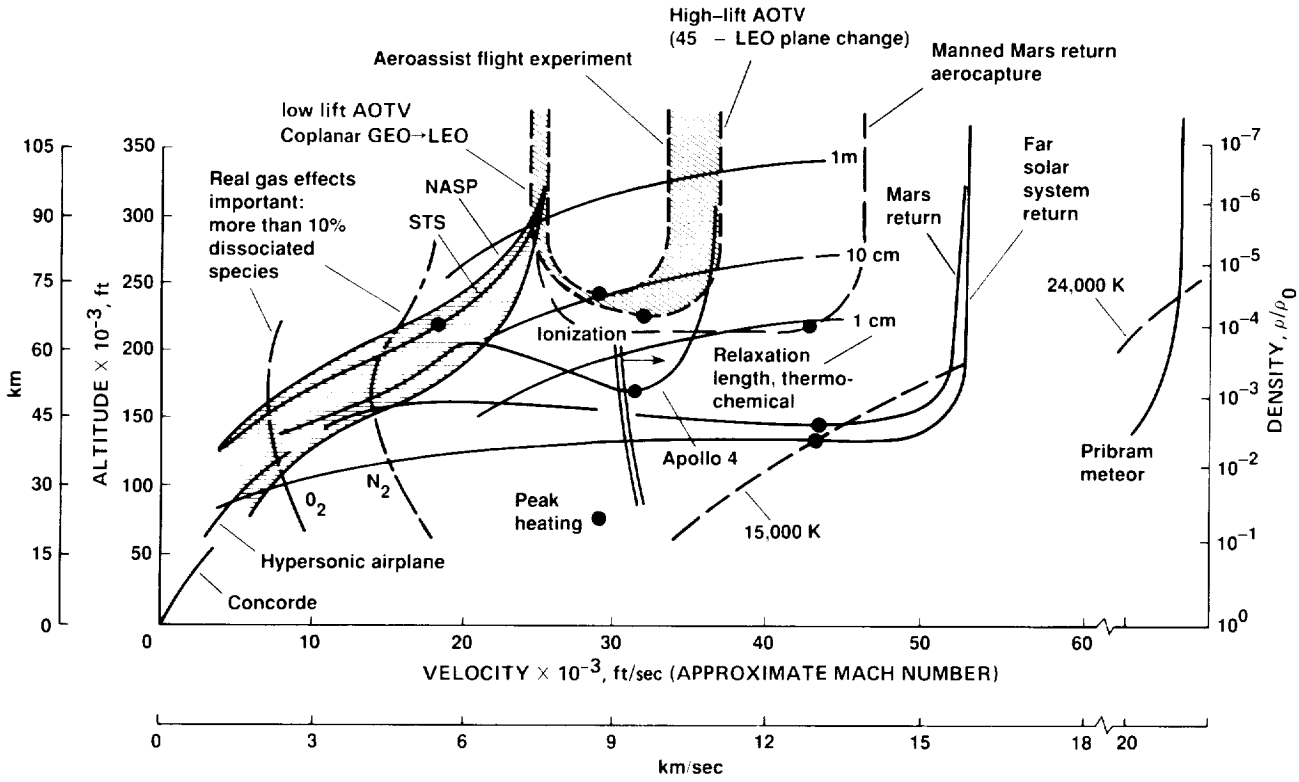

Figure 10-1.– Flight regime highlighting thermochemical nonequilibrium.

return from solar system missions as shown for the manned Mars return wherein the vehicle is captured by a dip into the upper atmosphere, exits, and then rendezvous with another vehicle orbiting Earth. An attempt to quantify the phenomena is shown by the solid lines labeled 1 cm, 10 cm, and 1 m. These lines were inferred from figure 10 of reference 2. They represent experimental correlations of the distance behind a normal shock wave required for the flow to equilibrate thermochemically and will be discussed in more detail in Chapter 11. For example, for the blunt-drag-configured, aeroassist flight-experiment vehicle being planned, the flow behind the bow shock tends to equilibrate in a distance of about 10 cm near peak heating (the total shock standoff distance is about 20 cm (ref. 3). For a lifting configuration, the flow field is more complicated. Nevertheless, an extensive literature on aeroassisted space transfer vehicles has been developed by the use of sophisticated approximate analysis. Such vehicles replace a costly near-Earth propulsive maneuver by an aerodynamic maneuver in the upper atmosphere. They are the key to economic utilization of Earth-moon space, the exploration of Mars, and other future space missions. Nonequilibrium flow phenomena affect forces, moments, and heat transfer to vehicles. Some discussion of these vehicle concepts will be made in the next chapter.

But in this chapter let us examine chemical nonequilibrium in a flowing gas in a simple way. The coupling of chemical rate equations to the flow-field equations, the solutions which result, and some useful notions will be illustrated. Importantly, all spatial variations in flow variables, thermodynamic quantities, and chemical composition occur because the chemical reactions proceed at a finite rate.

The flow model chosen for the analysis is that of a normal shock moving at velocity $\bar{U}$ into quiescent CO_2 at density ρ_∞.[1] It is like compressible flow in a constant-area duct (Chapter 1) wherein a normal shock wave alters the thermodynamic and chemical state of the gas—this time the latter changes at a finite rate. The corresponding flow field as seen by an observer traveling with the shock is shown in figure 10-2.

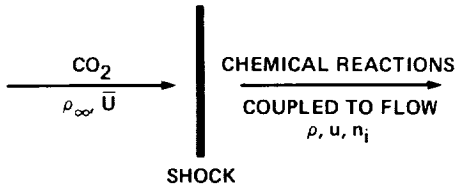

Figure 10-2.-- Flow of a compressible gas across a normal shock wave which leads to gaseous chemical reactions at a finite rate.

Flow-Field Equations and Boundary Conditions

The equations describing the flow field behind the shock are (neglecting transport phenomena):

$$\rho u = \rho_\infty \bar{U} = \text{constant} \tag{1}$$

$$\rho u \left(\frac{du}{dx}\right) = -\left(\frac{dp}{dx}\right) \tag{2}$$

[1]As of this writing, the current model of the Mars or Venus atmosphere is about 95% CO_2 and 5% N_2 (ref. 4). In 1962 the Mars atmosphere was considered to be less than 10% CO_2 while that for Venus was of the order of 10% CO_2 (ref. 5).

$$u\,du + dh = 0 \tag{3}$$

or, in the integrated form,

$$H = \frac{u^2}{2} + h = \text{constant} \tag{4}$$

for the continuity, x-momentum, and energy equations, respectively, where x is the distance behind the shock.

The enthalpy of the mixture of species is

$$h(p, \rho, n_1, n_2, \ldots, n_k) = \sum_{i=1}^{k} n_i \hat{h}_i \tag{5}$$

where n_i is now the number of moles of species i per unit mass of fluid and $\hat{h}_i$ is the enthalpy per mole of species i, or

$$\hat{h}_i = \int_0^T \hat{c}_{p_i}\, dT + \hat{h}_{i_0} \tag{6}$$

where $\hat{c}_{p_i}$ and $\hat{h}_{i_0}$ are the specific heat at constant pressure and enthalpy of formation on a per-mole basis.

The equation of state of the mixture is

$$p = \rho \hat{R} T \sum_{i=1}^{k} n_i \tag{7}$$

where $\hat{R}$ is the universal gas constant per mole (1.98717×10^{-3} kcal/g mole K).

The boundary conditions of the flow equations and the chemical-rate equation are specified immediately behind the shock and are at $x = 0$

$$\frac{\rho_\infty}{\rho_s} \equiv \varepsilon \tag{8}$$

$$u_s = \varepsilon \bar{U} \tag{9}$$

$$p_s = \rho_\infty \bar{U}^2 (1 - \varepsilon) \tag{10}$$

(for a strong shock ($p_\infty \ll p_s$)),

$$h_s = h_\infty + \frac{\overline{U}^2}{2} - \frac{u_s^2}{2} \tag{11}$$

$$n_1 = n_{1_s} = \frac{1}{M_1}, \quad n_2 = n_3 = n_4 = n_5 = n_6 = n_7 = n_8 = 0 \tag{12}$$

(that is, CO_2 passes the shock without reacting), eight species are considered, and M_i is the molecular weight of species i.

For simple illustrative purposes, it is assumed that $\hat{c}_{p_i}/\hat{R}$ is constant, such that the combination of boundary conditions given in equations (9)-(12) and the equation of state, equation (7), yields

$$\varepsilon = \left[2\left(\frac{\hat{c}_{p_1}}{\hat{R}} \right) - 1 \right]^{-1} \tag{13}$$

This completes the boundary conditions behind the shock wave.

The Modified Flow-Field Equations

It is convenient to rearrange the flow-field equations as follows. Equation (5) can be written in the differential form

$$dh = \frac{\partial h}{\partial p} dp + \frac{\partial h}{\partial \rho} d\rho + \sum_{i=1}^{8} \frac{\partial h}{\partial n_i} dn_i \tag{14}$$

which combined with equations (1)-(3) and (5) expressed as equation (6) yields

$$\frac{du}{u} = \frac{\dfrac{1}{\rho(\partial h/\partial \rho)} \displaystyle\sum_{i=1}^{k} \frac{\partial h}{\partial n_i} dn_i}{1 - u^2 \left[\dfrac{(\partial h/\partial p) - (1/\rho)}{-(\partial h/\partial \rho)} \right]} \tag{15}$$

which can be written as

$$\frac{du}{dx} = \frac{u}{1 - \frac{\rho u^2}{p} \cdot \frac{\sum_{i=1}^{k} n_i[(\hat{c}_{p_i}/\hat{R}) - 1]}{\sum_{i=1}^{k} n_i(\hat{c}_{p_i}/\hat{R})}} \left(\frac{\sum_{i=1}^{k} \frac{dn_i}{dx}}{\sum_{i=1}^{k} n_i} - \frac{\sum_{i=1}^{k} \frac{\hat{c}_{p_i}}{\hat{R}} \frac{dn_i}{dx}}{\sum_{i=1}^{k} n_i \frac{\hat{c}_{p_i}}{\hat{R}}} - \frac{\sum_{i=1}^{k} \hat{h}_i^{o} \frac{dn_i}{dx}}{\hat{R}T \sum_{i=1}^{k} n_i \frac{\hat{c}_{p_i}}{\hat{R}}} \right) \tag{16}$$

where dn_i/dx will be expressed subsequently (eq. 28).

From kinetic theory, the ratio of specific heat to the universal gas constant can be written

$$\frac{\hat{c}_p}{\hat{R}} = \frac{\hat{c}_v}{\hat{R}} + 1 = \frac{D+2}{2} \tag{17}$$

where D is the number of degrees of freedom of a molecule of species i. For monatomic gases D = 3 so that $\hat{c}_p/R = 5/2$; for diatomic gases D = 5 so that $\hat{c}_p/R = 7/2$; for triatomic gases D = 7 so that $\hat{c}_p/R = 9/2$.

From statistical mechanics, full vibrational excitation adds 1 to the ratio $\hat{c}_p/\hat{R}$ for diatomic species (refs. 6 and 7). For illustrative purposes it is assumed that $\hat{c}_{p_i}/R$ is fully excited vibrationally. Moreover, for the linear triatomic molecule its value is 7 according to reference 8. Electron excitation is not considered here. Its effect on the thermodynamics of the problem is discussed in reference 9, and will be mentioned subsequently. Its effect on reaction rates is currently being assessed, but is beyond the scope of our present considerations. Thus for full vibrational excitation (where the error in h_i at 5000 K is from ref. 8):

Species, i	CO_2	CO	O_2	O	C
$\frac{\hat{c}_{p_i}}{\hat{R}}$	7	9/2	9/2	5/2	5/2
Error in h_i at 5000 K	0.8%	3%	1%	2%	—

The set of differential equations with their boundary conditions describing the interrelated chemical and flow processes in that part of the flow field behind the shock that is not in chemical equilibrium is thus complete, and we turn our attention to the chemical reactions themselves and the rates at which they proceed.

Chemical Reactions

Behind the shock wave, the reactions assumed for the dissociation, ionization, and recombination of CO_2 and its components are (terminology is identified and discussed as follows):

r		
1	$\overset{(1)}{CO_2 + M \underset{k_{b1}}{\overset{k_{f1}}{\rightleftarrows}} CO + O + M}$	(18)
2	$\overset{(2)}{CO + M \rightleftarrows C + O + M}$	(19)
3	$\overset{(5)}{CO + M \rightleftarrows CO^+ + e^- + M}$	(20)
4	$\overset{(3)\quad(6)}{O + M \rightleftarrows O^+ + e^- + M}$	(21)
5	$\overset{(4)\quad(7)\quad(8)}{C + M \rightleftarrows C^+ + e^- + M}$	(22)

where species 1 through 8 are identified by numbers (1)-(8); r is the reaction number; k_{f_r} and k_{b_r} are its forward and backward reaction rate coefficients, respectively; the ratio k_{f_r}/k_{b_r} is the equilibrium coefficient K_{c_r}; α_{r_i} and β_{r_i} are the stoichiometric coefficients for species i for the reactants and products of reaction r, respectively (unity everywhere here); and M is any collision partner. Although it may be expected that electrons are more efficient than the large particles in producing ionizing reactions, no attempt is made to distinguish between electrons and larger particles as collision partners[2] and

$$n_M = n \tag{23}$$

The rate at which reactions in equations (18)-(22) proceed to the right is characterized by the forward reaction rate coefficient expressed either in the form given by collision theory

$$k_{f_r} = \frac{2PAd^2}{\sigma(s-1)!}\left(\frac{2\pi\hat{R}T}{M^*}\right)^{1/2}\left(\frac{E_{f_r}}{\hat{R}T}\right)^{s-1} e^{-(E_{f_r}/\hat{R}T)} \tag{24}$$

where M* is the reduced molecular weight corresponding to a collision partner M, and is $(1/M_i + 1/M_M)^{-1}$; P is the sterric factor; E_{f_r} is the activation energy for the forward reaction; A is Avagadro's number; d is the average diameter of the colliding pair; s is the number of classical

---

[2]For argon, it is generally agreed that electron collision partners are important to the rate at which equilibrium is approached behind shock waves, although there is little agreement as to the mechanism for initiating ionization (refs. 10-14).

For air at shock speeds up to 10 km/sec, ionizing processes listed in order of decreasing importance are atom-atom collisions, photoionization, electron impact, atom-molecule, and molecule-molecule collisions according to reference 15. However, the importance of electron impact increases with shock speed.

For carbon dioxide, although the ionization rate coefficients with electron collision partners are conceivably an order of magnitude larger than those with large particle collision partners, we do not know either within an order of magnitude and thus do not attempt to distinguish between them.

squared terms of energy contributing to the reaction; and σ is a constant. The corresponding Arrhenius form of the reaction rate coefficient is

$$k_{f_r} = B_{f_r} T^{\alpha_{f_r}} e^{-E_{f_r}/\hat{R}T} \tag{25}$$

The backward reaction rate is included in the equilibrium coefficient[3] expressed in either of two forms

$$K_{c_r} = \frac{k_{f_r}}{k_{b_r}} = \bar{\rho} \prod_{i=1}^{8} \bar{n}_i^{\,b_{r,i}-\alpha_{r,i}} = B_{c_r} T^{\alpha_{c_r}} e^{-(E_{c_r}/\hat{R}T)} \tag{26}$$

where the bar refers to equilibrium values, E_{c_r} refers to energy, and k_{b_r} is the backward reaction rate coefficient. Symbolically, for reaction r

$$\sum_{i=1}^{8} \alpha_{r_i} X_i \underset{k_{b_r}}{\overset{k_{f_r}}{\rightleftarrows}} \sum_{i=1}^{8} \beta_{r_i} X_i \tag{27}$$

Thus equations (1)-(6) are combined with equation (14) to yield equation (15), which can be written in the form of equation (16), for which the chemical rate equation for the rth reaction is needed. By use of equation (27) this can be formed as (refs. 6 and 16)

$$\frac{dn_i}{dx} = \frac{1}{\rho u} \sum_{r=1}^{8} (\beta_{r,i} - \alpha_{r,i}) k_{f_r} \left[\prod_{i=1}^{8} (\rho n_i)^{\alpha_{r,i}} - \frac{1}{K_{cr}} \prod_{i=1}^{8} (\rho n_i)^{\beta_{r,i}} \right] \tag{28}$$

which is used to solve equation (16).

If there are m types of atoms in addition to free electrons, (m + 1) of equation (28) can be replaced by m statements of conservation of atoms (in this case carbon and oxygen) of the form (where a_{z_i} is the number of atoms z in species i)

$$\sum_{i=1}^{8} a_{z_i} n_i = \sum_{i=1}^{8} a_{z_i} n_{i_s} \tag{29}$$

plus one statement that the number of ions equals the number of electrons (only singly ionized species are considered). In applying equation (29), we consider an atomic ion to be equivalent to one atom of the appropriate species. It is noted that equation (29) can be differentiated to provide m values of dn_i/dx for use in equation (16).

[3]The backward reaction rate is a misnomer for three body collisional backward reactions, especially in reaction 1, where the reaction does not proceed in the backward direction in a straightforward manner (ref. 17). Nevertheless, Fay (ref. 18) uses an equivalent reaction, $2CO + O_2 \rightarrow 2CO_2$, while reference 19 uses the reaction $CO + H_2O \rightarrow CO_2 + H_2$ to oxidize CO. But it appears that the reaction for oxidizing CO is a branched chain reaction which is not yet defined (ref. 17). Fortunately for our problem, the backward oxidation reaction for CO is not important, and our results are not affected significantly by our approach.

This completes the set of equations used to solve the nonequilibrium flow behind the shock wave. It is instructive to have the equilibrium conditions which the nonequilibrium properties eventually approach some distance behind the shock wave.

Equilibrium Conditions

The 13 equilibrium properties of interest (designated by a bar) include the flow velocity $\bar{u}$; thermodynamic properties $\bar{p}$, $\bar{r}$, and $\bar{T}$; and chemical concentrations $\bar{n}$, $\bar{n}_1 \ldots \bar{n}_8$. They are obtained from the simultaneous solution of the following 13 algebraic equations. By definition

$$\bar{n} = \sum_{i=1}^{8} \bar{n}_i \tag{30}$$

Statements of conservation of oxygen and carbon atoms are

$$\bar{n}_3 = 2n_{1_s} - 2\bar{n}_1 - \bar{n}_2 - \bar{n}_5 - \bar{n}_6 \tag{31}$$

and

$$\bar{n}_4 = n_{1_s} - \bar{n}_1 - \bar{n}_2 - \bar{n}_5 - \bar{n}_7 \tag{32}$$

The number of moles of electrons equals the number of moles of ions and therefore

$$\bar{n}_8 = \bar{n}_5 + \bar{n}_6 + \bar{n}_7 \tag{33}$$

The equation of state is

$$\frac{\bar{p}}{\bar{\rho}} = \bar{n}\hat{R}\bar{T} \tag{34}$$

The strong shock relations give

$$\bar{p} = \rho_\infty \bar{U}(\bar{U} - \bar{u}) \tag{35}$$

$$n_{1_s}\hat{h}_1^o + \frac{1}{2}(\bar{U}^2 - \bar{u}^2) = \sum_{i=1}^{8} \bar{n}_i \left[\left(\frac{\hat{c}_{p_i}}{\hat{R}}\right)\hat{R}\bar{T} + \hat{h}_i^o\right] \tag{36}$$

$$\bar{u} = \frac{\rho_\infty \bar{U}}{\bar{\rho}} \tag{37}$$

The remaining five equations will not be listed, but are simply equation (26) written for the five reactions given in equations (18)-(22).

Method of Solution

Solutions for the nonequilibrium flow field were obtained by numerical integration of the differential equations, equations (2), (3), (16), (28), subject to boundary conditions, equations (9)-(12), making use of equations (1), (7), and (13). The integration was performed numerically, making use of the Adams-Moulton predictor-corrector variable-step integration scheme (ref. 20). Values of dissociation energy and some of the other physical constants employed in the analysis were either obtained or estimated from information in references 21 and 22. The rate and equilibrium coefficients will be presented subsequently.

The set of 13 equilibrium equations (eqs. (30)-(34) plus the five equations, eq. (26), in which r takes on the value 1-5), some of which are nonlinear and transcendental, were solved in a direct way by the Newton-Raphson method (ref. 23, p. 213). In addition, the results were verified by the method of tracing the locus of roots described in reference 24.

Chemical Kinetics

Reaction-rate coefficients– The estimated values of the constants in the forward reaction-rate coefficients were obtained with the aid of collision theory and are listed in table 10-I in the Arrhenius form (eq. (25)). As in references 9, 25, and 26, it has been assumed for present purposes that $P = s = 1$ in the forward reaction-rate coefficient expression (eq. (24)), and that the activation energy equals the reaction energy. An equivalent assumption is that collision of pairs having total energy in a specific degree of freedom (such as translation) equal to or greater than the reaction energy will result in a reaction (ref. 16). The neglected effect that reaction rates tend to be lowered because not every such collision results in a reaction (i.e., P is actually less than unity) is compensated to some extent by the neglected effect that reaction rates tend to be raised because more than one degree of freedom may participate in the reaction (i.e., s is actually greater than 1). For these reasons (which are discussed more fully in ref. 25) and for lack of experimental evidence, we estimate reaction rates in accord with the above assumption, and the result appears in figure 10-3.

TABLE 10-I.– REACTION-RATE AND EQUILIBRIUM COEFFICIENT DATA (ref. 9)

r	Reaction	B_{f_r}, $\frac{cm^3}{g\ mol\ sec\ K^{\alpha_{f_r}}}$	α_{f_r}	E_{f_r}, $\frac{k\ cal}{g\ mol}$	B_{c_r}, $\frac{g\ mol}{cm^3\ K^{\alpha_{c_r}}}$	α_{c_r}	E_{c_r}, $\frac{k\ cal}{g\ mol}$
1	$CO_2 \rightleftarrows CO + O$	6.955×10^{12}	0.5	125.75	0.17141×10^{13}	–2.6294	135.73
2	$CO \rightleftarrows C + O$	7.238×10^{12}	.5	256.17	$.17713\times10^{7}$	–1.1106	268.57
3	$CO \rightleftarrows CO^+ + e^-$	7.238×10^{12}	.5	323.18	$.41958\times10^{-4}$	.72788	333.44
4	$O \rightleftarrows O^+ + e^-$	7.344×10^{12}	.5	314.05	$.42160\times10^{-10}$	1.9483	307.73
5	$C \rightleftarrows C^+ + e^-$	7.895×10^{12}	.5	259.84	$.39181\times10^{-6}$	1.0415	264.04

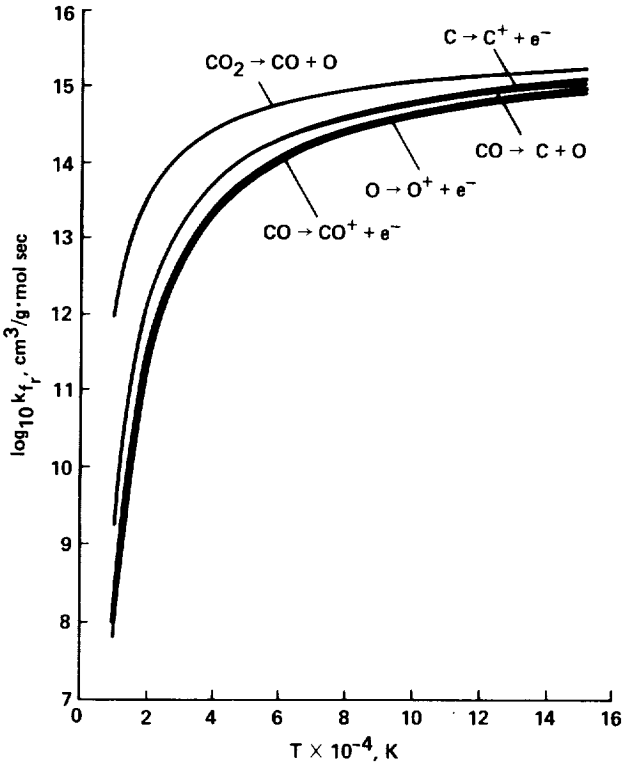

Figure 10-3.– Reaction-rate coefficient estimates (ref. 9).

At a temperature of about 20,000 K, the rate coefficients of the various reactions exhibit rather large overall differences ($\sim 10^2$ for example). Since the colliding pairs (electrons excepted) do not differ greatly in size or molecular weight, the large spread in the rate coefficients at low temperatures is attributable to differences in the activation energy E_{f_r} which appears as part of the exponent in equation (25). At very high temperatures, however, the entire exponent $E_{f_r}/\hat{R}T$ is small so that differences in activation energy are of diminishing importance and $k_{f_r} \sim T^{\alpha_{f_r}}$ ($\sim T^{1/2}$ in accord with the assumption $s = 1$). Thus at a very high temperature, the various reaction-rate coefficient estimates do not differ greatly from one another.

Equilibrium estimates– The equilibrium coefficients were obtained by empirically fitting data obtained from references 21 and 22 by use of the far right side of equation (26). The resulting values of the parameters in equation (26) are shown in table 10-I, and the equilibrium coefficients themselves are shown in figure 10-4.

Chemically Relaxing Flow-Field Results

Profiles of thermodynamic, kinematic, and chemical quantities in the nonequilibrium part of the flow field behind the shock were obtained by integration of equations (2), (3), (16), and (28) subject to their boundary conditions and with the use of the chemical rate coefficient estimates. The solution of the flow-field equations is fully coupled to the chemical relaxation equations.

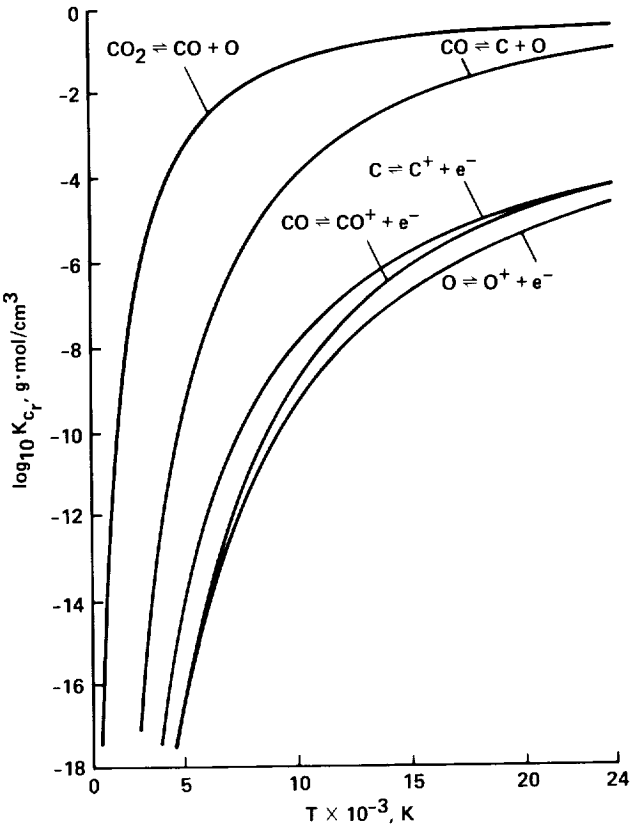

Figure 10-4.– Equilibrium coefficients (ref. 9).

An illustrative solution for a high shock speed and specified ambient density (15 km/sec and $\rho_\infty/\rho_0 = 10^{-4}$, respectively) is shown in figure 10-5. In part (a), all quantities have been made dimensionless with respect to their values immediately behind the shock wave. As chemical relaxation proceeds (increasing x), temperature diminishes monotonically. On the other hand, particle velocity first increases and then decreases while density varies in the opposite way with increasing distance behind the shock wave. This behavior has been discussed in reference 25. The variation of pressure and enthalpy in the flow field is very small, as would be expected from the appendix on flow-field sensitivity estimates which follows.

The mole fraction profiles of the eight chemical species are shown in figure 10-5(b). It is seen that CO_2 vanishes a short distance behind the shock wave. Both CO and O rapidly increase in concentration for a short distance behind the shock wave and then diminish because of further dissociation and ionization processes. Electrons are the predominant species in the flow field for x greater than 0.5 mm.[4] Although the nonequilibrium electron concentration has overshot the equilibrium value, it does approach that value when x is large. This behavior is observed in other examples and in references 9, 25, and 26 as well. It is interesting to see that the concentration of atomic oxygen remains high in much of the relaxation region.

[4]It should be noted that the electron concentration in the nonequilibrium profiles to be presented is probably slightly lower than it should be because doubly ionizing reactions have been neglected. However, for the ambient conditions considered in this analysis, doubly ionized species would tend to disappear as equilibrium is approached.

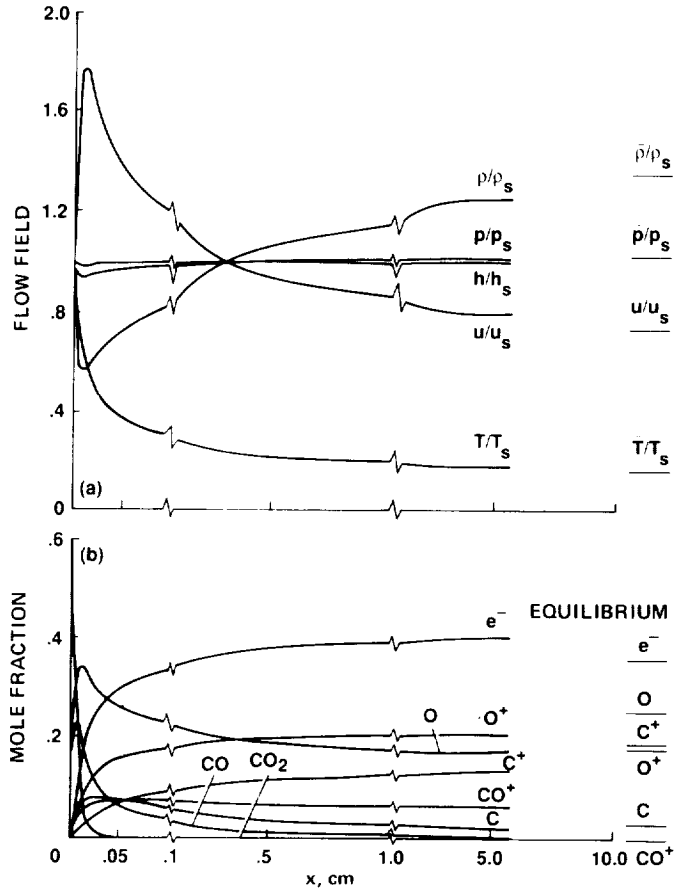

Figure 10-5.– Nonequilibrium profiles; $\overline{U}$ = 15 km/sec, $\rho_\infty/\rho_0 = 10^{-4}$ (ref. 9).

Profiles for a lower shock speed (9 km/sec) at the same low ambient density ($\rho_\infty/\rho_0 = 10^{-4}$) are shown in figure 10-6. It is noted that the density is far from its equilibrium value 10 cm behind the shock. The dominant species in most of the relaxation region is atomic oxygen. Interestingly, it achieves an almost constant value only 3 mm behind the shock in spite of the fact that CO is still dissociating into C and O. Thus the ionization of atomic oxygen keeps pace with the production of atomic oxygen throughout most of the relaxation region. The concentration of electrons and ions is relatively small at this lower shock speed. This figure may be compared with figure 5 of reference 26, in which ionization reactions were neglected. The thermodynamic and flow-field structure is much the same in either case, although the overall concentration of the nonionized species is higher in that reference, as would be expected.

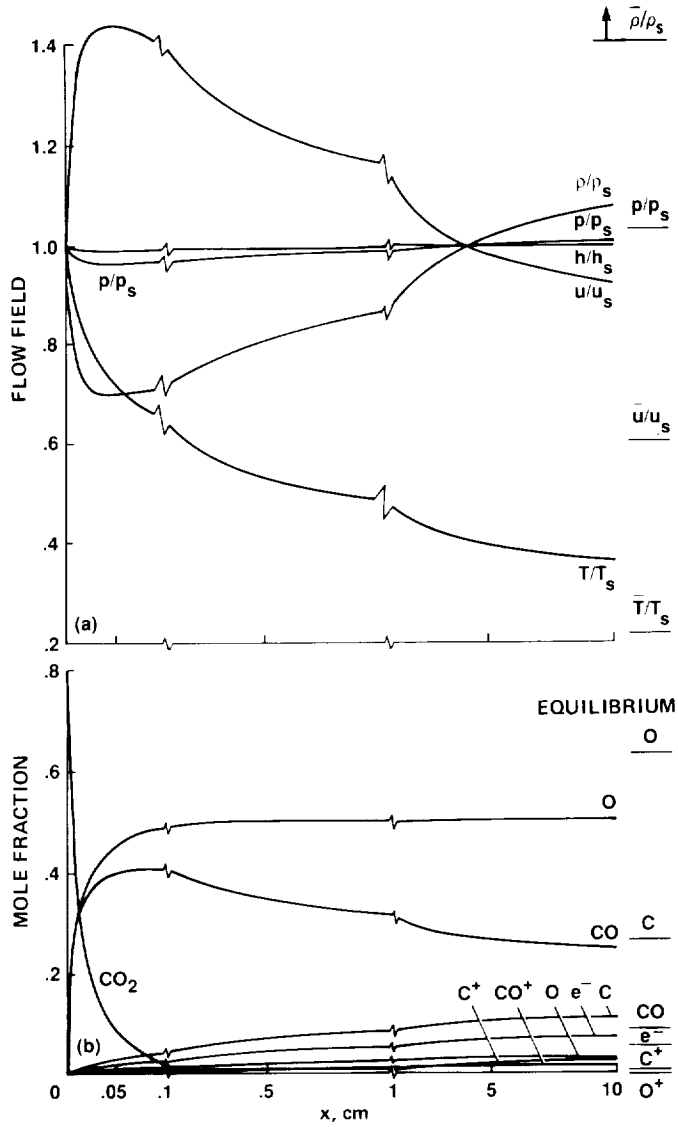

Figure 10-6.– Nonequilibrium profiles; $\overline{U}$ = 9 km/sec, $\rho_\infty/\rho_0 = 10^{-4}$ (ref. 9). (a) Thermodynamic and flow properties. (b) Species concentration.

A solution of a chemically relaxing flow field at much lower velocity is shown in figure 10-7 (from ref. 26). The first part shows the velocity and thermodynamic variation, while the second part shows the chemical species concentrations which correspond. The chemical relaxation distance for this example exceeds 10 cm. Again, pressure and static enthalpy were almost invariant, while temperature, density, and flow velocity varied significantly. The variation of mole fraction of CO and O were identical because there is no ionization, and the equilibrium value of CO_2 was essentially zero. The initial slopes of density and velocity behind the shock tended to depart further from equilibrium before they reversed themselves to approach the equilibrium values. The conditions which govern the initial slopes of these variables are derived in reference 25. Additional solutions are shown in both references 9 and 26.

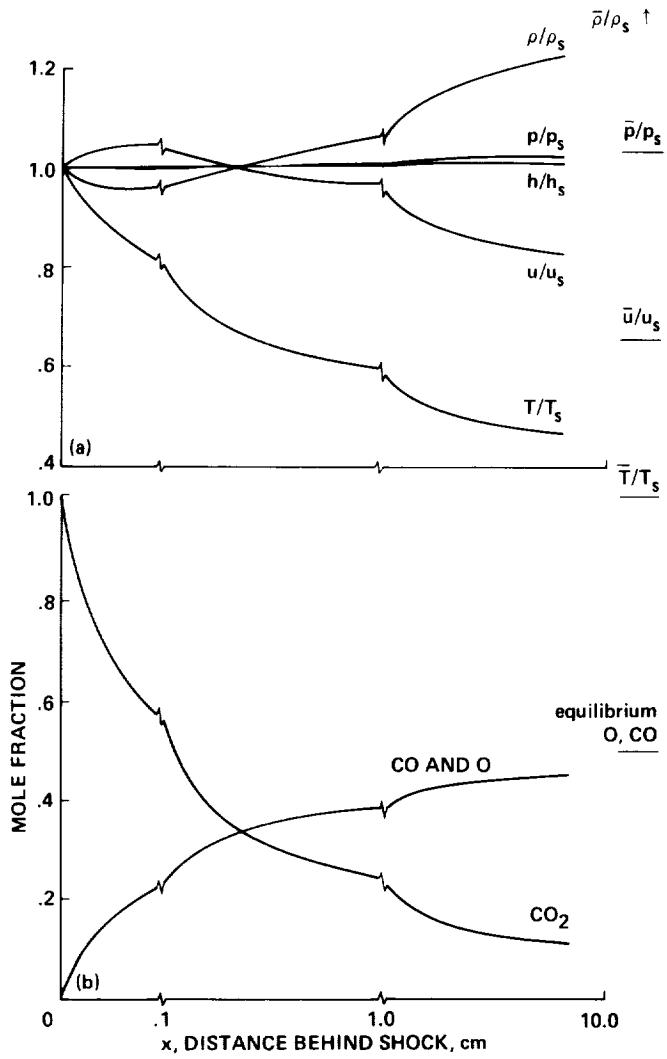

Figure 10-7.– Nonequilibrium flow-field profiles; $\overline{U}$ = 6 km/sec, $\rho_\infty/\rho_0 = 10^{-4}$ (ref. 25). (a) Velocity and thermodynamic properties. (b) Species concentration.

Relaxation Distance

Results of a large number of examples can be summarized in terms of a chemical relaxation distance, the distance behind the shock wave at which the overall chemical relaxation has gone a given fraction (or percentage) toward completion. The fraction of reaction completion is defined in terms of the total change in the number of moles per unit mass occurring in the distance x divided by the total change in number of moles per unit mass required to achieve chemical equilibrium and is

$$\eta = \frac{\sum_{i=1}^{8} n_i - n_{1_s}}{\sum_{i=1}^{8} \bar{n}_i - n_{1_s}} = \frac{n - n_{1_s}}{\bar{n} - n_{1_s}} \tag{38}$$

In all of the examples that were studied, n, and thus η, were monotonic throughout the relaxation region in spite of the fact that n_i is not monotonic for several species.

The relaxation distances for $\eta = 0.5$, 0.8, and 0.9 were obtained. The distance for 50% reaction completion is quite short, not more than 10^{-1} cm for the entire range of shock conditions studied (refs. 9 and 25). The distance for 80% reaction completion is roughly a decade higher than for 50% completion. Finally, the relaxation distance for 90% reaction completion is quite large, ranging from 10^{-2} to 10^{2} cm over the entire range of shock conditions, as shown in figure 10-8.

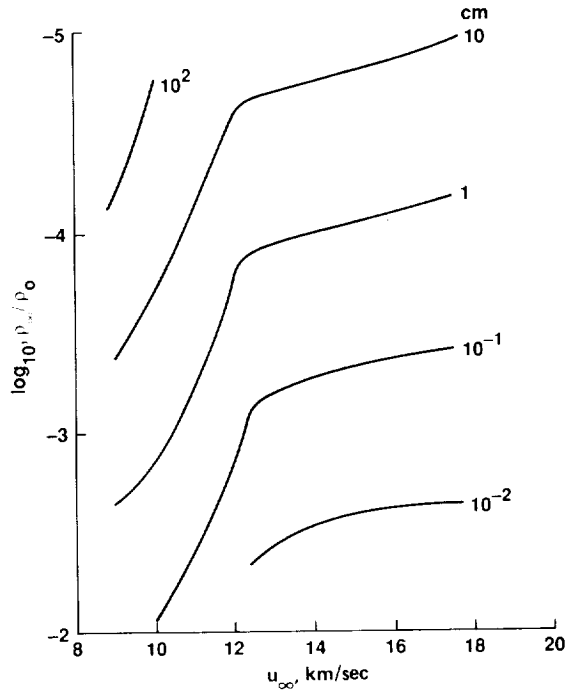

Figure 10-8.– Relaxation distance for 90% reaction completion (ref. 9).

It is worth mentioning that these relaxation distances are not very sensitive to the reaction-rate assumptions. It was noted in reference 25 that a two to three order of magnitude change in reaction rates results in only a one order of magnitude change in relaxation distance.

Concluding Remarks

The interdependent dissociative and ionizing chemical rate processes behind shock waves in carbon dioxide have been examined for shock speeds from 6 to 20 km/sec at ambient densities of 10^{-2} to 10^{-4} ratioed to standard Earth atmosphere density. Because of a lack of reaction-rate data for carbon dioxide and its components, reaction-rate coefficients have been estimated with the aid of some simplifying assumptions and collision theory. The effects of chemical relaxation on the flow field behind normal shock waves have been studied by use of the coupled fluid flow and chemical rate equations.

Results have been presented for both the equilibrium and nonequilibrium regimes behind the shock wave. At the higher speeds (15 km/sec), electrons are the predominant species in most of the nonequilibrium chemical relaxation region. Atomic oxygen is the predominant species in the lower-speed examples and is also present in high concentration at the higher speeds.

Equilibrium concentration of electrons is presented here in terms of mole fraction of the mixture and in terms of number of electrons per unit volume as in reference 9. The equilibrium concentration varies from about 5×10^{14} to 5×10^{18} electrons/cm^3 for a shock speed of 9 km/sec at a density ratio of 10^{-4} standard Earth atmosphere density to 20 km/sec at a density ratio of 10^{-2}. Results are also presented in the form of a chemical relaxation distance behind the shock wave.

The nonequilibrium results obtained are considered to be preliminary estimates for a number of reasons. They are based on estimates of chemical reaction-rate coefficients. Indeed, it is not certain that the reactions studied are the correct reactions. Not all of the conceivable reactions have been included in the analysis. The equilibrium results are in a somewhat better situation in that they are independent of any estimates of reaction rate coefficients. They are not influenced significantly by internal excitation phenomena for the high shock speeds considered.

Interestingly enough, the study of reference 9 shows that the influence of the state of internal excitation on most of the chemically relaxing flow field is small insofar as this influence is manifested through the thermodynamics of the problem. However, it is possible that dissociation and ionization processes may proceed more readily from excited states, in which case the internal state of excitation would be important in the entire chemical relaxation region.

Reference 9 shows that there is a small part of the nonequilibrium flow field just behind the shock wave in which the state of internal excitation of the various species has a significant influence on the flow properties. This region is likely to be important to nonequilibrium radiation problems; thus a knowledge of both the chemical and internal relaxation is important at high temperatures.

Knowledge of the behavior of these common chemical substances at elevated temperature is meager in spite of the fact that they have long been important species in many combustion problems. The behavior of these substances has acquired new significance relating to planetary entry problems. There is much to be learned from both the macroscopic and the subatomic points of view.

APPENDIX

FLOW-FIELD SENSITIVITY ESTIMATES

In the strict sense, all of the flow-field quantities ρ, u, p, h, and T and species concentration vary in the reacting flow field behind the shock. Some of these quantities, however, will vary more than others. The purposes of the following discussion is to show the relative variation of the quantities ρ, u, p, and h in the flow field behind the shock.

At some distance x behind the shock, the ratio of local density to the density immediately behind the shock is defined as g.

$$\frac{\rho}{\rho_s} \equiv g \tag{A1}$$

Thus the fractional change in ρ from ρ_s is

$$\frac{\rho - \rho_s}{\rho_s} = \frac{\Delta\rho}{\rho_s} = g - 1 \tag{A2}$$

The corresponding change in u is from equation (1)

$$\frac{\Delta u}{u_s} = \frac{1}{g} - 1 \tag{A3}$$

Similarly, from equation (2) the change in p (noting that $p_s \approx \rho_\infty \bar{U}^2 = \rho_s u_s \bar{U}$) is

$$\frac{\Delta p}{p_s} = \varepsilon\left(1 - \frac{1}{g}\right) \tag{A4}$$

where $\varepsilon = \rho_\infty/\rho_s$. Finally, the change in h if we assume that $h_\infty \ll h_s$ and $\bar{U}^2 \gg u_s$ and make use of the integrated form of equation (3) is approximately

$$\frac{\Delta h}{h_s} = \varepsilon^2\left(1 - \frac{1}{g^2}\right) \tag{A5}$$

If ε is of the order 10^{-1}, equations (A-1)-(A-5) show that a significant change in density in the relaxing flow behind the shock produces a significant change in velocity, but that pressure and static enthalpy are relatively unaffected. This qualitative behavior can be inferred without defining the specific relaxation process—which could be chemical, thermodynamic, or thermochemical. The process is expressed through other relationships which involve the equation of state, rate expressions, etc.

It is useful to make these estimates because they highlight the main features of the results before we have them. But more importantly, they sort out the most sensitive variables, density and fluid velocity (and temperature), which are affected significantly by relaxation processes, but not static

enthalpy and pressure. These notions are helpful in devising numerical schemes to compute relaxing flows efficiently. Thus the insensitivity of pressure means that numerical methods need not be tailored to allow for large pressure excursions. Making sensitivity estimates is a good habit to acquire. Such estimates in advance should influence the methodology, and may determine whether a computed solution is obtained at all.

REFERENCES

1. Park, C.: Radiation Enhancement by Non-Equilibrium in Earth's Atmosphere. AIAA Paper 83-0410, 1983.

2. Allen, R. A.; Rose, P. H.; and Camm, J. C.: Nonequilibrium and Equilibrium Radiation at Super-Satellite Re-Entry Velocities. AVCO Everett Research Lab. Res. Report 156, Sept. 1962.

3. Davy, W. C.; Park, C.; and Arnold, J. O.: Radiometer Experiment for the Aeroassist Flight Experiment. AIAA Paper 85-0967, June 1985.

4. Seiff, A.; and Kirk, D. B.: Structure of the Atmosphere of Mars in Summer at Mid-Latitudes. J. Geophys. Res., vol. 82, no. 28, Sept. 1977, pp. 4364-4378.

5. Kaplan, Lewis D.: A Preliminary Model of the Venus Atmosphere. Tech. Rep. 32-379, Jet Propulsion Lab., Pasadena, CA, Dec. 1962.

6. Vincenti, W. G.: Calculations of the One Dimensional Nonequilibrium Flow of Air Through a Hypersonic Nozzle. Stanford Univ. Depart. of Aeronaut. Eng. Interim Report to AEDC, May 1961.

7. Vincenti, W. G.; and Kruger, C. H.: Introduction to Physical Gas Dynamics. Wiley, 1965.

8. Wilson, A. H.: Thermodynamics and Statistical Mechanics. Cambridge Univ. Press, 1957, p. 136.

9. Howe, J. T.; and Sheaffer, Y. S.: Chemical Relaxation Behind Strong Normal Shock Waves in Carbon Dioxide Including Interdependent Dissociation and Ionization Processes. NASA TN D-2131, 1964.

10. Bond, J. W.: Structure of a Shock Front in Argon. Phys. Rev., vol. 105, March 15, 1957, pp. 1683-1694.

11. Petschek, H.; and Byron, S.: Approach to Equilibrium Ionization Behind Strong Shocks in Argon. Ann. Phys., vol. 1, no. 3, June 1957, pp. 270-315.

12. Weymann, H. D.: On the Mechanism of Thermal Ionization Behind Strong Shock Waves. Tech. Note BN-144, Inst. Fluid Dynamics and Appl. Math., Univ. Maryland, 1958.

13. Blackman, V. H.; and Niblett, G. B. F.: Ionization Processes in Shock Waves. Fundamental Data Obtained From Shock Tube Experiments, A. Ferri, ed. (AGARDograph no. 41), Pergamon Press, 1961, p. 221.

14. Frood, D. G. H.: The Problem of Ionization Relaxation for Moderately Strong Shocks in Monatomic Gases. AGARD Specialist Meeting, High Temperature Aspects of Hypersonic Flow, April 3-6, 1962. T.C.E.A., Rhode St. Genese, Belgium.

15. Lin, S. C.; and Teare, J. D.: Rate of Ionization Behind Shock Waves in Air. II. Theoretical Interpretation. Res. Rep. 115, AVCO Everett Research Lab., Sept. 1962.

16. Penner, S. S.: Chemical Reactions in Flow Systems. Butterworths Scientific Pub., London, AGARDograph 7, 1955.

17. Lewis, Bernard; and Von Elbe, G.: Combustion Flames and Explosions of Gases. Second ed., Academic Press, 1961, p. 5.

18. Fay, J. A.: Molecular Thermodynamics. Addison Wesley, 1965, p. 238.

19. Hirschfelder, J. O.; Curtiss, C. F.; and Bird, R. B.: Molecular Theory of Gases and Liquids. Wiley, 1954, p. 824.

20. Hildebrand, F. B.: Introduction to Numerical Analysis. McGraw-Hill Book Co., 1956.

21. Gilmore, F. R.: Properties of Air to 24,000°K. Rand Corp. RM-1543, 1955. (ASTIA Doc. AD-84052.)

22. Raymond, J. L.: Thermodynamic Properties of Carbon Dioxide to 24,000°K with Possible Application to the Atmosphere of Venus. Rand Corp. RM 2292, Nov. 1958.

23. Scarborough, J. B.: Numerical Mathematical Analysis. Fifth ed., Johns Hopkins Press, 1958.

24. Klopfenstein, R. W.: RCA Tech. Rep. PTR 949, Sarnoff Res. Ctr., RCA, Princeton, NJ.

25. Howe, John T.; Viegas, John R.; and Sheaffer, Yvonne S.: Study of the Nonequilibrium Flow Field Behind Normal Shock Waves in Carbon Dioxide. NASA TN D-1885, 1963.

26. Howe, John T.; and Viegas, John R.: Dissociative Relaxation of CO_2 Behind Normal Shock Waves. Paper presented at Interplanetary Missions Conf. of 9th Ann. Amer. Astronaut. Soc. Meeting, Los Angeles, Jan. 1963.

CHAPTER 11

HYPERVELOCITY AEROMANEUVERING FLIGHT AT VERY HIGH ALTITUDES

In recent years, interest has developed in the use of vehicles that can transport payloads from one orbit to another. Such vehicles could be space-based. The capability of such vehicles is greatly enhanced if propulsive maneuvers near Earth can be replaced in part or almost entirely by a shallow dip into the upper atmosphere where the maneuver is performed aerodynamically. Such vehicles are called aeroassisted space transfer vehicles (ASTV), or by some, aeroassisted orbital transfer vehicles (AOTV).

Thus a payload returned by these vehicles from a distant orbit (geosynchronous orbit (GEO)), for example, to a low Earth orbit (LEO) would experience an aerodynamic drag maneuver in the upper atmosphere before skipping out to rendezvous with another object in a low Earth orbit. Or the ASTV could be returning at hypervelocity from an orbit considerably farther than geosynchronous; from a libration center (a gravitational null point in the Earth/moon system) which is at lunar distance from Earth, or from a location outside the Earth/moon system altogether. Payloads may be enhanced greatly (doubled or even more) by the use of the drag aeromaneuver in the upper atmosphere rather than by a propulsive deceleration near Earth.

A second kind of aeromaneuver would transfer a payload from one orbit to a second orbit at a different orbital-plane inclination angle. The corresponding maneuver would involve a lateral banked turn which is performed using aerodynamic lift. Or there may be a combined lift and drag maneuver in the upper atmosphere by aeromaneuvering space vehicles..

In a primarily drag-type aeromaneuver, the vehicle configuration would be large and blunt, like an umbrella. Because of the blunt-bow shock wave, the heating to the vehicle would be radiative to a large extent. But the turning aeromaneuver requires a lifting capability, and would be more of a slender-winged configuration. Correspondingly, aerodynamic heating would tend to be high on the slender nose and on the leading edges of wings and control surfaces. It would be primarily convective heating.

A third vehicle concept studied in recent years is ground-based, would fly into orbit (perhaps), and eventually would return to land on Earth. It, too, would perform hypervelocity aeromaneuvers which would have to be done at very high altitude because of the heating problem. The primary heating may be on the ascent, but the technology of the lifting ASTV would be relevant to this concept at high altitude.

This family of vehicle concepts requires extensive research to form the broad technology base of a new generation of aerospace vehicles. It is necessary to understand real gas flow fields, aerodynamic heating, improved reusable materials and structures, thermal protection systems, efficient aeromaneuvering strategies, and guidance and control problems; and if the vehicle requires an air-breathing propulsion system—engine, fuel, and engine-airframe integration problems need to be defined and solved. That is, every relevant technology needs advancement.

Insofar as the ASTVs are concerned, some features of the flight environment can be assessed by extrapolating our current technology base. Consider, for example, the atmospheric drag maneuver by a blunt vehicle wherein radiative transfer is a dominant heating mechanism. We can infer the kinds of problems that need to be addressed. Figure 11-1 (adapted from Howe, ref. 1) depicts the return of a vehicle from GEO, and from a distance of five times GEO (5×GEO)—which is about 40% of the distance to

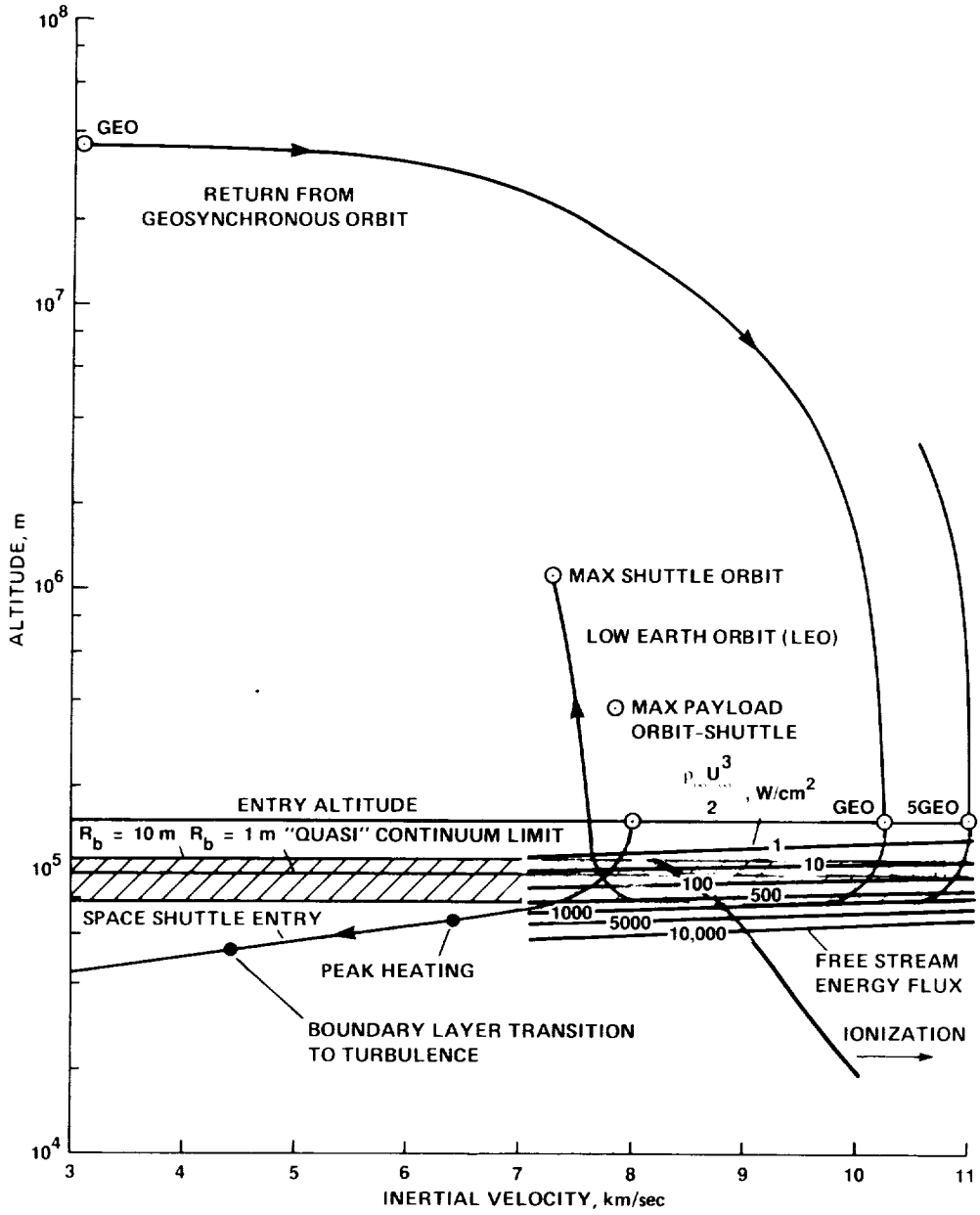

Figure 11-1.– Aeroassisted orbital transfer from distant orbits.

the moon. The figure would be essentially the same if the lunar distance return were shown. The ordinate is a log scale of altitude in meters, and the abscissa is the inertial speed relative to a rotating atmosphere in kilometers per second. The vehicle leaves GEO (about 35,000-km altitude) and arrives at the "top" of the atmosphere at an inertial speed of about 10 km/sec, decelerates by atmospheric drag to low Earth orbital speed of about 7 km/sec, exits the atmosphere, and rendezvous with the Space Shuttle (for example). The perigee in the atmosphere is at an altitude of about 80 km. Entry from 5×GEO or lunar return would be about the same because Earth escape speed is about 12 km/sec.

A Space Shuttle (STS) entry is shown for reference. Since the entry speed of an STS is about 7 to 8 km/sec, we see that the ASTV entry is about twice as energetic as the Shuttle entry (energy varies with the square of velocity). Moreover, since the ASTV decelerates at a much higher altitude than the Shuttle, the ASTV resides in a very energetic rarefied environment.

The two horizontal lines called "quasi-continuum limit" pertain to altitudes below which continuum theory can be applied with minor modifications (ref. 2), especially to large blunt objects. For the 10-m nose radius, that altitude is 112 km. Below an altitude of 103 km, continuum theory may be applied without modification. Most of the deceleration and heating occurs in the full continuum region because the air molecules need to be present to develop significant aerodynamic effects.

Some of the real gas phenomena that should be considered are shown in the figure. An important family of lines of constant free-stream energy flux ($\rho_\infty U^3/2$) in watts per square centimeter are shown on the right. They vary inversely with altitude in an exponential manner. They serve as an index to the severity of aerodynamic heating and of thermal-protection requirements. Experience has shown (ref. 3) that maximum heating can be as much as 10% of the free-stream energy flux. Thus, if a thermal-protection material can withstand 50 W/cm^2 without the need to be refurbished, these lines indicate that flight below an 80-km altitude is not advisable unless there is a significant improvement in thermal-protection materials. Detailed computations of heating rates indicate that these estimates are about correct.

Another important line on the figure is labeled the "ionization" threshold. Many mechanisms by which the hot gas cap can emit thermal radiation exist to the right of the line. Indeed, thermal radiation is the dominant heating mechanism for the blunt drag configuration. Moreover, the radiation is from air that is not in thermal or chemical equilibrium, as will be shown. Although vehicles have flown through this region routinely, the peak heating was at lower altitudes in a regime where the air is in equilibrium behind the bow shock wave. Thus the total contribution of nonequilibrium radiation to Apollo heating was about 1% and to the Space Shuttle about 5%; but for the drag-configured ASTV it is estimated to be about 50% (or more). Park (refs. 4 and 5) has explored ways to model the physical-chemical phenomena that produce nonequilibrium radiation.

Aeroassisted space transfer vehicle problems have been studied by approximate but highly sophisticated methods. Configurations for both high drag (lift/drag ratios of 0.3) and high lift (L/D ~ 2) have been defined that are stable, controllable, and of minimum weight (refs. 6, 7, and 8). Two configurations are shown schematically in figure 11-2. Each configuration can be placed into low Earth orbit in a single Shuttle payload. Note that the drag configuration is large (27 m in diameter), and is very blunt. It is not symmetrical, so that lateral aerodynamic forces can be generated to maneuver the vehicle aerodynamically to some extent, to make trajectory corrections.

The lifting surface shown on the bottom of the figure is an early version (Davies and Park (ref. 8)). A payload would be placed in the dead-air region, along with some propulsive capability.

The development of significant lift at high altitude is very difficult, so the lifting surface must be very carefully designed to accomplish that. Although simple Newtonian theory provided the basic shape shown, it was refined by applying rarefied viscous forces locally and integrating them over the entire surface. The configuration shown was the best of several configurations studied, which all had a common dimension and payload. This shape was the only one which produced the necessary aerodynamic stabilizing moments. Thus both a high-drag and a high-lift configuration appear to be the best candidates for ASTVs. No real use for an intermediate configuration was found. A combination of moderate drag

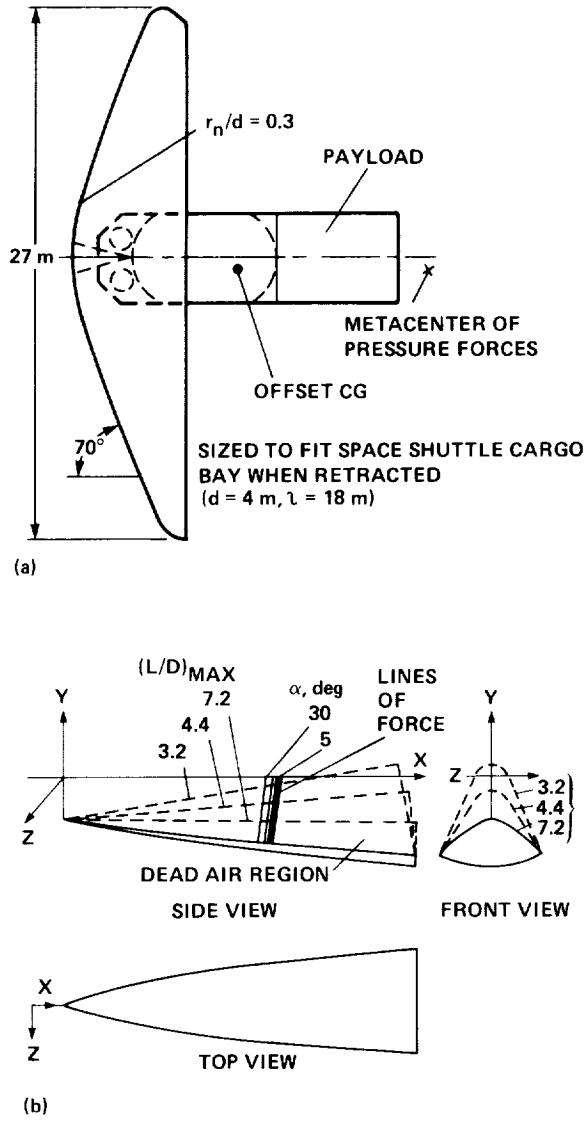

Figure 11-2.– ASTV configurations. (a) High-drag configuration. (b) High-lift surface.

and moderate lift does not appear to do anything well. Admittedly, these configurations appear somewhat ugly, but in time they acquire an undefinable appeal.

Both structural and thermal-protection weights have been estimated for these configurations (refs. 9 and 10). Moreover, clever flight strategies have been devised and mission capabilities were performed. A few of the round-trip mission payloads for the drag configuration are shown in figure 11-3. Although GEO is in the equatorial plane, other orbits are inclined to that, so that both an aerodynamic-drag maneuver and a propulsive plane-change maneuver (far from Earth) were involved in the analysis. Delivery (open bar), retrieval (shaded bar), and combined delivery-retrieval (solid bar) payloads for round-trip missions from low Earth orbit (Shuttle-compatible) were examined. It is noteworthy that the retrieval missions have a large payload capability which nonintuitively increases with distance in space. Although it is not shown, about 23 tons can be retrieved from a libration center (at lunar distance) by a vehicle which leaves the Space Shuttle weighing 30 tons (the Shuttle payload capacity). The retrieval

MAXIMUM PAYLOAD CAPABILITY FOR DELIVERY, RETRIEVAL, AND COMBINED DELIVERY-RETRIEVAL ROUND-TRIP SORTIE MISSIONS WITH 480-sec SPECIFIC IMPULSE ROCKET ENGINE

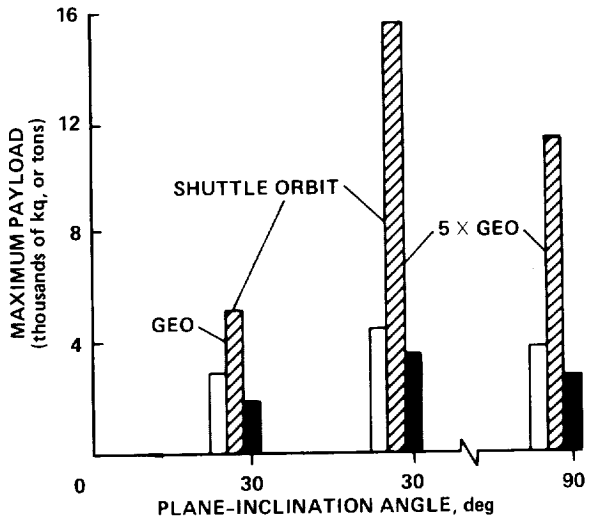

Figure 11-3.– ASTV mission payload capability.

time is less than 2 days. It may be advantageous to store space assets in space for retrieval in an emergency—rather than to store them on the ground where they cannot be deployed, even in bad weather.

The many mission analyses revealed a number of nonintuitive advantageous results. Reduction of aerodynamic loads and heating by use of multiple passes through the upper atmosphere has also been examined. Excursions to other planets have been studied as well (refs. 11 and 12). The simultaneous use of propulsion and aeromaneuvers has been considered (synergetic maneuvers).

For the drag configuration, an Aeroassist Flight Experiment (AFE) is being planned whereby a highly instrumented one-third-scale model will be launched by the Space Shuttle, driven into the atmosphere propulsively, perform the drag aeromaneuver, and skip out of the atmosphere to be retrieved by the Space Shuttle. Figure 11-4 shows two candidate ASTV configurations for AFE. The configuration on the right is the NASA Johnson Space Center (JSC) shape partially modified at the extreme diameter. As shown at the bottom of the figure, models of these configurations were flown in the Ames Ballistic Range Facility (by P. Intrieri). The resulting shadowgraphs show three things. First, the models are stable (they fly forward without tumbling and tend to seek a fixed orientation). Second, the shock waves and flow-field structure are visible to some extent. Third, the windows of the facility need to be replaced.

It appears likely that the modified JSC configuration will be chosen for the flight test. The radiometer experiment to be carried aboard the flight test vehicle is of special interest. The principle investigator for the experiment is W. C. Davy of NASA Ames Research Center (ref. 13). Radiative emission from the hot gas cap is especially interesting in the context of this monograph. Figure 11-5 shows a diagram of an ASTV with some shock-wave structure. The left side of the figure shows schematic profiles of temperature, chemical species, and radiative emission along the forward stagnation streamline. Immediately behind the bow shock, the gas is out of thermal equilibrium, and three temperatures are shown to characterize the gas locally; the translational (or large-particle) temperature, a vibrational temperature for diatomic species, and an electron temperature. If there are many diatomic

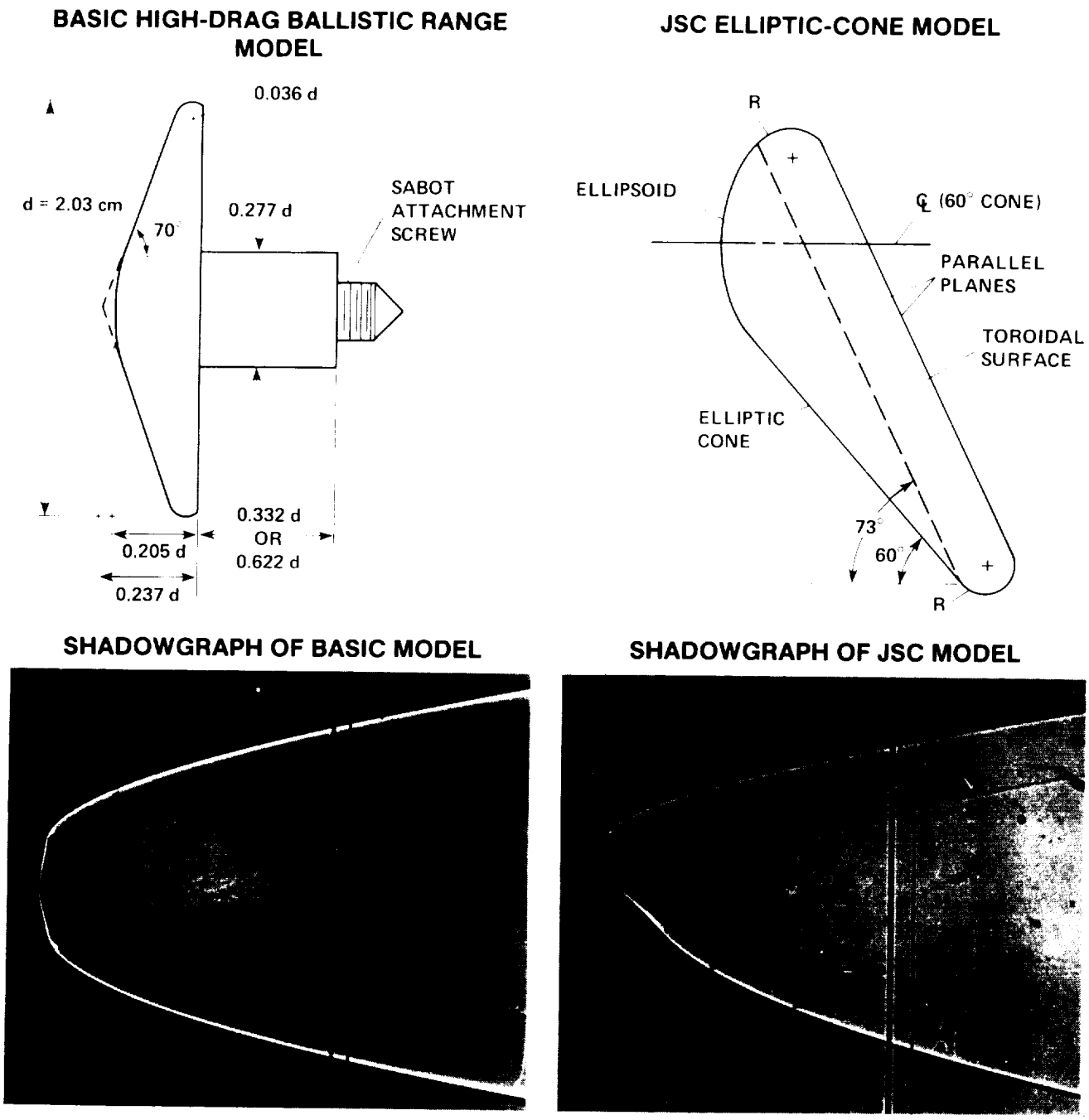

Figure 11-4.– AFE candidate configurations.

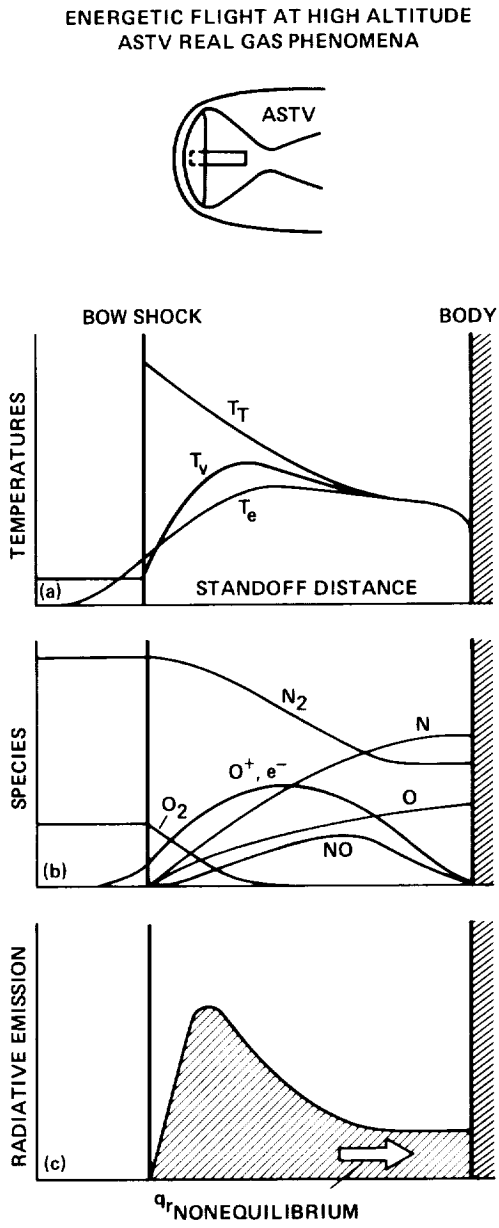

Figure 11-5.– Thermochemical nonequilibrium flow-field schematic.

species (O_2, N_2, NO, and their ions), many vibrational temperatures may need to be used. Behind the bow shock, air composition is atmospheric N_2 and O_2. These dissociate and ionize as flow proceeds toward the body until they (like temperature) approach a thermochemical equilibrium state. The corresponding radiative emission "overshoots" because of excessive temperature, excited chemical species, and a nonequilibrium chemical composition. Again, as the flow proceeds toward the body, the radiation tends toward a thermochemical equilibrium value. The extent of the thermochemical nonequilibrium effect was estimated in figure 10-1 where the three curved lines labeled 1 cm, 10 cm, and 1 m indicate the distance behind a normal shock wave required for the thermochemical state to approach within 10% of the equilibrium value. The estimates were made by use of shock-tube experiments by Allen, Rose, and Camm (ref. 14), correlated in figure 10 of that reference, which is reproduced in figure 11-6, where

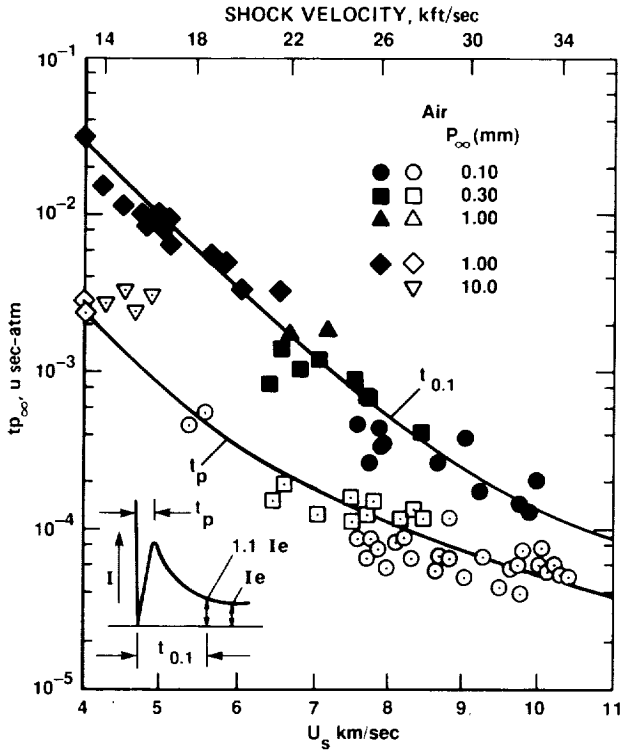

Figure 11-6.– Observed time duration of liminous front and time to peak in air plotted versus shock speed. The time $t_{0.1}$, in the laboratory coordinate system, is taken to a point at which the radiation intensity has decayed to a level 10% above equilibrium. Initial pressure is used as a scaling factor to correlate data obtained at different values of p_∞. The solid curves are empirical fits. (Adapted from ref. 14.)

the radiative emission overshoot of figure 11-5(c) appears schematically as the inset. Based on figure 11-6, if the estimates in figure 10-1 are related to a large, blunt, drag-configured ASTV, about 10 cm of the flow behind the shock is not in thermochemical equilibrium at peak heating at an altitude of 80 km as was noted in Chapter 10.

Flight in this domain is not well understood. In the context of the formalism used in this text, the extension to thermochemical nonequilibrium has been outlined in reference 15. Perhaps it is noteworthy that under the heading "The Formal Kinetic Theory of Polyatomic Molecules," that reference has a subheading, "Energy Interchange between Translational and Internal Motions is Difficult." The treatment considers a two-temperature model related by what is essentially an additional "equation of change" (see Chapter 4 of the present text). The transport expressions are also affected by the internal motion of the molecules. Difficult though it may be, a self-consistent formalism is advantageous. Significantly, the extension of the present formalism to include the effects of thermochemical nonequilibrium combines all fluid dynamic, physical, chemical, transport, radiative-transfer, and thermodynamic processes in a set of nonlinear, coupled, partial differential-integro equations. The terms in these equations can be ranked in a self-consistent way that identifies the important terms and eliminates the myriad terms that can be neglected, as was discussed in Chapter 4. The efforts to compute the many physical and chemical coefficients are reduced correspondingly. And when all is done, one can say with some confidence that this reduced set of equations is applicable and is self-consistent.

At present, we can get some estimate of the importance of thermochemical nonequilibrium from the lines mentioned in figure 10-1. For example, we may say that for the manned Mars return aerocapture maneuver, the effects may be negligible because less than a centimeter of the thick shock layer is affected near peak heating (see also ref. 16).

Aside from the simple estimates we have made of the boundaries within the flight domain wherein thermochemical nonequilibrium effects may be significant (see fig. 10-1), a more detailed treatment of the topic is beyond the scope of the present work. The reader is referred to reference 17, which deals with some aspects of the problem. The AFE flight experiment is expected to increase understanding of hypervelocity flight at very high altitudes, and the forces and heating that occur because of real gas effects.

Finally, with respect to hypervelocity lifting configurations, flight at very high altitudes reduces convective heating (to the leading edges of lifting and control surfaces because of rarefied gas effects), which leads to concepts that can result in vehicles that do not have to be refurbished after each flight. But although aerodynamic heating is diminished at high altitude, so is lifting capability. Figure 11-7 (private communication, M. E. Tauber, Ames Research Center, 1986) shows the degradation of the lift/drag ratio above about 80 km (the perigee determined by materials that can withstand the heating rates) for the Space Shuttle. The lifting ASTV shows some promise of improvement over the performance shown, although not a great improvement. Clearly, there is a tradeoff between tolerable heating and acceptable lift. At this writing, that tradeoff appears to allow up to a 40° low Earth orbital plane change capability by aeromaneuvering. This is a remarkable capability—a propulsive capability of 60° orbital plane change requires about as much propulsion as it takes to launch from Earth to low Earth orbit.

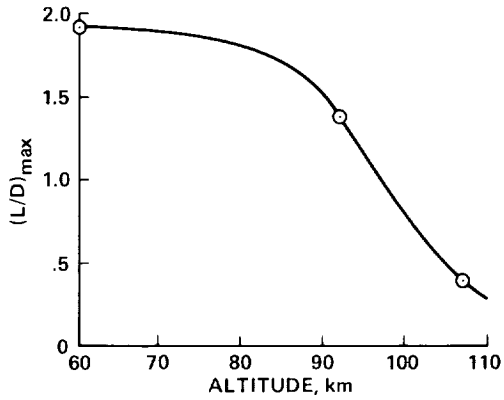

Figure 11-7.– Space Shuttle maximum lift/drag ratio variation (approximate).

For our purposes, we see that the real gas aerodynamic environment at hypervelocity opens a new era of flow-field research. Mach number is relatively unimportant; it deals primarily with compressibility effects of the gas. Velocity is very important; it deals with the energetics of the gas—thermal, chemical, and physical effects associated with real gas behavior. These effects are only partially understood, and at very high altitudes these effects become increasingly complicated.

Thus, hypervelocity flight, especially at high altitude, requires both computational and experimental research. Computation must include more than configuration, momentum, simple energy relations, and an equation of state. It must include these and much more. We might envision the complexity of solving a set of state, momentum, energy, diffusion, electric-charge conservation, finite-rate

chemistry, thermal relaxation, and electrodynamic equations that are nonlinear and coupled to one another. We must acquire the basic physical and chemical inputs to these equations, including transport phenomena; radiative properties; and physical, chemical, and thermal rate data. The development of computational codes may proceed as shown in figure 11-8. The three columns are intended to indicate a melding of computational fluid dynamic techniques, real gas aerothermodynamics, and physical and chemical inputs.

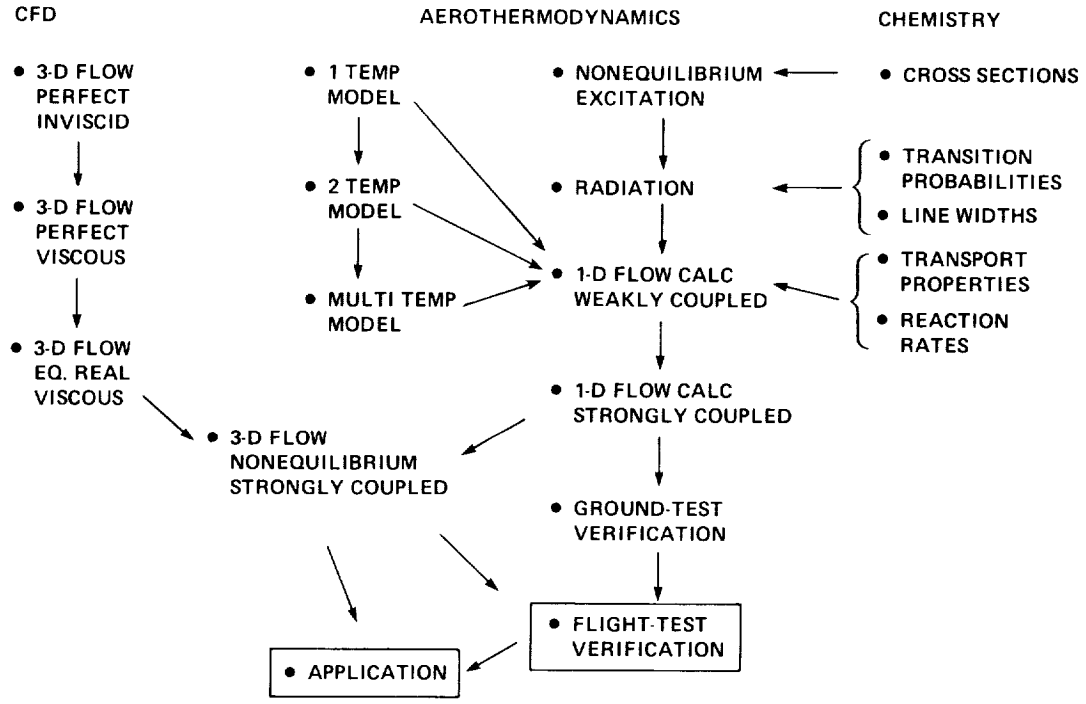

Figure 11-8.– Computational aerothermodynamic code development.

Moreover, hypervelocity simulation experimentally requires high-enthalpy research facilities. Heating test air in a reservoir by chemical means is not adequate. Gas flow through a high-enthalpy facility must be characterized and understood in detail. Moreover, computational developments must be validated by experiment (as well as flight test—fig. 11-8).

In proceeding into these poorly understood areas, we must be very thoughtful. A continual assessment of where we stand both computationally and experimentally is essential. Computationally, we must order the terms in the equations of change for configurations and flight conditions that are appropriate. We must reexamine transport and transfer phenomena and realize that both are affected by thermochemical rate processes. We must assess what problems are crucial to solve (some problems may be interesting, but unimportant) and make sure there is a correspondence among computation, ground-based tests, and flight tests. There must be a correspondence between codes and experiments—or we may be attempting to validate codes that are not valid. Experimentally, we must carefully consider the limits of ground-based experiments. A test in a wind tunnel in which the test gas is near liquifaction may be importantly different from flight at the same Mach number. Problems abound. But we are on the threshold. The possibilities of space utilization for science, commerce, and national and international goals are enormous.

REFERENCES

1. Howe, J. T.: Introductory Aerothermodynamics of Advanced Space Transportation Systems. J. Spacecraft Rockets, vol. 22, no. 1, Feb. 1985, p. 19.

2. Hayes, W. D.; and Probstein, R. F.: Hypersonic Flow Theory. Applied Mathematics and Mechanics, Vol. 5. Academic Press, 1959.

3. Page, W. A.; Compton, D. L.; Borucki, W. N.; Cliffone, D. L.; and Cooper, D. M.: Radiative Transport in Inviscid, Nonadiabatic Stagnation Region Shock Layers. AIAA Progress in Astronautics and Aeronautics: Thermal Design Principles of Spacecraft and Entry Bodies, Vol. 21. J. T. Bevans, ed., Academic Press, 1969, pp. 75-114.

4. Park, C.: Radiation Enhancement by Nonequilibrium in Earth's Atmosphere. J. Spacecraft Rockets, vol. 22, no. 1, 1985, pp. 27-36.

5. Park, C.: Assessment of Two-Temperature Kinetic Model for Dissociating and Weakly-Ionizing Nitrogen. J. Thermophys. Heat Transfer, vol. 2, no. 1, Jan. 1988, pp. 8-16.

6. Menees, G. P.: Thermal-Protection Requirements for Near-Earth Aeroassisted Orbital-Transfer Vehicle Missions. AIAA Paper 83-1513, 1983.

7. Menees, G. P.: Design and Performance Analysis of an Aeromaneuvering Orbital-Transfer Vehicle Concept. IAF Paper 85-139, 1985.

8. Davies, C. B.; and Park, C.: Aerodynamic Characteristics of Generalized Bent Biconic Bodies for Aero-Assisted Orbital-Transfer Vehicles. AIAA Paper 83-1512, 1983.

9. Menees, G. P.; and Park, C.: Design and Performance Analysis of a Conical-Aerobrake Orbital-Transfer Vehicle Concept. AIAA Paper 84-0410, 1984.

10. Davies, C. B.; and Park, C.: Optimum Configuration of High-Lift Aeromaneuvering Orbital Transfer Vehicles in Viscous Flow. AIAA Paper 85-1059, 1985.

11. Tauber, M. E.; and Yang, L.: The Heating Environment During Martian Descent. AIAA Paper 88-2671, 1988.

12. Menees, G. P.: Aeroassisted Vehicle Design Studies for a Manned Mars Mission. IAF/IAA Paper 87-433, Oct. 1987.

13. Davy, W. C.; Park, C.; and Arnold, J. O.: Radiometer Experiment for the Aeroassist Flight Experiment. AIAA Paper 85-0967, 1985.

14. Allen, R. A.; Rose, P. H.; and Camm, J. C.: Nonequilibrium and Equilibrium Radiation at Super-Satellite Re-Entry Velocities. AVCO Everett Research Laboratory Research Report 156, Sept. 1962.

15. Hirschfelder, J. O.; Curtiss, C. F.; and Bird, R. B.: Molecular Theory of Gases and Liquid. Wiley, 1954, p. 505.

16. Park, C.; and Davies, C. B.: Aerothermodynamics of Sprint-Type Manned Mars Mission. AIAA Paper 89-0313, Jan. 1989.

17. Park, C.: Nonequilibrium Hypersonic Aerothermodynamics. Wiley, 1990.

NASA
National Aeronautics and Space Administration

Report Documentation Page

1. Report No.	2. Government Accession No.	3. Recipient's Catalog No.
NASA RP-1249		

4. Title and Subtitle	5. Report Date
Hypervelocity Atmospheric Flight: Real Gas Flow Fields	November 1990
	6. Performing Organization Code

7. Author(s)	8. Performing Organization Report No.
John T. Howe	A-90143
	10. Work Unit No. 506-40-91

9. Performing Organization Name and Address	11. Contract or Grant No.
Ames Research Center Moffett Field, CA 94035-1000	
	13. Type of Report and Period Covered Reference Publication
12. Sponsoring Agency Name and Address	14. Sponsoring Agency Code
National Aeronautics and Space Administration Washington, DC 20546-0001	

15. Supplementary Notes

Point of Contact: John T. Howe, Ames Research Center, MS 229-3, Moffett Field, CA 94035-1000
(415) 604-6113 or FTS 464-6113

16. Abstract

Flight in the atmosphere is examined from the viewpoint of including real gas phenomena in the flow field about a vehicle flying at hypervelocity. That is to say, the flow field is subject not only to compressible phenomena, but is dominated by energetic phenomena. There are several significant features of such a flow field. Spatially, its composition can vary by both chemical and elemental species. The equations which describe the flow field include equations of state and mass, species, elemental, and electric charge continuity; momentum; and energy equations. These are nonlinear, coupled, partial differential equations that have been reduced to a relatively compact set of equations in a self-consistent manner (which allows mass addition at the surface at a rate comparable to the free-stream mass flux).

The equations and their inputs allow for transport of these quantities relative to the mass-averaged behavior of the flow field. Thus transport of mass by chemical, thermal, pressure, and forced diffusion; transport of momentum by viscosity; and transport of energy by conduction, chemical considerations, viscosity, and radiative transfer are included. The last of these complicate the set of equations by making the energy equation a partial integrodifferential equation.

Each phenomenon is considered and represented mathematically by one or more developments. The coefficients which pertain are both thermodynamically and chemically dependent. Solutions of the equations are presented and discussed in considerable detail, with emphasis on severe energetic flow fields. For hypervelocity flight in low-density environments where gaseous reactions proceed at finite rates, chemical nonequilibrium is considered and some illustrations are presented. Finally, flight where the flow field may be out of equilibrium, both chemically and thermodynamically, is presented briefly.

17. Key Words (Suggested by Author(s))	18. Distribution Statement
Hypervelocity flight; Planetary entry; Mass addition; Real gas phenomena; Aerodynamic heating; Gaseous radiative transfer; Reacting flows	Unclassified-Unlimited Subject Category - 34

19. Security Classif. (of this report)	20. Security Classif. (of this page)	21. No. of Pages	22. Price
Unclassified	Unclassified	260	A12

NASA FORM 1626 OCT 86

For sale by the National Technical Information Service, Springfield, Virginia 22161

NASA-Langley, 1990

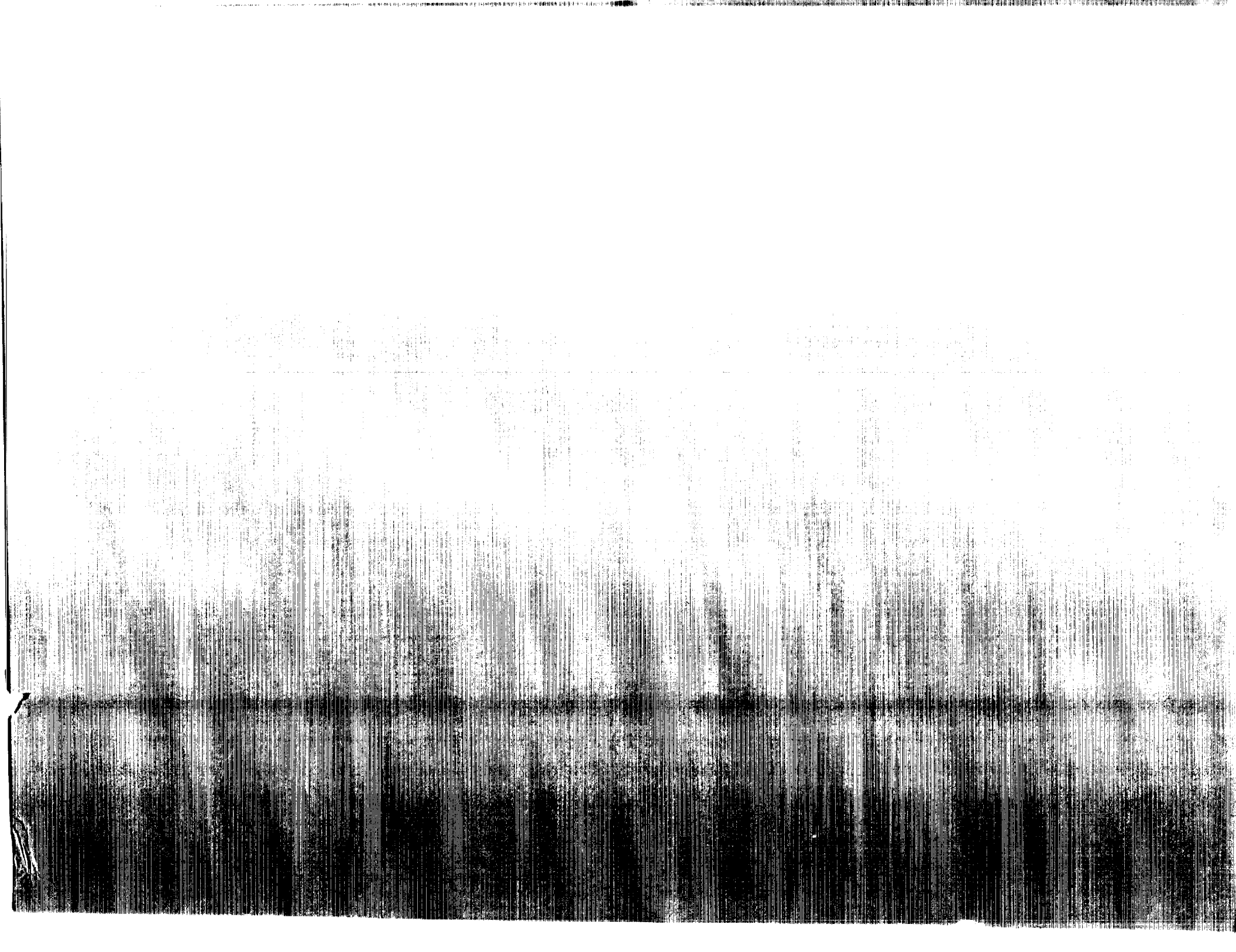

National Aeronautics and
Space Administration
Code NTT-4

Washington, D.C.
20546-0001

NASA